Mechanisms of Sill and Dyke Intrusion

Simon Allen Kattenhorn

Submitted in fulfillment of the requirements for the degree of Masters of Science

in the Department of Geology and Applied Geology

University of Natal (Durban)

1994

PREFACE

This thesis documents the research done by the said author, and is the author's own original work, unless specifically indicated to the contrary in the text.

ABSTRACT

Mechanisms of sill and dyke intrusion require an understanding of fracture growth, stress distributions and intensities, dilation, intrusion rates, hydraulic pressure, host-rock effects, en echelon fracture arrays, and flow direction. The methods of previous studies have been applied to natural sill and dyke examples of the Karoo Igneous Province in northern Natal.

An en echelon array of Jurassic dolerite sills occurs within Permian Ecca sediments along the Mhlatuze River, west of Empangeni. Dolerite emplacement occurred as two intrusive phases. The first phase resulted in thick, coarse-grained dolerite sills. The second phase produced relatively thinner, fine-grained sills. The intrusion of fine-grained dolerite into older sills is demonstrated by abrupt variations in the whole-rock and mineral geochemistry profiles across the sills. Syn-crystallisation effects such as crystal settling and fractionation, and post-crystallisation hydrothermal activity is also manifested in the mineralogical and geochemical changes across the sills. The fine-grained dolerite is associated with xenolithic dolerite which represents a contaminated magma propagation front of the fine-grained dolerite. The higher viscosity of the xenolithic dolerite hindered propagation, and was thus overtaken and engulfed by the main magma pulse.

Consistent sinistral offsetting of sill segments is interpreted to be the result of a fingered sill periphery intruding an en echelon fracture array. Dilation of individual segments, or fingers, occurred simultaneously. Subsequent interaction of near-tip stresses induced inwardly propagating curvature of adjacent segments in the array. Resultant linkage has produced a stepped-sill geometry; sill propagation and flow directions were orthogonal to the plane of linkage.

The flow direction is confirmed by shape preferred-orientations of acicular mineral grains within the chilled margins of the sills, indicating the direction of flow to be perpendicular to the plane of the en echelon array, and parallel to strike directions of offset surfaces that link adjacent sill segments.

Multiple dyke intrusion is examined at an outcrop of the Rooi Rand Dyke Swarm, along the Pongola River. Individual intrusive episodes are identifiable on the basis of chill-zone relationships. The pattern along the Pongola River suggests that younger intrusive episodes frequently intrude through the centres of older dykes. A three-dimensional analysis of en echelon dykelet segments allows a re-construction of the dilation history, and provides an explanation for the development of blunt-ended intrusion segments. Mineral geochemistry anomalies around dyke tips suggests possible facilitation of incipient fracture via decreases in mineral strengths manifested by geochemical changes. A statistical digital analysis of micro-phenocryst orientations within chilled dyke margins is shown to provide a viable method to ascertain magma flow directions within dykes, and may thus be a useful tool for future investigations.

CONTENTS

1. INTRODUCTION

The Karoo Igneous Province constitutes one of the largest continental flood basalt provinces in the world (Duncan, 1987). The lava remnants cover a surface area of approximately 140,000 km^2, principally in the Stormberg mountains of the eastern Cape Province, the Drakensberg mountains of Lesotho and Natal, the Lebombo mountains of northern Natal, Swaziland and the eastern Transvaal, the Nuanetsi region of Zimbabwe, and the Etendeka area of northern Namibia (Duncan, 1987). A consistent K/Ar age of 193 ± 5 m.y. (Fitch and Miller, 1984) for basalt lavas marks the flood basalt event as contemporaneous with the breakup of eastern Gondwana during the Jurassic.

Flood basalt volcanism was thus associated with a period of continent-wide crustal tension. This resulted in large-scale fracturing of the crust and extensive dolerite dyke and sill intrusion across Southern Africa, with total thicknesses exceeding total sediment thicknesses in some of the deeper parts of the Karoo basin (Brink, 1983). South Africa thus hosts much potential for the study of the mechanisms by which dykes and sills form.

In this thesis, detailed studies are described for dolerite sills along the Mhlatuze River, near Empangeni, and the Rooi Rand Dyke Swarm along the Pongola River, both sites situated in northern Natal.

An en echelon array of dolerite sills occurs within Ecca sediments along the Mhlatuze River, west of Empangeni. Consistent offsetting of sill segments is interpreted to be the result of a fingered sill periphery intruding an en echelon fracture array. Dilation of individual segments, or fingers, occurred simultaneously, with later linkage that resulted in a number of linkage-related features such as bent and rotated bridges, and a stepped-sill geometry. The classic interpretation of propagating sills stepping upwards towards the surface is thus abandoned in the interpretation of this sill array. Evidence provided by magma flow-induced phenocryst alignment is also presented.

The Rooi Rand Dyke Swarm outcrop along the Pongola River provides an excellent opportunity for the study of such intrusion features. Much of the investigation of this location is focussed on the determination of age relationships, intrusion mechanics, and to a greater extent an interpretation of magma flow direction and characteristics. The method of digital analysis has been applied to the determination of phenocryst orientation trends, producing successful results that give an indication of magma flow direction.

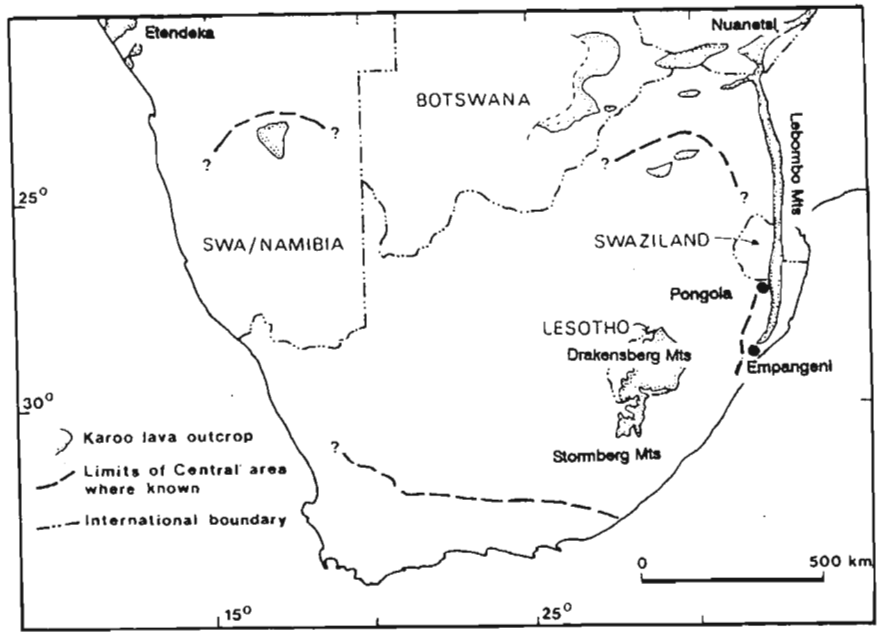

Figure 1.1. *Distribution of mafic lavas of the Karoo Igneous Province (after Marsh and Eales, 1984). Field locations at Empangeni and Pongola in northern KwaZulu-Natal are shown.*

The majority of the work in this thesis stems from previous work on the mechanics of intrusion by authors such as Jaeger and Cook (1969), Pollard (1969, 1973, 1976, 1978, 1987), Nicholson and Pollard (1985) and Gudmundsson (1983, 1984, 1990), amongst others. This, in turn, followed on from the breakthroughs made throughout this century in the field of fracture mechanics by authors such as Inglis (1913), Griffith (1924), Hubbert and Willis (1957), Irwin (1958), Murrell (1963, 1964), Jaeger (1967) and Kanninen and Popelar (1985), amongst others. Such has been the scale of development in the application of fracture mechanics principals to geology, that a detailed synopsis of these developments has been deemed necessary as an important introduction to the investigation undertaken in this thesis. The next two chapters thus deal exclusively with these developments, and provide a detailed account of the theories pertaining to the mechanisms of igneous intrusion, and the basic principles of fracture mechanics from which they were derived. Many of the premises of these two chapters will be applied to the field studies from northern Natal, indicating the extent of applicability and introducing methods by which existing principles may be tried and, if necessary, contested.

2. FRACTURE MECHANICS AND GEOLOGICAL APPLICATIONS

2.1 Introduction

The mechanisms by which dykes and sills develop and propagate are best understood through basic fracture mechanics. The mechanism of fracture initiation and growth in engineering materials may frequently be applied to the situation of a crack in the Earth's crust, taking into account the effects of magma pressure, local and regional stress conditions, as well as host rock properties. Kanninen and Popelar (1985) define fracture mechanics as "an engineering discipline that quantifies the conditions under which a load-bearing body can fail due to the enlargement of a dominant crack contained in that body." Developments in the field of fracture mechanics will be reviewed in this chapter, with emphasis on the geological applicability. Appendix 1 defines the symbols and nomenclature as well as defining principal stresses.

2.2 Navier-Coulomb Criterion

The Navier-Coulomb criterion for brittle failure considers the concept of shear failure in a material, as described by Price (1975). A surface will undergo shear failure when the shear stress acting on the surface is sufficiently large to overcome the cohesive strength of the material in addition to the frictional resistance to movement. The failure criterion may be expressed as

$$\tau = S + \mu_i \sigma_n \qquad (2.1)$$

where τ is the shear stress acting on the shear surface, S is the cohesive strength, μ_i is the coefficient of internal friction, and σ_n is the stress acting normal to the surface.

Robson and Barr (1964) used the Navier-Coulomb criterion to generate a graph of σ_{1c} versus σ_{3c}, showing regions of tensile failure, shear failure and no failure (Figure 2.1). The criterion for shear failure versus tensile failure is that $\sigma_{1c} = 2.169\ T_0$ (line 1 in Figure 2.1) where T_0 is the uniaxial tensile strength of the material.

A useful application of the Navier-Coulomb criterion is the prediction of the angle T that a shear plane will have with respect to the maximum principal stress (Price and Cosgrove, 1990)

$$2\theta = 90^o - \phi_i \qquad (2.2)$$

where ϕ_i is the slope of the Mohr failure envelope. The Navier-Coulomb criterion provides some fundamental relationships between failure and stress conditions within a material; however, there are certain irregularities in its geological applications, as mentioned by Roberts (1970). As mean stress $(\sigma_{1c} + \sigma_{3c})/2$ increases with depth, the

stress difference (σ_{1c} - σ_{3c}) required for shear failure becomes very large. Furthermore, T_0 has a value of 0.5 kbar or less, thus restricting tensile failure to the uppermost parts of the crust. This is contrary to the fact that known dilational intrusions extend down to an upper mantle source. These discrepancies resulted in the need for a different approach to the concept of fracture in a solid. Such was the Griffith Theory of crack propagation.

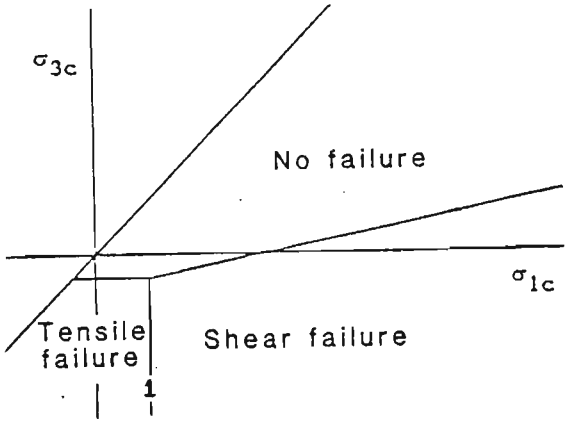

Figure 2.1. *A σ_{1c} versus σ_{3c} diagram representing failure criteria based on the Navier-Coulomb criterion of brittle fracture. Here, σ_{1c} is the maximum compressive principal stress, and σ_{3c} is the minimum compressive principal stress (from Robson and Barr, 1964).*

2.3 Griffith Theory

The Griffith Theory of crack propagation differs from the Navier-Coulomb criterion in that the solution for the state of stress in a material takes into account the effect of cracks and microscopic flaws. Inglis (1913) considered an elastic plate containing an elliptical hole with major axis 2*a* and minor axis 2*b* (Figure 2.2A). Assuming a uniform uniaxial regional **tensile** stress σ^r_1 acts in the plane of the plate at right angles to the major axis, and far from the hole, Inglis (1913) noted that a tensile stress acts at the point A (Figure 2.2A) at the tip of the elliptical hole. If the hole is not near the edge of the plate, and the material is not strained beyond its elastic limit, the value of this local tensile stress σ^a_{11} is

$$\sigma^a_{11} = \sigma^r_1\left[1 + \frac{2a}{b}\right] \tag{2.3}$$

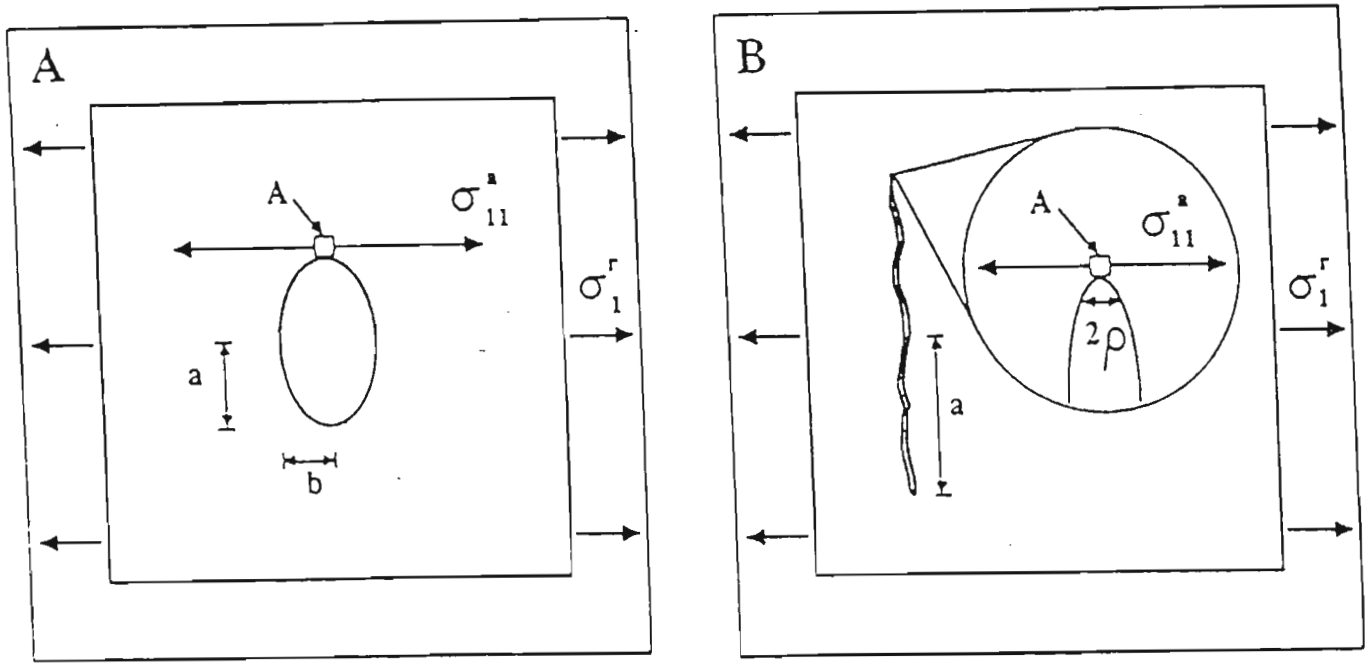

Figure 2.2. *A: An elliptical flaw in an elastic plate, according to the elastic model of Inglis (1913). The regional uniaxial tensile strength $\sigma^r{}_1$ produces a local tensile stress $\sigma_1{}^a{}_1$ at the flaw tip (A). Dimensions of the flaw are major axis 2a and minor axis 2b. B: Stress conditions around a crack in an elastic plate. The crack tip has radius of curvature ρ (from Pollard, 1987).*

Inglis (1913) further indicated that the stress at the tip of any slender hole (Figure 2.2B) may be approximated by the relation

$$\sigma^a_{11} \approx 2\sigma^r_1\left(\frac{a}{\rho}\right)^{1/2} \tag{2.4}$$

where ρ is the radius of curvature at the end of the hole. For the crack to begin propagating, the tensile strength T_a of the material must equal the stress at the crack tip, $\sigma_1{}^a{}_1$. At this point, therefore, the regional stress loading the plate would be

$$\sigma^r_1 \approx \frac{T_a}{2}\left(\frac{\rho}{a}\right)^{1/2} \tag{2.5}$$

Griffith (1924) adopted a similar approach to Inglis, but with emphasis on energy considerations. From atomic bonding theory, the theoretical tensile strength of an ideal brittle solid is T ≈ E/10, where E is Young's modulus. The vast discrepancy between theoretical and observed material tensile strengths was ascribed by Griffith (1924) to intense local stress concentrations at the tips of microscopic elliptical flaws. Solution of the stress concentration around an elliptical crack set in a two-dimensional, thin plate subject to a tensile stress σ_T (Figure 2.3A) suggests that crack propagation development occurs when the tensile stress at the tip equals the atomic bonding strength.

This occurs when

$$\sigma_T = [2AE/\pi a]^{1/2} \quad (2.6)$$

where A is the surface energy of the flaw and 2a is the length of the major axis of the elliptical flaw. Griffith (1924) obtained values for the critical stress (s_T) which were in good agreement with measured tensile strength values for large specimens of glass. The propagation of flaws in a plate subject to biaxial compression was also considered (Figure 2.3B).

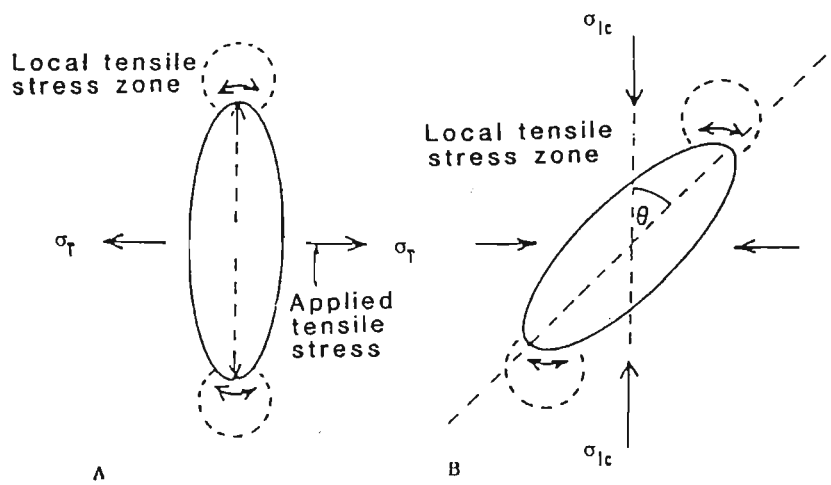

Figure 2.3. *"Griffith" elliptical flaws under conditions of A: uniaxial tensile stress (σ_T) and B: biaxial compressive stress (Price and Cosgrove, 1990).*

Griffith (1924) assumed that randomly oriented, elliptical microflaws were spaced on the plate in such a manner that the stress field associated with each flaw was independent of that of any neighbouring flaw. It was shown for a fracture oriented oblique to the applied stresses that there exists a tensile zone at the tip having a maximum when

$$\cos 2\theta = -(\sigma_1 - \sigma_3) / 2(\sigma_1 + \sigma_3) \quad (2.7)$$

where θ is the angle between the long axis of the flaw and the minimum principal **tensile** stress, σ_3. Furthermore, provided that $\sigma_1 \neq \sigma_3$ and $(3\sigma_1 + \sigma_3) < 0$, the tensile stress at the tip reaches the critical value of propagation initiation when

$$(\sigma_1 - \sigma_3)^2 + 8T(\sigma_1 + \sigma_3) = 0 \quad (2.8)$$

where T is the tensile strength, and σ_1 and σ_3 are positive when the stresses are tensile (Griffith, 1924). Equation

(2.8) indicates a non-linear relationship between the stresses, and can be expressed as a Mohr envelope (Murrell, 1958) with the equation

$$\tau^2 + 4T\sigma_n - 4T^2 = 0 \tag{2.9}$$

2.4 Fracture Propagation

2.4.1 Single cracks

Griffith (1924) considered fracture propagation in terms of energy conservation, with emphasis on fracture surface energies. For the situation of an elliptical hole in an elastic plate subject to a uniform tension (Figure 2.2A), the strain energy of the elastic solid, U_E, is

$$U_E = \pi a^2 \left(\sigma_1^r\right)^2 \left[\frac{(1-\upsilon)}{2\mu}\right] \tag{2.10}$$

where μ is the elastic shear modulus and ν is Poisson's ratio. The potential energy of the crack surface, U_S, may be related to the surface energy per unit area γ by

$$U_S = 4a\gamma \tag{2.11}$$

where 2a is the length of the crack surface. In order for there to be a total conservation of energy, the increase in surface energy of a growing crack must be accompanied by a net decrease in the potential energy of the loading device and the elastic solid. Griffith (1924) thus calculated the remote stress loading the plate to be

$$\sigma_1^r = \left[\frac{4\gamma\mu}{\pi a(1-\upsilon)}\right]^{1/2} \tag{2.12}$$

in order for fracture propagation to commence. A fracture may propagate under conditions of tension or compression. Where tension is the dominant force, the fracture lengthens in a plane perpendicular to the tensile stress (Price, 1975). Under compression, however, a fracture will only propagate along the regions of maximum tensile stress, such as those illustrated in Figure 2.3B. Brace and Bombolakis (1963) simulated Griffith crack behaviour, using an elliptical hole cut into a sheet of photoelastic material, and revealed that fractures propagate along a curved trajectory. Experiments on glass showed the fractures curving into parallelism with the direction of principal compression before ceasing to propagate.

Ingraffea and Ko (1981), working on fracture parameters for rock, considered cracks oriented with their long axes

at an angle θ to the maximum **compressive** stress σ_{1c}, as in Figure 2.3B. It was found that the cracks behave like elliptical holes for $\theta \leq 45^{o}$, when fracture propagation initiation occurs near the ellipse tip. For $\theta > 45^{o}$, the cracks are a poorer approximation to an ellipse, and in extensively microflawed material such as rock, the area over which the tensile stress concentration acts increases rapidly with T. At the same time, however, the stress gradient within this widening region undergoes a significant decrease. Under such conditions, failure tends to be controlled by slight local material weaknesses such as grain boundaries or intracrystalline defects.

2.4.2 Multiple cracks

For an elastic solid containing a number of cracks, certain approximations can be made to explain macro-failure. Griffith (1924) showed that each crack can be considered to be isolated from its nearest neighbour (Figure 2.4).

Griffith (1924) showed that if σ^{r}_1 and σ^{r}_3 satisfy the conditions $3\sigma^{r}_1 + \sigma^{r}_3 > 0$ (where σ^{r}_1 and σ^{r}_3 are positive when the stresses are tensile), then the critical crack will be perpendicular to σ^{r}_1. The tip will be under greatest tension, with a magnitude given by equation 2.3. If, however, $3\sigma^{r}_1 + \sigma^{r}_3 < 0$, the critical crack will be oblique to σ^{r}_1.

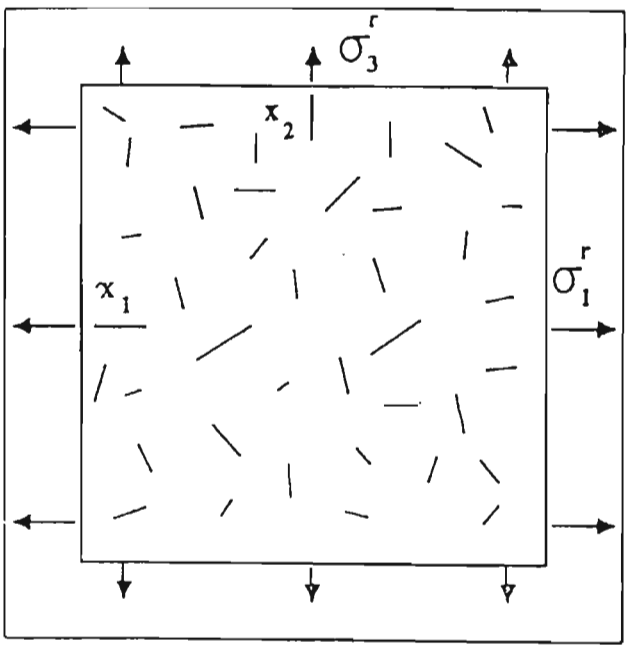

Figure 2.4. *The Griffith model for an elastic solid containing a number of non-interacting cracks. The maximum tensile stress is σ^{r}_1 and the minimum tensile stress is σ^{r}_3 (from Pollard, 1987).*

Stresses at the point of rupture can be expressed in terms of the uniaxial tensile strength, T_u, of the material, because at the point of rupture, $\sigma^{r}_1 = T_u$. Adapting (2.4), the local stress at the crack tip at the initiation of propagation is then (Pollard, 1987):

$$\sigma_{11}^{a} \approx 2T_u\left(\frac{a}{\rho}\right)^{1/2} \qquad (2.13)$$

(compare to equation 2.4). It must be noted that T_u is a bulk property of the material undergoing rupture, whereas the term T_a as used in equation 2.5, is a local property of the material at the crack tip. In summary, the two conditions of failure are thus governed by the criteria

$$\sigma^r_1 = T_u \qquad \text{for } 3\sigma^r_1 + \sigma^r_3 > 0 \qquad (2.14a)$$

$$(\sigma^r_1 - \sigma^r_3)^2 + 8T_u(\sigma^r_1 + \sigma^r_3) = 0 \qquad \text{for } 3\sigma^r_1 + \sigma^r_3 < 0 \qquad (2.14b)$$

Equation 2.14b follows from equation 2.8. The above criteria are convenient in that they obviate the need for the crack dimensions.

2.5 Effect of Hydraulic Pressure

Thus far, all hypothetical loading stresses proposed in the formulation of the fracture propagation criteria have been considered as being tensile, with σ^r_1 as the maximum tensile stress. Other authors (eg. Roering, 1968; Lajtai, 1969; Hancock, 1972) have found preference with the use of compressive regional stresses (σ_{1c} maximum and σ_{3c} minimum) to demonstrate the mechanisms of fracture propagation in the geological context. This is acceptable considering the fact that any sub-surface fracture within the crust would ordinarily be subject to conditions of tri-axial compression, rather than tension. In the context of this investigation, which will be dealing with features such as igneous dykes and sills, it must, however, be remembered that the fractures involved would be subject to the added effect of an internal hydrostatic, or perhaps magmatic, pressure. This would lead to an overall state of localised tension around such a fracture.

The concept of "effective stress" was introduced by Anderson (1938). In order to take into account the hydrostatic pressure P, acting on the internal boundaries of a dilating fracture, Anderson expressed the resultant stress conditions acting on the external boundaries of the fracture as $\sigma_x - P$ (where σ is compressive and x = 1,2 or 3). Prior to this, Stevens (1911) recognised the need to take internal magma pressure P into account when considering an intruding dyke. This would entail replacing σ^r_1 with $(P - S_h)$, termed the *driving pressure*, in equation 2.5, where S_h is the regional minimum compressive stress (i.e. $S_h = -\sigma^r_1$). The same applies to equation 2.12, except that the relevant elastic moduli would be those applicable to a volume of the Earth's crust with dimensions several times the dyke length.

Roberts (1970) adopted the Griffith theory approach, as treated by Odé (1960) and Jaeger (1962, 1967), which corrected for the use of effective stresses. A σ_{1c} versus σ_{3c} plot (Figure 2.5) shows that the zone of tensile failure of a rock is much larger than that predicted by the Navier-Coulomb theory (Figure 2.1).

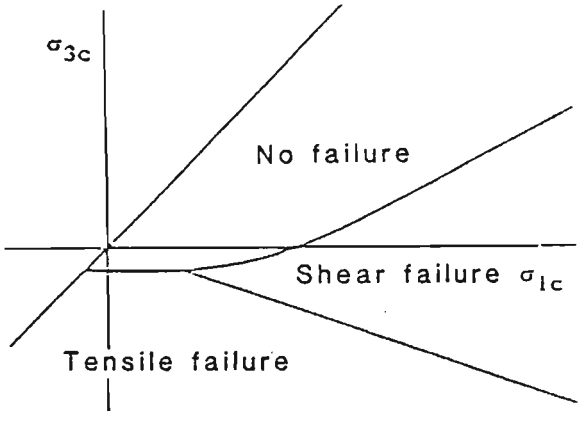

Figure 2.5. *A σ_{1c} versus σ_{3c} diagram representing failure criteria based on the Griffith theory of brittle failure, modified by Roberts (1970). As with Figure 2.2, σ_{1c} is the maximum compressive principal stress, and σ_{3c} is the minimum compressive principal stress.*

The method of revising the Griffith Theory to take hydrostatic pressure P into account was promoted by Murrell (1963, 1964) and has been termed the Griffith-Murrell theory of fracture (Roberts, 1970). The revised criterion for tensile failure versus shear failure is thus $3\sigma_{1c} + \sigma_{3c} = 4P$. Furthermore, magma will only intrude into an extending crack if the internal hydrostatic pressure P is greater than the component of compressive stress normal to the crack. This theory allows brittle failure to occur in the region of no failure (Figure 2.5) if the internal pressure is sufficiently large. The internal pressure must, however, exceed the normal stress by an amount equal to the uniaxial tensile strength T_u (Roberts, 1970). This model allows failure to occur to much greater depths than the Navier-Coulomb criteria of Robson and Barr (1964), and is thus directly applicable to situations such as dyke swarms that extend down to a mantle source.

Jaeger and Cook (1969) adapted the criteria of (2.14) to include the effect of magma pressure P in an extending crack. The value of P is *added* to the remote principal stresses σ^r_1 and σ^r_3 in the equations of (2.14).

2.6 The Stress Intensity Factor

Crack-tip propagation has also been considered in terms of the stress intensity factor, K. The value of K depends on the crack load, length and geometry. For the approximation of a sheet intrusion as an infinite blade-shaped body of constant length 2a, subject to uniform tension (Figure 2.6A), the stress intensity factor is given by (Pollard, 1987)

$$K = \sigma^r_1(\pi a)^{1/2} \qquad (2.15)$$

Similarly, for the approximation of a penny-shaped crack of diameter 2a (Figure 2.6B), the stress intensity factor becomes

$$K = (2/\pi)\ \sigma^{r}{}_{1}(\pi a)^{1/2} \tag{2.16}$$

The sphere of influence, K, around the crack tip is termed the K-dominant region (Figure 2.7).

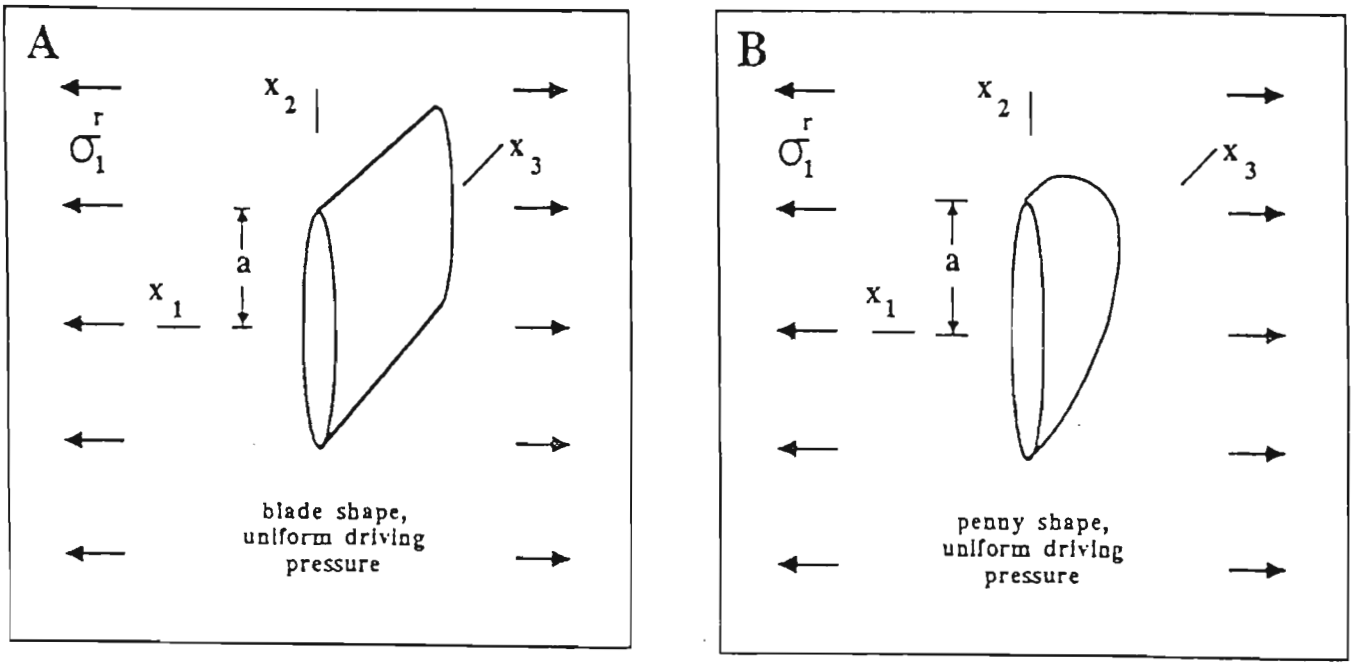

Figure 2.6. *Idealized crack geometries as (A) a blade-shape with constant length 2a, and (B) a penny-shape with diameter 2a (from Pollard, 1987).*

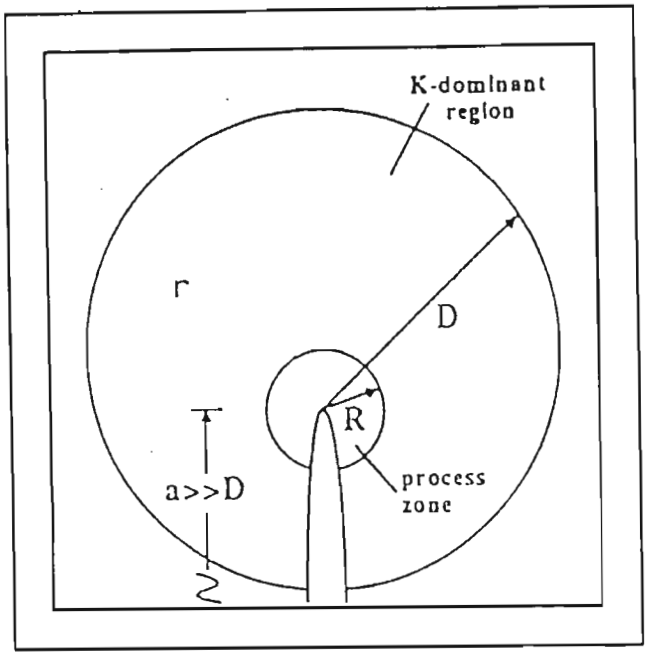

Figure 2.7. *The K-dominant region, r, (R < r < D) around the tip of a crack of length 2a. The region where r < R is dominated by inelastic processes, and is termed the process zone (Pollard, 1987).*

Crack propagation correlates with the stress intensity factor reaching a critical value K_c, called the *fracture toughness*. K_c is a property of the material dependent upon parameters such as loading rate, temperature, pressure, and chemical environment (Pollard, 1987). Via the process of stress corrosion, slow crack growth may occur for values of the stress intensity factor less than K_c (Spence and Turcotte, 1985), however, generally crack propagation will only commence once the applied tension has reached

$$\sigma_1^r = K_c\left(\frac{1}{\pi a}\right)^{1/2} \tag{2.17}$$

As before, $(P - S_h)$ may be substituted for $\sigma^r{}_1$ in the case of a magma-filled crack. Comparing with previous discussion, the form of (2.17) is not far different from Irwin's (1913) relation in terms of tensile strength (equation 2.5), or Griffith's (1924) energy balance considerations (equation 2.12). Clifton *et al.* (1976) have determined the fracture toughness values for a number of sedimentary rocks, such as sandstone (K_c = 0.57-1.46 MN $m^{-3/2}$), siltstone (K_c = 1.04-1.37 MN $m^{-3/2}$) and shale (K_c = 0.87-1.29 MN $m^{-3/2}$). Changes in K_c values as a result of pressure changes are documented for Indiana limestone by Schmidt and Huddle (1977).

Spence and Turcotte (1985) investigate crack propagation as applied to magma-filled cracks. Assuming a high-viscosity magma being injected at a rate sufficiently slow such that the flow is laminar, if the intruded medium is brittle (K_c « 1), the propagation of the fracture is limited by the viscosity of the magma and not the fracture toughness of the medium. If, therefore, magma is being injected into a pre-existing crack or joint, the fracture toughness may be approximated as being zero, and the dynamics of the system is a function of the magma viscosity.

2.7 Crack Modes

Cracks may be categorized into three types or modes, according to the relative displacement of opposing crack faces (Irwin, 1958). As demonstrated in Figure 2.8, mode I cracks involve only an opening displacement in the x_1 direction, perpendicular to the long axis of the crack; effectively a case of pure shear. Mode II cracks undergo a relative shear displacement perpendicular to the crack periphery, in the x_2 direction. Mode III cracks include an x_3 relative shear displacement, parallel to the crack periphery. This classification is relevant because each mode has associated with it a characteristic stress field in the K-dominant region, thus resulting in morphologically different propagation mechanisms and features for each mode.

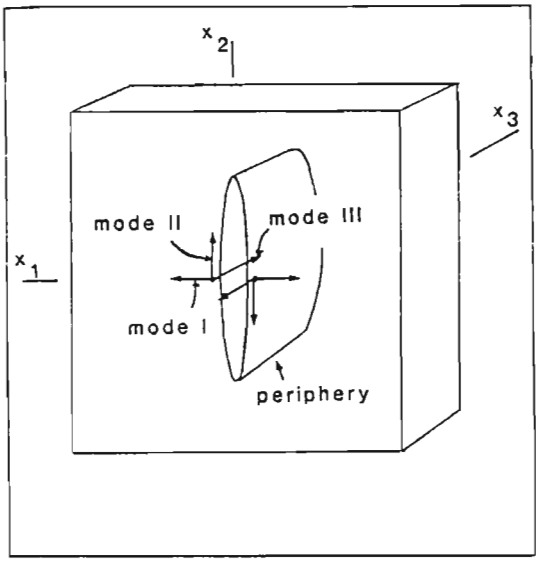

Figure 2.8. *Modes of crack propagation in relation to the relative displacement of opposing crack faces. Pure mode I opening displacements involve no relative shear motion. Relative shear displacements are perpendicular to the crack periphery for mode II cracks, and parallel to the periphery for mode III cracks (Pollard, 1987).*

3. AN ANALYSIS OF PLANAR INTRUSIONS

3.1 Introduction

Chapter 2 considered the genesis and development of fractures in brittle rock. As the fractures open, they may serve as conduits for hydrothermal or magmatic fluids. Planar magmatic ("sheet") intrusions in the lithosphere occur as dykes and sills. Dykes are frequently steeply inclined to vertical and are usually discordant with the intruded host material. For instance, in sedimentary rocks, dykes cut across the sedimentary bedding planes and enclosed sedimentary units. Sills are the compliment of dykes in that they are concordant sheet intrusions, frequently horizontal in undeformed host rocks. Dykes may act as feeders for sills at correspondingly higher crustal levels. Other hypabyssal intrusion features include pipes, phacoliths, laccoliths, lopoliths and diapirs (eg. Price and Cosgrove, 1990); however, this review will relate specifically to dykes and sills.

Examination of sheet intrusions is important as it allows inferences to be made regarding the state of stress at the time of intrusion. This chapter will approach the implications of this, as well as elucidating the mechanisms of intrusion, propagation and dilation, and the resultant features.

3.2 Propagation

3.2.1 Process Zone

Fracture propagation initiation has been examined in Chapter 2 in terms of the interplay between local and regional stresses, and other factors such as material tensile strengths, fracture toughness, and internal magma pressures. The K-dominant region and process zone were illustrated (Figure 2.5) and the mathematical formulae applicable to fracture propagation in the process zone were presented.

The *inelastic process zone* is the circular region about the tip of a propagating sheet intrusion within which small-scale fracturing of the host rock occurs in accordance with the stress configuration about the tip. The size of the process zone depends upon the grain-scale structure of the host rock (Peck *et al.*, 1985b), although the radius R may be approximated by (Pollard, 1987)

$$R \approx \frac{a}{2}\left[\frac{(P-S)}{(T_u+S)}\right]^2 \tag{3.1}$$

where P is the internal magma pressure, S is the regional compressive stress acting perpendicular to the intrusion, T_u is the tensile strength of the rock, and a is the half-length of the intrusion. From equation (3.1) it can be seen that the lengthening of a sheet intrusion results in a larger process zone. Conversely, longer sheet intrusions produce failure zones for smaller values of magma pressure and/or differences in remote stresses than shorter

intrusions (Rogers and Bird, 1987).

Pollard (1987) documents the various mechanisms that operate within the process zone of a dyke (Figure 3.1). These include dyke-parallel jointing, conjugate faulting along shear surfaces, and opening and sliding along planar discontinuities such as bedding planes.

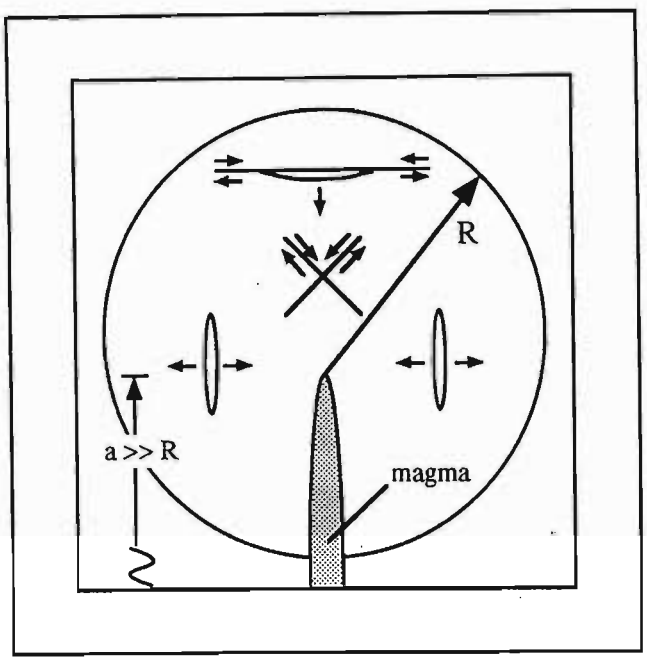

Figure 3.1. *Fracture mechanisms within the process zone. Features produced include dyke-parallel fracturing, conjugate faulting along shear surfaces, and opening and sliding along planar mechanical discontinuities such as bedding planes (Pollard, 1987).*

The production of dyke-parallel fractures about the tip is manifested in the region of the process zone subject to tension, and is thus termed *extension fracturing* (Pollard, 1973). Apart from the extension of the main, magma-filled fracture, dyke-parallel microfractures also form on either side of the central axis (Figure 3.2). This may occur in such a way so as to produce a conjugate-patterned set of dyke-parallel fractures on either side of the main fracture. The dyke-parallel fractures are concentrated close to the tip of the intrusion, decreasing in concentration and increasing in separation further away from the main fracture. As the main fracture extends, the microfractures become juxtaposed against the intrusion as dyke-parallel joints (eg. Delaney *et al.*, 1986; Ransome, 1991).

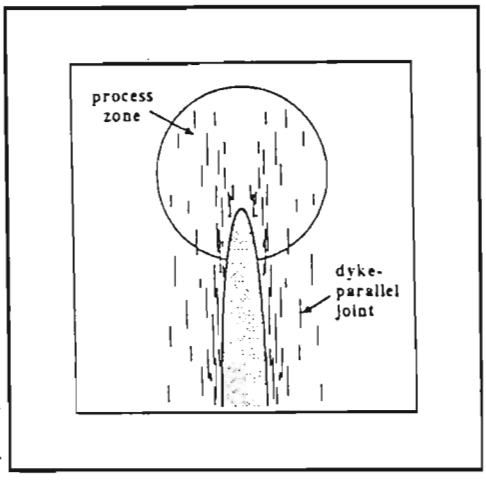

Figure 3.2. *Production of dyke-parallel fractures in the process zone. For increasing distances away from the main fracture, the fractures decrease in number and become more widely spaced. As the main fracture extends, the fractures remain alongside the intrusion as dyke-parallel joints (Pollard, 1987).*

Conjugate fault development along shear surfaces ahead of the tip, or *brittle faulting* (Pollard, 1973), occurs at about 30° to the minimum tensile stress, σ^r_3, and in regions of moderate confining pressure (4 -5km depth). Intrusion of magma along these shear surfaces would ordinarily not occur, but is possible for sufficiently high magma pressures (Roberts, 1970).

Sheet intrusion propagation is greatly facilitated by microfracture development in the process zone, as it allows extension to occur for very small values of (P - S). Propagation is inhibited by decreasing magma pressure, which may be caused by a deficient supply, crystallisation, viscous drag, or rheological variations (Pollard, 1973, 1987).

3.2.2 Intrusion Parameters

The emplacement of sheet intrusions is heavily dependent upon the regional stress configuration. Magma-filled fractures, and thus the associated process zone microfractures, are oriented in a plane perpendicular to the maximum regional tensile stress. Variability in the state of stress across a region being intruded would, therefore, result in a concomitant variation in the attitude of the resultant dykes or sills (Pollard, 1987). If the maximum tensile stress is only fractionally greater than one or both other stresses, the orientation of the intrusion will be less specifically defined by the regional state of stress.

An exception to the above conditions may arise when magma intrudes a pre-existing fracture. If the fracture is not oriented perpendicular to the least compressive regional stress direction, then dilation will only occur if the magma pressure exceeds the normal compressive stress resolved on the fracture plane (Pollard, 1987). The probability of a pre-existing fracture being intruded may be deduced from Figure 3.3, which plots the stress intensity ratio R_{si} versus the angle α between the least compressive regional stress S_h ($-\sigma^r_1 = S_h$) and the normal to the fracture. The stress intensity ratio is given by Delaney *et al.* (1986) as

$$R_{si} = \frac{(P_m - S_H) + (P_m - S_h)}{S_H - S_h} > -\cos(2\alpha) \qquad (3.2)$$

where S_H is the compressive stress orthogonal to S_h in two dimensions (see Figure 3.3), and P_m is the internal magma pressure after dilation. When applied to dyke emplacement, S_H is the maximum compressive regional stress, σ_{1c} (where $\sigma_{1c} = -\sigma^r_3$).

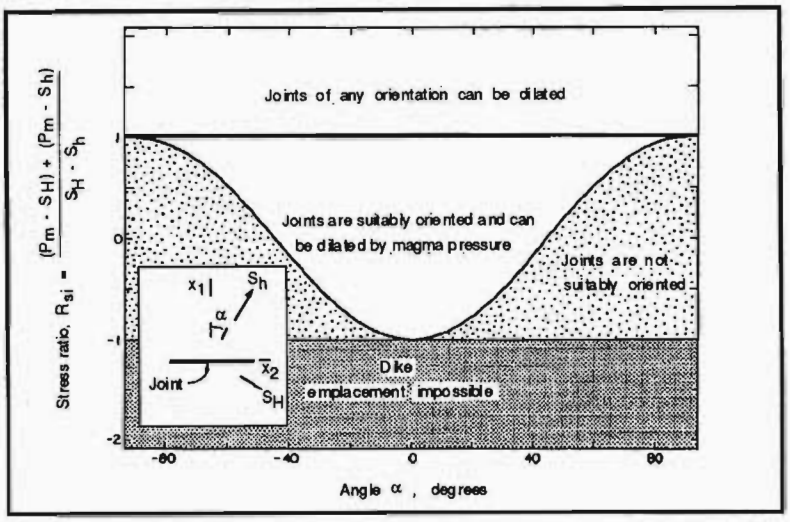

Figure 3.3. *Graph of stress intensity ratio R_{Si} versus the angle a between the least compressive stress S_h and the normal to a pre-existing crack undergoing dilation. Four dilation probability fields are defined. Inset is a section view of the fracture, indicating the conventions for the symbols used (after Delaney et al., 1986).*

The intrusion of magma into an unfractured host rock would thus be controlled by the regional state of stress. This will not necessarily be true for subsequent intrusions into the same region. The formation of dyke-parallel fractures in the process zone of a propagating dyke provides intrusion pathways for later dykes (Delaney *et al.*, 1986; Ransome, 1991). These dykes would thus only give an indication of the initial state of stress at the time of first dyke emplacement.

3.2.3 Effect of Planar Discontinuities

Closed planar discontinuities such as bedding planes, joints, unconformities, faults and foliation produce host rock inhomogeneities that may have a significant effect on an advancing planar intrusion. Figure 3.1 illustrates the effect of opening and sliding along planar discontinuities ahead of an advancing intrusion tip. This may affect the propagation direction in the case of a dyke advancing towards a horizontal bedding plane as the opened surface becomes filled with magma to produce a sill (Pollard, 1973). In deformed regions, dykes may tend to propagate along a foliation such as axial planar cleavage. Faults may act as stress release planes that intercept intruding dykes, or cause sills to "step up".

3.2.4 Driving Pressure

The emplacement of a sheet intrusion results in an amount of energy being imparted to the host rock as a result of magma pressure and viscous drag. This is manifested in the elastic host rock by an increase in the strain energy given by (Pollard, 1987)

$$U_E = \pi a^2 (P - S)^2 \left[\frac{1 - \upsilon}{2\mu} \right] \tag{3.3}$$

where (P - S) is termed the *driving pressure*, as introduced in section 2.5. It can be observed that equation (3.3) is equivalent to (2.10), regarding Griffith's (1924) examination of an elastic plate containing a slender hole, but with the maximum regional tensile strength σ^r_1 replaced by the driving pressure. Numerical solutions for (3.3) may be obtained using the approximation (Pollard, 1987)

$$\frac{t}{l} \approx \frac{(P - S)}{\mu/(1 - \upsilon)} \tag{3.4}$$

where t/l is the thickness-to-length ratio of the sheet intrusion, and $\mu/(1-\upsilon)$ is termed the *host rock stiffness*. The length l is the equivalent of the long axis dimension $2a$ (section 2.3). Knowing the elastic shear modulus μ and Poisson's ratio υ, (P - S) may be approximated by (3.4) and then substituted into (3.3) to calculate the strain energy imparted to the host rock.

The *driving pressure* should not be confused with the *injection pressure*, which is that part of the internal pressure of a magma required to overcome viscosity effects (Bradley, 1965).

3.2.5. Fluid Effects at a Propagating Tip

Thus far, fracture propagation and magma intrusion has been surveyed in terms of energy, stress and pressure considerations. Another parameter which should be taken into account is the presence of fluids around the tip of a propagating sheet intrusion. The manner in which these fluids occur is two-fold: either within the *extension fracture* ahead of the magma, or as pore fluids within the host rock that is being intruded.

The presence of a low-viscosity, high-velocity volatile phase associated with an intruding magma, may advance in the extension fracture ahead of the magma (Bradley, 1965; Currie and Ferguson, 1970; Pollard, 1973). This fluid may serve to increase the local pore pressure in the host rock surrounding the tip (Hubbert and Willis, 1957), which in turn, may decrease the fracture toughness.

The transfer of heat into a relatively cold rock hosting a mafic intrusion would result in a local thermoelastic change in the host rock stress. A consequent pore fluid expansion produces an elevated pore pressure at a rate sufficient to influence the factors governing host rock fracture (Delaney, 1982; Delaney *et al.*, 1986). Rogers and Bird (1987) ascribe the presence of interstitial pore fluids to a concomitant increase in the size of the process zone around the intrusion tip.

An additional fluid effect is the impact that the fluid may have on the chemical environment surrounding the tip.

Weakening of the host rock via chemical alteration may play an important rôle in the mechanism by which an intrusion propagates.

3.3 Morphology

Measurements of thickness t_1 at various distances l_1 from the termination of a sheet intrusion exposed in cross-section indicate that most sheet intrusions approximate to an elliptical shape. This elliptical model is defined by the relation (Pollard, 1973)

$$\frac{t_1}{t} = 2\left[\frac{l_1}{l} - \left(\frac{l_1}{l}\right)^2\right]^{1/2} \tag{3.5}$$

where t and l are the true thickness and length respectively, as shown in Figure 3.4. The ellipticity of sheet intrusions in cross-section has been frequently documented (eg. Pollard *et al.*, 1975; Pollard, 1976; Pollard and Muller, 1976; Ransome, 1991) and is accurate along the entire length l_p of the intrusion in the third dimension as long as $l_p > 2l$ (Pollard, 1976).

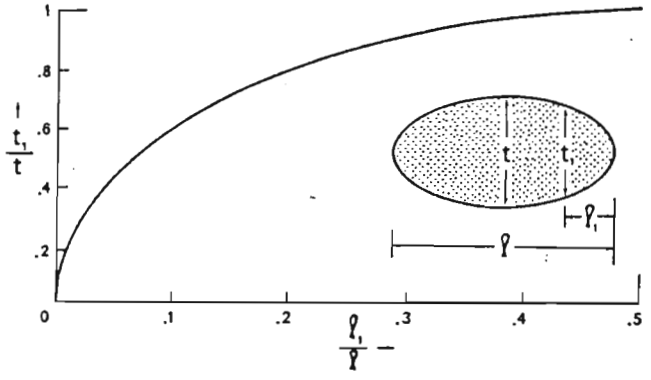

Figure 3.4. *Elliptical model of a sheet intrusion in cross-section. Contacts with an elliptical form will plot on or near the curved line defined in equation 3.5. Values of t_1 and l_1 are measured away from the tip of the intrusion (Pollard, 1973).*

A simple mathematical formulation of open fracture ellipticity may be obtained in a paper by Gudmundsson (1983).

Deviations from ellipticity may be induced where gradients in internal magma pressure or regional stress exist (Pollard, 1976). Intrusions may thus be produced with unusual shapes such as dumbbell, diamond, tear-drop or forms with greater lateral heterogeneity. These result from the intrusion being thinner in regions where there is less internal pressure or alternatively, a greater external stress. Variations would also be produced by changes in host rock ductility along the length of the intrusion (Pollard and Muller, 1976). Logically, the greater the length-to-

thickness ratio of a sheet intrusion, the greater the likelihood of a deviation from the elliptical model that would be expected to occur.

Smaller-scale features of sheet intrusion that occur as irregularities to the smoothness of the contacts include *steps*, *horns*, *bridges*, *buds*, *fingers* and *cusps* (Figure 3.5). *Steps* occur obliquely or perpendicular to the principal plane of the contacts and result from the coalescence of slightly out-of-plane adjacent intrusions. *Steps* may also be termed *offsets* (Bussell, 1989). *Horns* are thin off-shoots of the intrusion that protrude into the host rock along the outside edges of *offsets*, and are also termed *flanges* or *apophyses*.

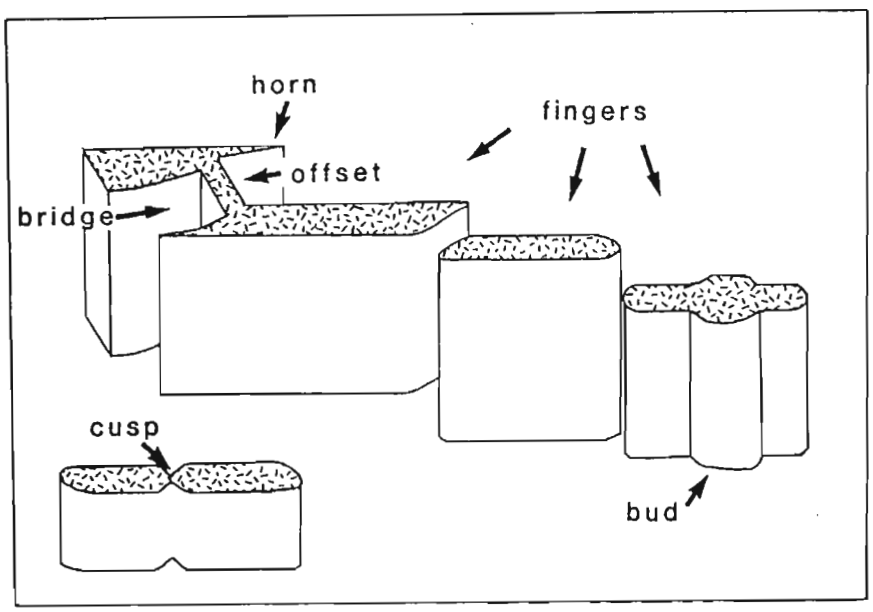

Figure 3.5. *Small-scale features of planar intrusions as described in the text.*

Bridges are blocks of host rock protruding into an intrusion at points of offsetting. On occasion, the bridges may be detached from the host rock. *Buds* are localized widened portions of sheet intrusions that form by brecciation and stoping of the host rock (Delaney and Pollard, 1981) and may serve to locally channelize magma flow. *Fingers* (or *segments*) are isolated planar intrusions that occur in groups of two or more, either along a common plane or slightly offset from each other. *Cusps* mark positions where adjacent *fingers* have coalesced in the same plane, and may be associated with wedges of deformed host rock (Pollard *et al.*, 1975).

3.4 Dykes

3.4.1 Initiation

The inception of a dyke propagating vertically away from a crustal primary magma chamber is dictated by the interplay between the internal magma pressure and the vertical stress. In Figure 3.6, a dyke containing magma with

density ρ_m is being intruded vertically into crustal rocks with an average density ρ_r. Adapting Price and Cosgrove's (1990) evaluation of such a condition, in order for the dyke to begin propagating, the magma pressure at depth z_m must at least equal the vertical stress σ_z, where $z_m = z_1 + z_2$. This equates to the statement that at depth z_m,

$$P_m = \rho_r g(z_1 + z_2) \tag{3.10}$$

(where P_m is the magmatic pressure in the primary magma chamber) thus predicting a near isotropic state of stress at depth z_m.

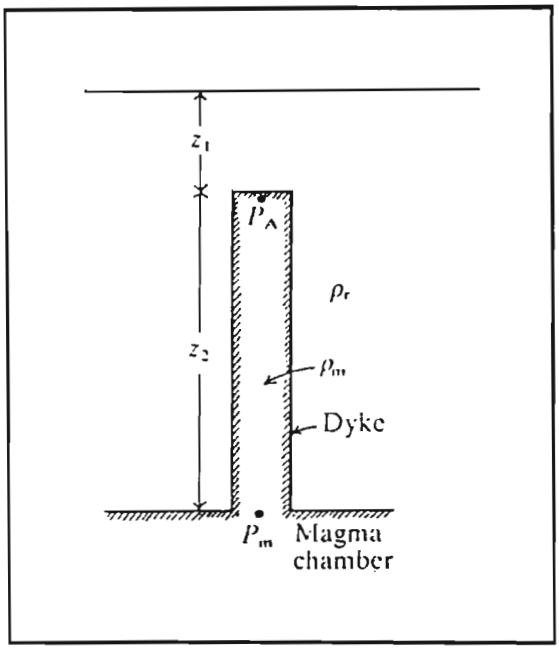

Figure 3.6. *Definition of symbols used in text to predict the conditions of dyke emplacement in the crust (Price and Cosgrove, 1990).*

When the dyke has reached the point *A* (depth z_1), the magma pressure P_A at the top of the intrusion is given by

$$P_A = P_m - \rho_m g z_2 \tag{3.11}$$

assuming the magma is at rest. The vertical stress at point *A* is $\sigma_z = \rho_r g z_1$. The excess of magmatic pressure over geostatic pressure (in other words, the *driving pressure*) at point A is thus

$$P_A - \sigma_z = z_2 g(\rho_r - \rho_m) \tag{3.12}$$

This is known as the *buoyancy equation* and demonstrates the importance of relative densities insofar as magma intrusion is concerned. Intrusion will be greatly inhibited where the density difference between magma and host rock is small, and is unlikely when $\rho_r < \rho_m$.

The applicability of (3.12) is limited to the condition of an immobile intrusion. While the magma is still flowing, viscous drag against the conduit walls must be overcome. A certain amount of the magmatic pressure must therefore be utilised to counteract viscosity effects (i.e. injection pressure). Equation (3.12) thus overestimates the excess magmatic pressure to some extent. Limitations are also provided by the onset of crystallisation, as this will induce density and viscosity variations.

When both sides of the buoyancy equation equate to zero, dyke propagation ceases until a driving pressure is re-established. Alternatively, depending on the stress configuration, dyke emplacement may give way to sill production.

If $P_A \gg \sigma_Z$, brecciation and stoping of the country rock may occur via *hydraulic fracturing*. The necessary condition would be

$$P_m > \sigma_x + T_u \tag{3.13}$$

where σ_x is the least compressive horizontal stress, and T_u is the tensile strength of the host rock. This is, however, only true for the condition where $\sigma_Z - \sigma_x < 4T_u$ (after Price and Cosgrove, 1990). If $\sigma_Z - \sigma_x > 4T_u$, shear failure will occur, with the possibility of inclined dyke formation.

Estimates of driving pressure for specific dykes may be made from a measurement of the width to length ratio (along a horizontal cross-section), the Young's modulus E and Poisson's ratio υ of the host rock, using the relation (Gudmundsson, 1983, 1990)

$$(P-S)=\frac{W}{L}\frac{E}{2\left(1-\upsilon^2\right)} \tag{3.14}$$

where (P - S) is the driving pressure (or overpressure) of the magma, and W/L is the dyke width to length ratio, equivalent to t/l in (3.4).

It must be assumed that dyke intrusion into a region under lateral compression is feasible provided that the internal magmatic pressure is suitably large (Roberts, 1970).

3.4.2 Propagation

The principal aspects of sheet intrusion propagation are described in section 3.2. There are further particular mechanisms concerning dyke propagation.

Field observations suggest that dykes are thinnest where their number is greatest (Gudmundsson, 1990). Presumably, this suggests that dyke thicknesses decrease as the source is approached. This assumption is adequate as increasing confining pressure with greater depth would necessitate a propensity for vertical propagation rather than increasing dilation. Predominantly vertical flow directions would thus be expected in close proximity to a primary source at depth.

Dykes probably become thicker and longer as higher crustal levels are approached. A region under effective tension may exhibit a more rapid decrease in both vertical and horizontal least tensile stress than occurs in the maximum horizontal regional tensile stress. This, coupled with an associated decrease in vertical magma pressures,

would favour dyke lengthening. Upper crustal levels would thus tend to be associated with a predominantly lateral dyke propagation direction (Ransome, 1991). A degree of vertical propagation would continue, possibly as a number of fronts along local stress reduced zones to produce fingers of magma ahead of the main intrusion, similarly to that documented by Pollard *et al.* (1975). The overall effect is shown in Figure 3.7.

Eventually, energy considerations would preclude further lengthening of the dyke, instead favouring sill development. Lateral dyke propagation may also be induced where the dyke encounters a *stress barrier*: a crustal layer of high horizontal compressive stress (Gudmundsson, 1990). Vertical propagation is resumed as soon as the stress barrier has been bypassed.

The production of fingers of magma advancing ahead of the main magmatic front (Pollard *et al.*, 1975; Pollard and Muller, 1976; Ransome, 1991) is a common effect. It has been explained by one method as being the result of the Hele-Shaw effect, which predicts that the interface between two substances of contrasting viscosities exhibits the fingering of one substance into the other (Pollard *et al.*, 1975). It is, however, doubtful whether the applicability of this effect to a magma intruding a solid host rock is significant. The production of fingers is more likely to occur along stress reduction zones or host rock anisotropies ahead of the magmatic front, such as pre-existing fractures, stress gradients due to variable host rock stiffnesses, or zones of decreased uniaxial tensile strength.

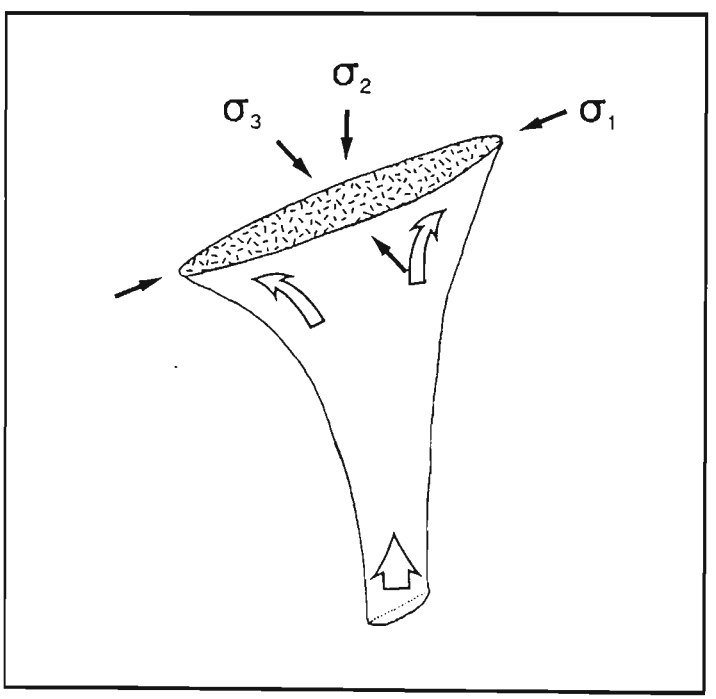

Figure 3.7. *Mechanism of dyke propagation whereby vertical propagation is associated with increased thickness and length, resulting in a transformation towards lateral dyke propagation at higher crustal levels, as confining pressures decrease.*

One of the most contentious arguments regarding dyke propagation is the propagation direction with respect to the intrusion features, such as offsets. Pollard *et al.* (1975) suggest that propagation occurs along the length of the

offset surface; a model that has received much support (eg. Delaney and Pollard, 1981; Nicholson and Pollard, 1985; Smith, 1987; Pollard, 1987). There are other authors, however, that advocate lateral dyke propagation, resulting in an array of offset fractures being successively dilated and filled with magma (eg. Currie and Ferguson, 1970; Gudmundsson, 1984; Sigurdsson, 1987; Halls, 1988; Bussell, 1989). The former model explains offsets as a consequence of the linkage of adjacent, slightly out of plane sheet intrusions (or fingers of magma), whereas the latter model ascribes offset formation to the way in which magma successively forces its way from one crack into the adjacent one in an array of offset cracks, with subsequent dilation.

Probably neither of the above models is always applicable. It has already been described how vertical dyke propagation can be transformed into lateral propagation at higher crustal levels. It would appear feasible, therefore, that both models may be applicable to dykes depending upon the circumstances.

3.4.3 Rate of Intrusion

The volumetric flow rate of a viscous fluid through a narrow slit is proportional to the cube of the slit dilation (Bird *et al.*, 1960). Under conditions of constant viscosity and driving pressure, the linkage and dilation of offset sheet intrusions would result in a volumetric flow rate increase to the order of n^3 (Bussel, 1989).

The flow rate of a specific intrusion is directly related to the magma viscosity. Magmas with low viscosities flow with greater ease than high-viscosity melts. Basaltic magmas thus flow much better, and with a greater velocity, than acidic magmas. Temperature is also an important factor as it affects viscosity directly, as shown by the Arrhenius equation

$$\eta = A_\eta e^{-E_\eta/RT} \tag{3.15}$$

where η is the shear viscosity (the ratio of shear stress to the corresponding rate of shear strain in a liquid), E_η is the activation energy per mole, and R is the gas constant (Carmichael *et al.*, 1974). Equation (3.15) indicates that increasing temperatures will result in decreasing viscosities, and thus higher flow rates. Other factors that influence viscosities include the magma geochemistry (Bottinga and Weill, 1972; Shaw, 1972), and the presence of water, which tends to increase viscosities in acidic magmas.

3.4.4 Dyke Swarms

Dykes do not necessarily occur as single, isolated features. They regularly occur as an assembly of parallel or sub-parallel units, termed a dyke swarm. Dyke swarms have been widely documented, such as in Iceland (Gudmundsson, 1983; Sigurdsson, 1987), Greenland (Wager and Deer, 1938), Ethiopia (Mohr, 1971), and Southern Africa (Saggerson *et al.*, 1983; Armstrong *et al.*, 1984; Wilson *et al.*, 1987; Hunter and Reid, 1987; Meth, 1991; Ransome, 1991). The dykes generally occur as a result of multiple intrusive events, with later dyke phases

frequently being emplaced within earlier dykes. Dyke swarm development, as opposed to single dyke formation, requires a substantially greater volume of magma, and a large degree of lateral crustal extension (Price and Cosgrove, 1990). The latter point indicates the conduciveness of ocean-floor spreading centres towards dyke swarm development.

The ratio of dyke material to original country rock selvages may be extremely small in a dyke swarm, indicating the considerable degree of lateral extension that may occur. An increase in the intensity of dyke occurrence along the length of a swarm may also be indicating the presence of an original magma chamber at a shallow crustal depth (Ransome, 1991).

An alternative mechanism of dyke swarm development involves crustal flexure. Wager and Deer (1938) attributed a dyke swarm in East Greenland to the effects of lithospheric flexure (Figure 3.8B). Roberts (1970) documented the stress configuration to be expected in a region of monoclinal crustal flexuring, and how this explains the development of a dyke swarm (Figure 3.8A). The upwarped region is characterised by maximum principal compressive stress trajectories that are steeply dipping to vertical, resulting in the formation of dykes. These trajectories curve around to a horizontal attitude in the downwarped region, resulting in sill development. Roberts (1970) used this model to explain major sill occurrences in Spitzbergen, and dyke swarm development in East Greenland and the Rooi Rand in South Africa.

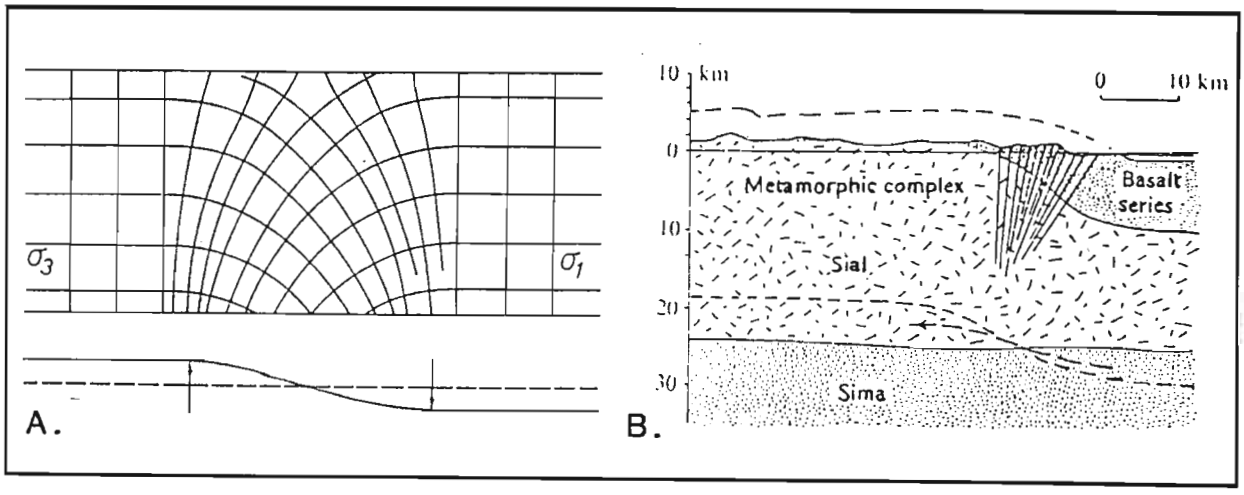

Figure 3.8. Dyke swarm development as a result of monoclinal lithospheric flexuring. *A*: associated stress configuration. The upwarped region is characterised by steep to vertical σ_1 (maximum compressive stress) trajectories and dyke swarm development, whereas the downwarped region exhibits shallow-dipping to horizontal σ_1 trajectories, and thus sill development (Roberts, 1970). *B*: dyke swarm of East Greenland associated with crustal flexure (Price and Cosgrove, 1990).

3.5 Sills

3.5.1 Initiation

Sills are intruded as shallow-dipping to horizontal planar bodies that are, by definition, concordant with bedding surfaces. They are an upper crustal feature, frequently emplaced within sediments of a relatively undeformed sedimentary basin underlain by a crystalline basement (Bradley, 1965).

Park (1989) envisages the preferential development of sills over dykes as a consequence of the overburden pressure decreasing to a value less than the driving pressure at high crustal levels. This corresponds to a minimum value of the vertical stress, σ_z. The development of a sill can more accurately be given by the condition

$$P_m = \sigma_z + T_u \tag{3.16}$$

where T_u is the host rock tensile strength measured perpendicular to the bedding planes. When a sill intrudes along a bedding plane or other pre-existing fracture, as is frequently the case, T_u can be approximated as being zero. The transformation of a dyke into a sill can be explained in terms of a change in the local stress configuration (Figure 3.9). Whereas σ_{1c} and σ_{3c} (compressional) act in a horizontal sense for a dyke, σ_{3c} rotates to a vertical orientation at the point of sill initiation.

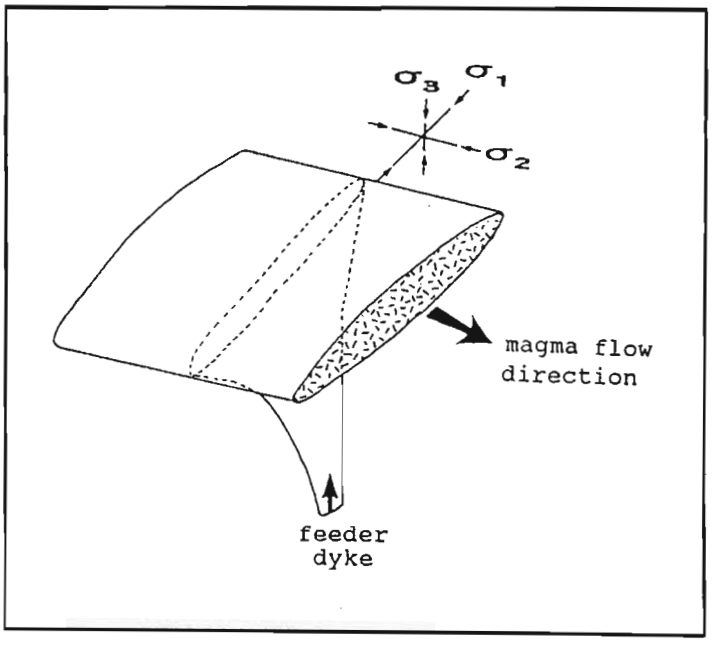

Figure 3.9. *Change in stress configuration as a dyke develops into a sill. The local compressive stresses are σ_{1c} (maximum), σ_{2c} (intermediate) and σ_{3c} (minimum).*

If σ_{1c} and σ_{2c} are very similar, magma flow may radiate in all directions to produce a penny-shaped sill, as described in section 2.6. If σ_{1c} is a dominant horizontal principal stress, then a blade-shaped body would be expected. Price and Cosgrove (1990) suggest that for sill development, the difference in magnitude of the horizontal and vertical stresses is very small.

The features associated with a propagating dyke tip were illustrated in Figure 3.1. One feature was the opening and sliding along mechanical discontinuities ahead of the dyke tip. This provides a feasible mechanism by which a dyke can efficiently evolve into a sill. An induced opening along a bedding plane ahead of an advancing dyke may become filled with magma and, if the above-mentioned stress conditions hold, a sill may develop along that bedding plane (Pollard, 1969). When bedding planes are absent, sill development must conceivably be attributed to the attainment of a point in the crust where a dyke begins to fracture the host rock in a horizontal plane and lift up the overlying strata. This mechanism would be aided by the existence of faults in the region, along which an upward displacement of the overlying strata can be accommodated. Inclined dykes will turn over into a sill at a conveniently situated bedding plane. The resultant sill will be asymmetrical (Pollard, 1969).

Another method by which sills can develop is documented by Gudmundsson (1990). Earlier formed sills can inhibit continued dyke propagation by absorbing the intruding magma or, if they are already solidified, by acting as a stress barrier.

For the case of a sill that is assumed to have a central source, an estimate can be made of the magmatic overpressure using the formula

$$P_m = \frac{32 h_o B z^3}{L^4} \tag{3.17}$$

where h_o is the maximum thickness of the sill, z is the depth within the crust, L is the width of the sill and B is the rigidity modulus, where $B = \upsilon^2 E/(\upsilon^2-1)$ (Johnson, 1970). The applicability of (3.17) is, however, restricted to cases where $L/z > 10$.

3.5.2 Intrusive Mechanisms

Sill development may occur by one of two mechanisms: hydrostatic or tectonic (Roberts, 1970). The hydrostatic hypothesis predicts sill development when the magma driving pressure exceeds the overburden pressure as described previously. The tectonic hypothesis explains sills that intrude in response to conditions of horizontal compression. As the sill propagates, it may step up or down in response to local changes in stress conditions brought about by factors such as crustal flexure, differential compaction or variations in the mechanical properties of the host rock (Gretener, 1969) or due to topographical variation (Bradley, 1965). Where such steps occur, the vertical opening displacement is constant and so dilation is not perpendicular to the sides of the intrusion.

Like dykes, an intruding sill may be characterised by a number of fingers of magma advancing ahead of the main propagation front (Pollard *et al.*, 1975). Initially these fingers are coplanar, however, progression into a number of slightly out-of-parent-crack plane segments may occur as a result of structural inhomogeneities (Pollard, 1978) resulting in an en echelon arrangement of sills. Presumably, this method of intrusion is restricted to situations where the host rock is poorly bedded or unbedded. Coplanar fingers that begin to coalesce may produce inter-finger cusps of relatively deformed host rock (Pollard *et al.*, 1975). Out of plane fingers that coalesce exhibit sharply offset contacts and may be associated with the development of horns and bridges.

3.5.3 Host Rock Effects

As sill dilation serves to uplift the overlying lithologies, the final shape is asymmetrical rather than elliptical (Price and Cosgrove, 1990). The host rock undergoes greatest displacement closest to the central area of the sill.

The propagation of a sill through a sedimentary bed may result in a number of host rock features. Stresses

imposed upon the sediments may result in deformation, especially if the sediments are relatively wet and unconsolidated. Krynauw *et al.* (1988) noted that such sediments at Grunehogna, Antarctica, had been deformed into large disharmonic folds by intruding sills in the mid-Proterozoic. Fluidization of the sediments resulted in the destruction of sedimentary structures, large-scale soft sediment deformation, partial melting and fusion of the sediments. Small-scale intraformational fault development also featured. Norman (1969) describes hornfels that was dragfolded during intrusion.

Remobilisation of partially molten sediments may produce rheomorphic vein injection into the igneous body. Such features have been noted in the Rooi Rand region (Meth, 1991), and near Empangeni, South Africa in this study.

Additional effects in more brittle host rocks include stoping, brecciation, strain concentration and contact metamorphism.

3.6 Stress Analysis

3.6.1 Intrusion Modes

It has already been advocated how a propagating fracture or an intrusion advancing into pristine host rock develops in response to the regional stress configuration. Fractures propagate orthogonally to the maximum tensile regional stress. In many instances however, magma-filled fractures develop in response to changes in the local stress field, induced by factors such as host rock inhomogeneities, topographical variation, density changes and interaction with adjacent intrusions.

The concept of crack modes was introduced in section 2.7. Applied to propagating sheet intrusions, three varieties of intrusion can be identified on the basis of the relative displacements of formerly juxtaposed points (Figure 3.10). Each mode is characterised by a unique state of stress that governs the propagation (Lawn and Wilshaw, 1975).

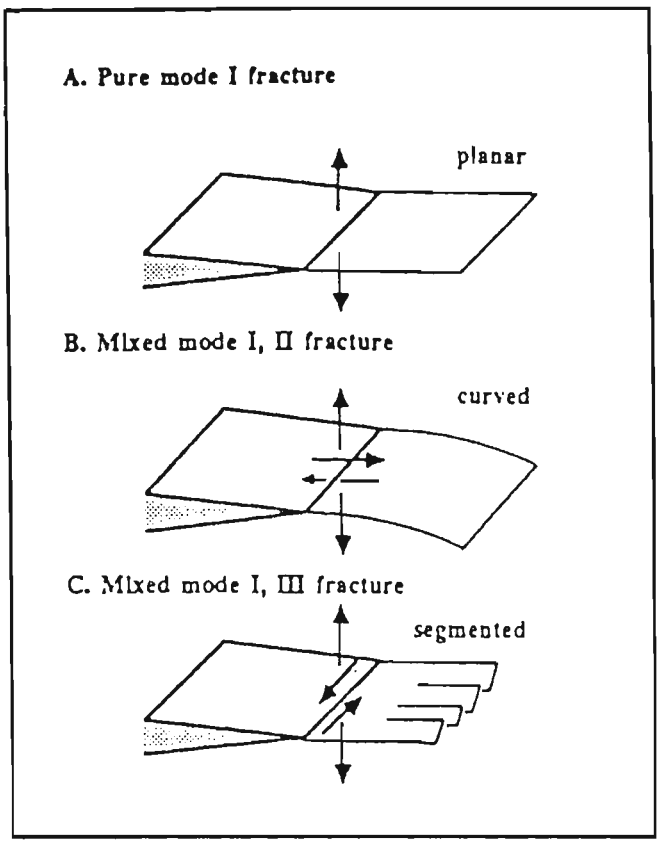

Figure 3.10. *Propagation paths of sheet intrusions based on the types of fracture modes. Pure mode I fractures involve opening displacements only, whereas mixed mode fractures include both opening and shear displacements and result in curved or segmented intrusion forms (Pollard, 1987).*

3.6.2 Stress Conditions around Propagating Tips

The state of stress around the termination of an intrusion propagating parallel to the maximum compressive stress σ_{1c} is dictated by the driving pressure and not σ_{1c} (Olson and Pollard, 1989). Pollard (1973) demonstrates the stress conditions around the tip of a propagating fracture or intrusion (Figure 3.11). A curvature develops in the maximum compressive stress trajectory very close to the intrusion tip. This curvature is bimodal in that it occurs to either side of the tip, thus producing a nett continued migration in the regional maximum compressive stress direction. Exceptions occur when the stress field on one side of the intrusion interacts with another stress field in some way, resulting in aberrations that may promote out-of-main-fracture-plane propagation. Such is the case when the stress fields of offset sheet intrusions interact (section 3.6.3). The principal shear stress concentration around the intrusion termination (Figure 3.11B) suggests the manner in which host rock deformation may occur (Pollard, 1973). Shear fractures may form along the shear stress gradient. Increased driving pressure could enable these shear fractures to be utilised by the intrusion as a propagation pathway.

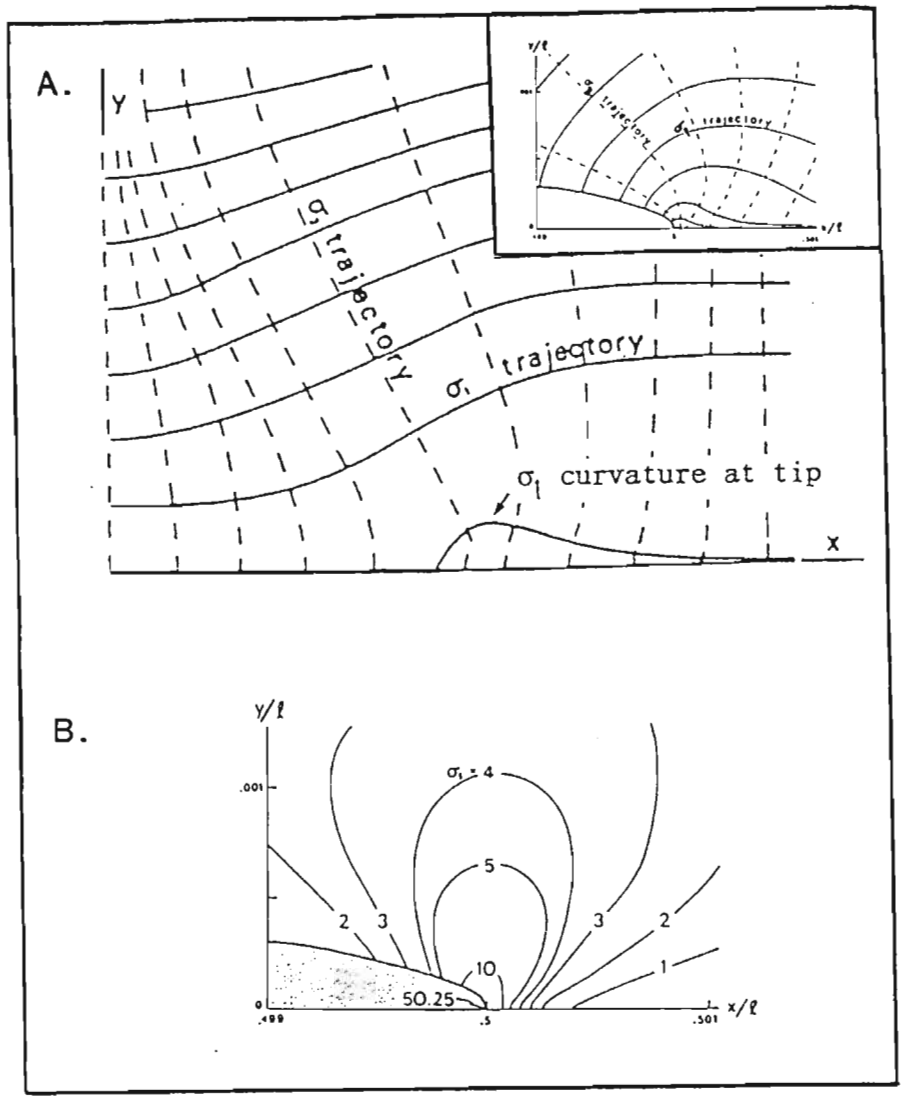

Figure 3.11. *A: stress conditions around one half of a propagating fracture. Inset is the stress configuration at the tip of a magma filled crack of length, l. The maximum principal compressive stress, σ_1, curves in towards the tip. B: principal shear stress (σ_s) concentrations around one half of the tip (Pollard, 1973).*

3.6.3 Interference From Adjacent Intrusions

The stress fields of offset, adjacent intrusion terminations may interact to produce a modified state of stress. The resultant stress field is directly related to the manner in which the two intrusions are spatially arranged (Pollard, 1973; Rogers and Bird, 1987; Ransome, 1991). Intrusions offset perpendicular to the lengths interact to a greater extent than those offset both perpendicular and parallel to the lengths. Adjacent intrusions frequently curve in towards each other, and this is readily explained by superimposing the stress fields for each to produce a resultant stress configuration (Figure 3.12).

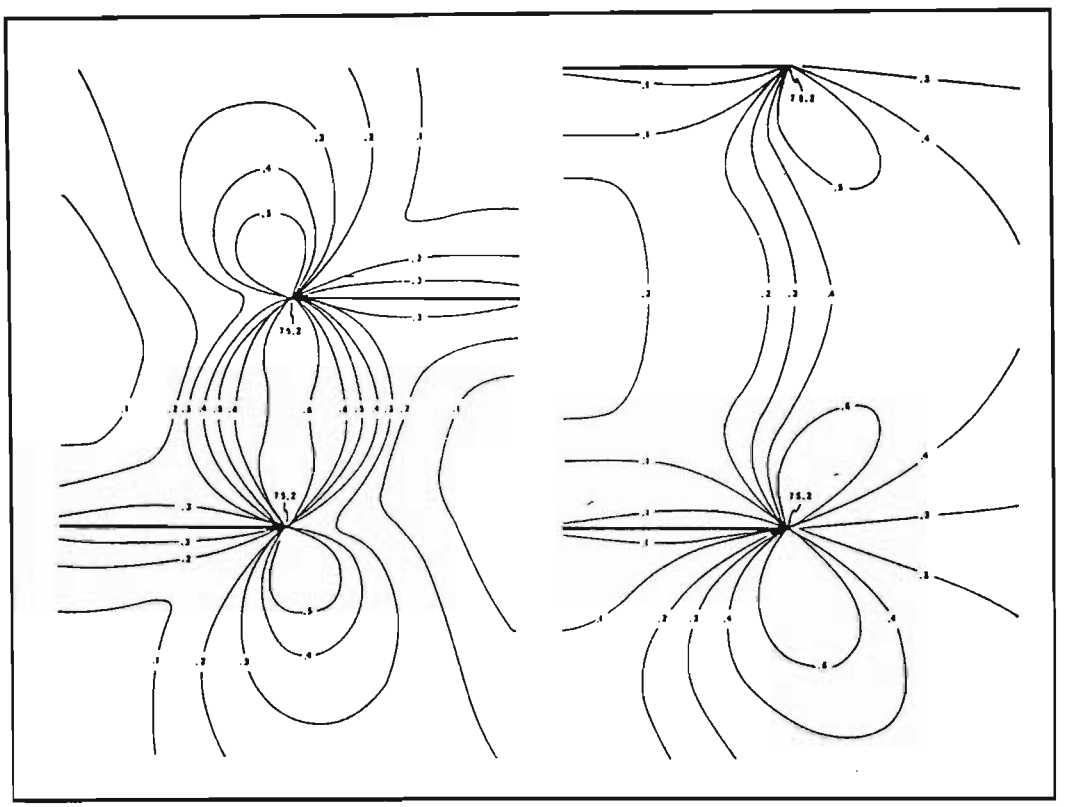

Figure 3.12. *Indication of the possible resultant principal shear stress concentrations induced by the interaction of adjacent offset intrusions. The nature of the stress distribution dictates whether the intrusions will converge or diverge (Pollard, 1973).*

Shear stress concentration between the two intrusions may result in convergence and linkage. This is particularly common for intrusions offset both perpendicular and parallel to the intrusion length. Such is the case for dykes and sills arranged en echelon (Nicholson and Pollard, 1985). The convergence of adjacent intrusions may be preceded by a small degree of initial divergence, which serves to minimize shear stress and maximize the tensile stress across the propagation paths (Olson and Pollard, 1989). Convergence is then induced by an inward rotation of the maximum tensile stress due to a change in the sense of shear resolved across the tip.

Where the intrusions are offset perpendicular to their strike lengths so that they are parallel, they have a greater tendency to diverge (Pollard, 1973). This divergence of parallel intrusions is less marked in regions that are under lateral tension, such as the case for most dyke swarms, where divergence of adjacent dykes does not readily occur.

Olson and Pollard (1989) introduce a method of interpreting the state of stress between offset adjacent vertical fractures in a environment under regional compression. The interaction of adjacent intrusions can be understood in terms of the *remote differential compression*, $\Delta\sigma$:

$$\Delta\sigma = S_H - S_h \tag{3.18}$$

where S_H is the maximum compressive stress and S_h is the least compressive stress. Crack morphology for different values of the remote differential compression are shown in Figure 3.13.

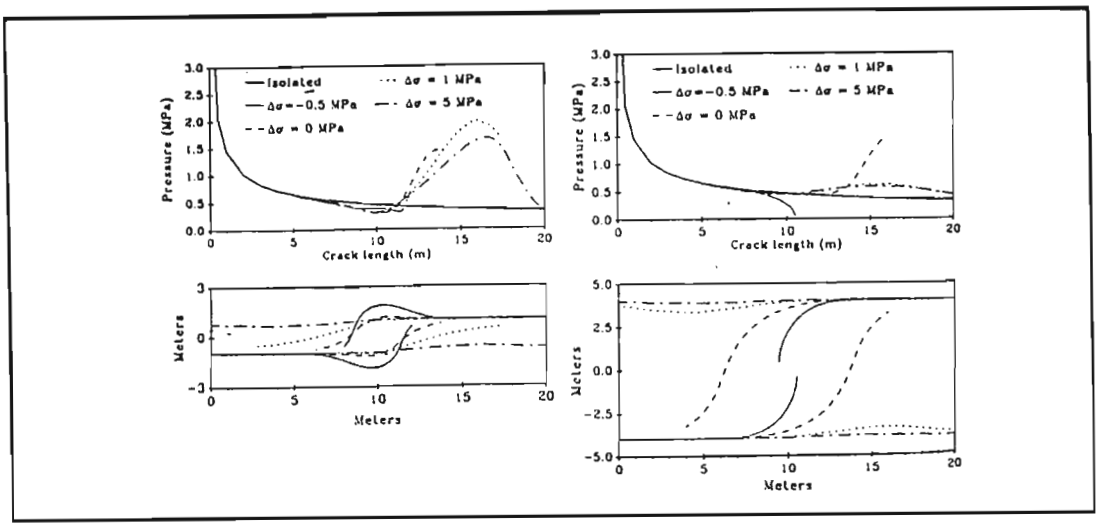

Figure 3.13. *Theoretical crack paths of offset, interacting adjacent cracks in relation to the remote differential stress Δσ. A: l/s = 10. B: l/s = 20, where s is the crack separation and l is the length of the crack array (Olson and Pollard, 1989).*

Under isotropic conditions ($\Delta\sigma. = 0$), initial divergence is followed by convergence. As $\Delta\sigma$ increases, the amount of convergence decreases and the cracks propagate asymptotically. Under tensile conditions ($\Delta\sigma < 0$), path curvature is exaggerated, and the cracks form T-type intersections (Olson and Pollard, 1989). Crack linkage frequently requires the precursor of an increased driving pressure. The exact geometries (Figure 3.14), are also a function of the host rock fracture strength.

3.7 En Echelon Geometries

3.7.1 Morphology

Fractured materials frequently display arrays of consistently offset cracks, sometimes overlapping, to produce a pattern described as **en echelon**. Anderson (1951) provided a qualitative analysis of en echelon dyke segments. Thereafter, documentation of en echelon features has been plentiful (eg. Hodgson, 1961; Ramsay, 1967; Roering, 1968; Lajtai, 1969; Hancock, 1972; Beach, 1975; Pollard *et al.*, 1982; Nicholson and Pollard, 1985). Some of these observations are specific to shear zone related fractures, which will not be analysed in this investigation.

Arrays of en echelon igneous intrusions are usually interpreted as stemming from a common parent crack that splits into a number of segments or fingers which rotate in a changing stress field along an axis parallel to the propagation direction. Emphasis is placed on the fact that the segments rotate out of the plane of the parent crack as a result of a change in the regional principal stress configuration. The rotating fractures trace out a helicoidal surface (Sih, 1981; Pollard *et al.*, 1982). The reason for the production of an array of helicoidally migrating fractures is one of simple energy conservation. Less energy is expired in the development of n cracks, each of width $2b$ than for a single rotated surface of width $2nb$ (Pollard *et al.*, 1982).

Crack segments within a single array generally display similar widths and thicknesses. There is frequently an amount of overlap, resulting in interactive crack-tip stress fields that cause the cracks to dilate asymmetrically, and sometimes sigmoidally. There is a finite number of cracks that may develop in any one array in response to the total possible energy expenditure and as a result of the development of stress reduction regions between dominant echelon fractures that inhibit cracks within these regions from developing into members of the echelon array (Pollard *et al.*, 1982).

The geometry of an en echelon array of rectilinear fractures can be defined by the parameters width $2b$, dilation 2∂, separation $2s$, overlap $2o$, centre spacing parallel to the array axis $2c$, centre spacing parallel to the cracks $2k$, twist angle ω, and the array width $2B$ (Figure 3.14).

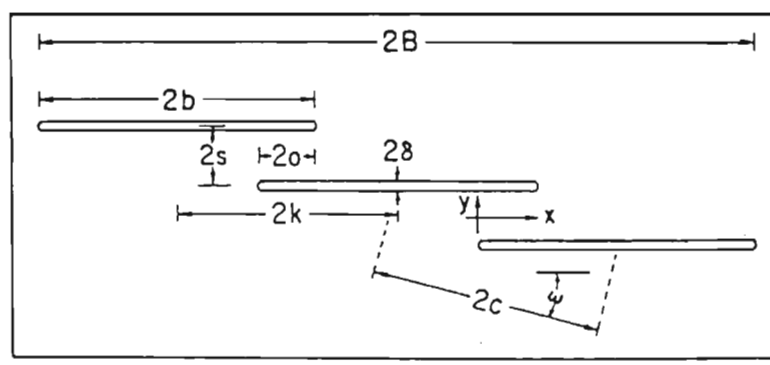

Figure 3.14. *Geometric features of an en echelon array of three rectilinear cracks with parameters width 2b, dilation 2∂, overlap 2o, separation 2s, centre spacing along the array axis 2c, centre spacing parallel to the cracks 2k, twist angle ω and array width 2B (Nicholson and Pollard, 1985).*

3.7.2 Shear Failure

The association of en echelon fractures with shear zones is well known (eg. Riedel, 1929; Lajtai, 1969; Hancock, 1972; Ramsay, 1980). However, the transmutation of a planar fracture or intrusion into an array of rotated segments is not conspicuously associated with shear. Beach (1975) proposes that en echelon configurations of cracks that rotated out of a common plane are tensile fractures. Delaney and Pollard (1981) suggest that both the parent and en echelon cracks are tensile fractures orientated perpendicular to the least compressive stress which is temporally or spatially variable. Olson and Pollard (1991) propose that en echelon fracture initiation is the most feasible mechanism for crack propagation because the associated mechanical fracture interaction promotes the most effective crack growth.

A highly probable explanation of en echelon fracture development (Pollard *et al.*, 1982) is this: the spatial rotation of a regional stress configuration is resolved on the plane of a propagating fracture as components of both normal and shear stress. The normal stress and the internal pressure combine to produce a mode I stress intensity

whereas the shear stress induces a mode III stress intensity. The latter initiates the development of en echelon segments (Figure 3.10).

Although the rotation of cracks out of the plane of a common fracture can therefore be associated with a resolved stress component, the cracks will eventually rotate into a plane that is once again perpendicular to the least compressive stress and must thus be classified as tension fractures. The degree to which the stress component is a valid parameter would probably depend upon the relative rates of fracture torsion and regional stress configuration variation, and is thus likely to be a function of the driving pressure and propagation rate (with slower torsion rates for higher propagation rates). This synopsis is in general agreement with the discussion of Pollard *et al.* (1982).

3.7.3 Linkage of En Echelon Cracks

Nicholson and Pollard (1985) recognise two end-member situations for dilating echelon fractures that have linked together (Figure 3.15). They are essentially geometrically defined, with one end-member exhibiting straight propagation paths and the other curved paths.

Cracks may produce straight propagation paths as a result of large separations or a large remote differential compression (Olson and Pollard, 1989). Linkage of such cracks is thus a consequence of dilation, with host rock bridges concentrating strain until the point of tensile failure is reached, causing crack linkage along the cross fracture. A subsequent increase in dilation results, and bent bridge formation. In conditions of low remote differential stress or small crack separations, pronounced crack curvature may lead to linkage. This again produces increased dilation and the induction of bent bridges which, unlike bridges associated with straight propagation paths, are not significantly strained. The formation of horns is common for both fracture varieties. Depending upon the exact conditions under which crack propagation, dilation and linkage occur, a large spectrum of possibilities between the two end-member situations may be produced (Nicholson and Pollard, 1985). In addition, the different frames of each end-member in Figure 3.15 can represent either simultaneous developments in successively more proximal sections along the advancing fracture, or a succession of events along a single cross section as dilation gradually increases.

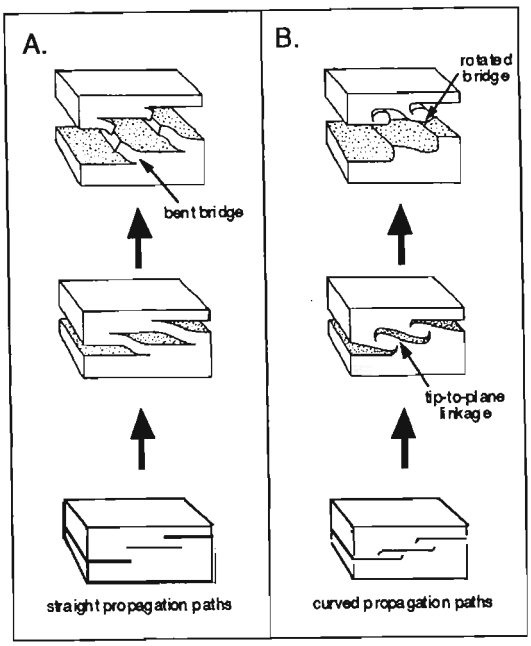

Figure 3.15. *Progressive development of dilating echelon segments that become joined. A: straight propagation path: dilation is accommodated by the bending of bridges of host rock. The failure of bridges along cross fractures leads to crack linkage. B: curved propagation paths: stress field interaction causes the propagating cracks to rotate towards each other. Tip-to-plane breakthrough links the cracks, resulting in increased dilation and the formation of rotated bridges (after Nicholson and Pollard, 1985).*

3.7.4 Flow Directions

If segments of en echelon offset intrusions advance as fingers from a common source, then the propagation and flow direction must be perpendicular to the plane of the page in Figure 3.14. Propagation thus occurs along the length of an offset surface (Pollard *et al.*, 1975), and must also be parallel to the long dimensions of horns. This is not necessarily true for all offset cracks (eg. Tweto, 1951; Bussel, 1989), but must be the case for en echelon arrays of fractures emanating from a common source.

3.7.5 Paleostress Interpretation

The orientation of en echelon crack arrays associated with shear zones can be utilised to infer the regional paleostress configuration that produced the cracks (Roering, 1968; Hancock, 1972). Similar generalisations cannot be made regarding echelon cracks that have rotated out of a common plane. It has already been described how en echelon segments rotate within a changing stress field and how the rate of rotation may not necessarily be as rapid as the rate of change in stress configuration. In cross-sections near to the parent crack, therefore, en echelon segments cannot be used as regional paleostress indicators with any great accuracy. More proximal cross-sections, where the segments are consistently oriented, are more likely to be good regional paleostress indicators (Nicholson and Pollard,

1985).

3.8 Dilation

An appraisal of dilation direction determination is provided by Bussel (1989). The dilation vector is determined by the relative offset of previously juxtaposed points along the fracture surface, which is governed by the mode of fracture. The amount of dilation that occurs may vary along the propagation path in response to variations in host rock ductility (Price and Cosgrove, 1990). An array of en echelon cracks may have a greatly enhanced dilation in comparison to an isolated crack of equal dimensions to the array (Pollard *et al.*, 1982), and crack interaction can result in sigmoidally dilated gashes. Nicholson and Pollard (1985) give the dilation ∂ of an isolated crack of width 2b as

$$\delta = \frac{\Delta p(1-\upsilon)b}{\mu} \tag{3.19}$$

where Δp is the driving pressure, υ is Poisson's ratio and μ is the elastic shear modulus.

4. SILL INTRUSION NEAR EMPANGENI

4.1 Introduction

One of the most impressive features of the Karoo Igneous Province is the volume of dolerite sills injected into Karoo Sequence sediments. Although there have been a number of petrological and geochemical investigations undertaken on these sills (eg. Walker and Poldervaart, 1949; Le Roex and Reid, 1978; Richardson, 1984), there has been little attempt at establishing intrusion mechanisms or flow directions of these dolerite sills.

The mechanism by which hypabyssal igneous rocks are emplaced is a topic of long standing in the scientific literature. Developments in the understanding of fracture mechanics involving brittle solids by authors such as Inglis (1913), Irwin (1957) and Jaeger and Cook (1969), as discussed in Chapter 2, have led to a better understanding of the mechanics of fracture and intrusion in the Earth's crust. This is testified in a number of geological works such as by Roberts (1970), Pollard (1973, 1987) and Pollard *et al.* (1982), in which mechanisms of dyke and sill intrusion are described (Chapter 3).

The aim of this chapter is to introduce a geomechanical perspective in the analysis of sill intrusion into Karoo Sequence sediments. Outcrops of dolerite sills have been investigated in northern Natal in an attempt to recognise features that provide evidence of the intrusion mechanism. Criteria have also been developed for the determination of absolute flow directions and recognition of the three-dimensional morphology of the sills. A study of the petrological and geochemical nature of the dolerites has proven to be a successful method for the identification of separate intrusive phases, the internal structure of multiple-intrusion sills, petrologic and geochemical gradients induced by intra-sill crystallisation effects, and the recognition of late-stage hydrothermal activity. Feature-specific measurements of sills have further allowed a reconstruction of local conditions of stress, strain, driving pressure and thermodynamic constraints.

Late Karoo dolerites of Jurassic age are intruded into Permian sediments of the Ecca Group along the Mhlatuze River, west of Empangeni, Natal. The sediments include sandstones of the upper Vryheid Formation and a variable sequence of mudstones and siltstones of the Volksrust Formation, previously documented by McCarthy (1960) and Tavener-Smith *et al.* (1988). Detailed mapping along the western bank of the Mhlatuze River led to the construction of a profile through the outcropping sediments and associated dolerite sills. This illustrates a number of morphological features of the sills, such as an en echelon geometry, that may be used to infer the emplacement mechanism. An investigation has also been made of dolerites that crop out in a dolerite quarry in the vicinity of the Mhlatuze River traverse. Dolerites have been analysed both petrographically and geochemically in order to distinguish specific characteristics and trends, as well as to obtain an understanding of Karoo dolerites situated in close proximity to the Lebombo Monocline, and how they compare to dolerites elsewhere in the Karoo Igneous Province, such as documented by Walker and Poldervaart (1949). Comparisons have also been made with results from previous investigations in the Lebombo region, such as by Cox and Bristow (1984), Sweeney (1988) and

Sweeney and Watkeys (1990).

4.2 Locality

The mapped portion along the Mhlatuze River is located approximately 16 km west of Empangeni (Figures 1.1 and 4.1). Fieldwork along the Mhlatuze River was restricted to the western bank, along which high cliffs of good outcrop occur. The traverse extends from the iron-girder bridge, where the old Empangeni-Eshowe road crosses the river, to a point 1800 metres downstream (south). A dolerite quarry, in which a number of dolerite sills crop out, is located 1 km northwest of the iron-girder bridge (Figure 4.1), and is operated by Baystone Sales of Richards Bay.

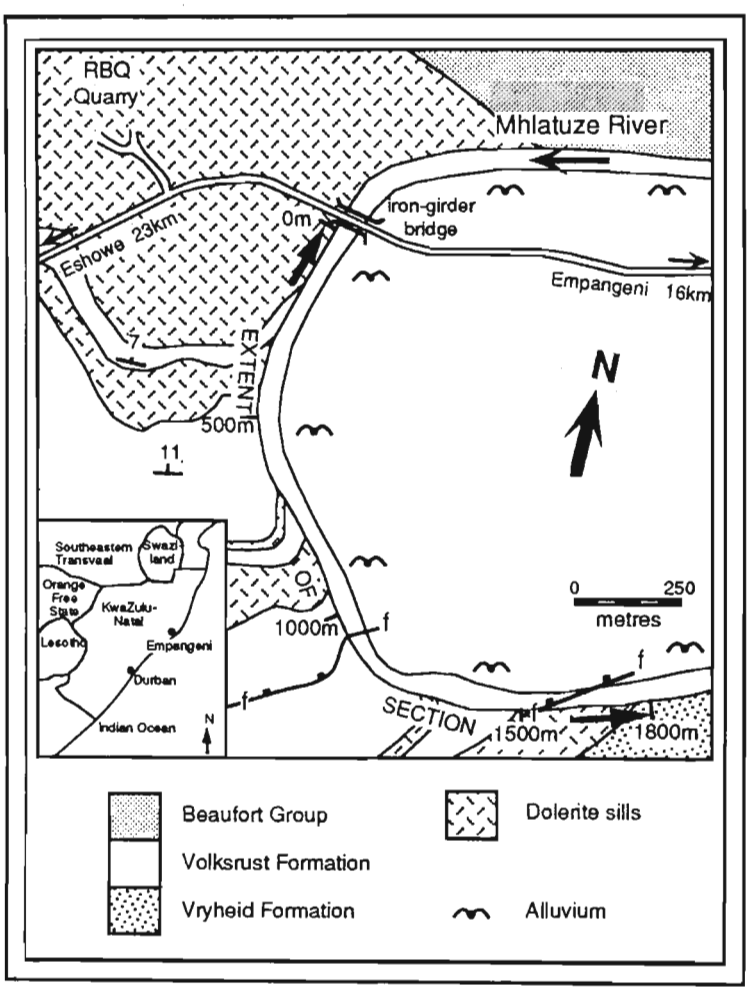

Figure 4.1. *Locality map with generalised geology, indicating the extent of the traverse along the Mhlatuze River, and the position of the dolerite quarry (from mapping in this study and after McCarthy, 1960).*

4.3 Local Geology

4.3.1 Ecca Group

The Karoo dolerite sills under investigation are restricted principally to the Volksrust Formation, although part of the traverse along the Mhlatuze River incorporates the upper vestiges of the Vryheid Formation. These formations mark the uppermost part of the Ecca Group (Figure 4.2).

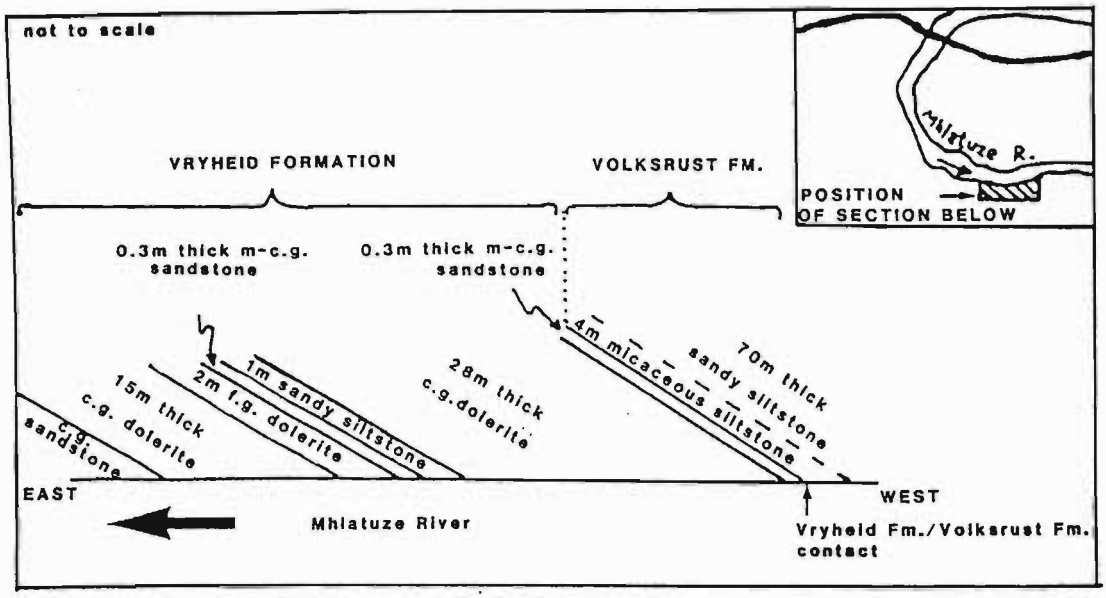

Figure 4.2. *Position of the Vryheid and Volksrust Formations in the local stratigraphy. Notations are: Fm.: Formation; c.g.: coarse-grained; m.g.: medium-grained; f.g.: fine-grained.*

The contact between the Vryheid and Volksrust Formations has been defined by Tavener-Smith *et al.* (1988) as the top of the uppermost sandstone bed within the sandstone-dominated Vryheid Formation. This contact occurs approximately 1500 m downstream from the iron-girder bridge. Dolerite intrusion occurred immediately below the contact, leaving a 0.3 m thickness of coarse-grained sandstone between the sill and the contact. Tavener-Smith *et al.* (1988) describe the sandstones here as being coastal to deltaic or lagoonal in origin. The Volksrust Formation consists of an approximately 200 m thickness of siltstones and mudstones which can be sub-divided into a number of discernable facies on the basis of sedimentological and palaeontological data. These facies have been tabulated together with an interpretation of the depositional conditions, similar to that given by Tavener-Smith *et al.* (1988), in Table 4.1. The sedimentary beds and incorporated sills dip to the northwest with inclinations varying between 7^{o} and 16^{o}.

FACIES TYPE	DESCRIPTIONS	INTERPRETATION
Interbedded silty mudstone/sandy siltstone	8m thick. Dusky blue to light grey. Includes a 0.6m thick f.g.sandstone bed with flaser bedding + thin lime -stone lenses + rippled bedding planes + twig and Glossopteris leaf imprints.	There was a source of woody material close-by. The mudstones with small ripples plus thin limestone may be lagoonal or from coastal inlet deposition, with sand from bars or barrier beaches.
Silty mudstone	≈40m thick. Dark grey. Micaceous. Bedding 244°/12°NW. Sandy siltstones up to 0.3m thick with clay draped ripple cross lamination. Glossopteris leaf- and Phyllotheca stem imprints present.	Possibly calm coastal embayment conditions with fluvially supplied plant debris, or deposition in a well vegetated lagoonal environment.
Sandy siltstone	≈50m thick. Colour varies through grey, light olive green and pale greyish green. Beds 300°/16°NE. Towards top, Glossopteris and Vertebraria root and stem structures occur.	Tavener-Smith *et al* (1988) reported Phyllotheca stems in this facies too. This suggests fresh water lake margins. The possible depositional environment was a lagoonal margin.
Mudstone	10m thick. Light grey and rubbly with some flaser bedding present.	Interpretation of this facies is difficult. Low energy environment; possibly highly bioturbated.
Clayey siltstone	15m thick. Dark grey with sand beds up to 0.2m thick. Bedding 225°/28°NW.	Comparison with adjacent facies suggests lagoonal or shallow marine. The sand beds may be the result of fluvial flooding or storm surges.
Sandy siltstone	≈70m thick. Dusky blue to dark bluish grey. Micaceous near base. Much Planolites and Scolicia-like trails with Siphonichnus and Teichichnus trails highlighted by calcite. 4m thick light grey micaceous siltstone at base of facies.	The abundance of marine related bioturbation effects suggests a shallow marine environment. This may have been in the vicinity of a river mouth with its associated supply of sand into the depositional basin.

Table 4.1. *Volksrust Formation sedimentary sequence with interpretations of depositional environment. The base of the sequence is at the bottom of the table.*

Dilation and dolerite intrusion was compensated by a vertical displacement of the intruded sediments, with no apparent elimination of strata. Strata of the Volksrust Formation are disturbed by fault drag along a zone of normal faulting 1150 m downstream of the iron-girder bridge (Figure 4.1), however, there has been no elimination of strata (Tavener-Smith *et al.*, 1988). The Volksrust Formation, which dominates the outcrop along the river traverse, is exposed from its basal contact to the iron-girder bridge, through an equivalent vertical thickness of 200 m. A light grey mudstone containing the terrestrial fossil Glossopteris crops out in the dolerite quarry, and may be related to the uppermost facies along the Mhlatuze River traverse. Due to the lack of any specific definition of the boundary between the Volksrust Formation and the overlying Emakwezini Formation of the Beaufort Group (defined by SACS (1980) as being composed of shale, mudstone, sandstone and minor coal seams), all siltstones and mudstones described here have been allocated to the Volksrust Formation, in agreement with the interpretation of Tavener-Smith *et al.* (1988). The Beaufort Group lower contact as shown in Figure 4.1, was defined by McCarthy (1960).

4.3.2 Dolerite Sills

The morphology of the dolerite sills along the Mhlatuze River is shown in Figure 4.3. Field observation suggests at least three phases of dolerite. The first phase produced thick (15 - 28 m), coarse-grained sills that crop out near the iron-girder bridge at the northern end of the river traverse, and along the junction between the Vryheid and Volksrust Formations (Figure 4.3). The sill at the northernmost extent of the traverse has an outcrop thickness of 27 m with no upper contact exposed. The grain size of the coarse-grained dolerite decreases markedly towards the sill margins as a consequence of more rapid cooling against the host rock.

The second dolerite phase resulted in comparitively thinner (2 - 5 m) sills of fine-grained to glassy dolerite. They occur along the entire length of the section, repeatedly dipping and stepping up towards the northwest. Along the northern part of the section (Figure 4.3) the fine-grained dolerite was emplaced into the earlier sills of coarse-grained dolerite approximately one quarter of the way up from the base. Where this has occurred, the fine-grained dolerite has chilled against the coarse-grained dolerite along both the upper and lower contacts. This enabled the determination of field relations and relative ages. The fine-grained dolerite sills are associated with a number of small-scale intrusion-related features such as offsets, horns and both bent and rotated bridges. The rotated bridges show evidence of permanent strain. This is most apparent in bridges of incompetent host rock but is true also for bent bridges composed of dolerite. An example at the 129 m mark along the traverse (Figure 4.3) incorporates a 3 cm thick granitic vein intermediate in age between the coarse-grained and fine-grained dolerites. A rotated bridge of coarse-grained dolerite exhibits deformation of the vein within the bridge (Figure 4.4).

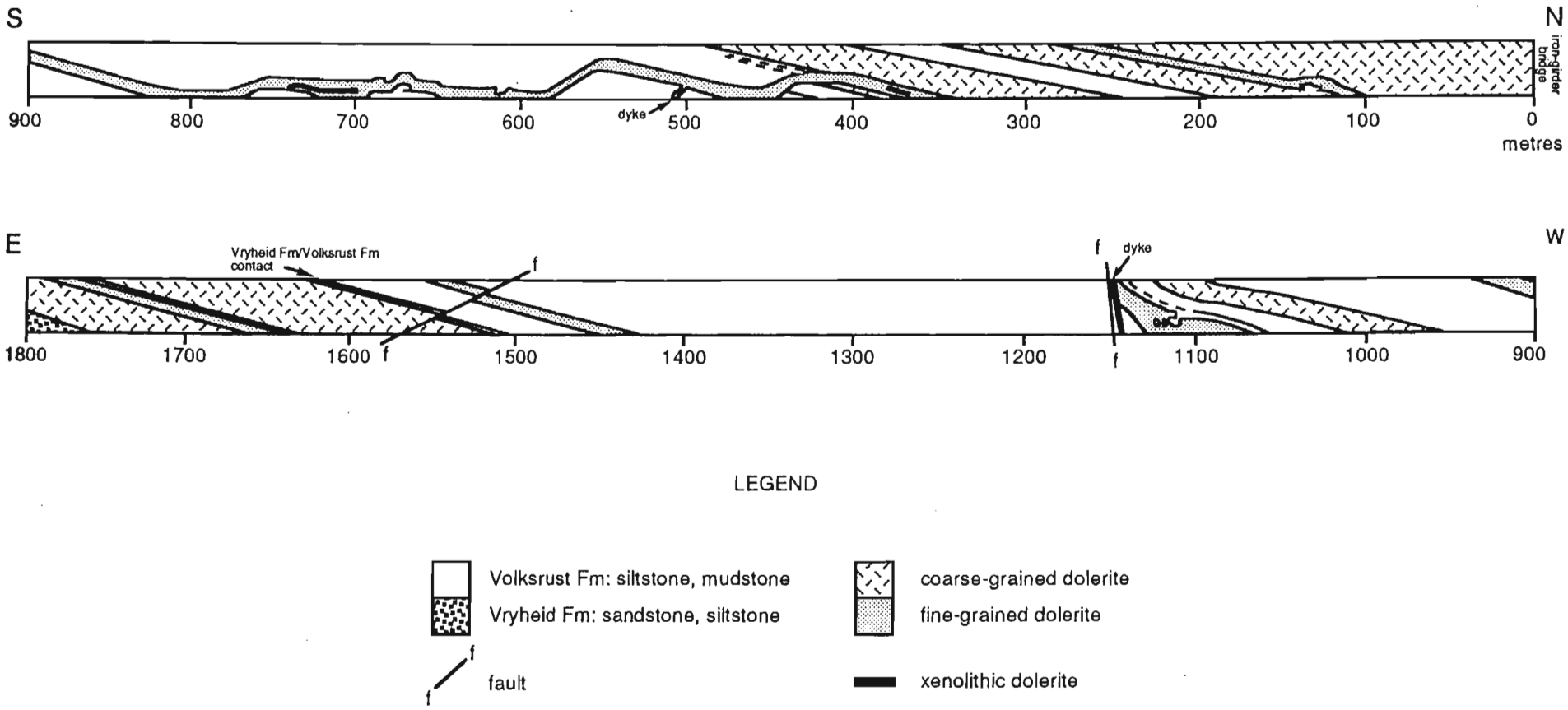

Figure 4.3. *Cross-section along the Mhlatuze River west bank indicating dolerite sill morphology along the traverse indicated in Figure 4.1.*

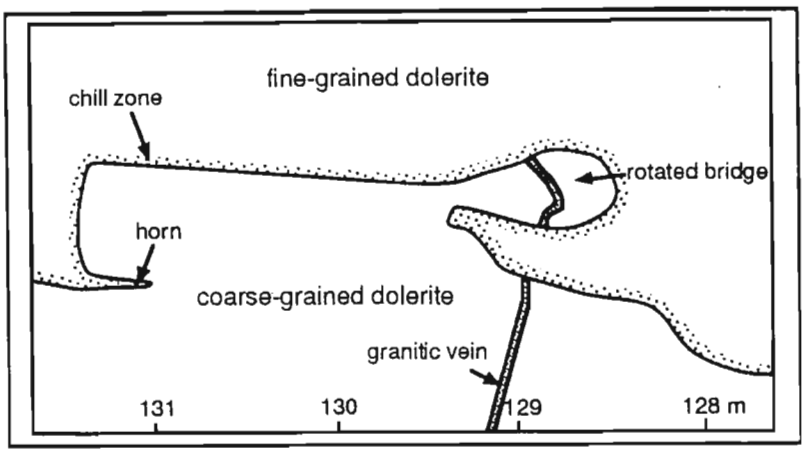

Figure 4.4. *A rotated bridge of coarse-grained dolerite within fine-grained dolerite at the 129 m mark. The strained bridge exhibits a deformed granitic vein that is intermediate between the two dolerite phases in age. Both end-member bridge types defined by Nicholson and Pollard (1985) are represented in close proximity to each other at this location.*

The third dolerite type is characterised by the incorporation of an assortment of xenoliths of crustal material, and will thus be termed the xenolithic dolerite. It occurs as two distinct blocks or wedges, both encapsulated within fine-grained dolerite (Figure 4.3). The first block, extending from the 350 m mark to the 360 m mark is 0.5 m thick. The second block, between the 700 m and 738 m marks, varies from 1 m to 1.5 m in thickness. The xenoliths are predominantly granite gneiss, with lesser amounts of quartz, feldspar, clay, mica schist and graphite xenoliths. They constitute approximately 60% of the rock, are rarely greater than 10 cm in diameter, and are elongate, defining a macro-foliation. Parallel to the foliation, there are also thin bands of increased deformation within which quartz xenoliths are ribbon-like, and granite gneiss and graphite xenoliths are increasingly foliated. The fine-grained dolerite has chilled against the enclosed xenolithic dolerite blocks which must, therefore, pre-date the fine-grained phase.

The xenolithic dolerite contains pyrite along the xenolith boundaries and within the matrix of fine-grained dolerite. Calcite amygdales are common, and pass through both the dolerite matrix and the xenoliths. They are characterised by dark chlorite rims and are predominantly less than 2.5 mm in diameter, although amygdales up to 17 mm across occur. The "matrix" of fine-grained dolerite displays a cooling induced decrease in grain size towards the edges of the blocks.

The terminologies "coarse-grained dolerite", "fine-grained dolerite" and "xenolithic dolerite", as outlined above, will be retained as the consistent means of dolerite nomenclature in this chapter.

4.3.3 Faulting

The Mhlatuze River section is faulted in two locations: at the 1150 m and 1520 m positions (Figure 4.3). The subvertical fault at the 1150 m mark has disrupted the strata for a distance of about 50 m to the north of the fault.

This appears to be the result of fault drag, induced by a downthrow on the northern side of the normal fault. Near the fault, the sediments are brecciated and deformed. The apparent fault plane is marked by two post-faulting dolerite dykes, 1.5 m and 0.3 m thick respectively. Despite the prominence of this fault and shatter zone, displacement is probably not extensive (Tavener-Smith *et al.*, 1988). The fault near the 1520 m mark has a downthrow of 1.5 m on the northern side and is a normal fault, contrary to its appearance in Figure 4.3 in which it resembles a reverse fault as a consequence of its orientation (strike and dip of 235¤/ 78¤ NW respectively) with respect to the orientation of the section (Figure 4.1).

4.4 Dolerite Petrography

Twenty one petrographic thin sections of dolerites along the Mhlatuze River traverse were examined (Appendix 2). The dolerites are all essentially tholeiitic, with sub-ophitic plagioclase and lesser amounts of pyroxene occurring as the predominant mineral phases. Most dolerites have undergone varying degrees of alteration involving chloritisation of pyroxene and sericitisation or calcitisation of plagioclase.

4.4.1 Coarse-grained dolerite

FELDSPAR: The coarse-grained sills generally consist of 50-70% plagioclase, ranging in composition from oligoclase to labradorite. The crystals are tabular and randomly oriented, and exhibit Carlsbad, albite and polysynthetic twinning. Near the sill margins, the amount of plagioclase increases to 70-75% of the rock, and occurs as both an unoriented, sub-ophitic acicular groundmass and a phenocrystic portion. The plagioclase is An_{35-55} (andesine/labradorite) and the phenocrysts are visibly zoned. Alteration effects include both calcitisation and sericitisation. Calcite replacement began along cleavage and twinning lamellae before moving to the grain boundaries. Sericitisation is common, occasionally in the form of sericitised exsolution lamellae. Small amounts of alkali feldspar (orthoclase) sometimes occur.

PYROXENE: Both clino- and orthopyroxenes occur in the dolerites in the form of augite and hypersthene respectively, although small amounts of pigeonite were noted from one sill. Pyroxene is represented by both phenocrystic and groundmass portions, with the latter arranged sub-ophitically with plagioclase. Away from the sill margins, augite and hypersthene occur in equal abundance, constituting a total pyroxene content of 30%. Closer to the sill margins, there is less total pyroxene (20-25%), with variable relative amounts of augite and hypersthene, although the amount of augite does not exceed 10%. Alteration effects include the ubiquitous chloritisation of both pyroxene types, and later calcitisation in close proximity to the sill margins. In addition, hypersthene is occasionally serpentinised along cracks and grain boundaries (Figure 4.5).

Figure 4.5. *Serpentinisation of hypersthene crystals along cracks and grain boundaries (arrowed). Sericitisation (S) of adjacent plagioclase is also evident, as well as chloritisation (C) of groundmass pyroxene.*

OTHER MINERALS: Interstitial glass comprises up to 15% of the coarse-grained dolerite. Accessory minerals include pyrite, titanomagnetite, ilmenite, sphene, biotite and quartz. The volume percentage of both phenocrysts and opaque minerals increases towards the lower margins of the sills, probably as a result of crystal settling of the larger and denser crystals in the magma. Up to 10% of the rock is constituted by primary phenocrysts of plagioclase, augite and hypersthene. Opaque minerals comprise up to 10% of the dolerite, predominantly pyrite, which is most concentrated near the sill boundaries. The euhedral biotite grains exhibit occasional pyroxene nuclei and may therefore be pre-chloritisation pseudomorphs of augite. Calcite-rich amygdales represent up to 5% of the rock, increasing in abundance towards the upper contacts.

4.4.2. Fine-grained dolerite

Compared to the coarser dolerites, this type has less plagioclase and more total pyroxene. Small amounts of interstitial glass usually occur. Cooling of the fine-grained dolerite from the contacts inwards has resulted in a small degree of fractionation so that substantial amounts of primary quartz and alkali feldspar occur at some of the sill centres.

FELDSPAR: Plagioclase constitutes 60-65% of the rock and is approximately An_{50} (labradorite). The grains are acicular and usually unoriented, although a flow fabric is present within some chilled, glassy margins of the sills. As was the case with the coarse-grained dolerite, plagioclase is most abundant near the sill base. Alteration by sericitisation is common near the sill margins.

PYROXENE: The greater amount of total pyroxene in the fine-grained dolerite in comparison with the coarse-grained dolerite is manifested by an increase in the augite content, which totals 20-25% of the rock. The augite grains are acicular and are frequently substantially chloritised. Where appreciable amounts of devitrified glass occur between the plagioclase grains, pyroxene is usually absent. Chloritised hypersthene never exceeds 15% of the rock volume, and is sometimes completely absent.

OTHER MINERALS: Green-brown biotite is usually present in amounts less than 5% but comprises up to 10% of the rock in places. Small nuclei of augite are remnants of the pyroxene grains that were pseudomorphed by the biotite. Biotite grains are frequently juxtaposed against titanomagnetite. A few biotite grains have calcitised rims. The opaque minerals present are titanomagnetite and pyrite, which are present in amounts up to 10%. Titanomagnetite is a primary mineral phase but pyrite is a secondary pseudomorphing phase concentrated along the sill margins, as in the coarse-grained dolerite. Calcite-rich amygdales are dispersed throughout the sills. Calcite is common in the dolerites, frequently in substantial amounts. This is especially true closer to the sill margins and it is probable, therefore, that calcite is a secondary mineral associated with late fluids migrating along the sill contacts. Pyrite probably formed in a similar manner as it too is concentrated along the sill margins. Calcite can also be a by-product of the alteration of pyroxene to chlorite (Hatch *et al*, 1972) but this reaction would probably not result in large quantities of calcite, as observed.

4.4.3 Xenolithic dolerite

The doleritic groundmass of the xenolithic dolerite consists principally of calcic plagioclase and hypersthene. The plagioclase is substantially calcitised and the majority of hypersthene grains are altered to chlorite. Pyrite occurs around xenocryst boundaries and along the foliation direction. Calcite-rich amygdales are common and have diameters of up to 17 mm. Sphene occurs in an accessory capacity. Most xenocrysts are quartz and K-feldspar (orthoclase), probably derived from disaggregated granite gneiss xenoliths of local basement origin. The quartz xenocrysts are frequently strained and embayed, and feldspar xenocrysts are disaggregated and calcitised (Figure 4.6). Some xenocrysts have been completely converted to calcite. Quartz equilibrium textures such as 120^{o} triple junctions suggest partial melting and recrystallisation. Partial melting would also account for the occurrence of amygdales within xenoliths. In thin section, graphite occurs as thin (20-200 microns) bands intercalated with a dolerite matrix, suggesting immiscibility during partial melting (Figure 4.7). The intrinsic grain size difference in the doleritic groundmass of Figures 4.6 and 4.7 reflects a cooling-induced grain size decrease towards the margins of the xenolithic dolerite blocks.

Figure 4.6. *Xenolithic dolerite (plane polarised light) with xenocrysts of embayed quartz and calcitised feldspar. The doleritic groundmass is comprised of plagioclase and chloritised hypersthene.*

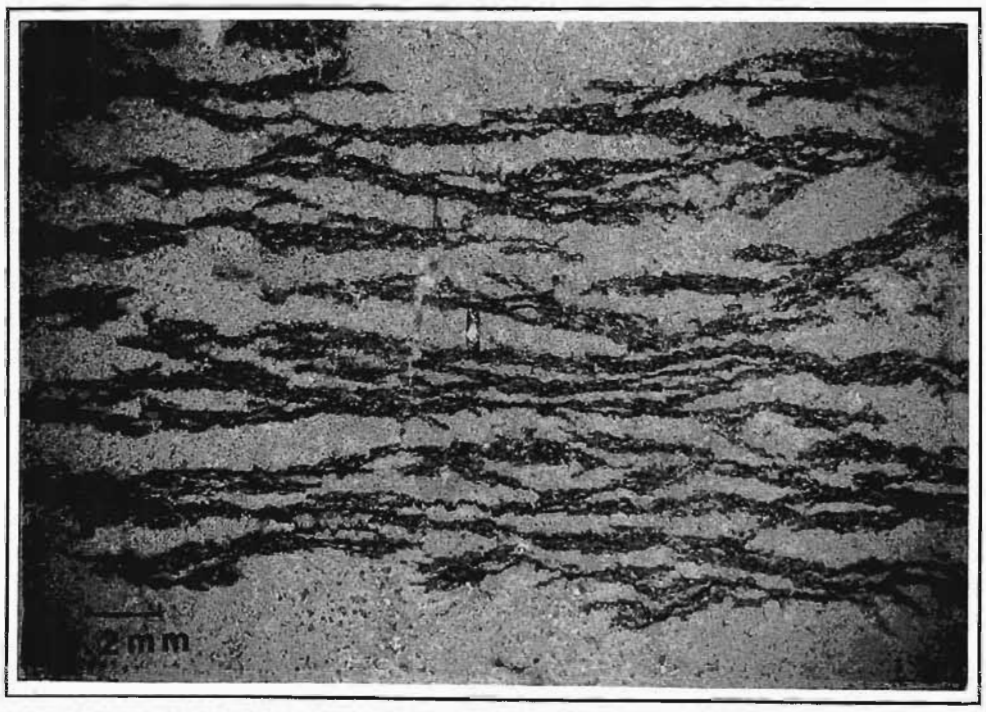

Figure 4.7. *Graphite component of the xenolithic dolerite as seen in plane polarised light. Thin graphite bands occur intercalated with dolerite groundmass as a result of immiscibility during partial melting of xenoliths of graphite or coal.*

4.4.4 Pyrite

Pyrite is the only opaque mineral in the dolerite sills that did not crystallise as a primary mineral phase, and its unusual nature and occurrence thus warrants specific regard. As mentioned above, it occurs in all of the sills present with an affinity to the sill contacts. This suggests that the sulphur for the pyrite was introduced as a component of late-stage fluids that migrated along the sill contacts. The pyrite characteristically occurs as rounded blebs up to 7 mm across. They have grown by pseudomorphing sericitised plagioclase and, to a lesser degree, chloritised pyroxene. This process was initiated along grain boundaries and then proceeded to incorporate the entire mineral. Unaltered plagioclase and pyroxene are not pseudomorphed by pyrite. Where unaltered pyroxene occurs around sericitised plagioclase, only the plagioclase grains are pseudomorphed by the pyrite (Figure 4.8). Embayments of pyrite into euhedral titanomagnetite occurs to a lesser degree (Figure 4.9). Within the xenolithic dolerite, the pyrite tends to grow along the foliation and along the xenocryst/dolerite boundaries. Finally, pyrite occurs along a contact plane between a fine-grained and coarse-grained dolerite sill, in the form of lineations defined by pyrite nodules that have subsequently been altered to limonite.

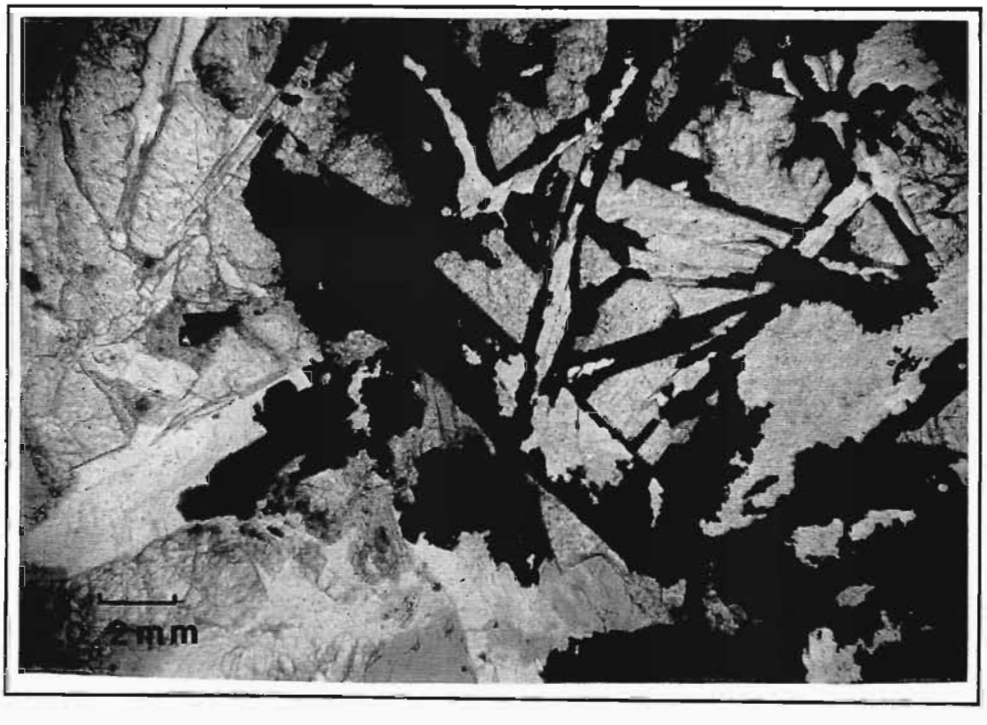

Figure 4.8. *Sericitised plagioclase being pseudomorphed by pyrite. The unsericitised portion of the plagioclase is not as embayed as the sericitised portion. The pyroxene grains are relatively unaltered, and have thus not been pseudomorphed by pyrite.*

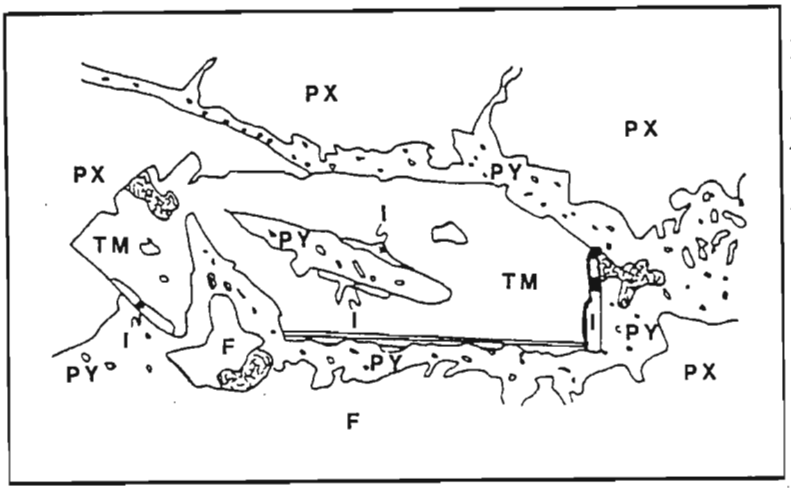

Figure 4.9. *Embayments of pyrite into euhedral titanomagnetite that exhibits ilmenite oxidation and exsolution lamellae. Note how pyrite grows by extending along grain boundaries. TM = titanomagnetite. PY = pyrite. I = ilmenite. PX = pyroxene. F = plagioclase feldspar.*

4.4.5 Amygdales

Amygdales occur within all the dolerites, but are most common in the fine-grained phase, increasing in concentration towards the tops of the sills. In three dimensions they are spherical, although a small number are distended along a principal axis. As mentioned previously, amygdales within the xenolithic dolerite are up to 17 mm across, however, within the other dolerites the amygdales have a diameter range of 0.1 mm to 1.5 mm. The infill sequence of the vesicles was generally uniform in all the sills:

1. Chlorite (at the rim)
2. Thomsonite
3. Calcite
4. Quartz (not always present)

The rims consist of green-brown, structureless chlorite, and are occasionally interspersed with small opaques. The next mineral phase is a rim of thomsonite: a zeolite characterised by radiating fibrous crystals. It was identified using analogies to descriptions of amygdale minerals within the Mfolozi River Formation basalts to the north of this location (Wheelock, 1978). Calcite constitutes the major portion of the amygdales. Small grains of quartz at the centre of some amygdales mark the last mineral that crystallised within the vesicle (Figure 4.10). A narrow, pale olive-green zone of leaching frequently surrounds the amygdales, predominantly within the glassy chill-margins. The amygdales within the fine-grained dolerite dyke at the 505 m mark along the river section (Figure 4.3) exhibit an enclosing ring of glass.

4.5 Sills in the Dolerite Quarry

The dolerite quarry is situated 1 km northwest of the iron-girder bridge at the northern end of the Mhlatuze River traverse, and is operated by Baystone Sales of Richards Bay. Present operations in the quarry are confined to the northern end, whereas the older, southern end has become filled with water (Figure 4.11).

Although the quarry is dominated by thick dolerite sills, outcrops of silty mudstone mark the basal contact of the stratigraphically lowest sill within the quarry. The mudstone is light grey and contains twig and leaf imprints of Glossopteris, and is thus very similar to the stratigraphically highest mudstone occurring along the Mhlatuze River section, and may belong to the same facies. The dolerites within the quarry were correlated at various points across the quarry on the basis of the relative heights above the silty mudstone contact.

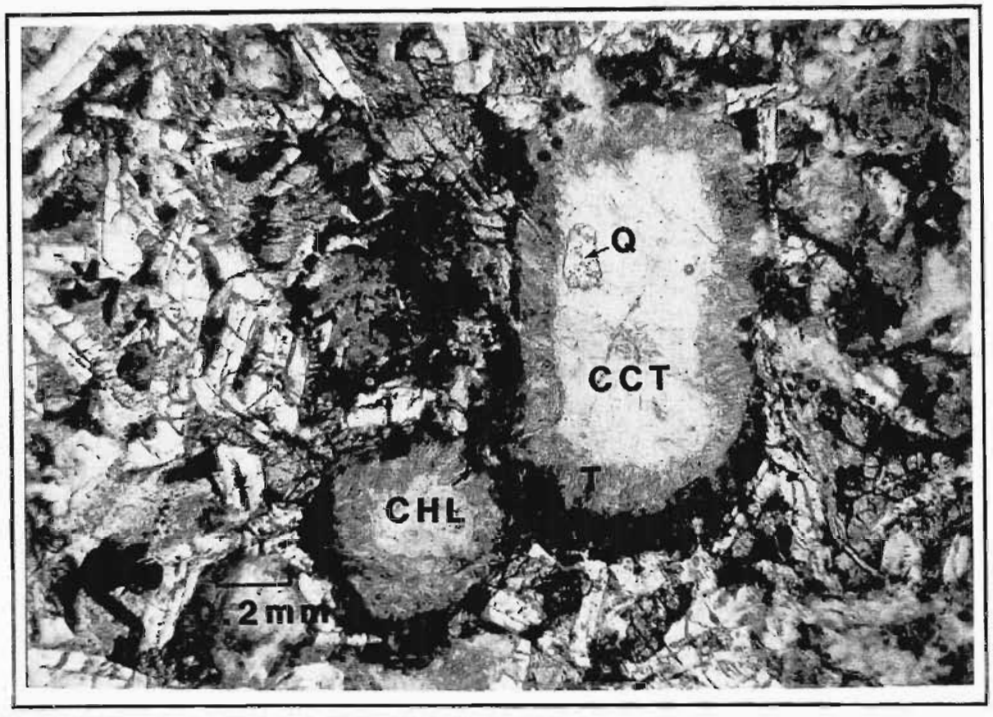

Figure 4.10. *Two amygdales displaying a typical infill mineral assemblage. The chlorite rims (CHL) encompass fibrous thomsonite (T), followed by calcite (CCT) and a small amount of quartz (Q). Most amygdales are spherical, but some are distended along a principal axis, such as the one shown here which has a long-axis length of 1.4 mm.*

As the dolerite sills generally dip towards the north, the greatest thickness of dolerite within the quarry occurs at the northern end. At this point, the dolerite attains a thickness of approximately 50 m (overlying the silty mudstone), with no upper boundary observed. This thickness of dolerite appears to occur as three separate sills. The lowest sill contacts against the silty mudstone and is 15 m thick. The sill above this is approximately 35 m thick, and only the first metre of the uppermost sill crops out above this. The sill contacts are not well defined and, therefore, recognition of the three sills was achieved on the basis of visual differences and petrography.

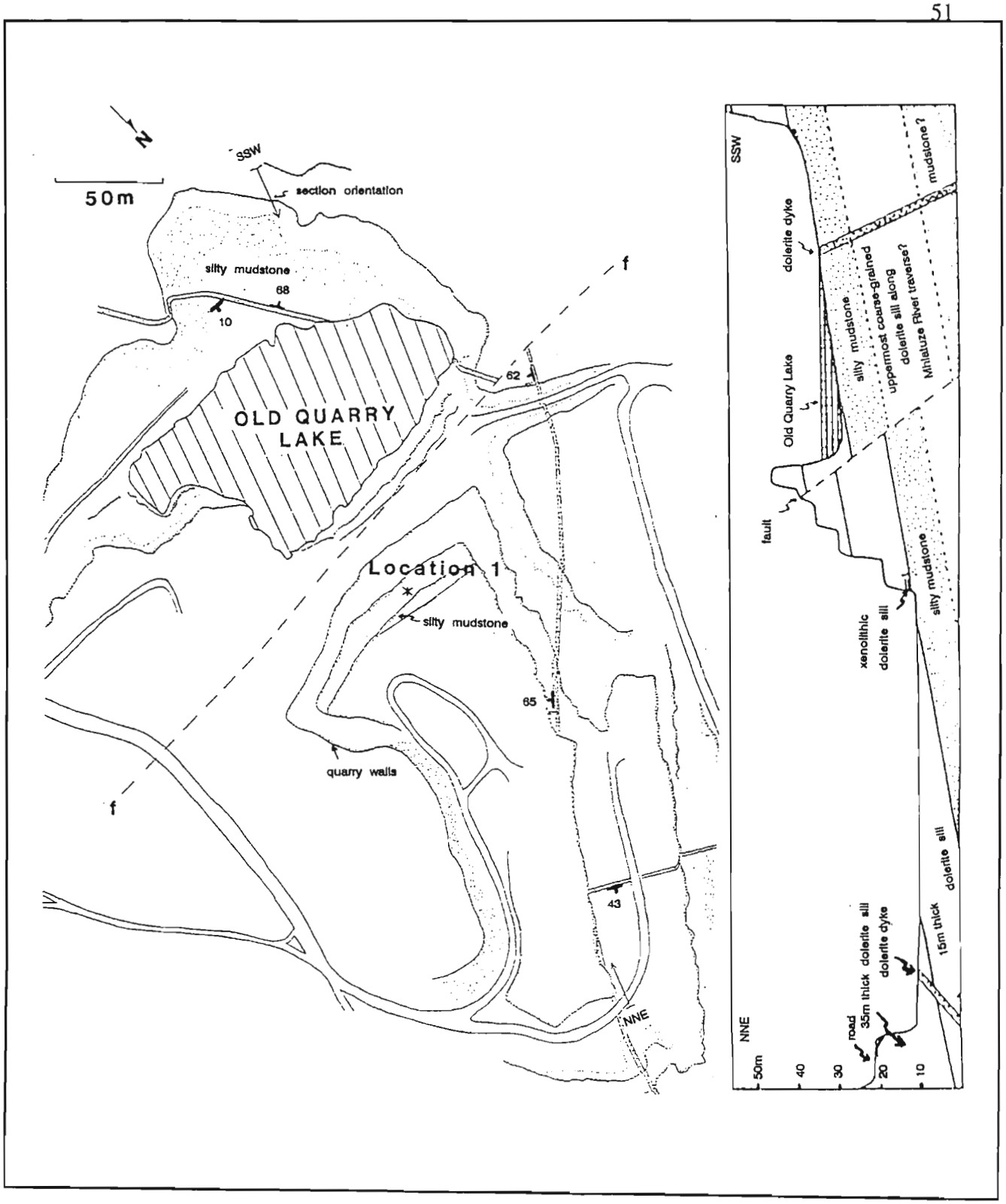

Figure 4.11. *Detailed map of the RBQ quarry. Inset: Cross-section showing the geology across the quarry from north-northeast to south-southwest.*

The variation in major mineral types through the 15 m thick sill (Figure 4.12) displays a prominent antipathetic relationship between the abundances of hypersthene and augite through the sill. The latter is more concentrated towards the base of the sill. Both plagioclase and the opaque minerals show greatest abundances nearer the sill base. The decrease in plagioclase content in the lowermost one metre of the sill is representative of the rapidly cooled, fine-grained base of the sill, which is also characterised by glomero-porphyritic phenocrysts of plagioclase and hypersthene. The 15 m thick sill exhibits a progressive increase in grain size from the base to the top. This is the result of a greater heat flux out of the base of the sill, which contacts against mudstone, than out of the top of the sill, suggesting that the overlying sill may have pre-dated the 15 m thick sill, and was still conducting heat into the surroundings when the latter sill intruded along its base.

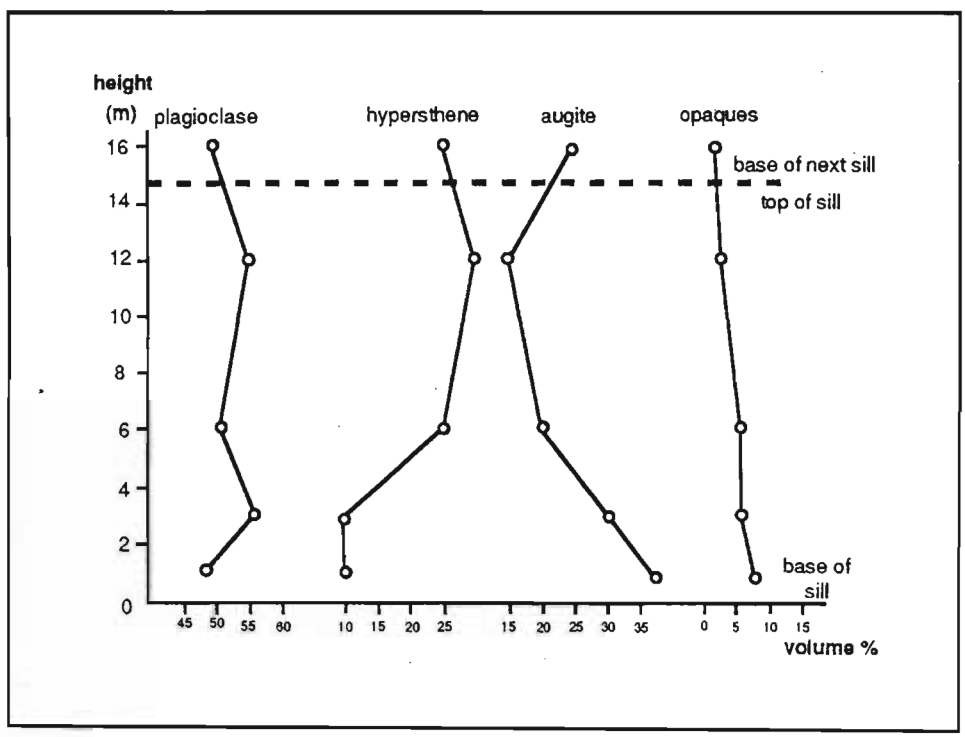

Figure 4.12. *Distribution of the main mineral phases through the 15 m thick dolerite sill within the dolerite quarry. The base of the overlying 35m thick sill is marked by a distinct change in the mineral abundance profiles.*

The base of the 35 m thick medium to coarse-grained dolerite sill above the 15 m thick sill is marked by a decrease in plagioclase and hypersthene content, and an increase in the amount of augite (Figure 4.12). The sill overlying the 35 m thick sill is poorly exposed, with only the basal metre visible. Characteristic pyroxenes of this dolerite display overgrowths of augite around hypersthene, with expansion cracks radiating into the augite, away from the hypersthene after it was serpentinised along internal cracks and the grain boundary (Figure 4.13).

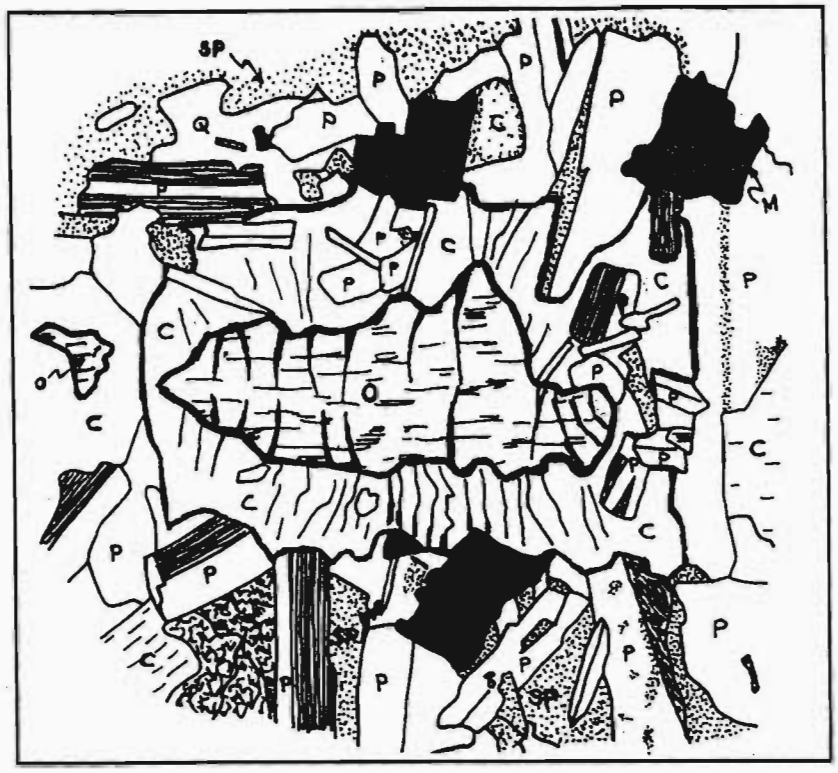

Figure 4.13. *Overgrowth of augite around serpentinised hypersthene, from the 35 m thick dolerite sill in RBQ quarry. Note the expansion cracks radiating into the augite due to serpentinisation of the hypersthene core. C = augite, O = hypersthene, P = plagioclase, Q = quartz, M = magnetite, SP = sericitised plagioclase.*

At one location within the quarry, the 15 m thick dolerite sill encapsulates a fine-grained dolerite sill that is xenolithic (Figure 4.11, location 1). This sill is a maximum of 2.5 m thick and contains a number of xenoliths of quartz, shale and dolerite. The sill is extraordinary in that although it occurs within another dolerite, it is totally enclosed within thin bands of mudstone at its upper and lower contacts. These slivers of mudstone are up to 0.4 m thick and are highly deformed. Many fragments of the shale were incorporated into the fine-grained sill, especially along the contacts. The dolerite groundmass is composed of highly sericitised plagioclase and chlorite, with some augite remnants. Quartz xenocrysts are embayed and sub-grains display 120° triple junctions. Feldspar xenocrysts are substantially calcitised. The xenocrysts define a prominent foliation direction. Pyrite has crystallised along the foliation direction, and pseudomorphs altered plagioclase. These characteristics compare well to the xenolithic dolerite along the Mhlatuze River. The obvious difference is the presence of the mudstone wedges along the contacts and the more sill-like appearance of this xenolithic dolerite.

As shown in Figure 4.11, there are three dykes traversing the dolerite quarry. They appear to pass through all of the sills within the quarry. The longest dyke strikes northeast to southwest across the quarry, and is associated with post-intrusion faulting along the intrusion plane, that has converted the dolerite to schist.

There is evidence for late-stage hydrothermal fluid flow along the dolerite sill contacts, as was suggested along the

Mhlatuze River section. The introduction of sulphides into the sills was one consequence of this fluid event, however, more specific evidence occurs along the contact between the 15 m thick dolerite sill and the underlying mudstone, as well as along partings within the mudstone. These surfaces are characterised by linear trails of pyrite nodules, similar to those observed along the Mhlatuze River on the contact plane between two juxtaposed sills. Smith (1987) describes linear ridges and grooves along a dyke contact that he ascribes to the "scouring and erosion of chilled, viscous magma near the dyke contact by more fluid magma flowing in the dyke's interior". Similar features were noted by Roberts and Sanderson (1971). These scour marks along the chill margin should thus give evidence of the magma transport direction. The appearance of the pyrite nodule lineations along the chill margins of the sills suggests that the pyrite may have nucleated along pre-existing grooves along the contact plane during fluid injection. Such grooves may have formed by the mechanism proposed by Smith (1987). However, this mechanism does not account for the existence of pyrite lineations along partings within the mudstone immediately adjacent to the sill contact. A possible extension of Smith's (1987) solution is the formation of grooves along the mudstone partings induced by sliding along the principal shear direction. This would parallel the magma transport direction in close proximity to the contact plane (Ross, 1986). The orientations of the pyrite lineations are shown as a rose diagram in Figure 4.14, and the overall trend may be indicative of the magma migration direction for the 15m thick sill. The pyrite defining the lineations has subsequently been altered to limonite, and a thin zone of iron staining extends into the mudstone along the migration planes.

Calcite and quartz veins are common in the dolerites within the quarry. Multiple pulse, episodic fluid injection into joints to produce quartz veins is discernable via internal chill margins. Three crystallisation events were identified in one quartz vein using this criterion (Figure 4.15).

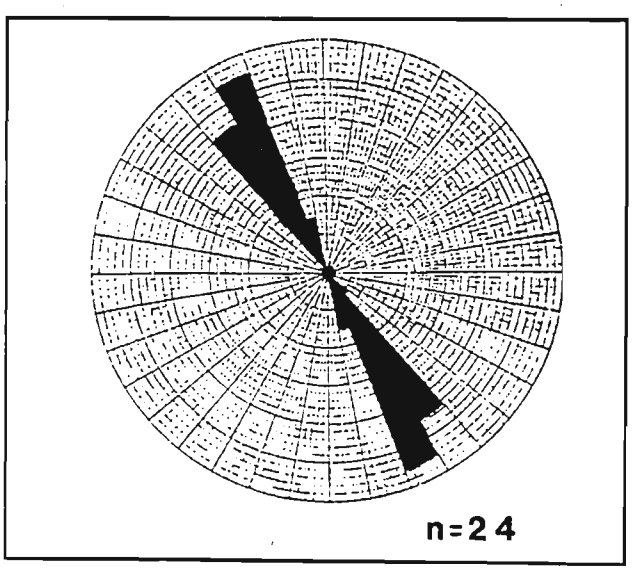

Figure 4.14. *Rose diagram showing the orientation of pyrite nodule lineations along fluid migration planes defined by dolerite/mudstone contacts at the southern side of Old Quarry Lake (Figure 4.11). The trend may be a representation of the magma migration direction (see text).*

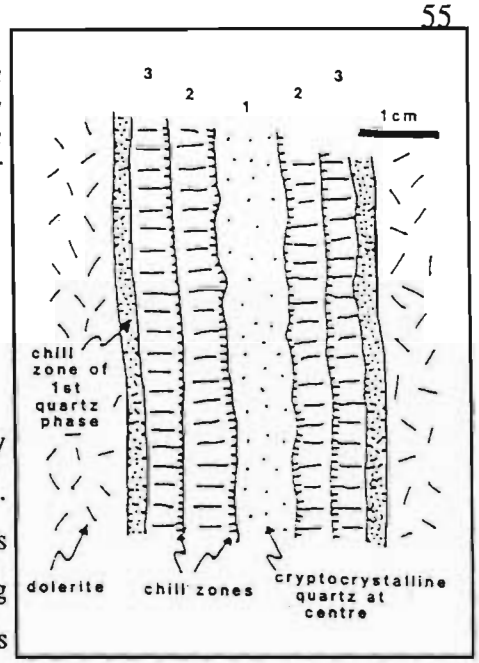

Figure 4.15. *Episodic fluid flow along joint planes demonstrated by a syntaxial quartz vein (on the northeast side of Old Quarry Lake) exhibiting three crystallisation events. The separate events are distinguished by the presence of chill margins within the vein, as with the criterion used for recognising multiple intrusion in dykes and sills.*

4.6 Flow Direction

The initial pulse of magma that intrudes a dilating fracture is rapidly quenched against the sides of the fracture to produce a chill margin. Consequently, any preferred orientation of crystals or phenocrysts is preserved in the frozen magma. The flow of magma into a dilating fracture is likely to produce a flow-parallel alignment, defined by crystals and phenocrysts of suitably high aspect ratio (eg. Roberts and Sanderson, 1971; Smith, 1987; Benn and Allard, 1989; Allard and Benn, 1989). This is most likely to occur against the walls of the intrusion, where the greatest velocity gradient occurs (Komar, 1976), together with high associated rates of shear (Barrière, 1976; Ross, 1986; Ildefonse *et al.*, 1992). Rapid quenching preserves this flow fabric which may thus provide information on the flow orientation, although not the absolute flow direction. Phenocrysts introduced with the magma pulse are unlikely to be accreted onto an inwardly advancing crystalline margin during periods of flow, as a result of hydrodynamic forces that induce flow differentiation (eg. Bhattacharji, 1967; Barrière, 1976; Ross, 1986; Platten and Watterson, 1987). The flow fabric is thus likely to be demonstrated in an aphyric margin by micro-phenocrysts and crystals growing along the shear direction. Flow differentiation effects are greatest for narrow fissures. Wide fissures may undergo differential accretion during episodic magma pulses, producing multiple aphyric and porphyritic zones (Platten and Watterson, 1987). In such cases, aphyric zones away from the absolute margin may presumably also provide evidence of the flow axis, or variations thereof between successive injection pulses.

The lower chill margin of one of the fine-grained sills sampled along the Mhlatuze River exhibits a preferred mineral orientation in a plane parallel to the contact, defined by quenched acicular pyroxene crystals (Figure 4.16). This effect is restricted to the chill margin of the sill and is thus assumed to be indicative of the principal shear plane and accordingly, the flow axis orientation. Measurements of crystal orientations (Figure 4.17) indicate a preferred orientation of 025°-030°; in other words an approximately north-northeast/south-southwest orientation axis. This compares well to the measured strike directions of a number of offsets and apophyses of the fine-grained dolerite sills near the 670 m mark along the Mhlatuze River traverse. If the preferred mineral orientation is indeed a result of shear along the magma flow direction, then the flow direction would have been along the offset surfaces, in agreement with the model of Pollard *et al.* (1975). The relatively shallow dip of the Volksrust Formation sedimentary beds, and associated shallow plunge of the flow axis down the dip, results in a negligible change in the inferred flow axis orientation when the beds and lineation are stereographically projected back to the horizontal plane.

The 025°-030° observed orientation is thus an accurate representation of the original flow lineation prior to local tilting.

Additional peaks in the mineral orientation frequency profile (Figure 4.17) occur at the 100° and 160°-170° orientations. These orientation peaks probably represent minor shear across the predominant flow/shear direction, or may be the result of an imbrication or tiling effect produced by stacked grains, similar to the tiles on a roof (Benn and Allard, 1989; Ildefonse *et al.*, 1992). A skewness in the distribution of orientations may also be attributed to differences in shape preferred-orientation for grains with differing aspect ratios (Benn and Allard, 1989).

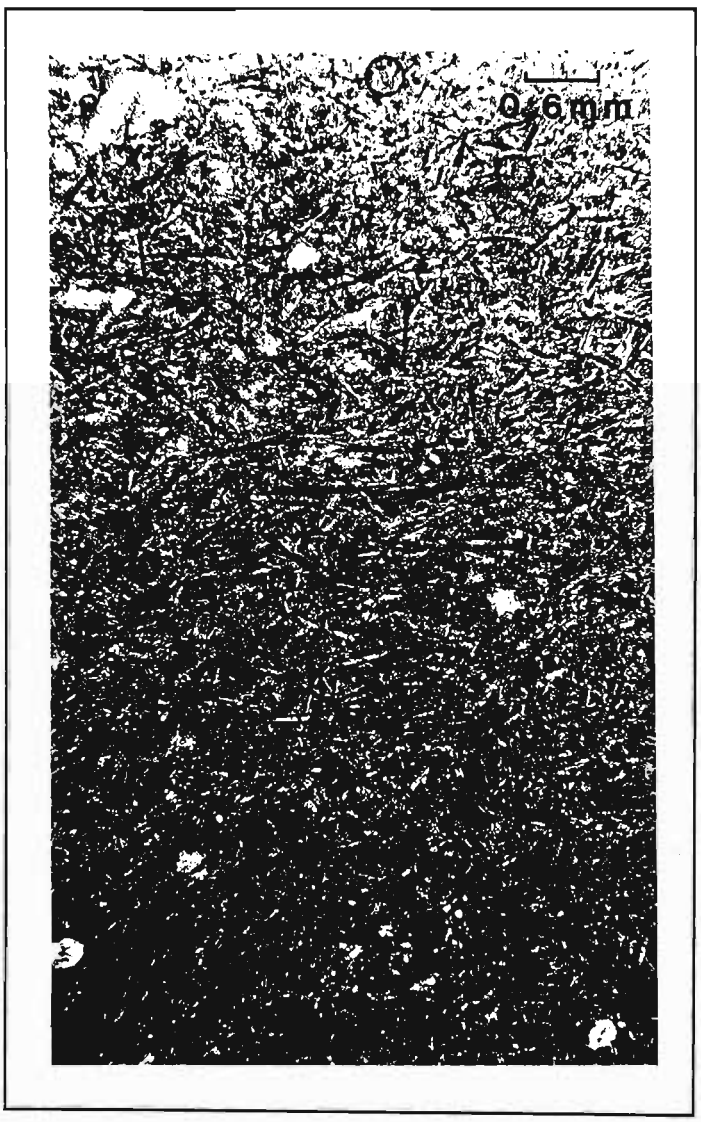

Figure 4.16. *Lower contact chill zone (inner extent) from a fine-grained sill at the 150 m mark along the Mhlatuze River. The dark, acicular grains are quenched pyroxenes that display a prominent preferred orientation along the magma transport direction. The plane of the figure is parallel to the sill margin.*

The orientation of pyrite nodule lineations in scour marks along the lower contact of a dolerite sill in the quarry (Figure 4.14) differs from the alignment of pyroxenes mentioned above by about 60°, suggesting different magma transport directions in these two cases if the criteria described for recognising flow directions by these methods is accurate. This suggests that the respective dolerite sills in these two instances represent different intrusive events.

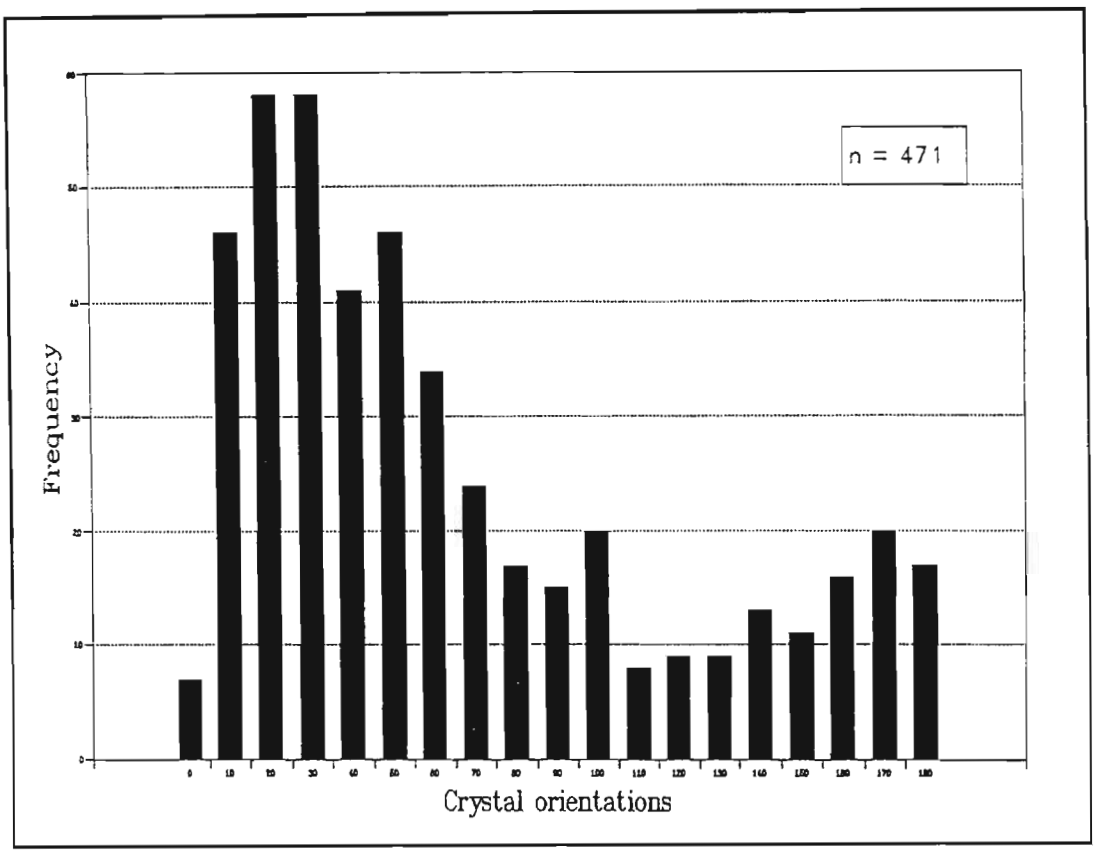

Figure 4.17. *Histogram showing a prominent preferred orientation of 025°030° for acicular pyroxenes within the chill zone of a fine-grained dolerite. This is assumed to represent the flow axis orientation. Smaller peaks may be the result of a tiling effect (see text).*

Benn and Allard (1989) propose a criterion by which absolute flow direction may be determined. In a case where the shear plane of a sheet intrusion is known (that being the wall of the intrusion), the obliquity between the magmatic foliation and the shear plane may be used to infer the magmatic shear sense, and thus the flow direction. In the case of a sill, this determination would have to be applied to a thin section cut in a plane perpendicular to the sill margin but parallel to the flow lineations. The shear sense would then be that which would rotate the magmatic foliation through the smallest angle to be in parallelism with the plane of the sill margin (Figure 4.18). In the case of the fine-grained dolerite, the determined shear sense along the lower contact, but parallel to the flow lineations is dextral towards the north-northeast, thus indicating flow to have been in that direction.

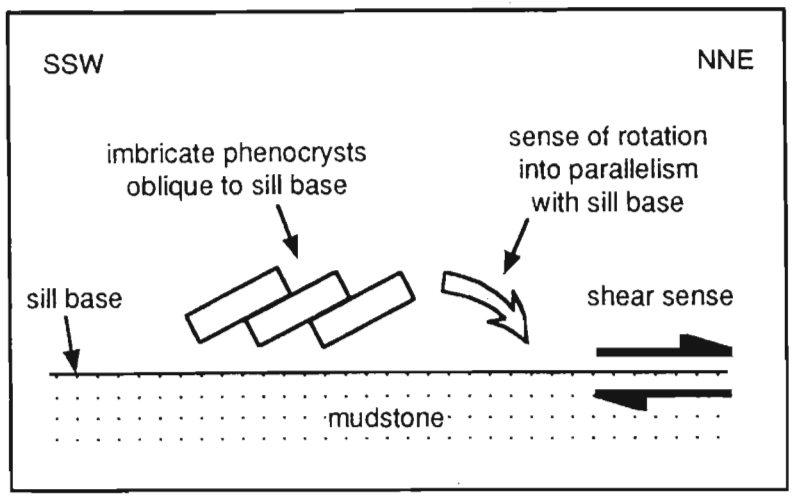

Figure 4.18. *Obliquity of magmatic foliation in a plane perpendicular to the lower margin of a fine-grained sill, and parallel to the flow alignment. For this section, rotation into parallelism with the sill margin indicates a dextral shear sense, and thus a flow direction towards the north-northeast.*

Although alignment of minerals and phenocrysts within the chill zone provides insight into the trend of the magma migration axis, it fails to predict the actual flow direction in cases where the principal shear plane is unknown. In dykes, this is seldom a problem as the general transport direction is upwards. Mineral orientations can thus be used to derive the angle of upward magma propagation. In the case of sills, and dykes that involved a dominantly lateral flow direction, this is not the case. Other criteria must, therefore, be used to derive the actual magma flow direction.

Smith (1987) recognised a number of flow lineation varieties from dykes in the Spanish Peaks, Colorado region, such as: (1) aligned phenocrysts; (2) scour marks; (3) elongated and aligned vesicles and amygdales; (4) cataclastic elongation of phenocrysts; and (5) drag-folding of wall rocks. The first two possibilities have already been covered and eliminated for absolute flow direction determination. It has already been stated that the amygdales associated with the Mhlatuze River sills are predominantly spherical, thus eliminating possibility 3. Drag-folding of the wall rocks did not occur here. The remaining possibility is cataclastic elongation.

In the case of the fine-grained dolerite, cataclasis has damaged some of the amygdales rather than the phenocrysts. This has resulted in cataclastic tails that may give an indication of the true flow direction (Figure 4.19). Using the absolute flow direction determined by the Benn and Allard (1989) method, the cataclastic tails are interpreted to occur on the lee side of the amygdale with respect to the flow direction. Amygdales may also be slightly distorted, with broadly convex surfaces facing the direction from which flow originates.

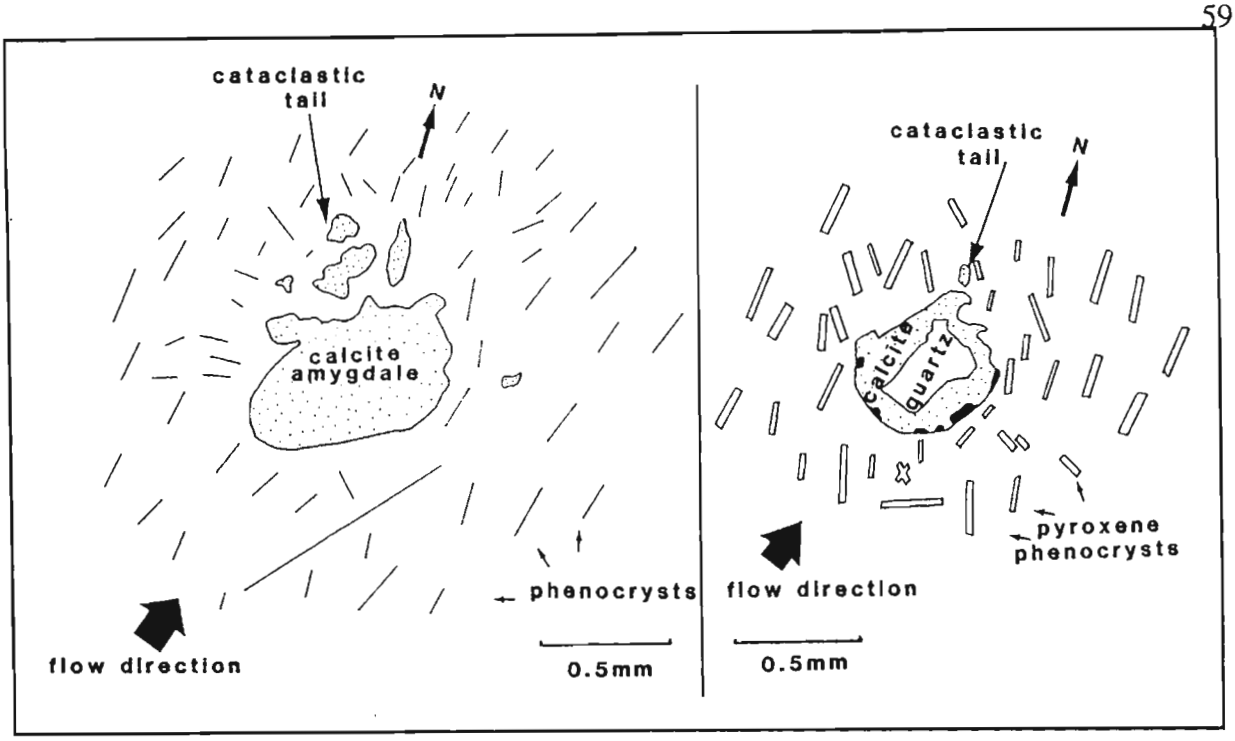

Figure 4.19. *Cataclastic tails are inferred to occur on the lee side of amygdales, with respect to the flow direction. Both examples therefore suggest flow towards the north-northeast. Amygdales may also appear broadly convex on the surface facing the direction from which the flow originates. From the fine-grained dolerite lower chill margin at the 150 m mark along the Mhlatuze River.*

Another possible method that may be used to confirm the criterion used above to determine the flow direction, is the pattern defined by micro-phenocrysts flowing around larger phenocrysts. Flow disturbance around rigid particles rotating in a flow is controlled to some extent by the shape and size of the particle (Ildefonse *et al.*, 1992). Large phenocrysts that have relatively low aspect ratios (i.e. similar lengths and breadths) exhibit less flow alignment than more elongate grains. Consequently, the amount of flow disturbance around the phenocryst is frequently enough to affect the pattern defined by acicular micro-phenocrysts that are generally oriented in the direction of flow. In particular, the lee side, or "flow shadow" region, of the phenocryst displays a high degree of heterogeneity in the orientation of micro-phenocrysts in comparison to the edge facing the flow direction, where the micro-phenocrysts are aligned against the phenocryst edges (Figure 4.20). In general, the "flow shadow" region displays a lower concentration of micro-phenocrysts compared to the phenocryst edge facing into the flow (Figures 4.20 and 4.21). The conclusions drawn from the observation of micro-phenocryst patterns again suggests flow to be towards the north-northeast in the fine-grained dolerite.

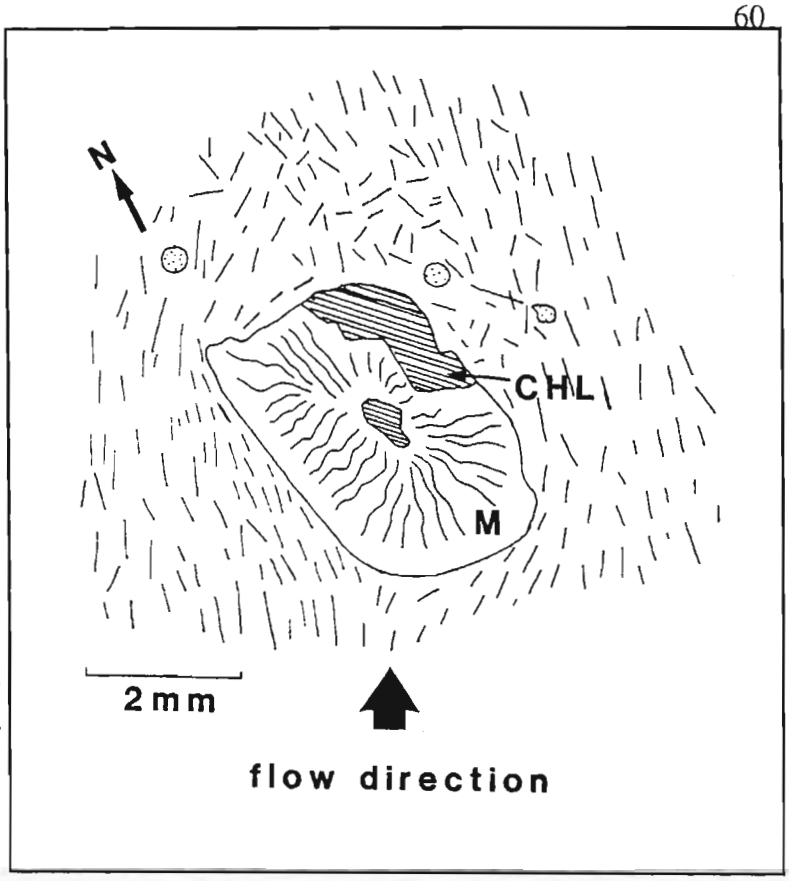

Figure 4.20. *Disruption of the flow alignment of acicular pyroxene microphenocrysts in the flow shadow region of a feldspar phenocryst that has been transformed to myrmekite (M) and chlorite (CHL). Flow appears to be towards the north-northeast. From the fine-grained dolerite at the 150 m mark along the Mhlatuze River.*

Figure 4.21. *(below) Decrease in the concentration of plagioclase microphenocrysts in the flow shadow region of an anorthoclase phenocryst in the lower chill zone of the fine-grained dolerite at the 150 m mark along the Mhlatuze River. Flow sense is from left to right.*

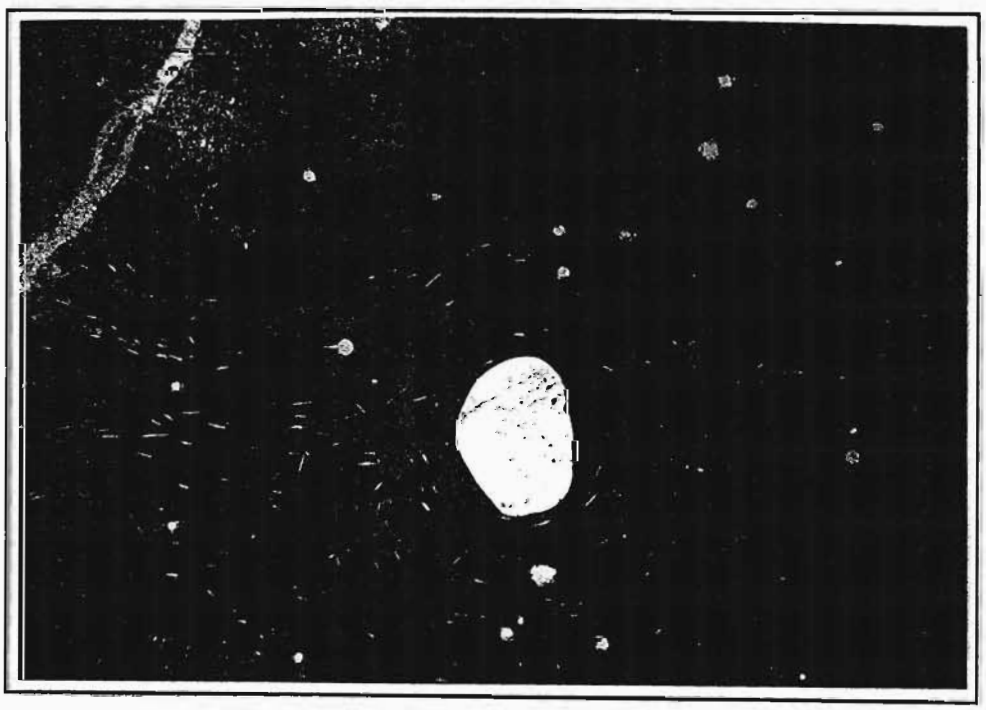

4.7 Mechanics of Intrusion

4.7.1 Fingered En Echelon Sills: Discussion

A generalised analysis of the mechanism of sill emplacement was provided in section 3.5. In summary, dykes intruding the crust form sills at high crustal levels due to the overburden pressure decreasing to a value less than the magmatic driving pressure (Roberts, 1970; Park, 1989). A propagating sheet intrusion has associated with it an inelastic process zone about the intrusion tip, and within which small-scale fracturing of the host rock occurs (Pollard, 1987). The orientation of the fractures, and thus the propagation direction of the sill, is strongly influenced by the regional stress configuration. Sheet intrusions and associated microfractures are oriented in a plane perpendicular to the least compressive stress, σ_{3c}. In the case of sills, σ_{3c} is vertical and so the resultant morphology of the sill is dependent upon the relative values of σ_{1c} and σ_{2c}.

Planar discontinuities such as bedding planes, unconformities, faults, joints and foliations produce host rock anisotropies that can have a marked effect on an advancing planar intrusion, by acting as preferred propagation pathways. The Volksrust Formation sediments are reasonably well bedded, possibly suiting sill intrusion. However, the outcrop pattern of the dolerite sills (Figure 4.3) suggests the initial existence of a number of offset dolerite segments that became joined at adjacent tips, resulting in the upward stepping attitude presently displayed.

Pollard *et al.* (1975) documented a sill at Shonkin Sag, Montana, that intruded as a number of fingers along a common plane, rather than one continuous sheet. Fingered intrusions are visualised as extending away from a common magmatic front along preferential propagation paths (Figure 4.22). Such paths are likely to be dictated by regions of reduced minimum compressive stress, host rock anisotropies, pre-existing fractures or stress gradients due to variable host rock stiffnesses. Although the fingers are initially co-planar, progression into a number of slightly out of parent-crack-plane segments may occur as a result of structural inhomogeneities (Pollard, 1978). The fine-grained dolerite sills along the Mhlatuze River can be interpreted in this manner although there is a consistent unidirectional sinistral offsetting (Figure 4.3) that has resulted in the sills defining an en echelon array.

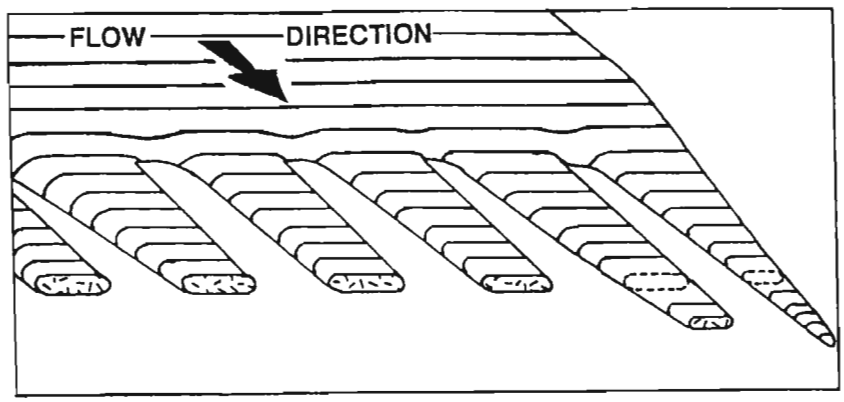

Figure 4.22. *Mechanism of fingered sill intrusion along preferential propagation pathways ahead of the main propagation front (after Pollard et al., 1975).*

Documentation of intrusive en echelon arrays in the literature has thus far principally been in relation to dyke-like bodies rather than sills. They have been suggested to be inherently associated with the presence of a shearing action (Lajtai, 1969; Hancock, 1972; Ramsay, 1980; Rickard and Rixon, 1983), whilst Beach (1975) suggested that tensile en echelon arrays may also occur in the absence of shear zone activity. Pollard *et al.* (1982) ascribe the formation of an en echelon pattern to a parent fracture splitting into a number of helicoidal segments within a changing stress field that effectively resolves a mixed-mode I-III stress intensity along the crack edge (Figure 3.10). Multiple crack production incurs a lesser amount of energy expenditure than would occur if the entire parent crack were to be rotated. Crack torsion thus induces a re-orientation in a plane perpendicular to the spatially or temporally variable least compressive stress direction (Delaney and Pollard, 1981). In the case of sills, this effect would presumably rotate individual sill segments within the changing stress field resulting in an en echelon array that is discordant with the sedimentary bedding.

The Mhlatuze River sills are concordant with the sedimentary bedding. It is, therefore, unlikely that the present arrangement of sinistrally offset, bedding-concordant sills arose in the field of a rotating stress configuration. *The consistent sinistral offset (as in Fig. 4.3) and lack of any apparent parent-crack plane negates the probability of the sills having formed as simple deviations from a co-planar attitude induced by structural inhomogeneities or host rock anisotropies.*

It needs, therefore, be asked whether or not intruding sills have the ability to produce true en echelon arrays as defined for dykes, propagating as bedding-concordant fingers (in the case of sills) ahead of a common parent magmatic front and then rotating out of the plane of the parent crack. Consistently offset sills that display an en echelon morphology in cross section, but where each array segment is bedding-concordant, are thus not necessarily true en echelon features *as defined above*. This author has not encountered any definite documented cases of en echelon sill segments that have been emplaced discordantly with sedimentary bedding planes, as would be expected in

the instance of a rotating regional stress field along the propagation length of an initially bedding-concordant intruding sill. Harley and Charlesworth (1991) document an "imbricate-like" diabase sill array from the eastern Transvaal. The array is associated with deformed host rocks and a degree of shearing between adjacent sill segments induced by a changing stress field that has resulted in the segments producing a highly overlapping en echelon appearance and an apparent discordance with surrounding strata. These authors, however, did not consider the possibility of the array being a syn-fracture-growth development affected by stress fluctuations associated with syn-Bushveld Complex tectonics, but rather a post-sill-emplacement deformation feature.

Where en echelon sill segments are bedding-concordant, it must be assumed that either bedding planes or a pre-existing set of en echelon fractures, more conducive to magma injection than bedding planes, preceded the formation of the en echelon sill array.

Olson and Pollard (1991) propose that en echelon fracture initiation occurs as a result it being the most effective mechanism for crack propagation because the associated mechanical fracture interaction promotes growth. The propagation of fingered sills along such fractures implies that the fractures in the en echelon array dilate simultaneously, with linkage of adjacent tips being a later effect due to tip-stress interaction and resultant tip curvature. This is in accordance with the proposal by Pollard *et al.* (1975) that magma propagation occurs along the length of an offset surface.

From the above discussion, it is proposed that two distinct varieties of en echelon arrays occur (Figure 4.23). The first variety involves intrusion into a region undergoing a resolved simple shear stress, due to a rotation of the regional stress configuration, resulting in the breakdown of the periphery of a sheet intrusion into a number of segments or fingers that rotate out of the plane of the parent fracture, tracing out a helicoidal surface. The ultimate effect is to re-establish an equilibrium situation where the individual segments are once again oriented perpendicular to the least compressive stress, as proposed by Delaney and Pollard (1981). This mechanism is applicable to en echelon dyke segments associated with a shear zone. In the case of sills, the resultant en echelon array should theoretically occur emplaced discordantly with horizontal sedimentary bedding, assuming the parent fracture to be bedding-concordant.

The second variety involves the formation of an en echelon array, the individual segments of which *do not undergo any rotation out of the plane of the parent fracture*. The periphery of the sheet intrusion either breaks down into a number of segments or fingers that propagate ahead of the parent fracture in an en echelon manner, or segments intrude a pre-existing set of en echelon fractures that are susceptible to intrusion and dilation. Alternatively, the individual fingers of the array may be derived from individual sources, rather than from the break down of a single parent fracture. These too would intrude in an en echelon manner in the presence of a pre-existing en echelon fracture array. The occurrence of this pre-existing array is in accordance with the proposed method of efficient fracture growth via an en echelon geometry (Olson and Pollard, 1991). This mechanism is applicable to both dykes and sills that have intruded en echelon arrays of vertical and horizontal fractures respectively.

It must be noted that discordance and concordance with sedimentary bedding exhibited by sills that formed via the two proposed mechanisms respectively, is only applicable where the parent sill is bedding-concordant. En echelon fingers propagating from the periphery of such a source would thus be bedding-discordant via the first mechanism, and bedding-concordant via the second mechanism (Figure 4.23). In the case of the Mhlatuze River en echelon sill array, it can be concluded that mechanism *B* produced the existing sill geometry. Furthermore, it seems likely that it is the most common mechanism of en echelon *sill* formation. Offset fingered intrusions may develop without the presence of a pre-existing set of fractures too, however they are likely to be characterised by the occurrence of host-rock deformation at the leading edge of the fingers, as well as in the cusp region separating adjacent or offset sills (Pollard *et al.*, 1975).

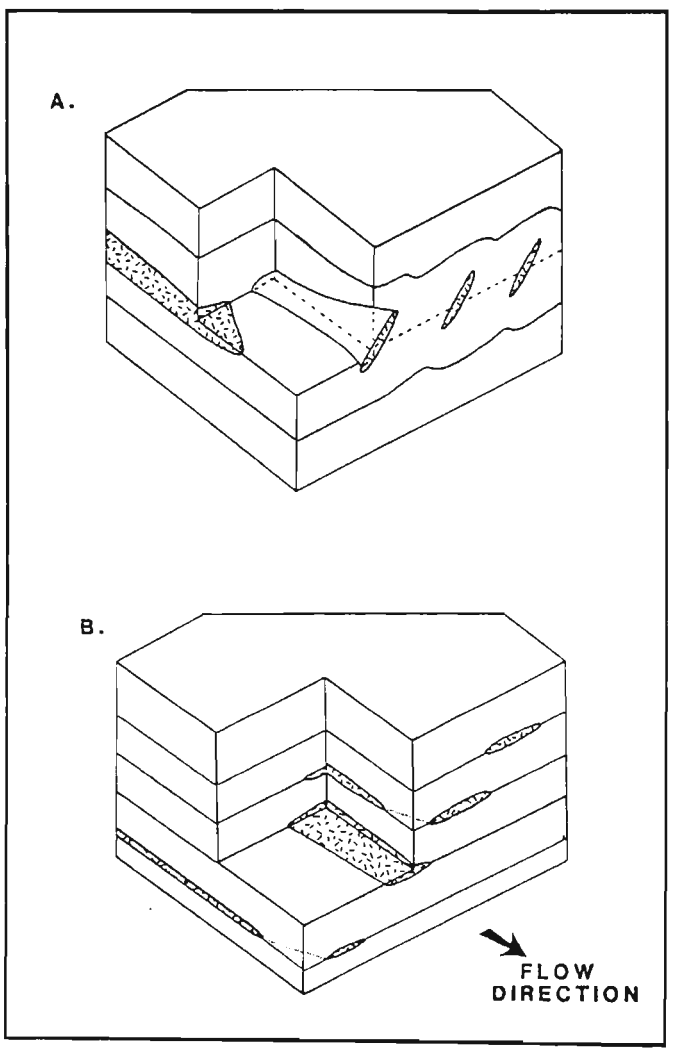

Figure 4.23. *Two proposed mechanisms for the formation of an en echelon sill array. (A). The periphery of the bedding-concordant parent sill breaks down into a number of helicoidal segments that rotate in a changing stress field to produce an en echelon array of bedding-discordant segments. (B). A pre-existing en echelon array of fractures is intruded and dilated to produce an en echelon array of bedding-concordant sills.*

4.7.2 Sill Linkage

Nicholson and Pollard (1985) recognise two end-member situations for dilating en echelon fractures that have linked together (refer to section 3.7.3). They are essentially geometrically defined, with one end-member exhibiting straight propagation paths and the other curved paths. Where propagation paths of adjacent fractures remain relatively straight, cross-fractures develop through intervening bridges and linkage results in increased dilation and bent bridge formation. Thin offshoots on one or both outside edges of the offset intrusions are called horns. Where pronounced crack curvature occurs, crack tips simply propagate into the inside edge of the adjacent fracture resulting in linkage, increased dilation, and rotated bridges that are relatively unstrained.

The cross-section along the Mhlatuze river (Figure 4.3) suggests that for conditions where adjacent sill segments had high vertical and/or lateral separations, linkage occurred via an inward curvature between adjacent offset sills that

linked tip-to-tip. In places where fractures were closely spaced or overlapping, however, increased sill interaction has resulted in the production of abrupt offsets, horns and bent bridges where the propagation paths were straight, and tip-to-plane linkage with rotated bridge development where the propagation paths were curved. Such features occur in close proximity to the 135 m, 615 m, 670 m and 1120 m positions along the river. The development of the features at the 670 m mark may be interpreted in terms of bridge fracture and failure (Figure 4.24). The existence of closely associated bent and rotated bridges places the Mhlatuze River array of sills between the two end-member states of Nicholson and Pollard (1985), the occurrence of which thus appears to be attributable to the extent of initial fracture spacing, measured both perpendicular and parallel to the long axis of the sills as seen in two dimensions. Rotated bridges of mudstone host are frequently notably strained and deformed, contrary to the inference of Nicholson and Pollard (1985) that curved propagation path end-member rotated bridges are not significantly strained.

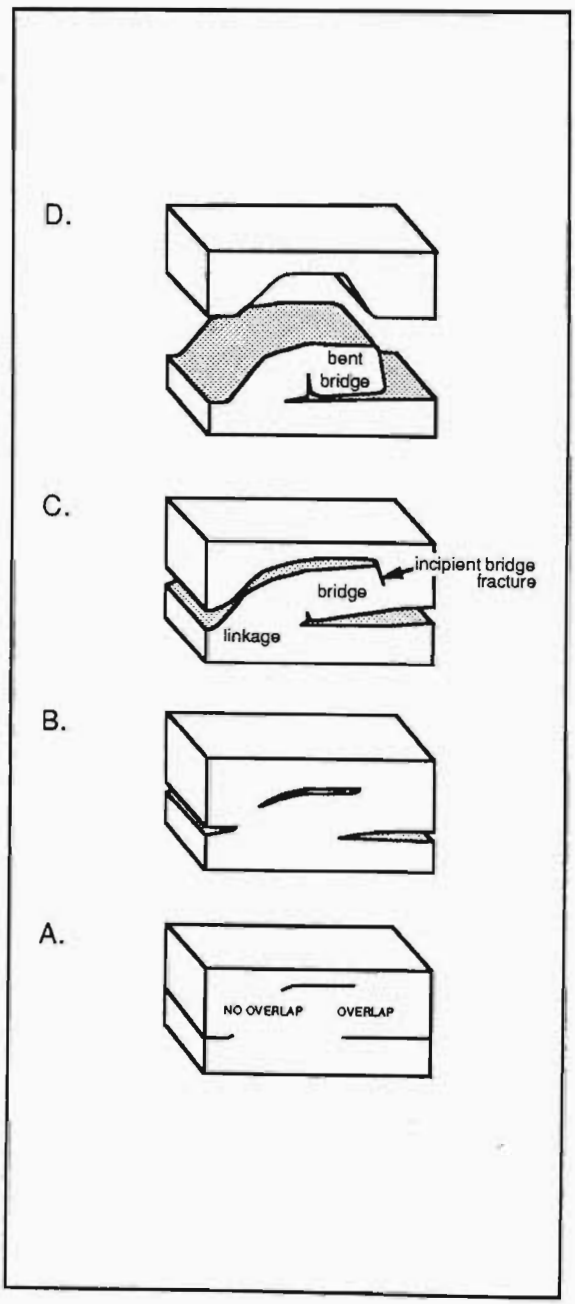

Figure 4.24. *Dilation history of the fine-grained dolerite sill near the 670 m mark (Figure. 4.3). (A) Initial crack geometry. (B) Initial dilation. (C) Tip-to-tip linkage of non-overlapping segments. (D) Present morphology after bridge fracture and increased dilation.*

Between the 1115 m and 1125 m marks (Figure 4.3), a rotated mudstone bridge was split along fissile-sediment partings by intruding magma on three occasions, resulting in three isolated xenoliths of mudstone in the dolerite adjacent to the remnant of the rotated bridge. This is probably a localised *in situ* effect along the three-dimensional length of the rotated bridge, in order to have produced the exhibited bridge-affiliated geometry of the xenoliths.

Linkage induced by crack curvature is explained in terms of the local stress conditions at the crack tips (section 3.6.2). Where offset cracks occur, the stress fields associated with adjacent tips interact. The dilation of one of the cracks resolves a shear stress on the surface of the other (Olson and Pollard, 1989). This results in the rotation of the σ^r_1 (maximum tensile or least compressive) trajectories which, in turn, induces a curvature in the crack paths, thus minimizing the shear stress and maximizing the tensile stress across the propagation paths. Crack convergence may be preceded by an initial amount of divergence as a result of the initial resolved shear sense on the crack surfaces. Divergence of interacting

cracks causes a reversal in the resolved stress sense, rotation of the maximum tension about the tip, and curvature in towards the adjacent crack. Linkage tends to be tip-to-plane rather than tip-to-tip (Pollard *et al.*, 1982), although this is not consistently true for the Mhlatuze River sills because of the extent of both lateral and vertical offset of adjacent en echelon sill segments in places, as previously outlined.

Olson and Pollard (1989) interpret the state of stress between offset adjacent vertical fractures in terms of the *remote regional compression* $\Delta\sigma = S_H - S_h$, where S_H and S_h are the maximum and least compressive stresses respectively, and measured in the plane perpendicular to that containing the crack (section 3.6.3). They conclude that extreme curvature occurs under tensile conditions ($\Delta\sigma < 0$). The amount of curvature then decreases steadily through isotropic conditions ($\Delta\sigma = 0$) into situations where S_H is dominant ($\Delta\sigma > 0$), eventually attaining an asymptotic propagation trend. The exact fracture behavior will also be a function of the driving pressure and the host rock fracture strength. The applicability of Olson and Pollard's (1989) analysis to sills remains untested, however, if the same principles apply, the amount of curvature exhibited by the Mhlatuze River sills would require stress conditions approaching isotropy. These are the proposed conditions under which sill emplacement occurs (Price and Cosgrove, 1990, p76).

4.8 Discussion and Intrusion Reconstruction

In order for the previously discussed effects of adjacent, en echelon fractures and intrusions to be applicable to the sills under investigation, it must be shown that separate en echelon fingers dilated simultaneously, interacted and consequently joined. This is necessary as sills have been documented stepping upwards in the direction of propagation. Such an effect may be induced by parameters such as crustal flexure, differential compaction or variations in the mechanical properties of host rocks (Gretener, 1969), or due to topographical variation (Bradley, 1965).

In the case of the Mhlatuze River sills, it has already been concluded that propagation and flow occurred approximately towards the north-northeast. This gives credence to the proposal that propagation occurred orthogonally to the plane containing the en echelon pattern, with simultaneous dilation of the sills, followed by later linkage to produce the present morphology. Propagation ***along*** the offset surfaces (Pollard *et al.*, 1975), which would be expected for the case of linked en echelon fingers (see Figure 3.15), was confirmed via the similarity between the flow direction and strikes of offset edges. Furthermore, magma emplacement in an en echelon pattern accounts for the plethora of linkage-related features that occur.

Magma emplacement occurred as at least two intrusive events, with the initial phase involving a greater volume of magma and producing sills with a considerably greater thickness than the subsequent fine-grained dolerite sills with enclosed xenolithic dolerite. The first phase of intrusion cannot accurately be described as en echelon on the basis of the Mhlatuze River outcrop scale. The coarse-grained sills are too massive for any large-scale geometrical morphology to be recognised. The fine-grained phase, however, can be confidently classified as being geometrically

en echelon. The fractures dilated by the fine-grained phase may have been activated within the process zone of the initial phase. This would explain why these fractures were not initially dilated by the coarse-grained phase. As previously mentioned, Figure 4.3 illustrates a fine-grained sill contained within a coarse-grained sill at the northern end of the traverse. This mechanism of multiple intrusion has been described for dyke swarms (eg. Saggerson et al., 1983), but may be an indication of horizontal crustal tension and is thus not directly comparable to multiple sill intrusion. The existence of a zone of incomplete crystallisation within a sill may act as a plane of weakness for a subsequent intrusive phase, thus producing a composite sill. However, near the 130 m mark (Figure 4.3), there is a zone of offsetting characterised by both a bent and a rotated bridge, suggesting brittle behavior in the earlier sill during intrusion of the fine-grained phase. Furthermore, this region of bridging contains a deformed granitic vein which is post-coarse-grained but pre-fine-grained dolerite in age (Figure 4.4), indicating a significant time break between these two intrusive phases. Nevertheless, there was some factor that induced a preferential intrusion into the earlier sill rather than into the relatively weaker fractured mudstone host. Horizontal cooling joints occur in the coarse-grained sills and may, therefore, have acted as planes of weakness during the second phase of intrusion.

It has already been proposed how the field relationships between the xenolithic and fine-grained dolerite types suggests the former to be an early association of the latter. Although the xenolithic dolerite is totally enclosed within the fine-grained dolerite, suggesting intrusion of the former into the latter (as with the composite sills at the northern end of the section), field observation indicates that the fine-grained dolerite has chilled against the enclosed xenolithic dolerite blocks. The xenolithic dolerite thus pre-dates the fine-grained dolerite. In no instances are any field relationships between the xenolithic and coarse-grained dolerite exhibited, however, the 350 m mark along the section (Figure 4.3) reveals an arrangement of xenolithic dolerite enclosed within the fine-grained dolerite, which itself has intruded into the coarse-grained dolerite sill. It is therefore assumed that the xenolithic dolerite post-dates the coarse-grained dolerite, having intruded as an early association of the fine-grained phase. This is credible under the proposed model of emplacement mechanics involving the propagation of a number of fingers of dolerite ahead of the main magma sheet. It is proposed that the tips of the advancing fingers of the fine-grained dolerite phase became concentrated in a xenolithic component, derived via stoping of intruded host rocks or alternatively due to the feeder dyke to the sill having passed through a major active fault zone at depth (McCarthy, 1979). The granite gneiss xenoliths are most common and are derived from the local basement, but xenoliths of sedimentary origin also occur. Graphite xenoliths probably formed from incorporated fragments of coal derived from the Vryheid Formation coal seams. Frankel (1969) stressed that a basaltic melt would have to contribute such a large amount of its latent heat of crystallisation during the assimilation of a large amount of crustal material, that very little of its original mass would remain as liquid. The amount of SiO_2 that a basaltic melt can digest is strongly influenced by the temperature of the melt and the surface area of the incorporated granitic block (Watson, 1982). There is evidence of partial melting and a degree of liquid immiscibility, and the low diffusivities of SiO_2 and Al_2O_3 further promoted preservation of the partially molten xenoliths as pods of unassimilated material in the magma. The general flattened, elongate appearance of the xenoliths may have resulted from re-crystallisation under conditions of compression plus extension. This would occur in the zone between the lines of no finite longitudinal strain and no infinitesimal longitudinal strain on a simple shear strain ellipse (zone 2 of Ramsay, 1967), and is assumed to be associated with

simple shear induced by increasingly viscous magma flow near the propagating sill tip.

A disadvantage of fingered intrusions is the rapidity with which heat may be lost to the country rock. In the case of the Mhlatuze River sills, the proposed scenario is that the xenolith-rich tips of the dolerite fingers lost a considerable amount of latent heat in the partial assimilation of xenolithic material and by cooling against the country rock fairly early during intrusion. This cooling is demonstrated by the marked decrease in grain size of the xenolithic dolerite blocks from centre to margin. This effect became a hinderance to propagation by increasing the magma viscosity. The tips of the fingers thus effectively began acting as plugs (Figure 4.25), with magma pressure causing a build-up of uncontaminated magma behind the xenolithic plugs, perhaps also inducing the deformation bands within. This resulted in widening and dilation of cracks or bedding planes in the process zones of the fingers, and the xenolithic plugs were subsequently overtaken by the magma, which chilled against the xenolithic portion. The xenolithic blocks thus became isolated within the magmatic flow which cooled around it to produce the fine-grained dolerite. Some xenoliths were plucked away from the enclosed blocks resulting in the presence of isolated xenoliths distributed randomly within the fine-grained dolerite. This may be the equivalent of the "Effingham-type" dolerite documented by McCarthy (1960; 1979), Frankel (1969) and Absolom (1970).

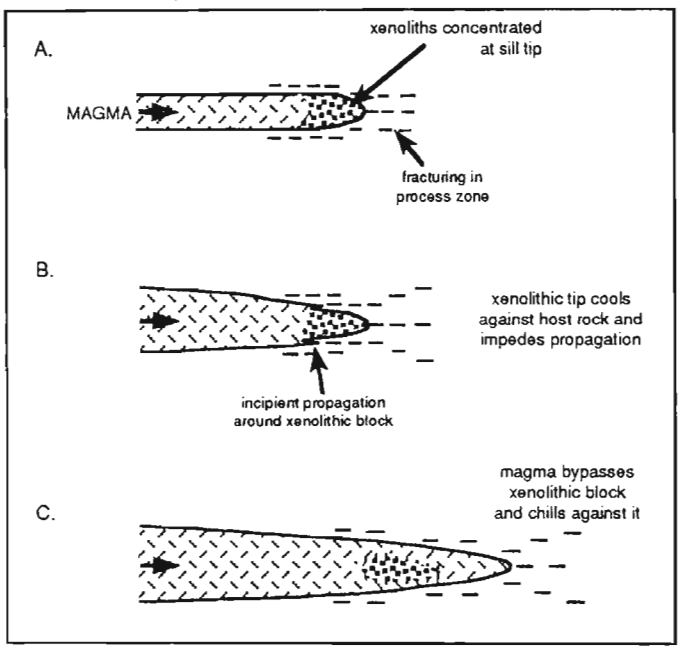

Figure 4.25. *Origin of the xenolithic dolerite blocks within the fine-grained dolerite. The xenolith-concentrated propagation front of the fingered fine-grained dolerite intrusive phase (A) cooled against the host rock, impeding magma propagation (B). Magma driving pressure build-up behind the obstruction led to bypassing and incorporation of the xenolithic block (C).*

The base of the 15 m thick dolerite sill in the RBQ quarry (Figure 4.11) contains xenolithic dolerite encapsulated within fine-grained dolerite, but exhibiting a marginal wedge of deformed mudstone between the xenolithic dolerite and the enclosing sill. This provides evidence of the xenolithic dolerite having initially contacted against sedimentary host rock before being engulfed by an advancing magmatic front. In this case, the sediment against the contact was also preserved when the main magma pulse bypassed the xenolithic tip.

A close examination of Figure 4.3 indicates an apparent change in the morphology of the sills in cross-section near the 450 m mark along the traverse. This is a result of a bend in the course of the Mhlatuze River at this point (Figure 4.1). From the 0 m to the 450 m mark, the river flows south-southwest, but then curves around to a southeasterly orientation beyond the 450 m mark until the 1250 m mark, from which point the river flows approximately eastwards. Used in conjunction with the determination of the propagation and magma flow direction of the sills, it can be seen that the river course is only oriented at a high angle to the sill propagation direction beyond the 450 m mark, which is thus the only extent of the traverse that exemplifies the en echelon nature of the sills. Before the 450 m mark the river cuts through the sills at a shallow angle to the propagation direction, and this causes the sills to appear laterally wider than beyond the 450 m mark (Figure 4.26). The Mhlatuze River section thus provides an example of how the true morphology of a sheet intrusion may be misconstrued if the section orientation is not properly visualised in conjunction with the three-dimensional morphology of the intrusion.

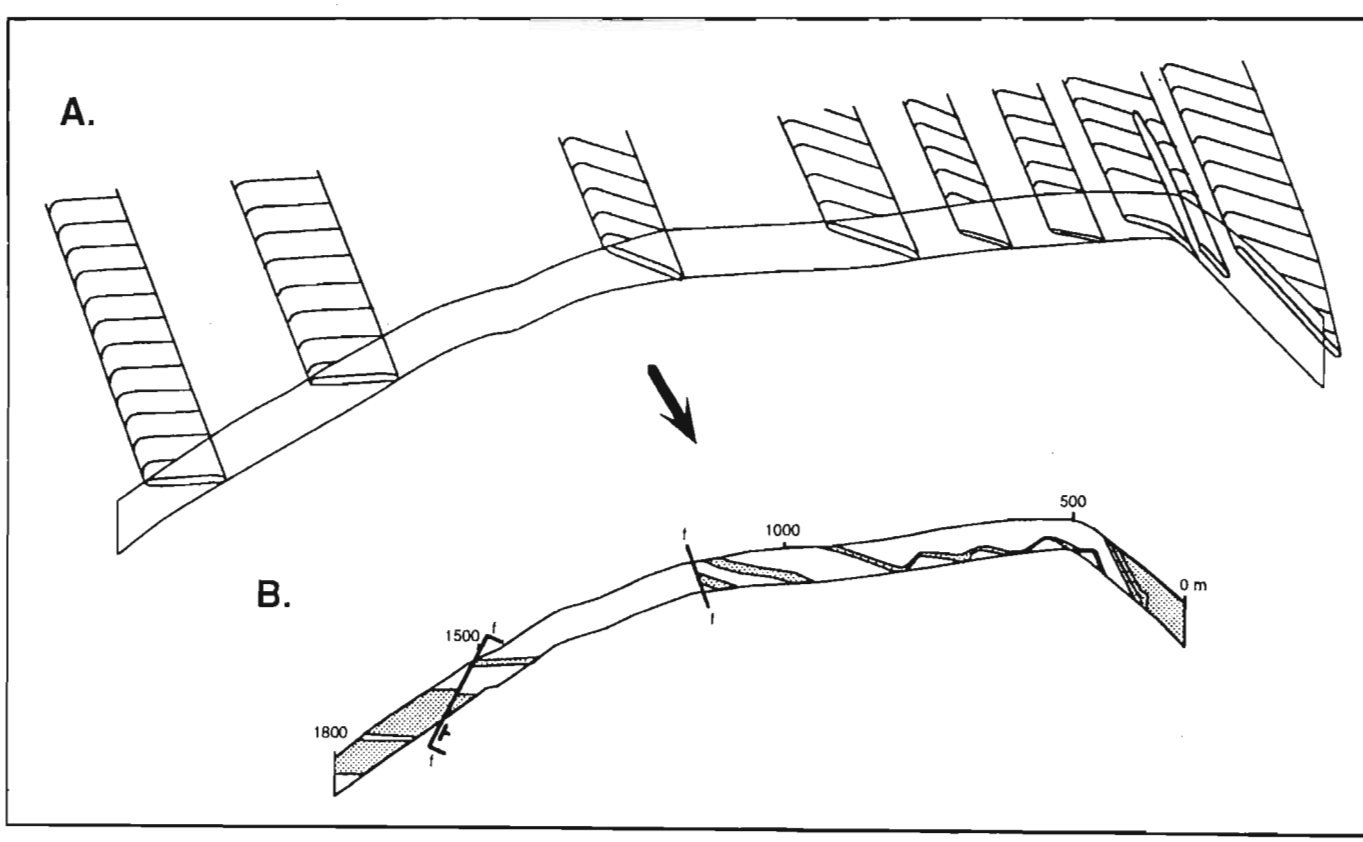

Figure 4.26. *Simplified three-dimensional representation of the fine-grained sills (shown prior to linkage) along the Mhlatuze River, with respect to the trend of the river bank. The 0-450 m range of the traverse intersects the dolerite sills at a low angle to the propagation and magma flow direction, resulting in an increase in the apparent width of the sill when compared to the en echelon segments beyond the 450 m mark. All other geological features have been omitted for better clarity.*

4.9 Application of Fracture Mechanics Equations

The interpretation of the intrusion mechanics of the Mhlatuze River dolerite sills as presented above can now be complimented and compared with some geometrical and mathematical applications using documented formulae and definitions as presented in Chapters 2 and 3.

The en echelon morphology of the sills is defined by a number of sill fingers or segments that linked together in the later stages of dilation. The geometrical parameters defining en echelon intrusions are given by Pollard *et al.* (1982) and Nicholson & Pollard (1985) as width $2b$, dilation 2∂, separation $2s$, overlap $2o$, centre spacing parallel to the array axis $2c$, centre spacing parallel to the cracks $2k$, twist angle ω, and array width $2B$ (see Figure 3.14). The Mhlatuze River fine-grained dolerite sills do not display consistent values of these parameters, as the values vary from sill to sill. Ranges of respective values for sills outcropping from 320 m to 900 m along the river section (Figure 4.3) are calculated to be:

2b: 120m - 170m
2∂: 2m - 5m
2s: 18m - 36m
2c: 114m - 190m
2k: 110m - 187m
ω : 11^{o}

For the above estimates, the dolerite from 580-750 m along the section (Figure 4.3) has been approximated as being equivalent to one sill segment in the array, despite a number of relatively minor offsets along its width. Values of the geometrical parameters for the northernmost fine-grained dolerite along the section have not been included because the three-dimensional attitude of the river bank with respect to the sill in this region of the section, as discussed previously, would result in false representations of the true values. The value of 2B can not be evaluated from the river outcrop, as the full extent of the en echelon array is unknown. There is no overlap of sill segments, therefore 2o = 0. The value of 11^{o} for ω is almost identical to the dip of the sedimentary bedding. This similarity, existing in conjunction with the shallow gradient of the river explains why the en echelon geometry of the sills is demonstrated with such clarity along the river bank. If either _ or the river gradient had been considerably larger, the exposed en echelon geometry as observed along the river bank would have been lost.

The range in values for most of the geometrical parameters of the sills implies that the Mhlatuze River sill array does not involve an ideal situation of dilated en echelon fractures. Nicholson and Pollard (1985) proposed the use of these parameters for intrusions with straight, rather than curved propagation paths. It has already been suggested that the sills may represent a situation intermediate between the two end-member types of Nicholson and Pollard (1985). Furthermore, much of the theoretical analysis by authors such as Pollard are derived within homogeneous brittle-elastic media. The intruded sediments along the Mhlatuze River are not homogeneous; anisotropies are provided by bedding planes and possibly differential stress gradients produced by previous, localised intrusions. These effects have detracted from the theoretical behavior of the sills, however, the overall geometry compares well with

theoretical predictions of effects such as linkage, suggesting the sill-tip stress distributions to have obeyed theoretical predictions despite the presence of anisotropies. It is, therefore, suggested that theoretical observations and mathematical applications, such as described in Chapters 2 and 3, may have significant application to geological situations such as the Mhlatuze River sill array, where deviations from ideal conditions are encountered. Mathematical applications for the Mhlatuze River sill array will, therefore, be attempted and evaluated for applicability.

Values for the geometrical parameters of the fine-grained dolerite array may be utilised to estimate intrusion related characteristics such as the magma driving pressure and strain imparted to the intruded host rocks. Pollard (1987) provides a relation by which magma driving pressure (P - S) may be estimated (refer to section 2.2.4) using the geometrical parameter thickness-to-length ratio t/l, and the physical constants Poisson's ratio υ and elastic shear modulus μ:

$$\frac{t}{l} \approx \frac{(P-S)}{\mu/(1-\upsilon)} \tag{4.1}$$

The sill thicknesses, t, (dilation) were listed previously as 2∂, and the lengths, l, (as defined for 4.1 by Pollard, 1987) are the equivalent of the parameter width, 2b. Thickness-to-length ratios of the sills vary from 0.0173 to 0.0287. Using a reasonable estimate for shales of $\upsilon \approx 0.15$ for Poisson's ratio (Carmichael, 1989), and a shear modulus of 1.4×10^{10} (Turcotte and Schubert, 1982), the driving pressure values have an estimated range of 2.9 - 4.7×10^{8} Pa.

Gudmundsson (1990) gives an equation for the evaluation of driving pressures for dykes:

$$(P-S) = \frac{W}{L} \cdot \frac{E}{2\left(1-\upsilon^2\right)} \tag{4.2}$$

In this case, the width-to-length ratio W/L is the equivalent of the thickness-to-length ratio t/l in (4.1), and E is Young's modulus. Applying (4.2) to the Mhlatuze river sills, using $E = 0.2 \times 10^{11}$ Pa (Turcotte and Schubert, 1982), the estimated driving pressure range is 2.0 - 3.4×10^{8} Pa. These values are slightly lower than those obtained via (4.1), but still in the same magnitude range.

An important point to note is that the effect of pre-existing fractures or bedding planes prior to magma intrusion probably result in equations 4.1 and 4.2 producing slightly over-estimated values for P.

When such equations are used, care must be taken insofar as the parameter nomenclature is concerned. Pollard *et al.* (1982) and Nicholson and Pollard (1985) define the long axis of the intrusion in cross section as width $2b$, and the short axis as dilation 2∂. Pollard (1987) labels the long axis as length $2a$ and the short axis as thickness $2b$.

Gudmundsson (1990) labels the short axis width *W* and the long axis length *L*. The adoption of a standard nomenclature would obviate confusion arising from such inconsistencies. It is proposed, therefore, that the parameters be named using the terms *width* for the long axis (in cross section), and *thickness* or *dilation* for the short axis. The term *length* should be reserved for the longest axis in the third dimension, with respect to the plane of the cross section.

The calculated value for the magma driving pressure (P - S) may be used to estimate the amount of strain imparted to the host rock during intrusion (Pollard, 1987) using the equation:

$$U_E = \pi a^2 (P - S)^2 \left[\frac{1 - \upsilon}{2\mu} \right] \tag{4.3}$$

(section 2.4) where 2a is the long axis width of the intrusion. From (4.3), the estimated strain energy imposed to the host rock mudstones is 3.6 X 10^{10} N m^{-1} (using 2a = 130 m and (P-S) = 3.0 X 10^8 Pa). Again, this is probably an overestimate. As the fractures were probably pre-existing, the strain imparted upon the rock resulted in widening of the fractures rather than creation of them. This deviation from theoretical experiments in isotropic elastic media may be the cause of the range in sill widths and thicknesses.

The overburden stress σ_z imposed on the Volksrust Formation sediments at the time of dolerite intrusion can be estimated using the formula $\sigma_z = \rho g z$, where ρ is the density of the overlying stratigraphy, z is the depth in the crust, and g is the acceleration due to gravity. The local stratigraphy is tabulated as Table 4.2, with sedimentary unit thicknesses as documented by Wolmarans and du Preez (1986) and Linström (1987).

GROUP	FORMATION	AGE	THICKNESS
Lebombo	Letaba basalt	Jurassic	3 600 m
	Clarens	Triassic	45 m
	Nyoka	Triassic	250-285 m
	Ntabene	Triassic	200-260 m
Beaufort	Emakwezini	U. Permian	380 m
Ecca	Volksrust	Permian	200 m

Table 4.2. *Estimated thicknesses of the presumed local stratigraphic succession at the time of dolerite emplacement within the Volksrust Formation.*

Using the stratigraphic thickness data in Table 2, two variations of the overburden stress may be estimated: either excluding or including the great thickness of extruded basalts. Using approximate densities of 2400 kg m^{-3} for the sedimentary package and 2740 kg m^{-3} for the basalts (Turcotte and Schubert, 1982; Carmichael, 1989), the overburden stress is approximately 2.53 X 10^7 Pa if the basalts are excluded, and 1.2 X 10^8 Pa if the basalts are included. Despite which of these values is more accurate, a notably higher value was obtained for the magma driving pressure. This could be taken to suggest that extrusion had begun at the time of sill emplacement in this vicinity,

as the overburden stress may have been too small to prevent magma from reaching the surface. Alternatively, the existence of a fracture array that preceded magma injection may be an indication that the calculated driving pressure was overestimated slightly, as suggested previously. Nevertheless, an increase in the driving pressure to a value greater than the overburden stress certainly prompted the development of sills in this region of the stratigraphy, as is adequately demonstrated by the theoretical equations for fracture in homogeneous brittle-elastic media.

4.10 Dolerite Geochemistry

Mineral geochemical data were obtained via electron microprobe analysis, and is listed in Appendix 3. The whole-rock volatile-free analyses (Table 4.3) represent various positions through the dolerite sills. Samples were analysed by XRF at the Department of Geochemistry at the University of Cape Town, using the method and detection limits described by Duncan *et al.* (1984). In this section, the geochemical data are displayed principally in the form of graphical plots, with interpretations provided in the text. The main objective of the geochemical evaluation is to develop another method of distinguishing between intrusive phases of different ages as this can assist in the interpretation of the intrusion mechanics.

4.10.1 Mineral Geochemistry

(A) PLAGIOCLASE:

The plagioclase data for the dolerites are represented on anorthite-albite-orthoclase ternary diagrams (Figure 4.27), showing variations from cores to rims. The margins of the thick, coarse-grained sills are medium-grained compared to the sill centres. As crystallisation in a sill initiates at the sill margins, and progresses inwards, the medium-grained marginal dolerite crystallised before the central coarse-grained dolerite. Plagioclase compositions are similar throughout the coarse-grained dolerite, and so mineral variations from sill margins to centres are not apparent. This is demonstrated by the orthoclase versus anorthite graphs for the plagioclases (Figure 4.28) which show different trends in the fine-grained and coarse-grained dolerites. The similarity in the plagioclase compositions throughout the coarse-grained dolerite sill may be the result of renewed magma influxes into the cooling sills, negating the expected crystallisation trend of decreasing An content of the plagioclases from sill margins to centres. A trend of decreasing An and increasing Or content of plagioclases from cores to rims throughout the coarse-grained dolerite defines an upward movement from right to left across the graph. This reflects the core-to-rim compositional zoning that occurs in individual plagioclase grains. Small grains in the groundmass tend to plot higher along this trend towards the left, as a result of late crystallisation.

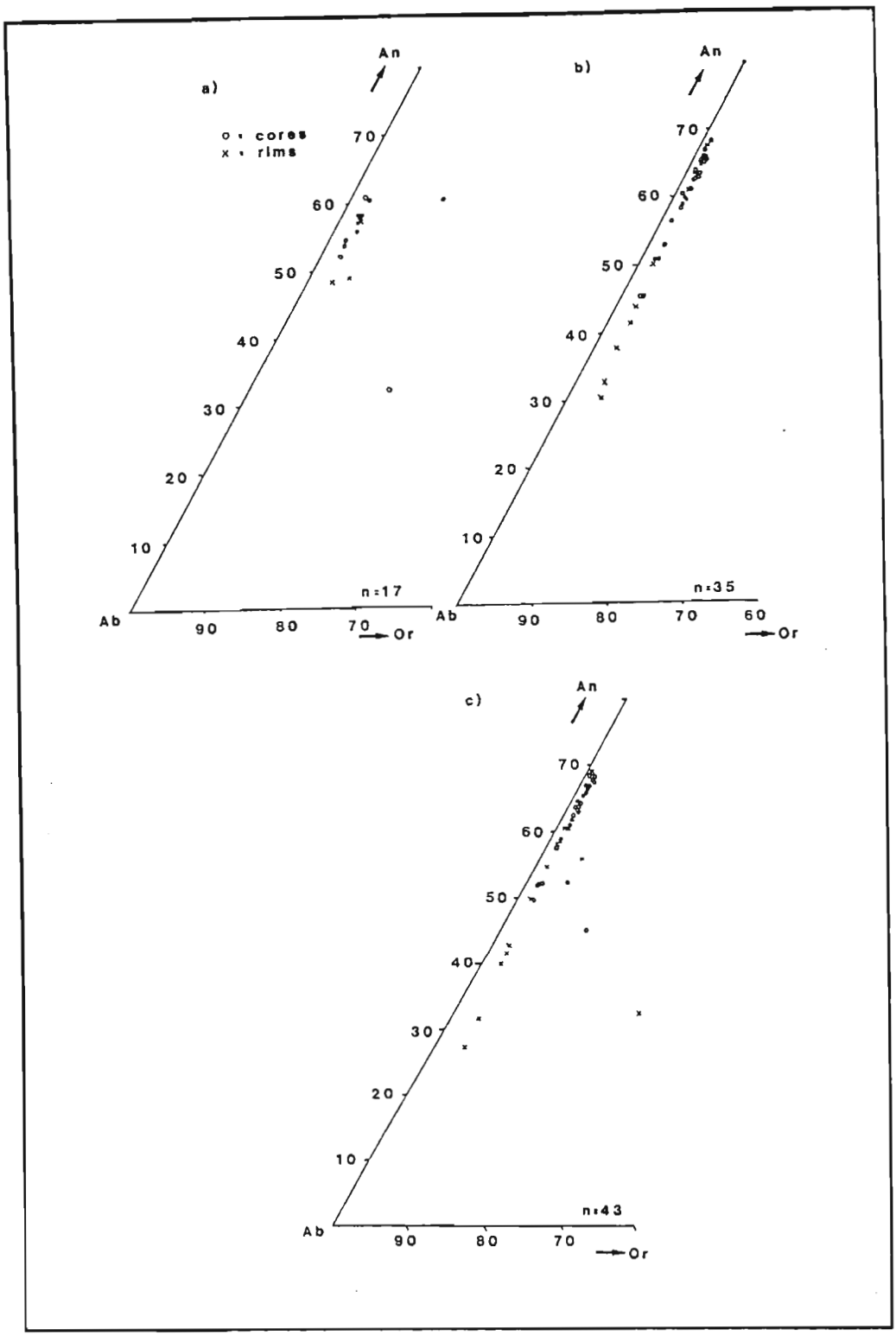

Figure 4.27. *Anorthite-albite-orthoclase diagrams for plagioclase crystals in the dolerites. Variations from cores to rims are as indicated. (a) Coarse-grained dolerite (margins). (b) Coarse-grained dolerite (centres). (c) Fine-grained dolerite.*

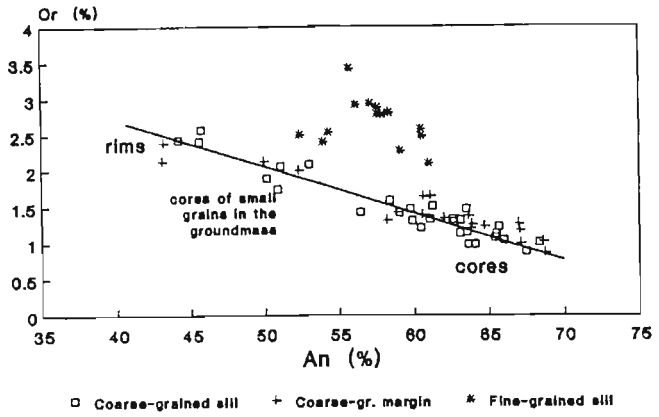

Figure 4.28. *Orthoclase versus anorthite graph showing differences between the fine-grained dolerite and coarse-grained dolerite plagioclases. The variation from cores to rims in the latter are as indicated.*

Although Figure 4.28 does not demonstrate identifiable mineralogical compositional variation from sill centres to margins in this example, there is a noticeable difference between the fine-grained and coarse-grained sill plagioclase compositions. The fine-grained sill plagioclases have higher Or values and a smaller An range. Figure 4.28 is, therefore, effective at differentiating between sills of varying ages.

A number of profiles through various plagioclase grains are shown in Figure 4.29 for SiO_2, Al_2O_3, CaO and Na_2O. The general trend is a normal zoning decrease in CaO and Al_2O_3, and an increase in SiO_2 and Na_2O from the cores to the rims of the plagioclase grains. There are, however, a number of exceptions to this trend, as indicated. This is apparent in the plagioclases from the central portion of the coarse-grained sills. Normal zoning trends near the plagioclase cores have reverse zoning trends superimposed at the grain rims. This again may be indicative of renewed magma influxes producing oscillatory-zoned plagioclases. This effect is less common for the sill margin plagioclases due to crystallisation termination prior to later magma influxes into the sill centres. Trends in the fine-grained dolerite plagioclases are more difficult to define as a result of grain-size considerations. Basic normal zoning profiles are recognisable.

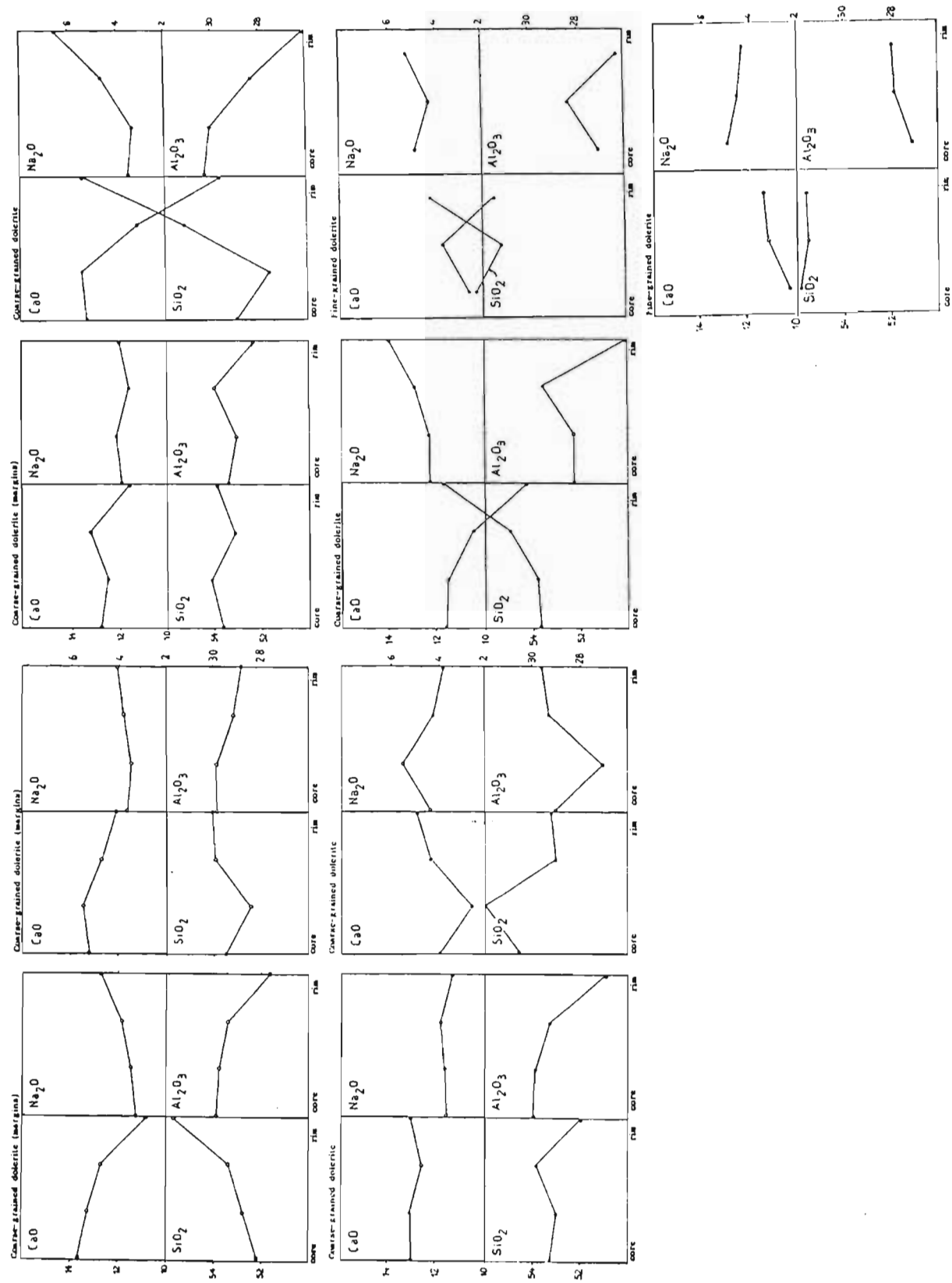

Figure 4.29. *Core to rim zoning of dolerite plagioclase grains.*

(B) PYROXENE:

Enstatite-ferrosilite-wollastonite ternary diagrams have been used to indicate the pyroxene compositions in the various dolerites (Figure 4.30). Orthopyroxene plots towards the base of the diagram, in the range En_{60-80}. The core to rim trend in orthopyroxene is shown by a movement towards the ferrosilite corner. Clinopyroxenes generally plot near the centre of the triangle, in the field of augite, as defined by Deer *et al.* (1966), although early pyroxenes near the coarse-grained sill margins are more iron-enriched, plotting closer to the Fs corner. The apparently random compositional variations from cores to rims in many of the pyroxenes is not in accordance with the expected En decrease caused by movement down the solvus isotherms, such as described by Lindsley and Anderson (1982) for co-existing clino- and orthopyroxenes. The coarse-grained sill centres exhibit normal zoning trends but the sill margin pyroxene trends are more erratic, perhaps due to rapid crystallisation along the margins, or later superimposed alteration effects.

Core to rim variations are totally random in the fine-grained sill, suggesting a disequilibrium situation. Separate fields of pyroxenes for the dolerites are demonstrated by the relative atomic proportion plots of Al^{3+} versus Mg^{2+} (Figure 4.31) and Ti^{4+} versus Mg^{2+} (Figure 4.32). The latter figure shows the higher titanium content in the fine-grained dolerite pyroxenes with respect to the coarse-grained dolerite. Sill margin to centre mineral compositional variation in the coarse-grained dolerite is more apparent in the pyroxene data than the plagioclase data described previously.

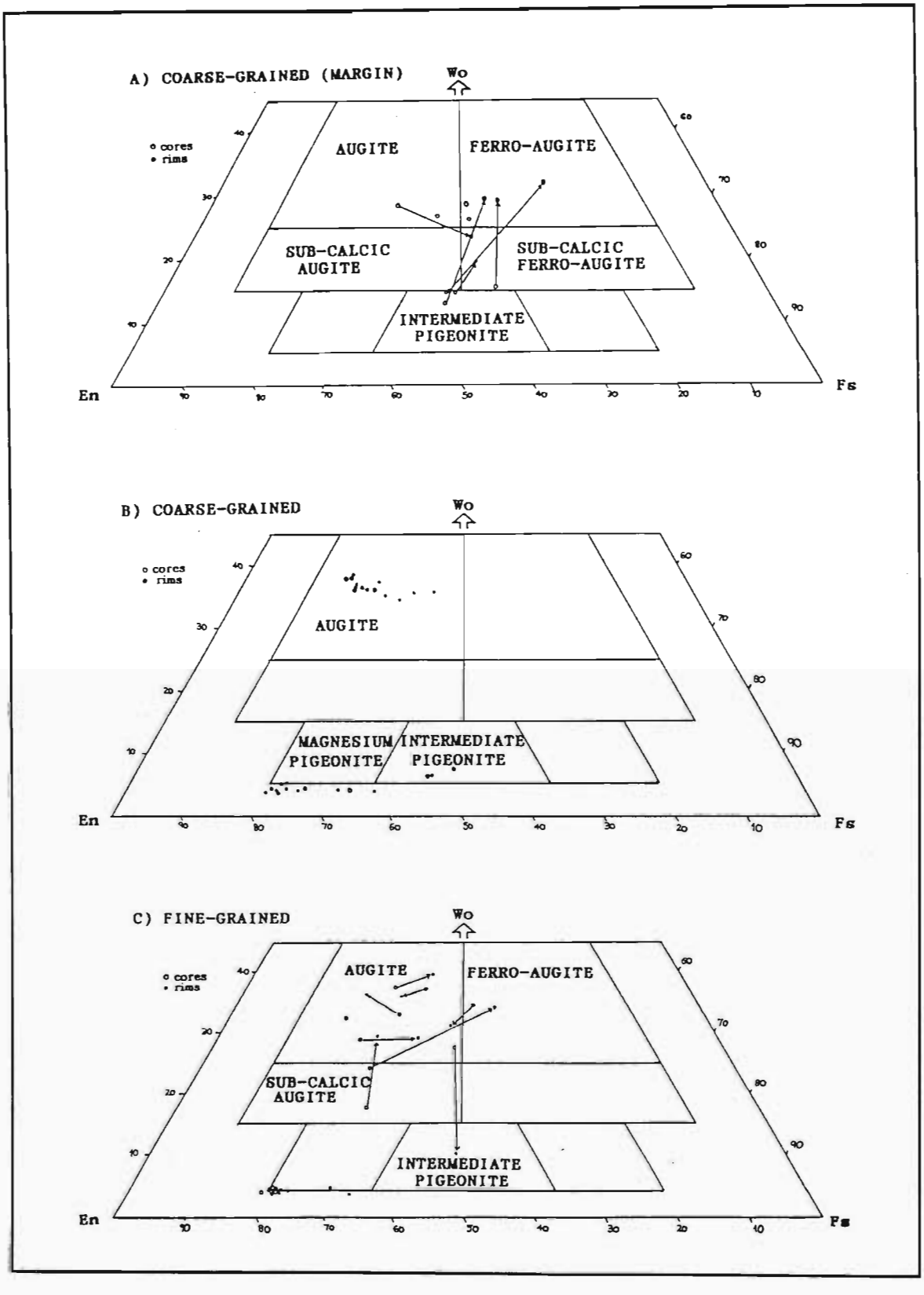

Figure 4.30. *Enstatite-ferrosilite-wollastonite diagrams showing pyroxene compositional variations in the dolerite sills. Core to rim variations of specific grains are indicated by solid connecting lines.*

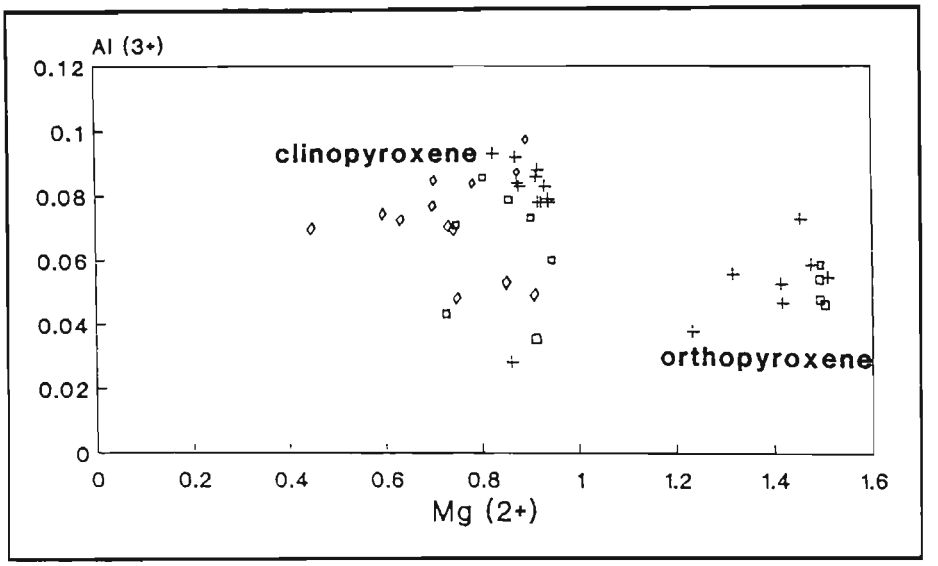

Figure 4.31. *Al^{3+} versus Mg^{2+} for pyroxenes in the dolerites. Separate fields for the fine-grained and centre and margin coarse-grained types are apparent. + = coarse-grained dolerite. □ = coarse-grained margins. ◊ = fine-grained dolerite.*

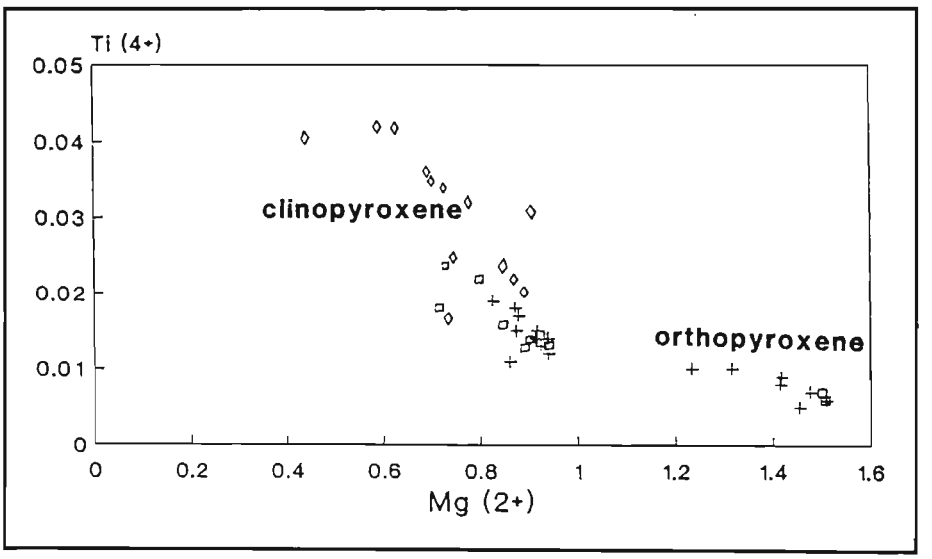

Figure 4.32. *Ti^{4+} versus Mg^{2+} for pyroxenes in the dolerites. The various fields for the dolerite divisions are apparent. Note the higher titanium values in the fine-grained dolerite pyroxenes. Symbols are as in Figure 4.31.*

4.10.2 Whole-rock Geochemical Evaluation

The whole-rock volatile-free XRF analyses (Table 4.3), which represent various positions across the thickness of the dolerite sills, show that the dolerites under investigation are enriched in silica (55-56%) compared to the whole-rock values of 52.5% for the average Karoo dolerite (Walker and Poldervaart, 1949). They are comparatively depleted in MgO and CaO, reflecting the absence of olivine. An exception is the xenolithic dolerite (53.09% SiO_2), which is has a more "Karoo-like" whole-rock geochemistry, although it is slightly MgO-enriched and CaO-depleted.

Overall, the composition of the dolerites is typical of the "normal" Karoo basaltic magma type found along the southern Lebombo (Cox *et al.*, 1967; Sweeney and Watkeys, 1990). Geochemically, the dolerites fall into the basaltic andesite field, except sample SK91-8 (from the centre of the fine-grained sill) which lies in the andesite field (Figure 4.33). The latter is a silica-rich fractionation end-product of the fine-grained sill. Whole-rock geochemical analyses can determine multiple intrusion phases where visual discrimination is difficult. This is demonstrated by the variation in major and minor elements plotted across the composite sill at the northern end of the river traverse (Figure 4.34). The position of the fine-grained sill approximately one quarter of the way up from the base of the coarse-grained sill is obvious. Removal of the fine-grained sill from the profiles would cause the lower and upper coarse-grained divisions to match up almost perfectly, thus demonstrating their initial correlation before the fine-grained phase intruded. The data may be an indication that the fine-grained dolerite is more evolved than the coarse-grained phase. The differences, however, are accentuated by the effect of quartz and potassic feldspar concentration towards the centre of the fine-grained sill, as well as pyrite concentration along the margins.

The major element concentrations are plotted against MgO in Figure 4.35. The dolerite types are clearly recognisable. The centre of the fine-grained dolerite sill is characterised by lower MgO values than the margins, whereas the trend moving from the margin of the coarse-grained dolerite sill towards the centre, is one of increasing MgO values. The xenolithic dolerite has a much higher MgO concentration than the other dolerites. The trace elements La, V, Ba, Rb, Sr and Zr are plotted against MgO in Figure 4.36.

Table 4.3. Whole-rock geochemistry of dolerites between 0 m and 200 m along the Mhlatuze River traverse (Fig. 4.3). Major element oxides are in weight %; trace elements are in parts per million.

Sample:	SK91-3	SK91-4	SK91-5	SK91-6	SK91-7	SK91-8	SK91-9	SK91-11	SK91-12	SK91-13	SK91-15	Ave. Karoo
SiO_2	55.69	55.86	55.73	55.71	55.70	61.51	55.86	55.63	55.34	55.23	53.09	52.5
TiO_2	1.20	1.21	1.20	1.12	1.33	1.70	1.36	1.02	1.04	1.04	1.26	1.0
Al_2O_3	14.61	14.66	14.71	14.99	14.69	13.35	14.56	15.38	15.19	15.09	15.75	15.4
Fe_2O_3	11.23	10.66	10.66	10.51	11.29	10.58	11.24	9.84	10.12	10.14	10.82	11.5
MnO	0.16	0.15	0.15	0.15	0.18	0.15	0.18	0.14	0.15	0.15	0.15	0.2
MgO	4.92	4.94	4.92	5.27	4.56	2.17	4.54	5.80	5.72	5.80	8.70	7.1
CaO	8.10	8.33	8.40	8.55	8.40	6.20	8.54	8.78	8.48	8.43	7.38	10.3
Na_2O	2.56	2.64	2.63	2.42	2.23	1.74	2.05	2.26	2.53	2.69	2.10	2.1
K_20	1.29	1.32	1.36	1.05	1.41	2.32	1.43	0.94	1.23	1.23	0.51	0.8
P_2O_5	0.24	0.23	0.24	0.22	0.22	0.29	0.22	0.19	0.20	0.20	0.25	0.1
	100.00	100.00	100.00	100.00	100.00	100.00	100.00	100.00	100.00	100.00	100.00	101.0
Mo	< 0.6	0.9	0.7	1.1	1.4	1.6	1.2	0.7	< 0.6	< 0.6	0.8	
Nb	10.9	11.0	10.8	10.1	9.3	14.3	9.6	9.6	9.2	9.1	7.9	
Zr	145	145	144	129	209	318	217	121	121	118	134	
Y	30	30	30	28	41	55	42	26	25	24	27	
Sr	388	395	395	396	244	216	222	406	414	419	515	
U	1.9	< 1.7	< 1.7	< 1.7	< 1.7	2.5	< 1.7	< 1.6	< 1.6	< 1.6	2.3	
Rb	33	32	34	27	31	51	29	23	33	32	17.8	
Th	5.1	4.7	3.8	3.3	4.9	9.6	3.7	4.1	6.0	4.7	2.5	
Pb	7.9	7.7	5.4	7.6	10.6	14.0	7.7	6.2	6.5	4.8	< 2.5	
Ba	515	621	517	442	455	689	458	414	481	494	383	
Sc	20	21	21	21	34	35	34	19	19.8	19.1	28	
S	412	361	434	821	1091	847	1363	1164	1387	702	358	
La	28	30	30	25	25	36	25	27	26	29	17.2	
Ce	64	63	61	57	53	82	58	53	56	53	42	
Nd	28	28	27	28	30	47	31	24	27	25	22	
Cs	< 5.6	< 5.6	< 5.5	< 5.5	< 5.7	< 5.8	< 5.7	< 5.5	< 5.5	< 5.5	< 5.7	
Co	38	39	39	39	30	19.6	30	40	41	42	52	
Mn	1126	1128	1148	1115	1423	1231	1389	1061	1028	1057	1175	
Cr	81	73	82	92	81	32	79	124	114	118	375	
V	212	211	200	203	177	152	182	182	171	170	220	
Ga	20	21	21	20	20	21	20	20	20	19.6	19	
Zn	94	97	93	93	119	123	117	86	83	83	101	
Cu	35	35	33	29	10.5	11.6	9.9	33	33	35	23	
Ni	40	40	42	44	< 2.1	< 2.1	< 2.1	53	50	52	84	

Sample heights above base of coarse-grained sill (as in Fig. 4.34):

SK91-3: 0.5 m
SK91-4: 1.5 m
SK91-5: 5 m
SK91-6: 8.5 m
SK91-7: 9.5 m
SK91-8: 11 m
SK91-9: 12.5 m
SK91-11: 13 m
SK91-12: 22 m
SK91-13: 34 m
SK91-15: xenolithic dolerite
Ave. Karoo: from Walker and Poldervaart (1949)

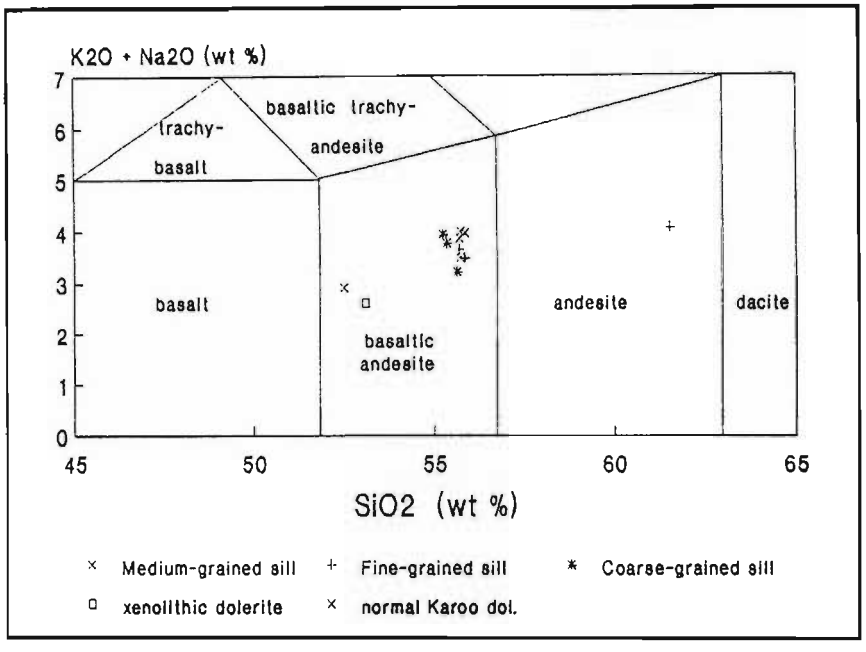

Figure 4.33. *TAS (total alkali silica) diagram (K_2O+Na_2O versus SiO_2) indicating the geochemical field of the sills to be basaltic andesite. The sample within the andesite field is a silica-rich fractionation end-product at the centre of the fine-grained sill. Diagram fields after Sabine (1989).*

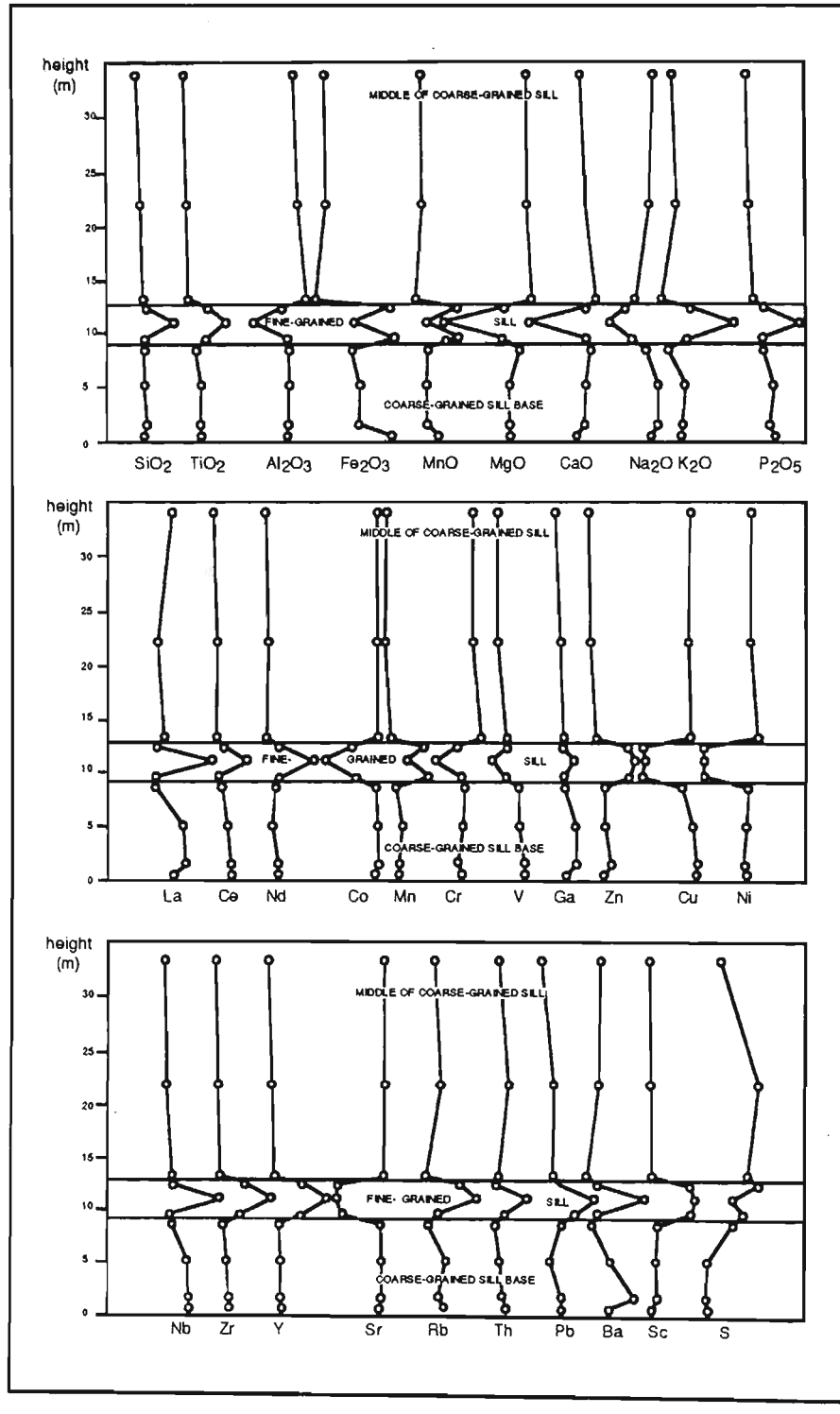

Figure 4.34. *Geochemical profiles showing relative changes in composition across the composite dolerite sills in the 0 - 200 m region of the Mhlatuze River traverse in Figure 4.3. Heights are measured above the base of the coarse-grained dolerite sill. Absolute values are given in Table 4.3.*

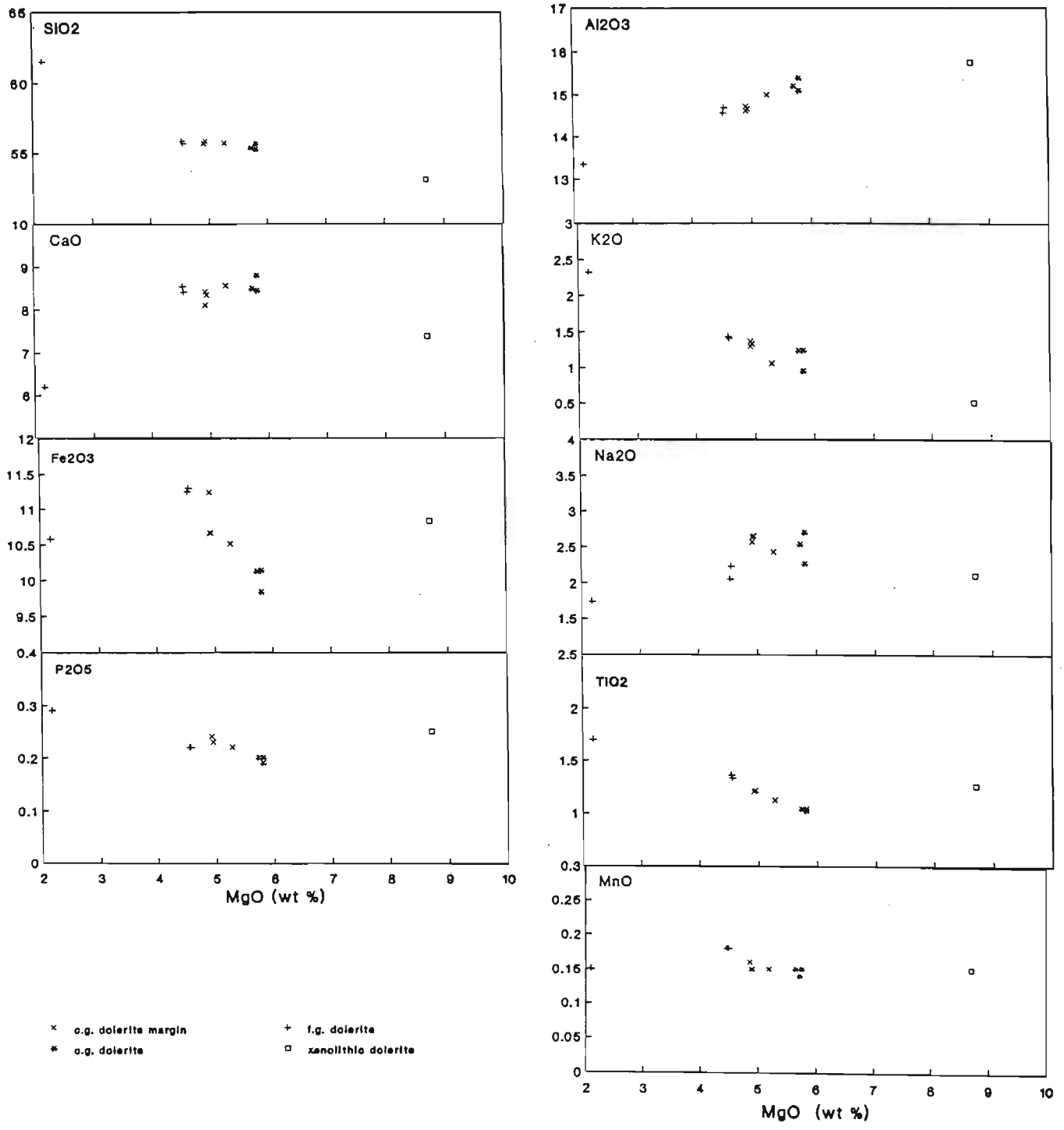

Figure 4.35. *Major element variation diagrams plotted versus MgO. The points represent the various dolerite types as indicated. (n=11).*

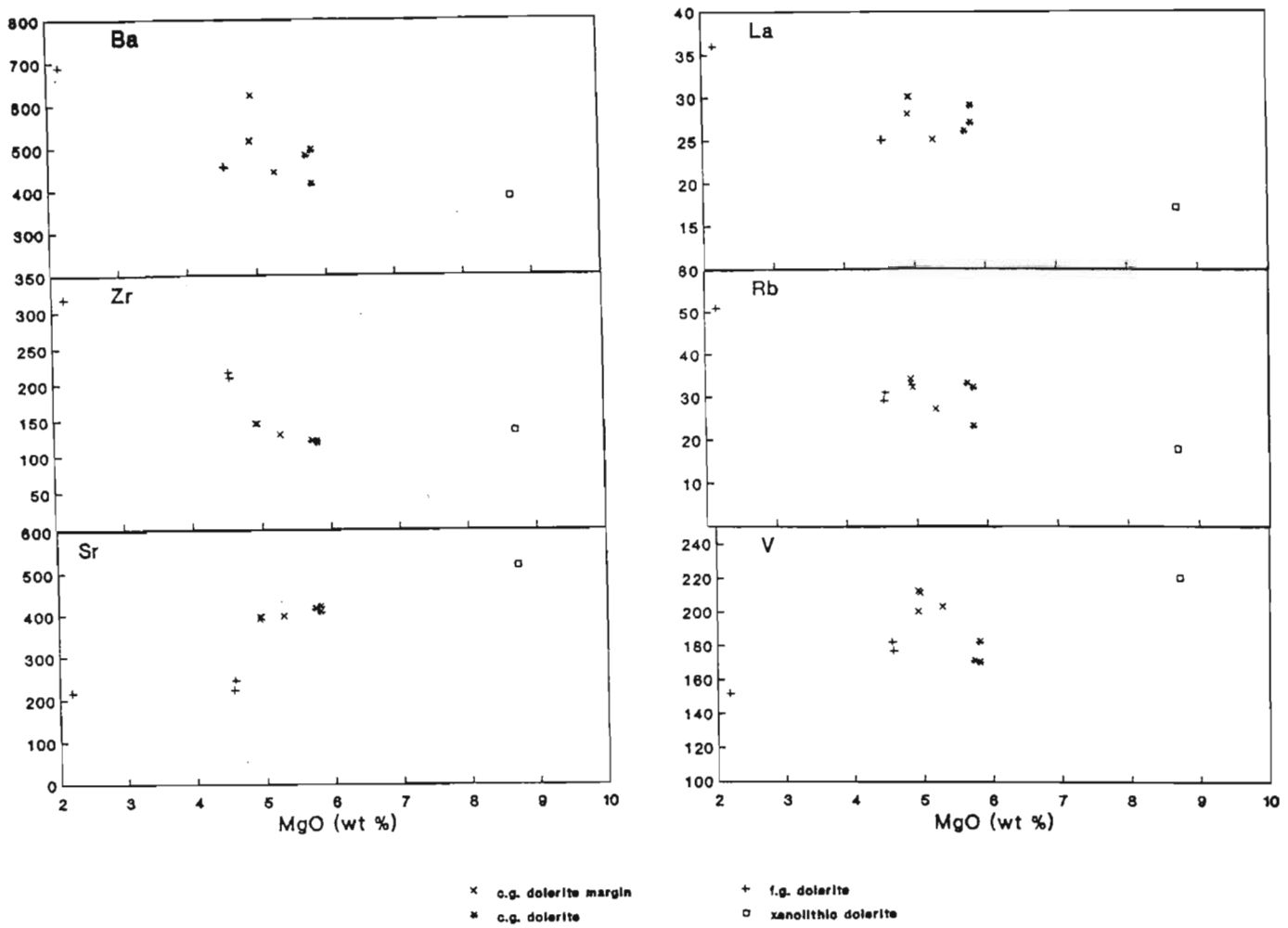

Figure 4.36. *Trace element variations in the dolerites plotted versus MgO.*

An investigation of the geochemistry of the Sabie River Basalt Formation of the Central Lebombo (Sweeney, 1988) led to the recognition of three basalt groups: the normal-, low-iron-, and high-iron-groups. The latter two groups comprise the "enriched" (high-K) basalt division recognised by Cox and Bristow (1984). Although the dolerites under investigation here are situated beyond the southern end of the Lebombo basalts, they are geochemically similar to the "normal" group. The main differences are higher silica and lower iron contents within the dolerites. The "normal" basalts are thought to indicate derivation from post-Archaean lithospheric mantle, away from the Kaapvaal Craton (Sweeney and Watkeys, 1990). Fields for "normal" basalts were identified for various other plots (Figure 4.37) and the dolerites again correlate well. A strontium normalised comparison of yttrium and neodymium (Figure 4.38) defines two distinct slopes for the fine- and coarse-grained dolerite phases. This difference may be reflecting a decreasing Al_2O_3 content towards the centre of the fine-grained sill, resulting in a lower Sr content and thus a more gentle slope in Figure 4.38.

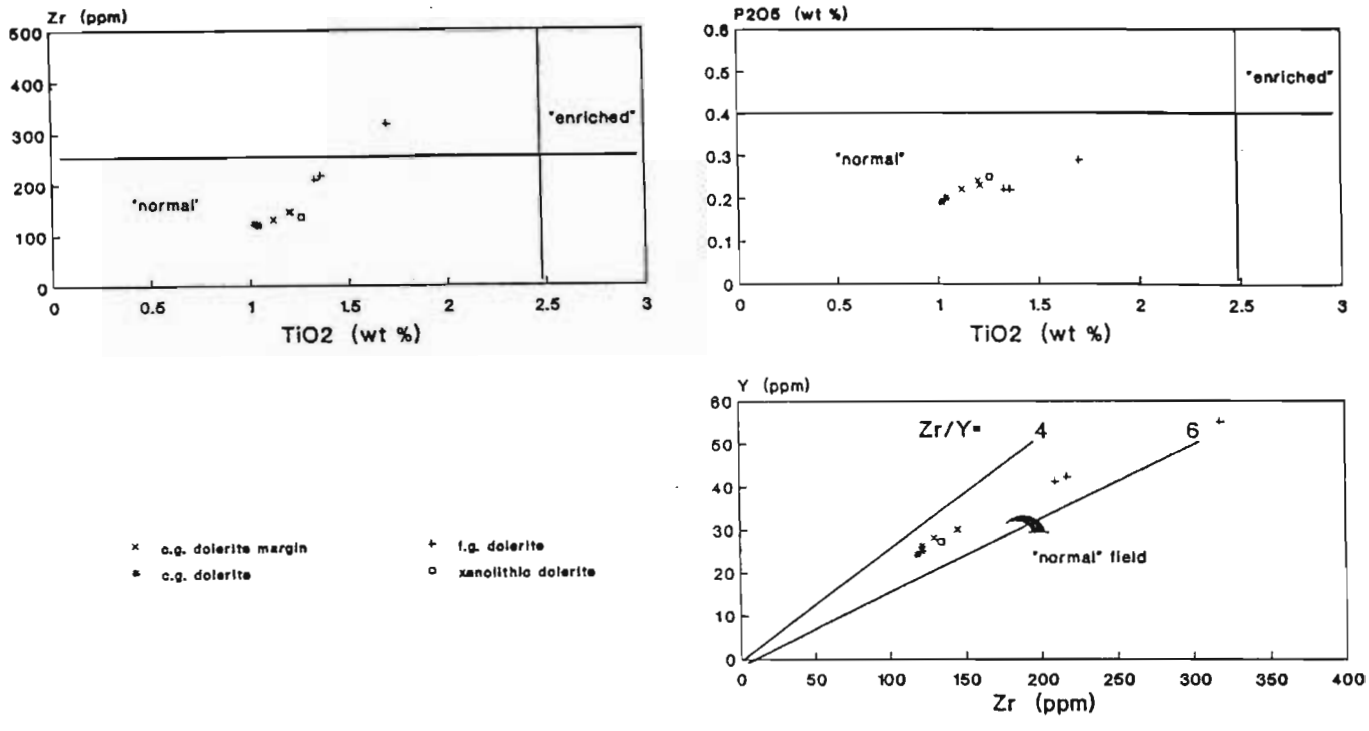

Figure 4.37. *Trace element plots for the dolerites, showing correlation with the "normal" basalt fields (after Sweeney and Watkeys, 1990).*

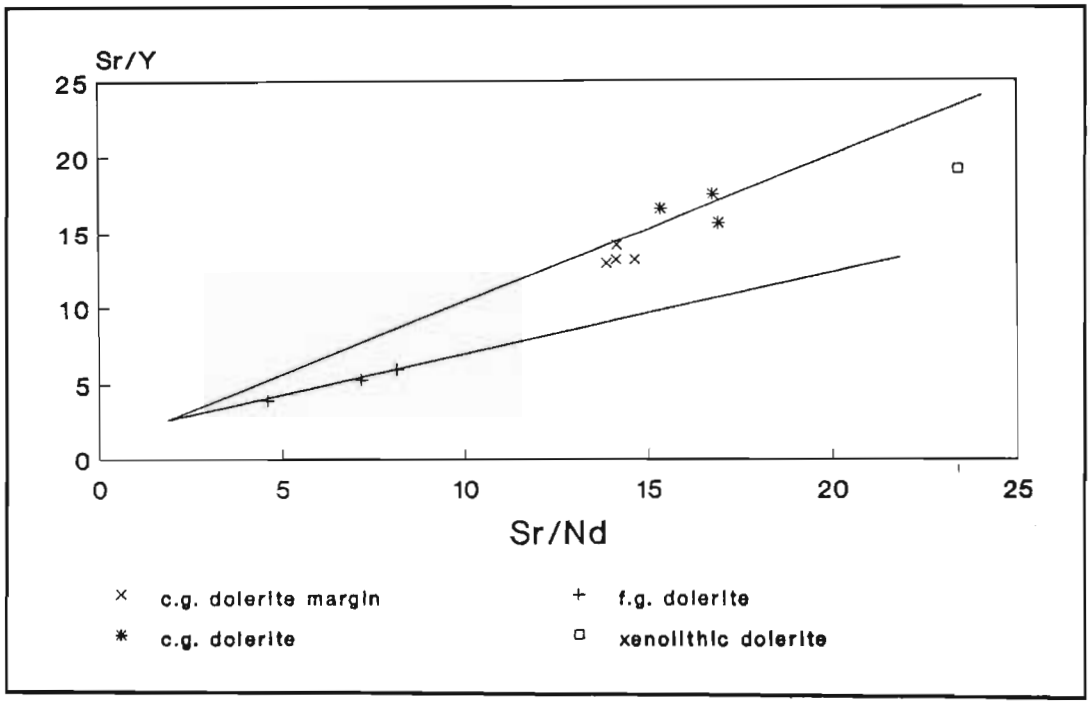

Figure 4.38. *Sr/Y versus Sr/Nd indicating notably different slopes for the fine- and coarse-grained dolerites, due to the lower Sr values in the fine-grained phase.*

The silica enrichment of the dolerites with respect to "normal" basalts and Karoo dolerites may be due to crustal contamination or magma evolution via fractionation. Geophysical work in the Lebombo region indicated the presence of a positive anomaly in the crustal gravity data (Darracott and Kleywegt, 1974). This anomalous zone was traced as far south as Durban, and it is interesting to note that this zone coincides with the coastal band of silica-enriched "Effingham-type" dolerites (Frankel, 1969), which are not found elsewhere in the Karoo Igneous Province. The dolerites under investigation here also occur within the anomalous crustal gravity zone, and so the silica contamination may be a crustal effect rather than parental magma effect.

4.10.3 Mineral Control on Whole-rock Geochemical Variations

Chemical variation diagrams that display both XRF whole-rock data and microprobe mineral data can be used to show which minerals controlled the changing geochemistry at various stages of crystallisation (Cox *et al.*, 1979). Analyses for the coarse-grained dolerite are shown in Figure 4.39. In the coarse-grained dolerite, there is no dominating mineral that defines the chemical variation, however, plagioclase and clinopyroxene appear to be having a greater effect than orthopyroxene. Petrographic studies suggested that plagioclase was the first mineral to crystallise, and this is demonstrated by the points for the coarse-grained dolerite sill margins plotting closer to the plagioclase field than the points from the sill centre. From the SiO_2 and CaO diagrams, it has been estimated that clinopyroxene and orthopyroxene crystallised out in the ratio of 3:1, and plagioclase and orthopyroxene in the ratio of 3.5 : 1. Plagioclase is thus the most abundant mineral, as was suggested in the petrographic analyses. Another observation can be made from the Fe_2O_3 plot, where it can be seen that the crystallisation trend of the dolerite (decreasing Fe_2O_3 content towards the sill centre) is mimicked by the clinopyroxene variation trend, whereas the opposite effect occurs for the orthopyroxenes, which become more Fe-enriched away from the sill margin. This may be reflecting the increasing CaO and MgO concentration away from the sill margins, with subsequent formation of Ca-Mg clinopyroxene, thus allowing Fe to substitute preferentially into orthopyroxene. The whole-rock geochemical variation in the fine-grained dolerite (Table 4.3 and Figure 4.34) represents the effects of fractionation from the margins towards the centre of the sill. Petrographically, the centre of the sill was observed to contain substantial amounts of quartz and K-feldspar; a liquid evolution effect due to the crystallisation of plagioclase and pyroxene at the sill margins. The K-feldspar presence is reflected in the trace element concentrations (Figure 4.36). Barium and rubidium, which can be substituted for potassium in the feldspar lattice, show increases towards the sill centre. Strontium, however, which substitutes for calcium, decreases in this part of the sill, thus suggesting K-feldspar control.

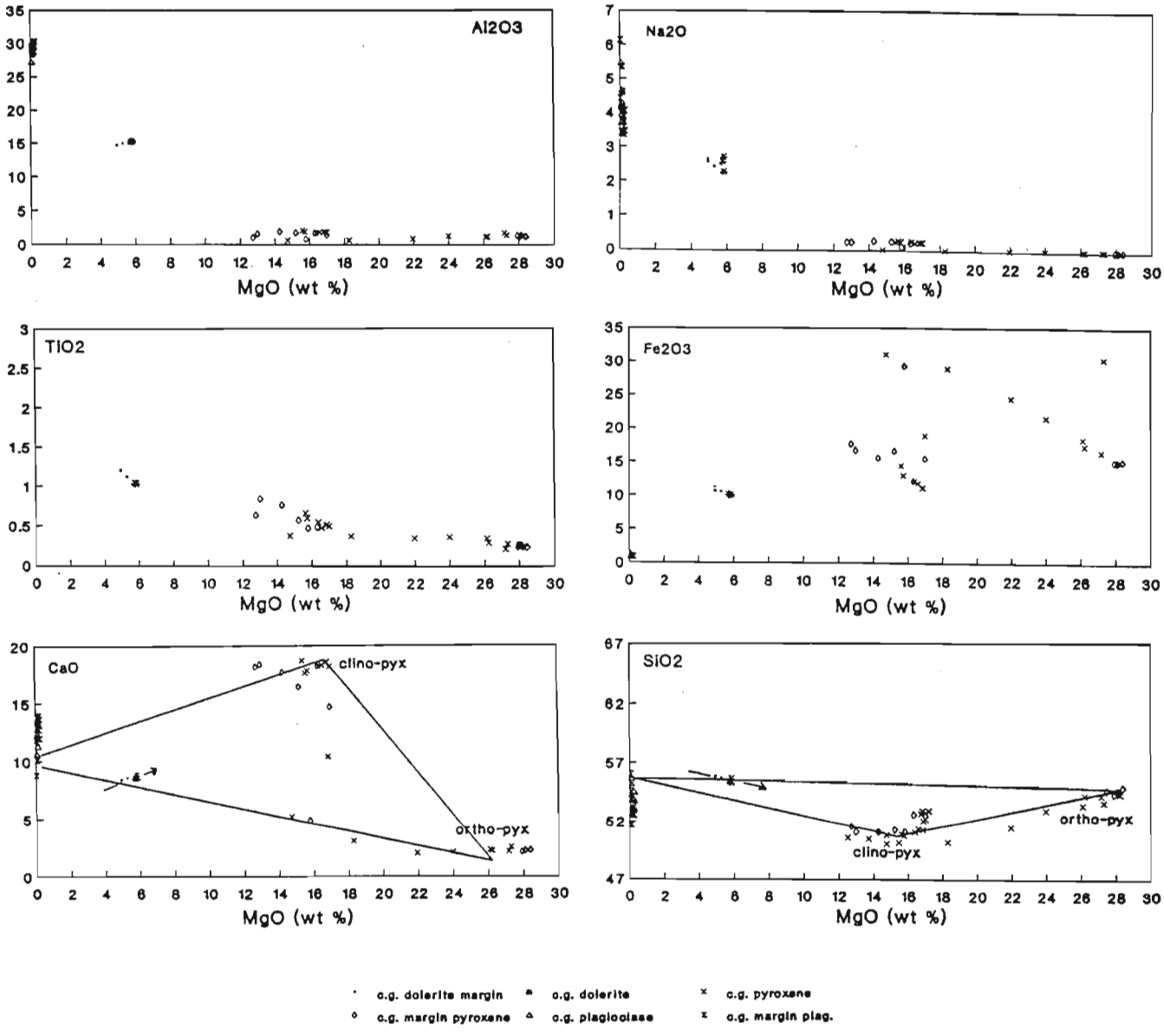

Figure 4.39. *Chemical variation diagrams showing mineral control of whole-rock geochemistry changes in the coarse-grained dolerite (see text). Mineral fields are as labelled.*

4.10.4 Basalt Discrimination Diagrams

Two basalt discrimination diagrams (Figures 4.40 and 4.41) indicate different fields for the fine- and coarse-grained dolerites. Figure 4.40 shows the relative amounts of niobium, zirconium and yttrium present in the dolerites, which all plot in the "within-plate tholeiite" field. The titanium-zirconium-strontium plot however (Figure 4.41), places the dolerites in the calc-alkaline basalt field. This may be showing the effect of a certain amount of crustal contamination, during which time the alkalis were remobilised as a consequence of their high diffusivities (Watson, 1982). Post-crystallisation alteration effects are another possibility. The most important feature of these diagrams is the recognition of separate fields for the different dolerite types; possibly an effective tool in situations where multiple phase composite dykes or sills are under investigation.

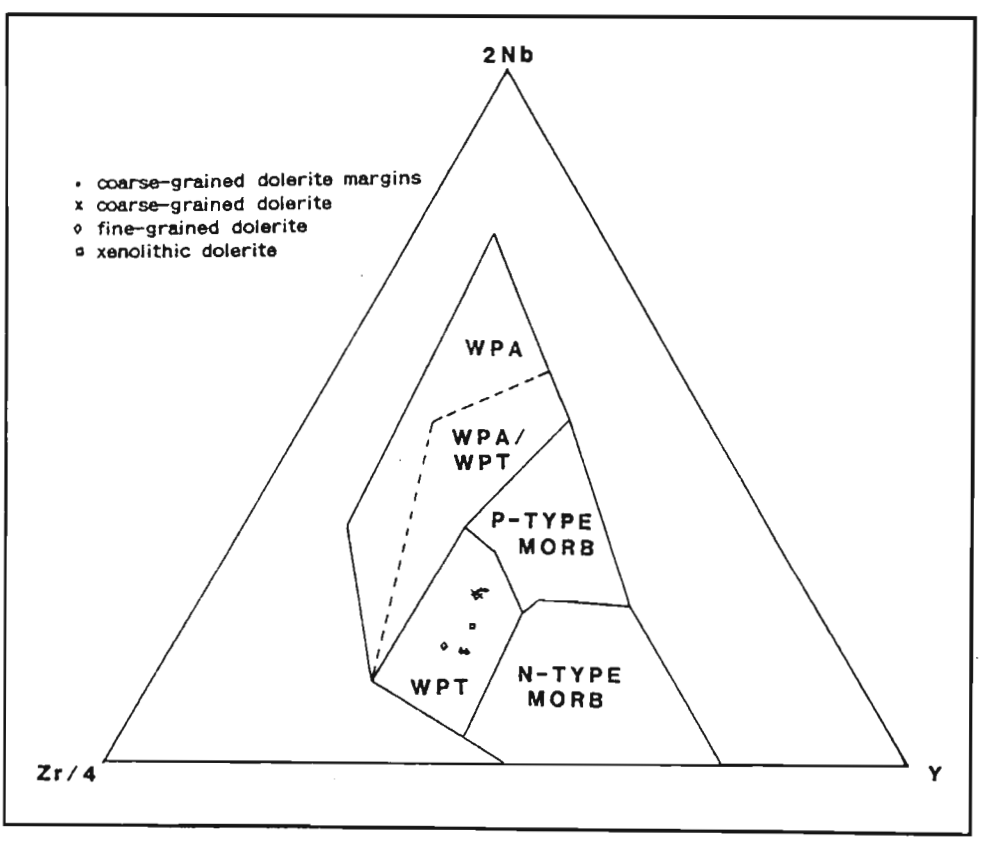

Figure 4.40. *2Nb - Zr/4 - Y diagram (after Meschede, 1986) showing the dolerites plotting in the within-plate tholeiite field. WPA = within-plate alkali basalts; WPT = within-plate tholeiites.*

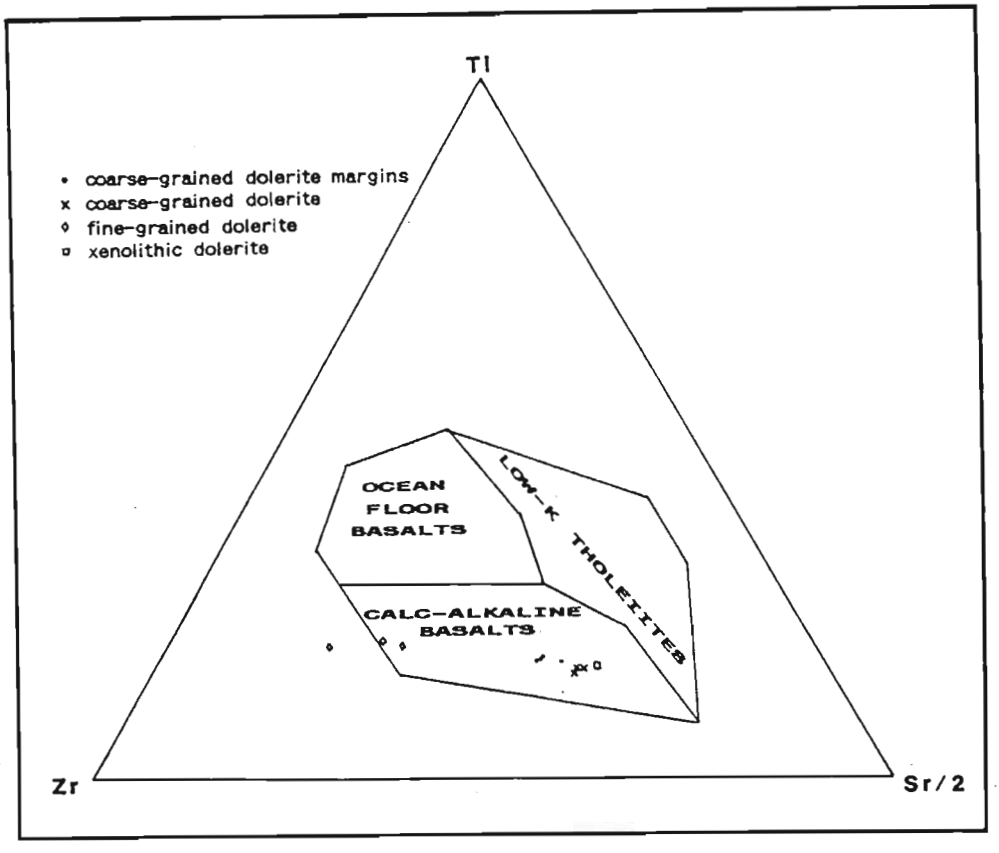

Figure 4.41. *Ti - Zr - Sr/2 diagram (after Pearce and Cann, 1973) with the dolerites falling into the calc-alkaline field (see text).*

4.10.5 Geochemical Evaluation Discussion

An evaluation of the intra-sill characteristics allows a detailed understanding of sill intrusion with respect to both emplacement and crystallisation. When injection of magma is complete, cooling and crystallisation are the predominant processes occurring in the sill. Crystal settling, fractionation and hydrothermal activity induce petrographic and geochemical gradients across the sills as seen in the mineralogical content and whole-rock chemistry.

In all sill phases, plagioclase was the first mineral to crystallise, followed by pyroxene. Where chilling occurred along the sill margins, pyroxene did not form and plagioclase crystals are set in a matrix of glass. Crystal fractionation resulted in a decrease in the basaltic nature of the fine-grained sills at the centres, with the crystallisation of primary quartz and K-feldspar. This is reflected in the whole-rock geochemistry, with increases in SiO_2 and K_2O, and decreases in Al_2O_3, Fe_2O_3, MgO, CaO and Na_2O towards the sill centre. Late-stage

hydrothermal fluid activity along sill margins induced calcitisation and introduced the components necessary for the formation of pyrite, which pseudomorphed altered pyroxene and plagioclase against the sill margins, and explains the Fe and S anomalies along these contacts.

The dolerite geochemical data allow a number of applications to be identified with regards to the recognition and differentiation between separate intrusive phases; in this case between the coarse- and fine-grained dolerite phases respectively. Mineral chemical characteristics such as illustrated for plagioclase on an Or versus An graph (Figure 4.28) or via core to rim variations (Figure 4.29), and illustrated for pyroxene core to rim variations (Figure 4.30) and Ti^{4+} concentrations (Figure 4.32), effectively demonstrate differences between the two dolerite intrusive phases. Whole-rock geochemical data are just as effective, such as via absolute whole-rock compositional variation across a composite sill (Figure 4.34), variable Harker-type diagram compositional trends (Figure 4.35), trace element concentrations (Figures 4.36 and 4.38), and basalt discrimination diagram fields (Figures 4.40 and 4.41). Finally, different mineralogical controls on whole-rock variation trends (Figure 4.39) may also be evident for different intrusive phases. All of these geochemical characteristics may prove useful as tools for the identification of separate intrusive events in areas where multiple intrusive activity has occurred, such as has been applied for the Mhlatuze River dolerite sills.

5. DILATION AND MAGMA FLOW IN DYKES

5.1 Introduction

The mechanics of formation, dilation and intrusion of dykes were summarized in Chapters 2 and 3. In this chapter, specific examples will be utilised to demonstrate the mechanism by which a dyke dilates, possible chemical controls on fracture development, and the dynamics of magma flow in a thin dyke. The methods of dyke intrusion will be illustrated by multiple intrusion event recognition in a dyke swarm, as well as a determination of the successive opening steps for an individual dyke within the swarm in order that the intrusion mechanics may be demonstrated. Chemical controls on fracture propagation at the tip of the latter dyke will be investigated using microprobe analyses of minerals through which fractures are propagating on a microscopic scale. The dynamics of magma flow in a thin fissure will be determined using digitally analysed phenocryst orientations, allowing the determination of a magma flow direction.

Samples for these exercises were obtained from a well exposed outcrop of the Rooi Rand Dyke Swarm along the Pongola River, 150 km north of Empangeni (Figure 5.1).

5.2 Rooi Rand Dyke Swarm

The Rooi Rand Dyke Swarm is a basaltic (dolerite) dyke swarm in the southern Lebombo region that extends a distance of approximately 200 km from Hluhluwe in the south to central Swaziland in the north, and has been documented by authors such as Bristow (1976), Armstrong (1978), Saggerson *et al.* (1983), Armstrong *et al.* (1984), Hunter and Reid (1987) and Meth (1991).

The dyke swarm is represented by a multiple phase assortment of dykes that were emplaced 188 ±5 million years ago (K-Ar date; Cleverley, 1977), and consists of both single and composite intrusions (Saggerson *et al.*, 1983). The dyke swarm trends essentially north-south, dips steeply to the west at 65^{o}-75^{o}, and attains a maximum width of about 20km (Armstrong *et al.*, 1984). The intensity of intrusion decreases with increasing distance from the centre of the swarm, and was associated with an average crustal extension of 40 per cent (Saggerson *et al.*, 1983). The dykes range in thickness from 25m to very thin dykelets, and were "emplaced towards the final stages of eruption of the Sabie River Formation and during the main period of faulting, tilting and warping to which the Lebombo region was subjected" (Armstrong *et al.*, 1984) in response to the fragmentation of eastern Gondwana during the Jurassic.

Geochemically, the Rooi Rand dykes display major element variation trends typical of iron-enriched continental tholeiite suites that result from the fractionation of a clinopyroxene + plagioclase + olivine gabbroic assemblage (Armstrong *et al.*, 1984). Recognition of individual intrusive episodes has been attempted on the basis of geochemical variation trends by Meth (1991).

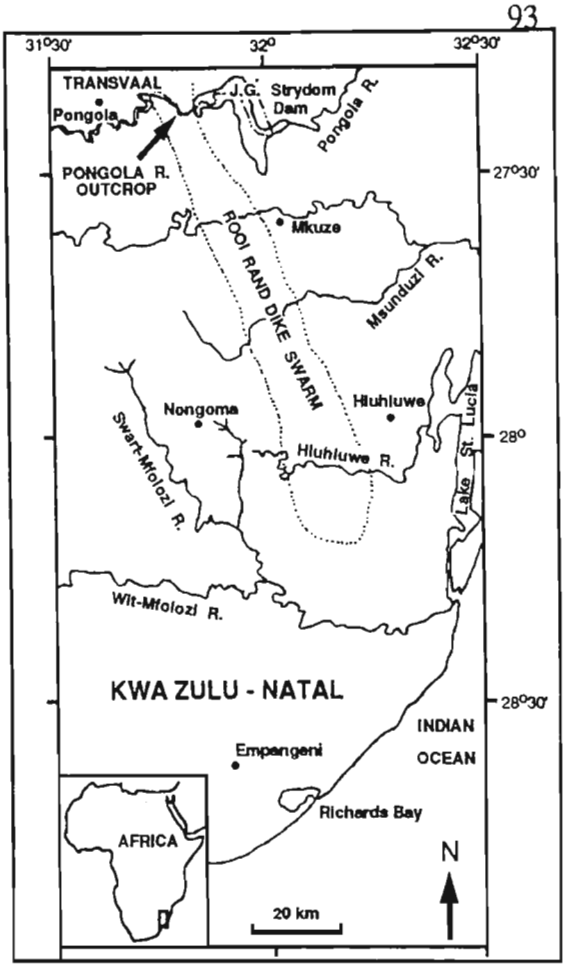

Figure 5.1. *Location of the Pongola River outcrop of the Rooi Rand Dyke Swarm in northern Natal. After Eales et al. (1984).*

5.3 Mechanics of Multiple Dyke Intrusion

The attitude of the Rooi Rand Dyke Swarm outcrop along the Pongola River is illustrated in Figure 5.2. Meth (1991) recognised up to eight episodes of intrusion on the basis of field relationships and geochemical data, but this has been modified to ten episodes in Figure 5.2. The dykes have intruded through an older, Karoo-age dolerite sill, which is preserved as isolated wedges within the swarm, suggesting the Rooi Rand episode to be comparatively younger than the extended period of dolerite intrusive activity in the Karoo Igneous Province. Comparative ages of juxtaposed dykes are frequently best recognised on the basis of chill margin relationships. However, where intrusion of later dykes into older intrusions has occurred, there sometimes occurs a chill-on-chill effect whereby only one chill margin of each phase of a composite dyke is preserved, with the exception of the final intrusive phase (Saggerson *et al.*, 1983). Where later phases intrude along the chill margin of an older phase, that chill margin may be obliterated and replaced by the chill of the later phase. Chill margin relationships must, therefore, be studied with caution in order that the correct sequence of events can be interpreted.

Armstrong (1978) recognized five different intrusion events using chill margin relationships. Meth (1991) identified the individual dolerite phases on the basis of chill margin relationships and grain sizes as shown in Figure 5.2. A similar approach was used by Saggerson *et al.* (1983). Although this is a somewhat crude method considering the number of intrusive phases present, it has proved to be a fairly accurate field method of identification, and is supported by the geochemical data (Meth, 1991). Many of the thinner dykes exhibit steps and offsets and en echelon

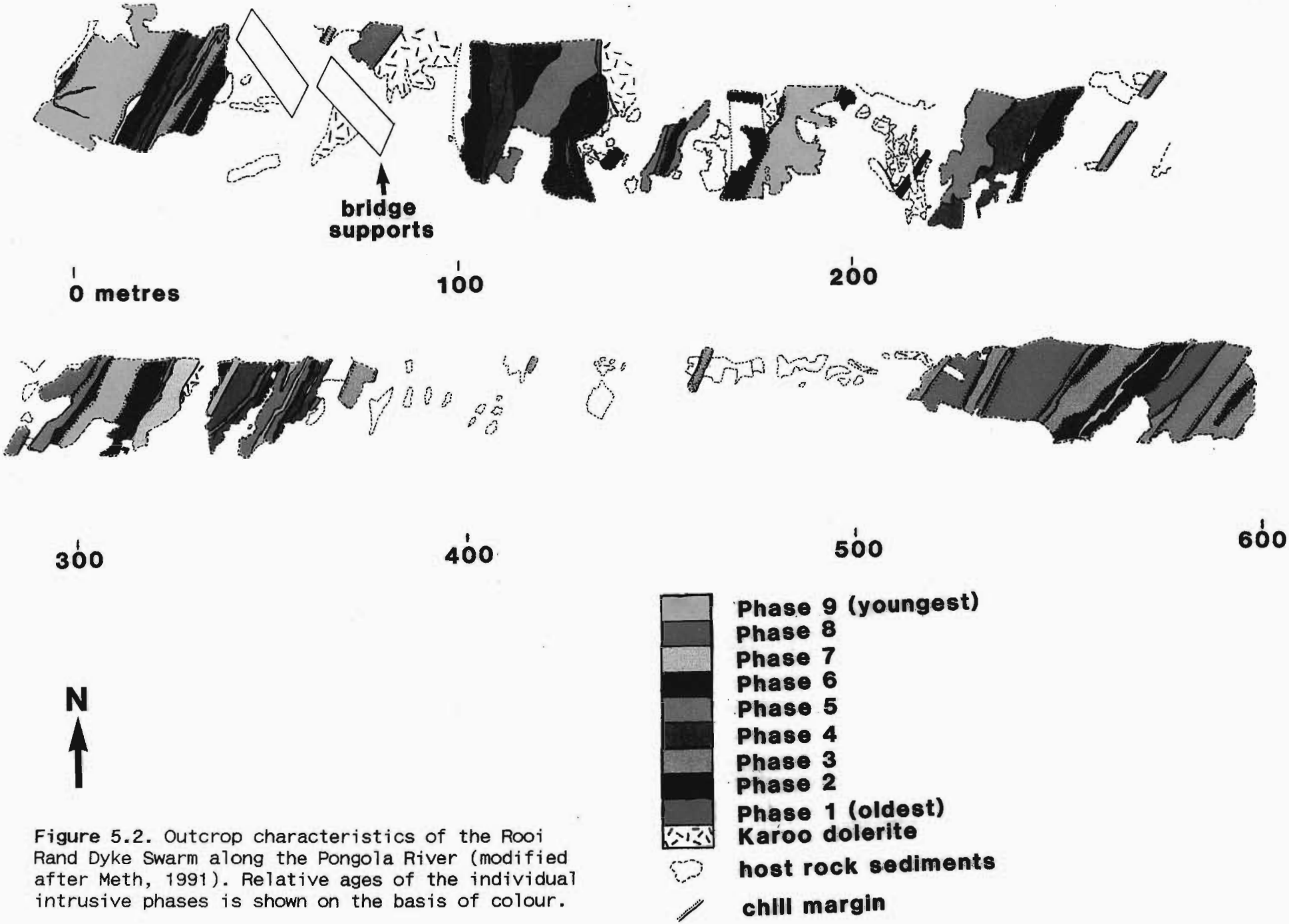

Figure 5.2. Outcrop characteristics of the Rooi Rand Dyke Swarm along the Pongola River (modified after Meth, 1991). Relative ages of the individual intrusive phases is shown on the basis of colour.

patterns, with linkage of adjacent segments in accordance with the models described in Chapter 3. Cooling joints at right angles to the dyke margins are occasionally intruded by later dolerite phases, although thicknesses of such dykelets are limited to a few centimetres. At the 360m mark along the river traverse (Figure 5.2), a blunt-ended dyke is associated with a number of thin offshoots (Figure 5.3) that may provide an explanation as to the mode of formation of blunt-ended dykes (pers. comm. Watkeys, 1992). Dilation of the dyke is associated with a shear component in the adjacent rocks, resulting in shear fracture dilation and intrusion that compensates for the amount of dilation occurring in the main dyke body. Evidence for such a shearing effect is apparent on a microscopic level, as will be described in the following section.

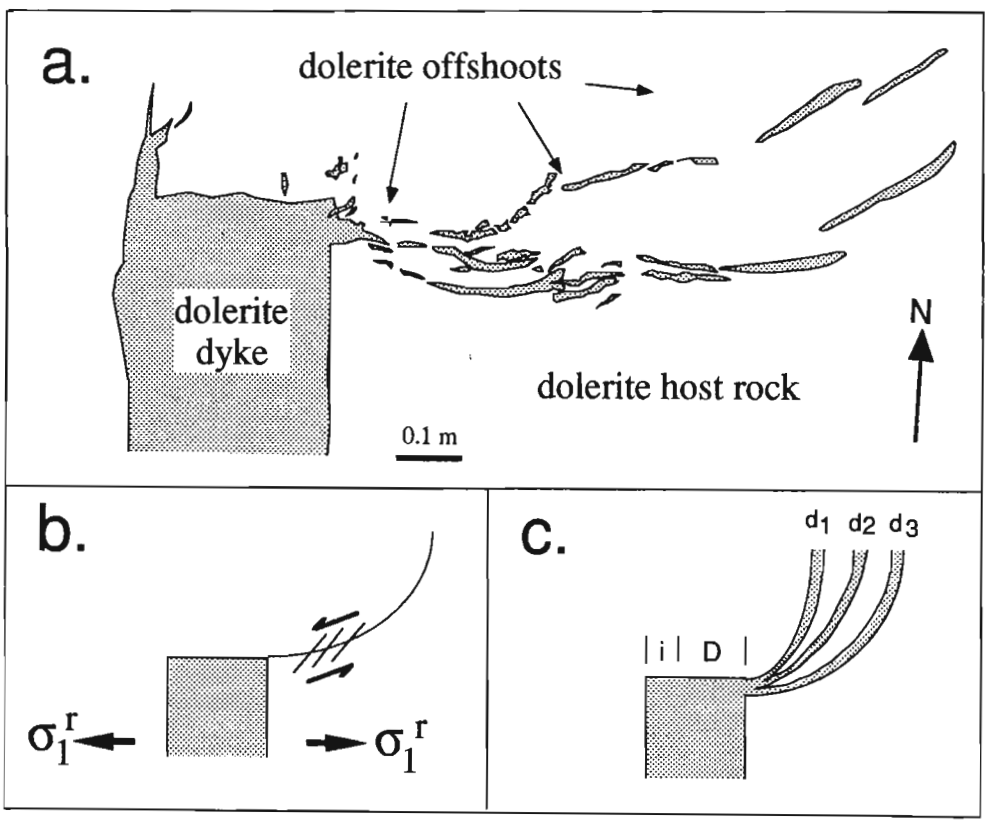

Figure 5.3. *(A): Multiple offshoots of dilated shear fractures adjacent to a blunt-ended dyke at the 360 m mark along the Pongola River outcrop. (B): The proposed zone of left-lateral shear curves gradually into parallelism with the dyke plane with increasing distance from the dyke. The maximum regional tension is* σ_1^r*. (C): Cumulative dilation of the shear fractures is D (=*d_1 + d_2 + d_3*). Additional dilation in the dyke, i, is the initial elastic dilation of the dyke prior to development of a shear zone into the adjacent host rock essentially orthogonal to the dyke plane.*

A recurring feature of the dyke swarm is the tendency for later dyke phases to intrude into older dykes, frequently through the centres of the earlier formed dykes (Figure 5.2). The presence of chill margins indicates that earlier phases cooled and solidified before the intrusion of subsequent phases (Saggerson *et al.*, 1983). It must therefore be explained why later intrusions are emplaced within older, solidified dykes, rather than into the adjacent country rock of predominantly shale. According to Pollard (1987), an intruding dyke tip is associated with a process zone within which substantial fracturing of the country rock occurs (Chapter 3). These fractures are juxtaposed against the sides

5.4 Dilation History of an En Echelon Dyke

5.4.1 En Echelon Dyke Development

As most of the dykes in the Pongola River cutting have greater dimensions than the outcrop itself, absolute dilation reconstruction can only be attempted for the thinner dykelets which are more wholly exposed. Such an example occurs at the 345 m mark along the river, where a 3.5 cm thick dyke is composed of a number of linked en echelon segments. Slabs of rock cut perpendicularly to the plane of the dyke (both vertically and horizontally), allowed the construction of a three-dimensional representation of the dyke, showing the changes that occur along the propagation direction at a zone of offset and linkage (Figure 5.5).

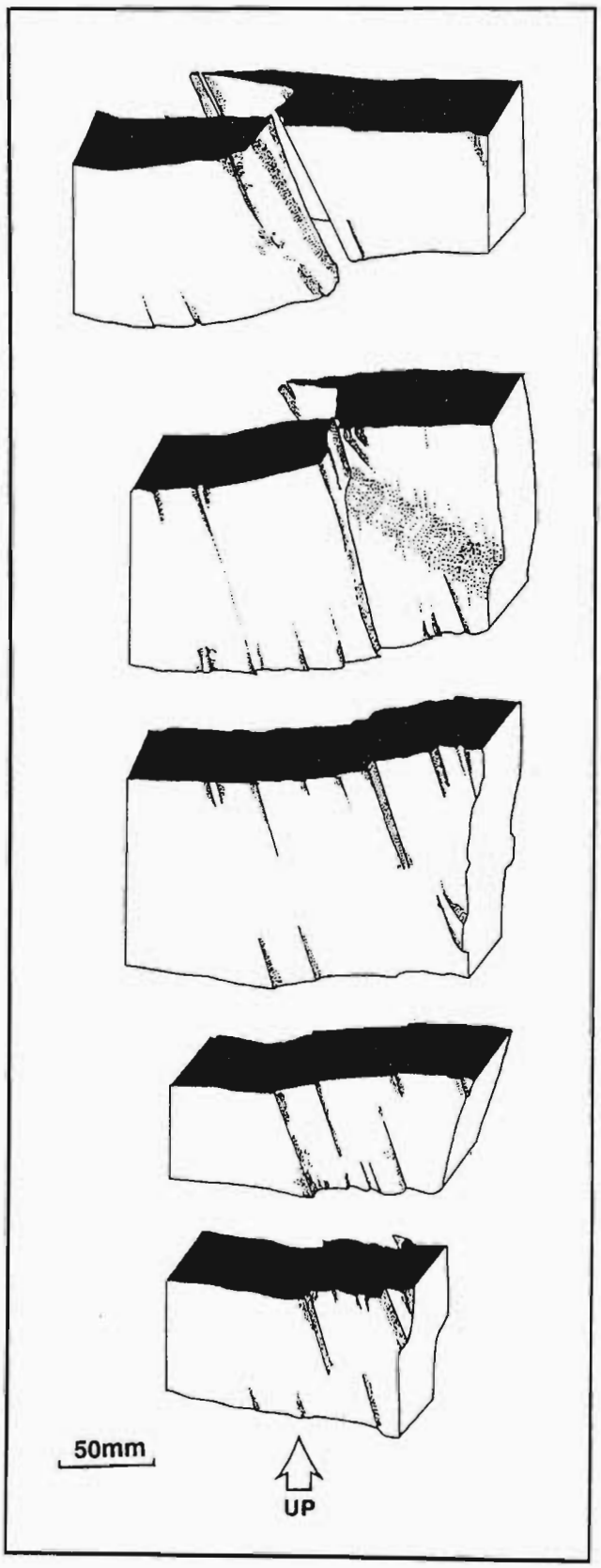

Figure 5.5. *Three-dimensional representation of a 3.5 cm thick dyke that splits into two offset segments along the propagation direction. This resulted in the formation of blunt-ended dykes and horn development. Vertical thickness is approximately 30 cm.*

In this figure, it can be seen that a single dyke at a deeper level divides into two offset segments along the propagation direction. Most literature studies document en echelon intrusions that begin as offset, individual segments that link due to the interplay of near-tip stresses (Pollard *et al.*, 1982; Nicholson and Pollard, 1985; Olson and Pollard, 1989 & 1991). Segmentation of dykes into en echelon segments along the propagation direction has been frequently proposed to explain the occurrence of en echelon segments (Anderson, 1951; Pollard, 1987; Price and Cosgrove, 1990). Such segments are envisualised to rotate in a changing stress field out of the plane of the parent dyke.

In the case of Figure 5.5, it can be seen that the offset in the horizontal plane is accompanied by a simultaneous offset in the vertical plane. This suggests that the formation of the en echelon segments is not the result of fragmentation of the dyke front in a changing stress field, but rather due to the dilation of an adjacent, offset fracture. There is thus no rotation of the en echelon dyke segments with respect to the parent dyke. This may suggest that the emplacement of an intrusion occurs via a repetitive splitting ("deconstruction") and relinking action ("construction") that serves to minimize the energy expenditure during intrusion (Pollard *et al.*, 1982). A developing horn on the outside edge of one of the segments (Figure 5.5) begins to curve in towards the adjacent dyke segment further along the propagation direction due to the nature of the near-tip stresses. Assumedly, this horn would link with the adjacent dyke segment further along the propagation direction to form a single dyke once again. This proposed mechanism of "constructive" and "deconstructive" en echelon behavior may be quite common, and it obviates the need for a higher crustal, rotating stress field in order to produce the en echelon segments. There is no reason for a region undergoing crustal extension, such as the tectonic regime of the Rooi Rand Dyke Swarm, to have rotating crustal stress patterns.

Figure 5.5 reveals that the major offset and associated horn, as well as the minor offsets along strike, propagated obliquely towards the surface. This may be a reflection of magma migration upwards and towards the south, away from a deeper, more northerly magma source. Such features plunge at between 48^{o} and 80^{o} towards the north. Minor offsets are of very limited extent along the dyke length, suddenly appearing and then disappearing again a few centimetres along the direction of propagation. The southward-directed magma pressure may be the reason for the formation of a single horn on the southern edge of the one dyke segment, rather than on the outside edges of both dyke segments, as is often the case. The initial development of the horn occurs with rapid growth away from the tip of the dyke segment, with the lower edge of the horn plunging at 26^{o} to horizontal. Further along the magma propagation direction, the lower edge of the horn rotates to a steeper inclination, attaining an attitude similar to the other features described above. This suggests the horn is attaining a state of equilibrium with the propagating magma, at which point the dominant feature is the near-tip stress interaction and consequent rotation in towards the adjacent dyke segment.

Horn growth and curvature may be better understood when investigated on the microscopic level. Figure 5.6 shows a photomicrograph of a horn tip. From the orientations of microphenocrysts in the glassy groundmass of the

horn, it appears that the horn tip was associated with a degree of magmatic turbulence. Furthermore, the dolerite country rock through which the horn is advancing has undergone a marked degree of cataclasis ahead of the horn tip, perhaps due to stresses induced by dilation of the horn. The existence of cataclastic dolerite fragments in the glassy groundmass suggests that the horn may advance by a simple erosive effect of the turbulent magma against the cataclastic host rock at the horn tip.

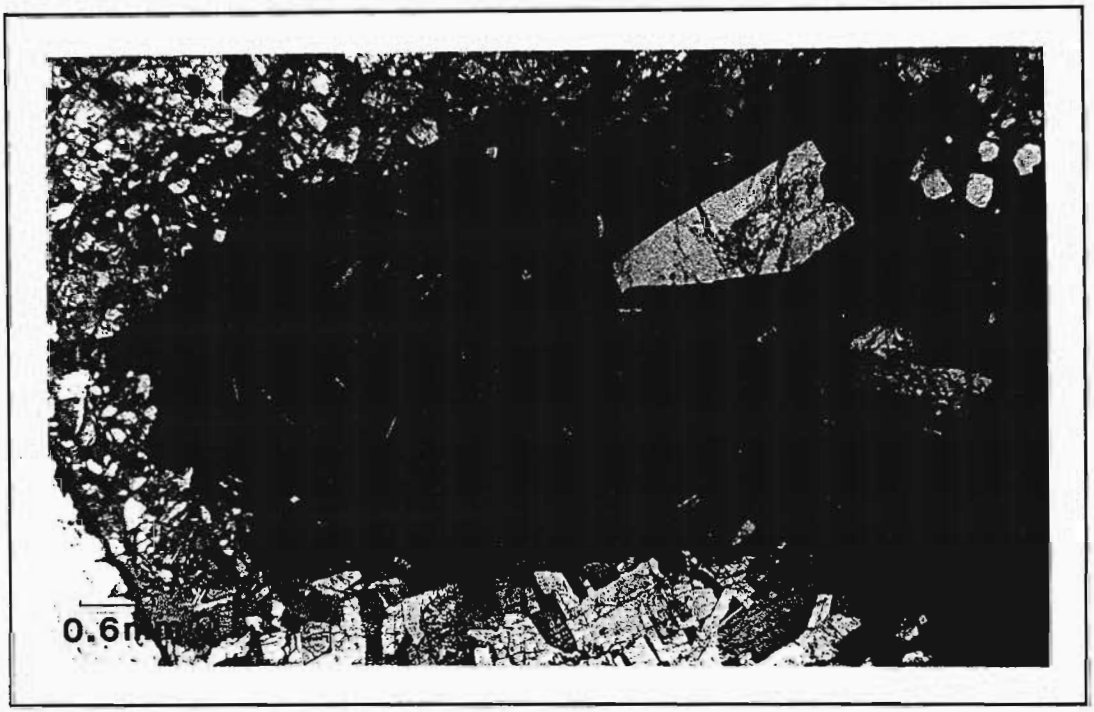

Figure 5.6. *Photomicrograph of the tip of the horn in Figure 5.5, showing cataclasis of the dolerite host rock ahead of the tip and magmatic turbulence at the tip, as suggested by microphenocryst orientations in the glassy groundmass. Dyke locality: 345 m mark in Figure 5.2.*

The effects of horn dilation and propagation in the host rock ahead of the horn tip is better illustrated in Figure 5.7. Microfractures in the host rock ahead of the tip curve in towards the adjacent dyke segment (not shown in the figure), and cause a significant degree of cataclasis of the host rock. This curvature of the microfractures is very similar to the pattern of stress trajectories predicted by Ramsay (1967) for the case of a "constant horizontal supplementary stress system", such as might be produced by the magma pressure at the horn tip. Furthermore, curvature of the microfractures may induce curvature of the horn itself, in towards the adjacent dyke segment.

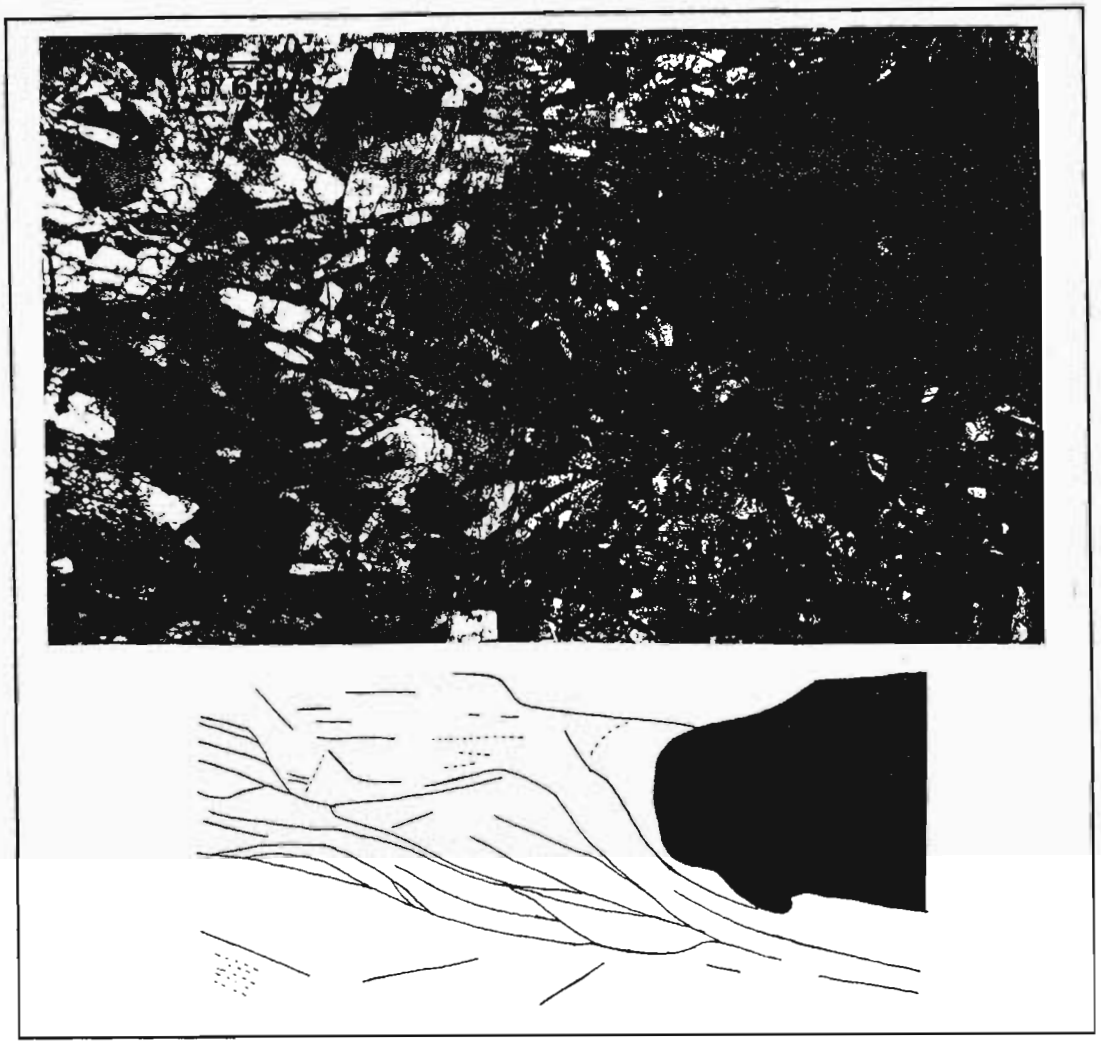

Figure 5.7. *Photomicrograph of fractured dolerite host rock ahead of the tip of an advancing horn. Microfractures curve in towards the adjacent dyke segment (above the field of the photograph) causing cataclasis of the host rock and promoting horn growth and curvature. Inset: detailed representation of the fracture pattern. Dyke locality: 345 m mark in Figure 5.2.*

5.4.2 Blunt-Ended Offset Segments: Dilation Reconstruction

The three-dimensional dyke representation in Figure 5.5 indicates that the "deconstruction" of the dyke produced two offset segments with essentially rectangular ends. Such blunt-ended dykes are frequently observed in the field, and the effect is also common in sills. As fracture dilation is assumed to produce elliptical openings (Pollard, 1973), there must be some additional mechanism that results in the formation of blunt-ended planar intrusions. In the case of the dyke in Figure 5.5, a reconstruction of the dilation history, and microscopic analysis allows clarification of the mechanism responsible for such dyke geometries.

The dilation history has been reconstructed for the region around the offset, blunt-ended terminations of the two dyke segments of Figure 5.5 in Figure 5.8.

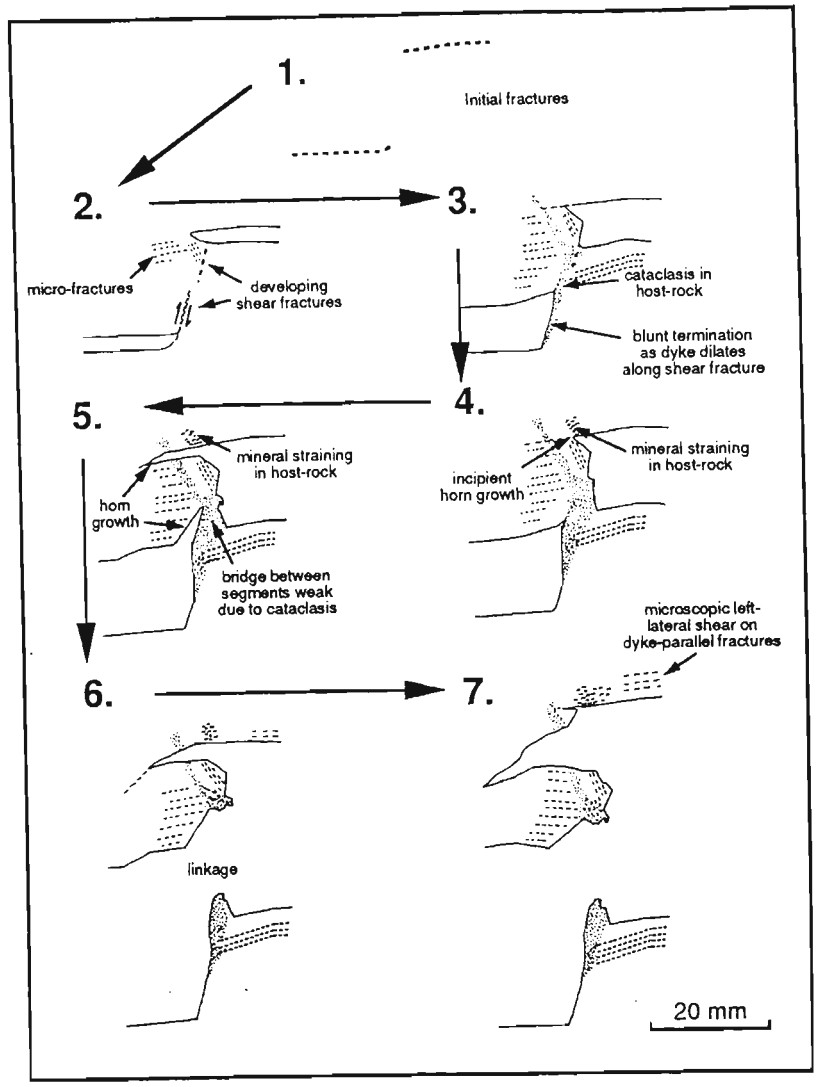

Figure 5.8. *Reconstruction of the dilation history of the offset dyke segments (Figure 5.5) at the 345 m mark in Figure 5.2, showing the formation of blunt-ended dyke terminations, cataclasis of the country rock, shear fracture development and mineral straining.*

The microscopic occurrence of a zone of cataclasis of the dolerite country rock in the interconnecting region between the offset dyke segments, and along the edges of the blunt-ended dyke terminations, suggests that dilation may have been accommodated by movement along through-going shear fractures in the region between the two dyke segments, similar to the mesoscopic effect described in the previous section (Figure 5.3). Such fractures may have originally developed due to the interplay of near-tip stresses around the offset dyke segment terminations. Movement along these shear fractures (right-lateral in Figure 5.8) during dilation of the segments resulted in cataclasis of the country rock. It appears that partial dilation of one of the shear fractures occurred in the dyke segment that lacks normal horn development (Figure 5.8), thus instigating linkage along a horn that propagated at a high angle to the dyke termination. The formation of a horn along the outer edge of one dyke segment, yet almost perpendicular to

the other dyke segment, resembles the "monocline" stress field distribution described by Roberts (1970) to explain the existence of sills on one side of a monocline, and dykes on the other. Figure 5.8 also shows that a left-lateral displacement occurred along dyke-parallel fractures on either side of the dyke segments. This is probably indicative of a left-lateral shear motion parallel to the strike of the dyke segments, produced by a translational dilation component and possibly the frictional effects of magma propagation upwards and towards the south as described previously (Figure 5.5).

5.4.3 Effect of Dilation on Host Rock Minerals

The mechanism described above for the formation of a blunt-ended dyke assumes dilation accommodation via movement along shear fractures. It would be expected that such displacement along shear fractures in the region between the offset dyke segments would induce strain in the host rock on the outer edges of the segments, opposite the zone of shear fracture displacement. Such effects are visible on a microscopic level for the region of host rock shown in Figure 5.8. The host rock is a medium-grained dolerite composed of clinopyroxene (augite) and plagioclase. Dyke dilation resulted in straining of plagioclase grains as shown in Figure 5.8. Strain effects include the bending of elongate grains, the production of mechanical twins, and the formation of subunits within bent/rotated /strained grains (Figure 5.9), similar to the effect detailed in pyroxenes from a granophyric gabbro from the Lebombo region (Saggerson and Logan, 1988).

Figure 5.9. *Subunit development in a strained plagioclase grain (surrounded by pyroxene) against the outer edge of a dilating dyke segment (Figure 5.8) at the 345m mark in Figure 5.2. Subunits display individual twinning laws.*

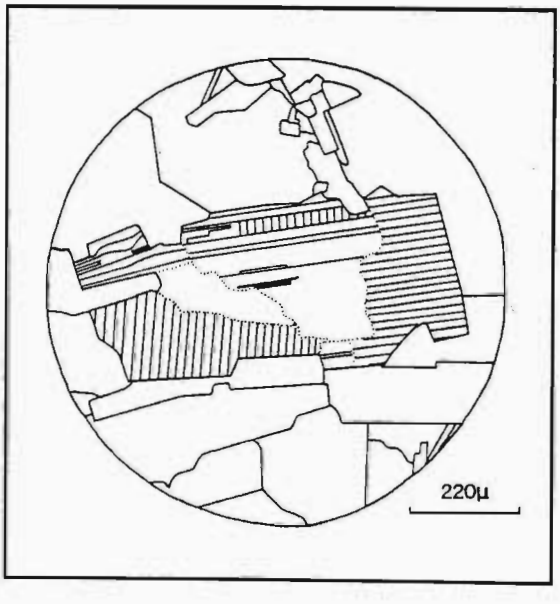

Work on pyroxenes suggested lattice defect migration to planes corresponding most closely to directions of maximum stress (Saggerson and Logan, 1988). Perhaps a similar effect is occurring in the plagioclase here, with different subunits obeying different twin laws as a result of stress concentration. The formation of mechanical twins results from simple shear of the lattice on the twin glide in the twin glide direction (Tullis, 1975). Successive

atomic planes parallel to the twin glide plane are displaced over one another, as may be occurring in specific subunits in Figure 5.9. Mechanical twins may involve mirror-imaging across a twin plane, as is demonstrated by plagioclase grains exhibiting a "herringbone" effect, caused by a number of twins being rotated and thus reflected across a twin plane oblique to them (Figure 5.10).

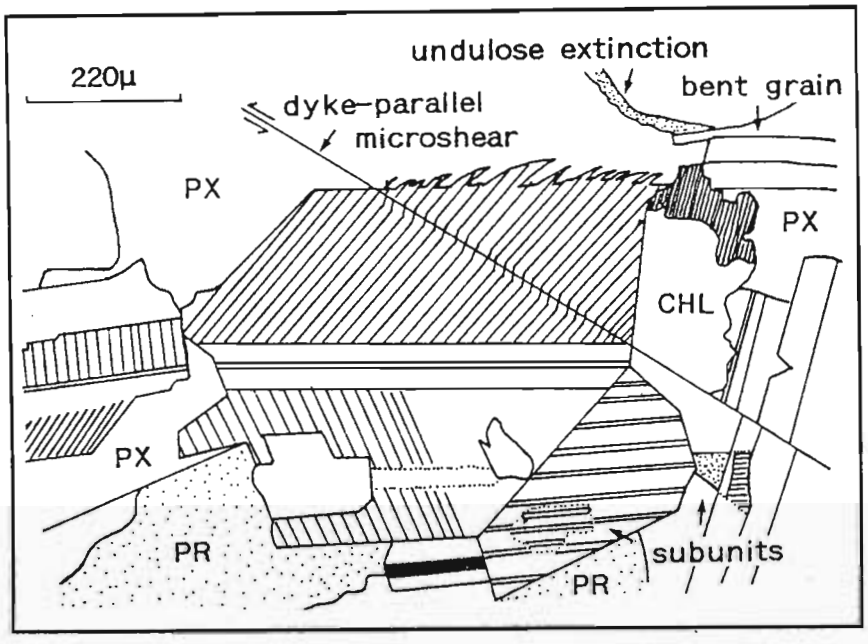

Figure 5.10. *"Herringbone" effect in plagioclase due to mechanical deformation across a suitably oriented twin plane. PX = pyroxene, CHL = chlorite, PR = prehnite. All other grains are plagioclase. Note the subunit development, undulose extinction bands, and plagioclase grain bending. Locality: 345 m mark in Figure 5.2.*

Additional effects observed in plagioclase include grain annealing, sericitisation and a thermal-induced alteration to prehnite. Deformation is minimal in the pyroxene grains. A small amount of grain bending and subunit development has occurred. The most visible effect is the production of an undulatory extinction. Alteration is by chloritisation, and is most common adjacent to the offset and cataclasis zone, where the pyroxene grains are strained.

5.5 Chemical Controls on Fracture Development

The importance of magmatic fluid effects at the tip of a propagating fracture was suggested in section 2.2.5. Pollard (1987) recognised the need for the investigation of the contact and near-tip regions of dykes in order that the conditions of temperature, pressure, and chemical environment during propagation might be evaluated. Thus far,

aspects of fracture development have been considered in terms of stress conditions and the mechanical properties of the fractured materials. The role of chemical conditions around a propagating tip is poorly understood. The possibility exists that magmatic fluids preceding the magma influx at a fracture tip interact with the host rock in a way that is conducive to the production of a chemically weakened propagation route. This might be assumed to be an effective method of fracture propagation where the driving pressure is not large enough to mechanically fracture the host rock. The chemical environment ahead of the tip of the propagating horn in Figure 5.5 has been analysed using an electron microprobe, so that chemical changes associated with fracture development may be examined. The geochemical analyses are listed in Appendix 4. Chemical analyses were performed and documented as a function of the distance from the fracture passing through the mineral grain (plagioclase or pyroxene) so that changes in chemistry may be recognised in the proximity of fracture.

5.5.1 Fracture of Plagioclase

The trends in fractured plagioclase grains are decreases in CaO and increases in Na_2O, FeO and MgO moving towards the fracture. SiO_2 and Al_2O_3 variations are less well defined, although the latter usually displays a slight decrease within 6 microns of the fracture. MgO values decrease between 50 and 20 microns approaching the fracture but then increase again within 6 microns of the fracture. This may be an indication of MgO mobility towards the region of fracture from a zone of radius 20 microns from the fracture tip. Figure 5.11 illustrates chemical changes in the vicinity of a fracture, expressed relative to the CaO concentrations. The effect of MgO behaviour is well demonstrated in the CaO/MgO graph.

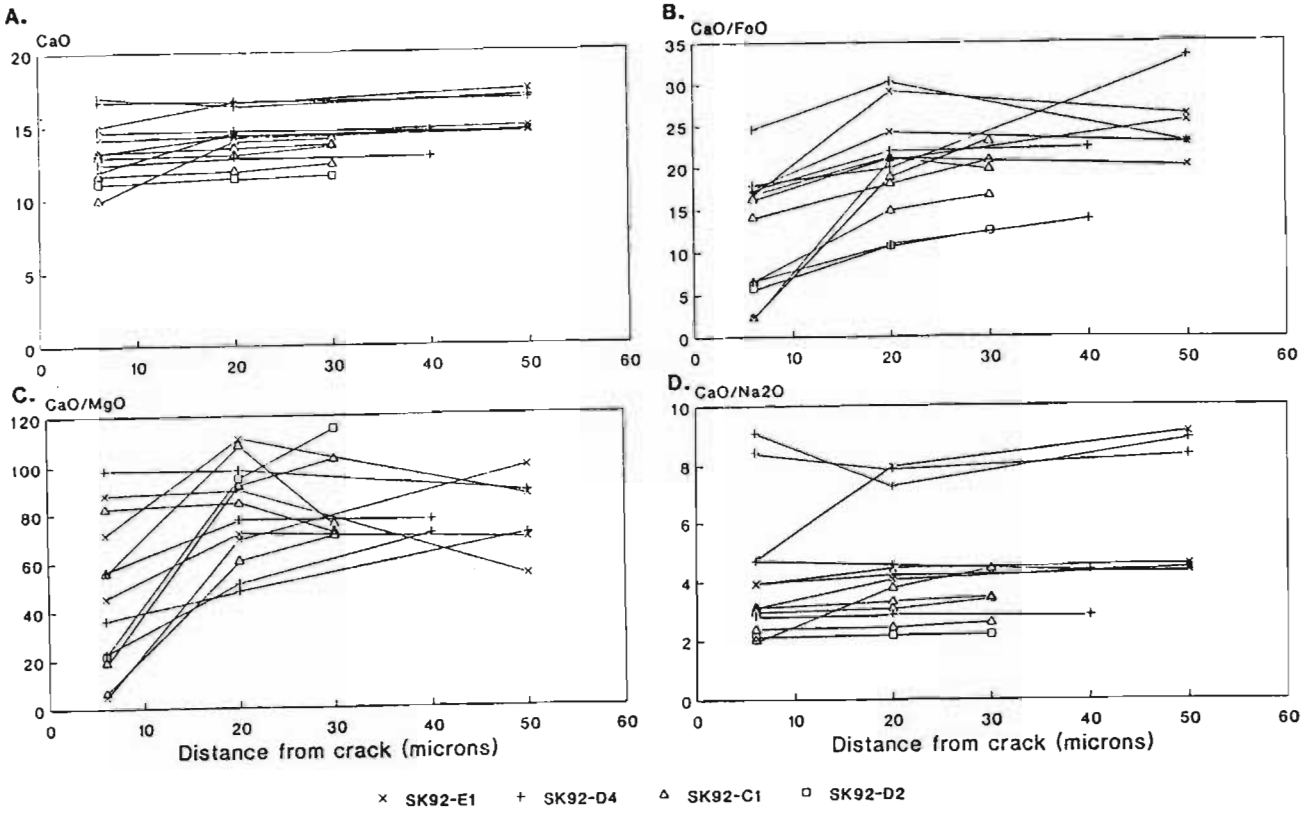

Figure 5.11. *Chemical variations in fractured plagioclase as a function of distance away from the fracture. A. CaO (wt %) variation. B. CaO/FeO variation. C. CaO/MgO variation. D. CaO/Na_2O variation.*

5.5.2 Fracture of Pyroxene

Geochemical variations in pyroxene adjacent to fracture zones are less well defined than the plagioclase trends. Variations are generally very slight and the trends in specific elements may be variable from grain to grain. In most cases, increasing proximity to the fracture is associated with slight decreases in the CaO content and an increase in FeO within 6 microns of the fracture. The MgO and Al_2O_3 values show little to no variation. Geochemical variations in pyroxene grains are displayed in Figure 5.12, showing slight increases in FeO/MgO and Al^{3+}/Mg^{2+} moving towards the fracture.

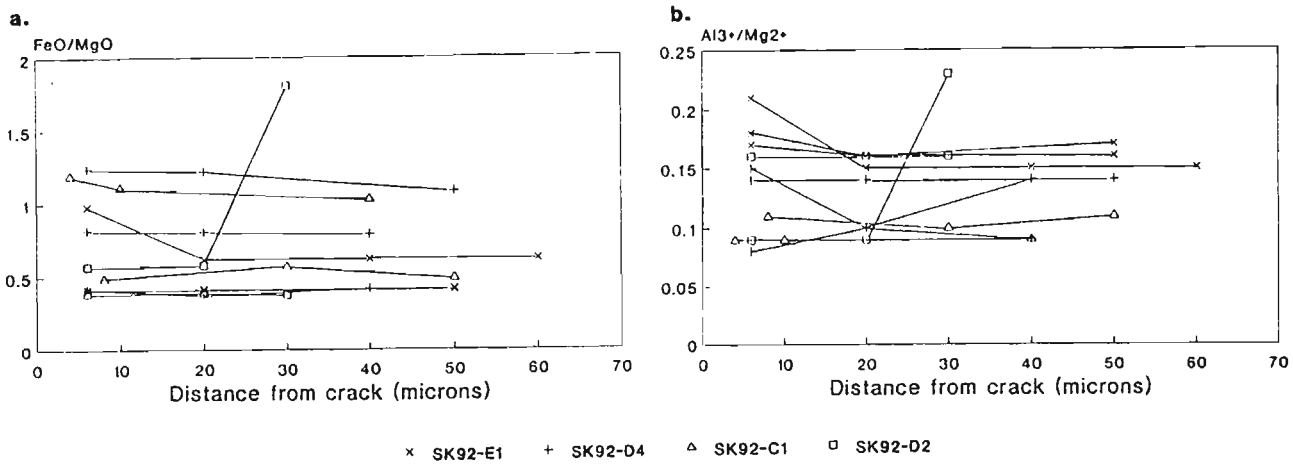

Figure 5.12. *Geochemical variations in pyroxene grains in the vicinity of a through-going fracture. (a) FeO/MgO variation. (b)* Al^{3+}/Mg^{2+} *variation.*

5.5.3 Discussion

From Figures 5.11 and 5.12, it can be seen that fractures advancing ahead of a propagating intrusion tip are associated with geochemically altered minerals. The problem posed by this observation is the actual timing of this geochemical change induced in the plagioclase and, to a lesser extent, pyroxene grains. Ion-enriched magmatic fluids might be expected to precede an advancing magma front, and fluid-rock interactions may well occur in a way that is conducive to the promotion of fracture by lowering the fracture strength of the minerals. However, the possibility also exists that the observed chemical variations are the result of post-intrusion alteration due to fluids moving along *pre-existing* fractures. Much of the chemical change within the minerals is the result of the mobilisation of elements with a highly ionic character, such as CaO, Na_2O and MgO, perhaps induced by ion-enriched magmatic fluids, however, the exact cause of the chemical changes, and the impact on the fracture susceptibility cannot be conclusively determined.

5.6 Dynamics of Magma Flow in a Thin Fissure

5.6.1 Introduction

The dynamics of magma flow in a dilating fracture was introduced in section 4.6. Magma flowing through a fissure has the greatest velocity gradient and the highest rate of shear along the fissure walls (Komar, 1976; Barrière, 1976; Ross, 1986; Ildefonse *et al.*, 1992). Such high rates of shear will frequently induce a preferred orientation of crystals with suitable aspect ratios (Roberts and Sanderson, 1971; Smith, 1987; Allard and Benn, 1989; Benn and Allard, 1989). These preferred orientations may be preserved as the magma chills against the country rock.

Determination of flow orientations may be deduced from information on the crystal orientations (Tweto, 1951; Ross, 1986; Platten and Watterson, 1987) as was performed for the dolerite sills along the Mhlatuze River in section 4.6. Another effect of hydrodynamic forces in a flowing magma is flow differentiation (Bhattacharji, 1967; Barrière, 1976) whereby phenocrysts are concentrated at fissure centres by either the wall effect, the Magnus effect, or the Bagnold effect. This is most effective in narrow fissures.

In this section, shape-preferred orientations of phenocrysts in glassy dykes from the Rooi Rand Dyke Swarm will be examined so that flow effects may be recognised, and flow directions determined. This will be accomplished via digital analysis of microscope thin sections in order that a full statistical analysis may be made of the orientations of crystals of variable aspect ratio.

5.6.2 Magma Flow Effects in a Thin Fissure

Digital analysis of microscope thin sections was performed using the KONTRON VIDAS system at the Electron Scanning Microscope Unit at the University of Natal at Pietermaritzburg. A video camera attached to a polarizing microscope conveys an image to a computer monitor that is connected to the VIDAS program. VIDAS then converts the camera image into a digital image on the monitor screen. The digital image may then be manipulated via various command functions that clarify objects, such as by sharpening the boundaries and discriminating objects from the background, and will allow for the selection of specific objects for digital analysis. Such operations were performed on thin sections taken from Rooi Rand Dyke samples using a macro program specifically constructed for this purpose. The macro is given in Appendix 5 together with an explanation of VIDAS commands.

Digital analysis can be used to demonstrate the effects of flow differentiation in a thin fissure. Figure 5.13 provides photographic evidence of flow effects in a 16mm thick fissure, showing alignment of microphenocrysts in a glassy groundmass near the margins of the fissure, and random orientations together with a flow differentiation-induced volume increase of microphenocrysts towards the centre of the fissure.

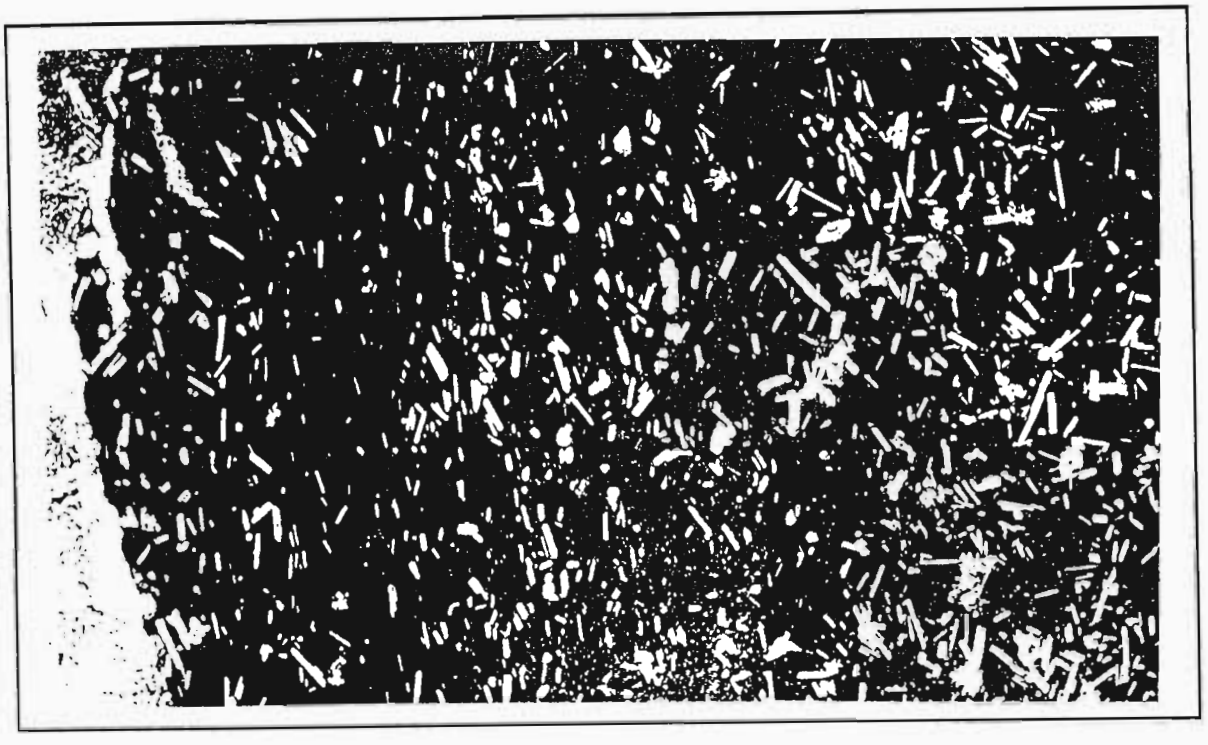

Figure 5.13. *Photographic representation of magma flow effects from the margin to centre of a 16 mm glassy dolerite dykelet. Microphenocryst alignment is greatest along the margin (left), becoming more random towards the dykelet centre where the volume of microphenocrysts is increased by flow differentiation.*

Such magma flow effects may be demonstrated by digital analysis. The histograms of Figure 5.14 illustrate the orientations of microphenocrysts from the margin to centre of the dykelet shown in Figure 5.13. The variation away from the centre is evident from the peak position of the superimposed Gaussian distribution curves:

Distance from margin	Gaussian Mean
< 1 mm	89.99°
1 - 2 mm	85.06°
2 - 4 mm	85.38°
4 - 6 mm	78.99°
6 - 8 mm	79.29°

where 90° represents the angle at which point the acicular microphenocrysts are in parallelism with the dyke wall. ANGLEDMAX is defined as the angle between the positive x-axis (of the microscope cross-hair) and the DMAX orientation of the object, where DMAX is the longest diameter of an object, obtained by selecting the largest of the Feret diameters measured in thirty-two different directions (an angular resolution of 5.7°). With this resolution, acicular microphenocrysts such as those under investigation, have a DMAX which approximates to the long-axis length measured parallel to the crystal faces, and therefore ANGLEDMAX gives an accurate representation of the

orientations of microphenocrysts. From Figure 5.14, it can be seen that there is a decrease in the ANGLEDMAX mean moving away from the dyke margin, as well as a greater distribution of orientations (increasing variance) and a decreasing kurtosis. Preferred orientations are thus most common against the dyke margins where the flow velocity and the rate of shear is greatest. Orientations are more random at the dyke centre due to a decreased flow velocity and shear rate, and probably also due to an increased amount of inter-phenocryst interaction induced by flow differentiation effects.

Microphenocryst orientations around the offset region of the en echelon dyke segments illustrated in Figures 5.5 and 5.8 are illustrated in Figure 5.15. The preferred, dyke margin-parallel orientation of microphenocrysts is evident against the dyke walls, becoming more random towards the centres. Larger phenocryst concentration at the dyke centres is probably due to flow differentiation. The patterns defined by microphenocryst orientations is often dictated by flow conditions around the larger phenocrysts, and suggests flow to be laminar against the dyke walls, but more turbulent at the phenocryst-enriched centres.

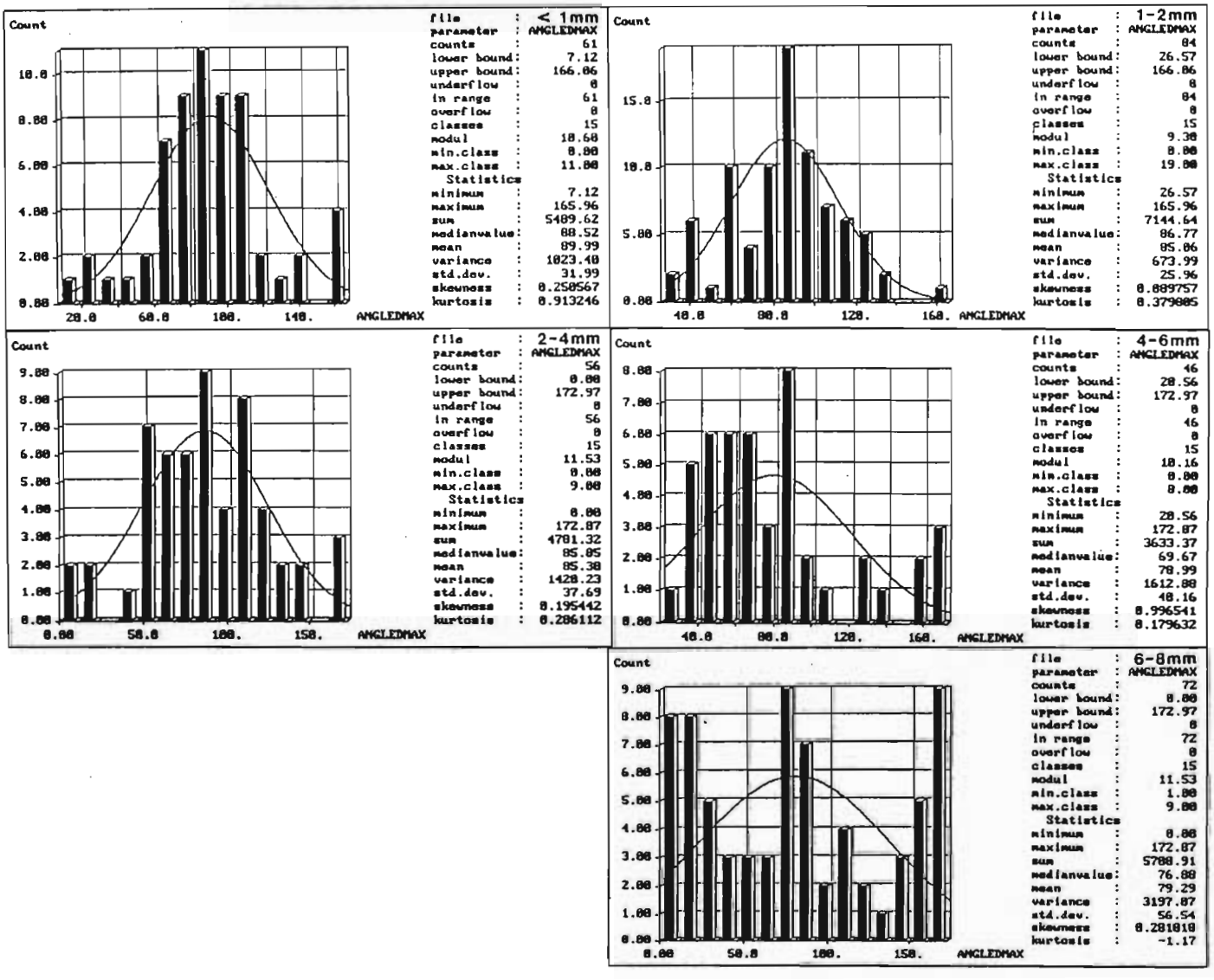

Figure 5.14. *Results of digital analysis of the dyke in Figure 5.13 for various distances from the dyke wall, as labelled. Histograms display the ANGLEDMAX population versus frequency of occurrence. Micro-phenocrysts parallel the dyke walls where ANGLEDMAX = 90^{0}. Preferred orientations are most common against the dyke wall, whereas orientations are more random towards the dyke centre.*

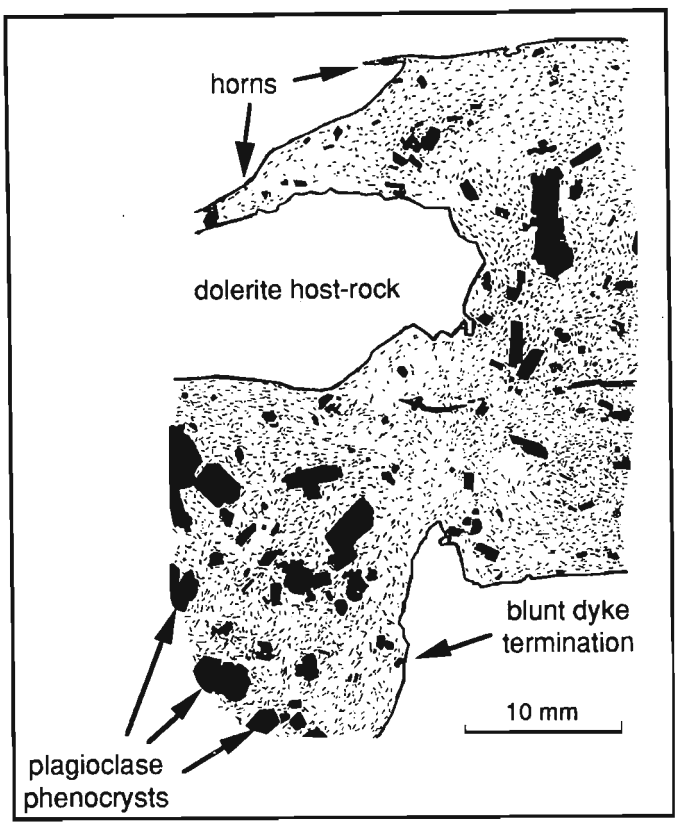

Figure 5.15. *Pattern of phenocryst and microphenocryst distribution and orientation at a point of offset of two en echelon dyke segments, as shown in Figure 5.8.*

5.6.3 Flow Direction Determination from Digital Analysis

In the previous chapter, flow directions were calculated for dolerite sills along the Mhlatuze River using the method of phenocryst long-axis orientations, and shear-sense deductions along the lower contact via the method of Benn and Allard (1989). Determination of flow directions was performed using thin sections taken along the chilled sill contact, where rapid cooling preserves the flow fabric defined by the phenocrysts aligned under high-shear conditions. In the case of sills, absolute flow directions are difficult to determine because the possible horizontal flow sense suggested by the flow fabric may be either one of two opposing directions along this fabric. The Benn and Allard (1989) method is thus an essential procedure in the determination of an absolute flow direction. In the case of dykes, however, it may usually be assumed that the flow sense is upward (unless phenocryst orientations indicate lateral magma movement), and thus an absolute flow direction may be deduced from the flow fabric. This assumes no post-emplacement strike-parallel rotation or tilting of the dykes. Measurements must again be made from thin sections taken against the chilled margins, where the high rates of shear produce a dyke wall-parallel alignment.

Before a digital analysis of flow direction is performed on a Rooi Rand dyke, it is necessary to define the three-dimensional axes used to describe planes in space. Figure 5.16 illustrates the reference axes used to define the three orthogonal planes represented by the thin sections to be analysed.

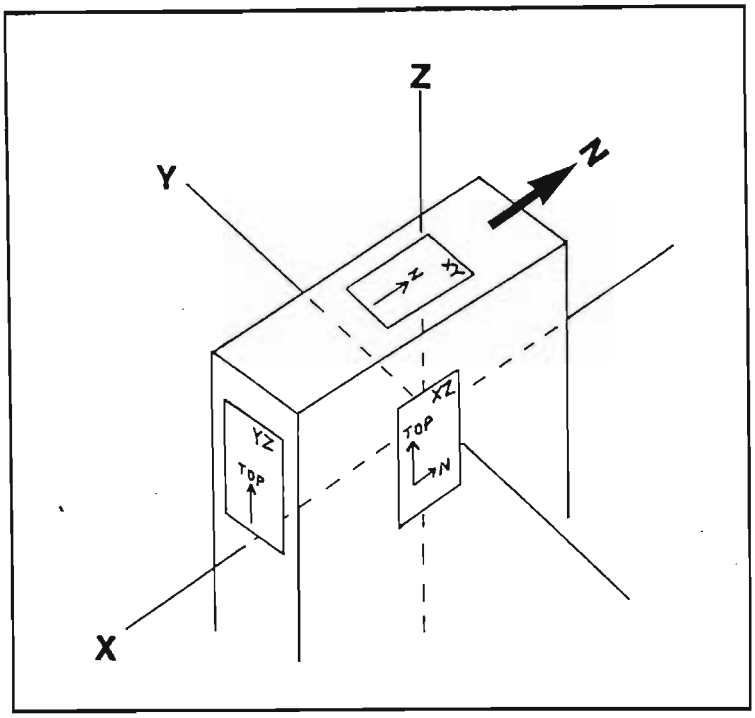

Figure 5.16. *Reference axes used to define the planes of the thin sections used for flow direction digital analysis in a Rooi Rand dyke.*

The x-axis parallels the strike of the dykes, trending north-south. The y-axis is perpendicular to both the dyke walls and vertical. The z-axis is vertical. The three planes under analysis are thus:

1. XY : occurs in the horizontal plane. The ***north*** direction is represented by ANGLEDMAX = 90°.

2. YZ : occurs in the vertical plane, perpendicular to the dyke wall. The ***top*** direction is represented by ANGLEDMAX = 90°.

3. XZ : occurs in the vertical plane, parallel to the dyke wall. The ***north*** direction occurs for ANGLEDMAX = 0° and the ***top*** direction occurs for ANGLEDMAX = 90°. The ***south*** direction is thus represented by ANGLEDMAX = 180°.

A further point to note is that the dyke wall-parallel alignment of micro-phenocrysts increases for a decreasing aspect ratio, represented in the VIDAS system by the parameter FSHAPE, defined as the ratio DMIN/DMAX, where DMIN is the shortest Feret diameter, obtained via the same method as DMAX. Acicular phenocrysts, with much higher lengths than widths (small FSHAPE values), exhibit a greater tendency for alignment against the dyke walls. This is demonstrated in the scattergram in Figure 5.17, which plots FSHAPE versus ANGLEDMAX and displays a V-shaped pattern towards the ANGLEDMAX = 90° position, reflecting an increasing alignment with the dyke walls for a decreasing aspect ratio. Low aspect ratio phenocrysts display an additional alignment at 90° to the dyke walls, perhaps indicating grains being "rolled" along perpendicular to their lengths.

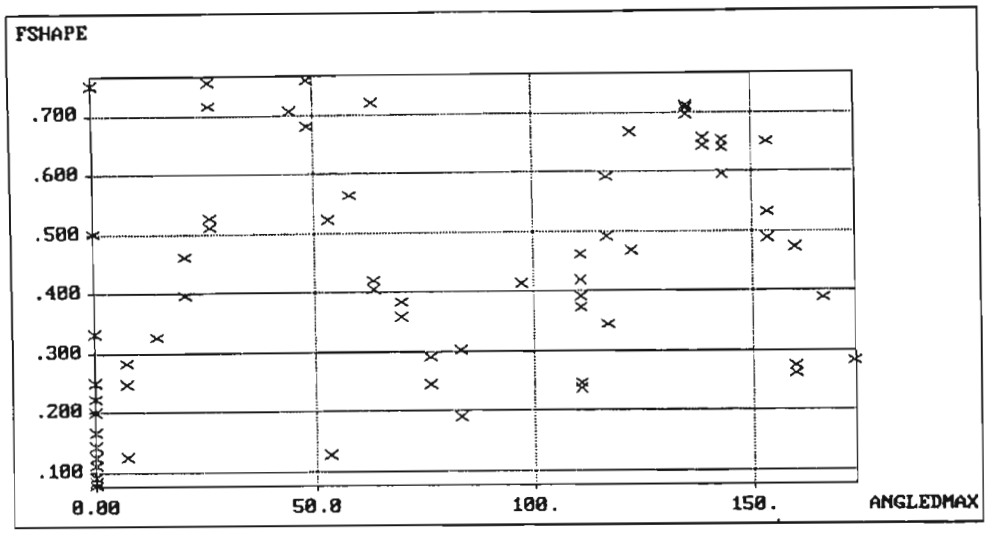

Figure 5.17. *A scattergram of FSHAPE versus ANGLEDMAX showing a V-shaped pattern towards ANGLEDMAX = 90^{o} as a result of a higher degree of low aspect ratio phenocryst alignment with the dyke walls.*

The results of phenocryst orientation digital analysis for the Rooi Rand dyke described in Figure 5.5 are presented as Figure 5.18 (data given in Appendix 6).

In the XY and YZ planes, the histograms have Gaussian curve means of 89.28^{o} and 87.32^{o} respectively, indicating a high degree of alignment of phenocrysts with the dyke wall. A dyke wall-parallel alignment occurs in both of these mutually orthogonal planes due to the thin sections representing oblique cuts through the grains. This suggests that the phenocrysts have a three-dimensional alignment with both a vertical and a horizontal component. In other words, magma flow was not vertical in this Rooi Rand dyke. This is confirmed by the results from the XZ plane, which has a histogram Gaussian curve mean of 112.84^{o}. This suggests (Figure 5.16) that magma flow was southward directed in this vicinity, at an angle of approximately 23^{o} from vertical. The southward directed flow is in agreement with the inference made earlier on the basis of the orientation of the horn and minor offsets along the dyke wall. In Figure 5.18, although it is only the XZ plane that determines the absolute flow direction, it is important that the wall-parallel alignment is confirmed in the XY and YZ plane statistics, as this gives proof of the high rate of shear induced by magma flow along the dyke margin, subsequently preserved as a flow fabric in the chill margin. Poorer results will be procured from measurements taken too far from the dyke wall, or where the chill margin has been destroyed by remelting.

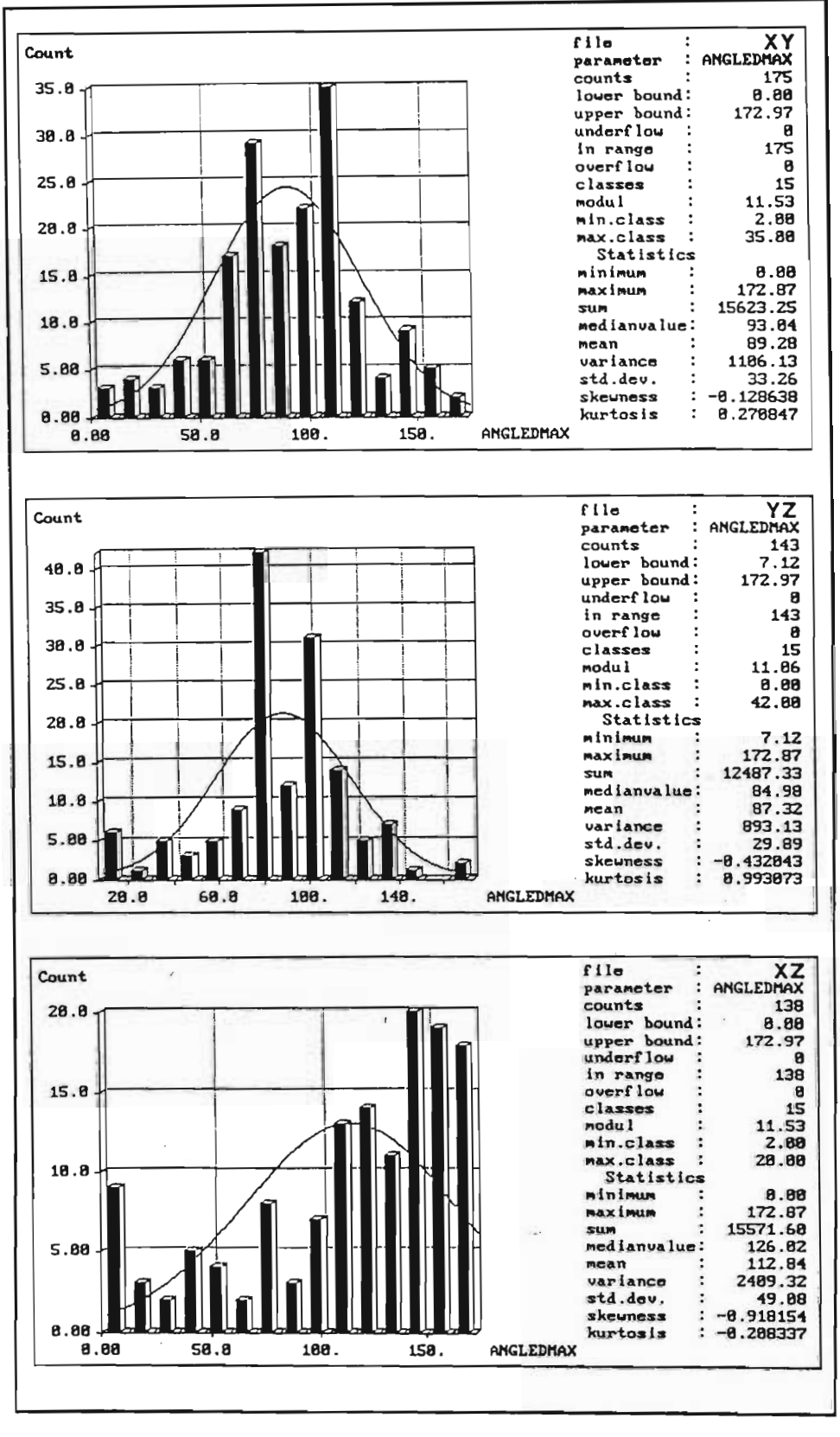

Figure 5.18. *Results of digital analysis performed on phenocryst orientations less than 2mm from the wall of the Rooi Rand dyke shown in Figure 5.5. The three graphs represent mutually orthogonal thin-sections labelled as in Fig. 5.16.*

6. DISCUSSION AND CONCLUSIONS

This investigation was performed with the aim of providing a broad-based characterization of the mechanisms by which fractures propagate and dilate to form dykes and sills. The intrusive mechanisms are frequently inherent in the geometrical nature of an intrusion. In this thesis, the mechanisms introduced by Inglis (1913) and Griffith (1924) to explain fracture propagation, subsequently developed and applied to hypabyssal intrusions by authors such as Pollard, have been described and evaluated on the basis of comparison with field examples, such as the Mhlatuze River dolerite sills and the Rooi Rand Dyke Swarm. In addition, further developments have been achieved regarding the relationship between geometrical features and magmatic flow directions, and the geochemical features of composite intrusions and fracture tip process zones.

Since 1969, the work of David Pollard on the mechanisms of intrusion has paved the way to a better understanding of the geometrical nature of dykes and sills, having inspired many authors to further such developments. The analysis of planar intrusions provided in Chapter 3 documents much of the theory behind the intrusion mechanics involved. Factors such as intrusion initiation, propagation, process zone behavior, driving pressures, intrusion rates, host rock effects, stress distributions and controls, and en echelon array development and linkage introduced the basis on which the Mhlatuze River sills were investigated.

First impressions of the dolerite sills within shales and mudstones along the Mhlatuze River, near Empangeni, suggest a simple upward stepping nature by which magma migrated towards the surface along planes of weakness. However, a comparison of the sill features with the documented characteristics of linked en echelon intrusion arrays suggests that such a mechanism may be invoked to explain the sill geometry. Features such as bent and rotated bridges and offsets indicate that separate sill segments dilated individually and subsequently underwent tip-to-tip linkage as a result of tip stress interactions. The dependence of sill tip curvature and overall sill geometry on parameters such as the sill separation and degree of overlap was also documented.

Justification for the application of the en echelon array mechanism for the sills was provided by calculations of the magmatic flow direction. Chill zone flow fabrics defined by phenocrysts indicate the magmatic flow to have been perpendicular to the plane in which the en echelon geometry occurs. Flow was thus along the offset surfaces and not upwards from one sill segment to the next. Each sill segment thus dilated individually under conditions of crustal stress that were conducive to en echelon fracture development. Linkage was a later feature that resulted in offset and rotated bridge production.

Identification of this mechanism for sill intrusion is important because it obviates the need for out-of-parent-crack-plane rotation of individual sill segments propagating ahead of a parent fracture to explain an en echelon geometry, as has been suggested by many authors (eg. Sih, 1981; Pollard *et al.*, 1982). The Mhlatuze River sills are bedding-concordant. There is no evidence that individual segments have undergone rotation. A similar observation was made for a dyke from the Rooi Rand Dyke Swarm (Chapter 5).

The true geometry of an intrusion may be misrepresented where variations occur in the outcrop face orientation. Such an effect was demonstrated for the Mhlatuze River sills, where changes in the river course caused associated variations in the outcrop nature of the sills and a distortion of the sill array geometry. Such effects must be considered during intrusion analysis.

Geochemical analysis of the dolerite sills allowed the nature of composite sills to be determined, providing a method by which individual intrusive phases may be recognised. This is a useful tool in situations where interpretations are hampered by poor outcrop occurrences.

Mechanisms of multiple dyke intrusion were described in Chapter 5. The Pongola River outcrop of the Rooi Rand Dyke Swarm was used to describe some of the features associated with such intrusion types. Individual intrusive episodes and relative ages may be predicted on the basis of chill zone relationships. Geochemical variations provide further evidence (Meth, 1991). Linkage of adjacent offset dyke segments is associated with significant cataclasis and deformation of host rock minerals. Geochemical anomalies in the process zone of propagating fractures suggests that mineral chemical changes may be facilitating fracture and linkage. It has been concluded that later intrusions are emplaced into the centres of pre-existing dykes rather than along the weaker contacts and dyke-parallel fractures as a result of uncrystallised dyke centres at depth providing paths for later intrusions (eg. Gudmundsson, 1990) that continue to propagate through the centres of crystallised dykes at higher crustal levels.

The dynamics of magma flow in a thin fissure was statistically investigated via the method of digital analysis, which demonstrated the effects of flow differentiation and the effects of shear stress decrease towards dyke centres. Higher shear stresses along the margins result in a high degree of phenocryst alignment. Such flow fabrics, when preserved as a chill margin, may be used to predict the magma flow direction in a dyke. Digital analysis of a flow fabric from a Rooi Rand Dyke suggests magma flow to have been upwards and towards the south, at approximately $23^{\square}$ from vertical. The digital analysis method introduced in this investigation may provide a fast and accurate method by which flow directions can be determined, and can greatly contribute to future intrusion mechanism investigations.

ACKNOWLEDGEMENTS

The author kindly acknowledges the assistance provided by: D. Meth, A. Bullock, T. Rebelo, D. Rickard, B. Dudley, S. Schütte, V. Hugo, R. Uken, K. Gifford-Nash, E.P. Saggerson, J. McCarthy and S. Lee. In addition, appreciation is expressed to C. Harris at the Department of Geochemistry, University of Cape Town, for assistance with the whole-rock analyses, and to E. Todd of Bay Stone Sales for allowing access to the RBQ Quarry. Helpful comments on papers based on the content of parts of this project, by C. Roering, W.M. Schwerdtner, and Agust Gudmundsson are also acknowledged. Sincere thanks to the reviewers of this thesis.

No graduate research project works its way to completion without the guidance, patience and support of an esteemed advisor. My sincerest gratitude to Mike Watkeys for introducing me to a satisfying project, and putting me on the road to future endeavours.

This project was financed in part by a FRD M.Sc. Bursary and the University of Natal Research Fund.

"Limitless are the choices of he who dares to dream."

APPENDICES

APPENDIX 1: SYMBOLS AND DEFINITIONS

A. TABLE OF SYMBOLS

t	-	shear stress
S	-	cohesive strength
μ_i	-	coefficient of internal friction
σ_n	-	stress acting normal to a surface
T_o	-	uniaxial tensile strength
T	-	angle between shear plane and maximum principal stress
ϕ_i	-	slope of Mohr failure envelope
l,L,2a	-	elliptical crack major axis (see also for sheet intrusion)
t,W,2b	-	elliptical crack minor axis
σ^r_1	-	maximum uniaxial regional tensile stress
σ^r_3	-	minimum uniaxial regional tensile stress
σ_{1c}	-	maximum compressive stress
σ_{2c}	-	intermediate compressive stress
σ_{3c}	-	minimum compressive stress
ρ	-	radius of curvature at a crack tip
T,T_a	-	tensile strength of a material
E	-	Young's modulus
$\sigma_1{}^a{}_1$	-	maximum local tensile stress at a crack tip
σ_T	-	critical tensile strength at instant of crack propagation
A	-	surface energy of a crack
ω	-	angle between long axis of a crack and σ^r_3
U_E	-	strain energy of an elastic solid
μ	-	elastic shear modulus
ρ	-	Poisson's ratio
U_S	-	potential energy of a crack surface
γ	-	surface energy of a crack surface per unit area
P	-	hydrostatic pressure acting on the internal boundaries of a dilating fracture
P_m	-	internal magma pressure
S_h	-	minimum regional compressive stress ($= -\sigma^r_1$)
S_H	-	maximum regional compressive stress
K	-	stress intensity factor
K_c	-	fracture toughness
R_{si}	-	stress intensity ratio
W,2b,t	-	thickness of a sheet intrusion
L,2a,l	-	length of a sheet intrusion perpendicular to flow direction
l_p	-	length of a sheet intrusion parallel to flow direction
ρ_m	-	magma density
ρ_r	-	average density of crustal rocks
g	-	acceleration due to gravity
P_A	-	magma pressure at the top of a vertical intrusion
η	-	shear viscosity
E_η	-	activation energy per mole
R	-	gas constant
h_o	-	maximum sill thickness
z	-	depth within the crust
L	-	width of a sill
B	-	rigidity modulus

Δs	-	remote differential compression
2∂	-	dilation thickness of a fracture
2s	-	separation between fractures
2o	-	overlap between two fractures
2k	-	centre spacing parallel to adjacent cracks
2c	-	centre spacing parallel to crack array axis
ω	-	twist angle of a fracture array
2B	-	width of a fracture array
D,∂	-	dilation
$(P-S),\Delta p$	-	magmatic driving pressure

B. DEFINITION OF PRINCIPAL STRESSES

During the course of the last few decades, and the corresponding advances in the field of fracture mechanics, there has been much conflicting usage of principal stress nomenclature in the geological literature. Initial work by authors such as Inglis (1913) and Griffith (1924) defined the principal stresses as used in the field of engineering. This involved the use of σ_1 for the maximum **tensile** stress and σ_3 for the minimum **tensile** stress. However, Robson and Barr (1964), Roberts (1970) and Pollard (1973), amongst others, use an alternative definition. The most logical reference stress axis system for rocks situated at depth is a system undergoing triaxial compression. For this reason, geologists tend to use this stress axis system, in which σ_1 is the maximum **compressive** stress, σ_2 is the intermediate **compressive** stress and σ_3 is the minimum **compressive** stress.

The equations that have become the framework of the mathematical aspects of fracture mechanics were thus developed for systems undergoing tension. Direct applicability to compressive environments has generally been inferred in subsequent developments. A problem with this, however, is that rock reacts differently under compression compared to conditions of tension (Jaeger and Cook, 1969), reacting very much weaker under tension than under compression.

In this thesis, a complete historical analysis of the topic of fracture mechanics and geological applications has required that both tensional and compressional systems be referenced at various stages. The nomenclature for the stresses (whether tensional or compressive) is consistent in this thesis, and should be referenced against the list of symbols presented above.

APPENDIX 2: PETROGRAPHIC DESCRIPTIONS

Sample localities are shown on section maps at end.

1. COARSE-GRAINED DOLERITE:

SAMPLE NO.

SK90-5 : Plagioclase: (70%) Oligoclase (altered) with myrmekitic intergrowths.
Clinopyroxene: (15%) Pigeonite (chloritised). Sub-ophitic texture.
Orthopyroxene: (15%) Possibly enstatite (chloritised).
Other : Opaque minerals include pyrite (≈1%).

SK90-6 : Plagioclase: Acicular and unoriented. Calcite alteration.
Clinopyroxene: Highly chloritised.
Orthopyroxene: Highly chloritised. Some calcite replacement.
Other: ≈10% opaques. ≈10% phenocrystic content.

SK90-7 : Plagioclase: Zoned phenocrysts. Sericitisation.
Clinopyroxene: Augite. Chloritisation. Some phenocrysts.
Orthopyroxene: Phenocrysts larger than cpx. Dark green alteration rims. Chloritisation.
Other: ≈10-15% opaques. Largest phenocrysts are plagioclase.

SK90-8 : Plagioclase: Sericitised andesine phenocrysts.
Clinopyroxene: Smallest phenocrysts. Much chloritisation of groundmass augite.
Orthopyroxene: Largest phenocrysts with dark alteration rims. Groundmass opx highly chloritised.
Other: Less than 1% opaques. No calcitisation present.

SK90-9 : Plagioclase: (75%) Andesine. Groundmass sericitised.
Clinopyroxene: (10%) Augite (chloritised).
Orthopyroxene: (5%) Hypersthene (chloritised). Dark reaction rims.
Other: Small amounts of quartz and biotite. Opaques (≈5%).

SK90-11 : Plagioclase: (70%) Labradorite. Tabular to acicular. Some small alkali feldspar grains (orthoclase). Sericite exsolution lamellae in some plagioclase crystals.
Clinopyroxene: (<10%) Augite (highly chloritised). Tabular or elongate crystals.
Orthopyroxene: (10-15%) Hypersthene. Highly chloritised.
Other: Opaques (3-5%). Amygdales (3-5%).

SK90-13 : Plagioclase: (50%) Tabular and euhedral grains (sericitised).
Clinopyroxene: (25%) Augite (fresh) defines sub-ophitic texture.
Orthopyroxene: (25%) Hypersthene (chloritised).
Other: Opaques (≈3%).

SK90-18 : Plagioclase: Fresh andesine/labradorite.
Clinopyroxene: Sub-ophitic augite (chloritised).
Orthopyroxene: None.
Other: Biotite with pyroxene nucleii. Pyrite pseudomorphs sericitised plagioclase and less commonly chloritised pyroxene.

SK90-28 : Plagioclase: (60%) Labradorite. Unoriented and tabular.
Clinopyroxene: (10-15%) Augite. Sub-ophitic texture.
Orthopyroxene: (10-15%) Enstatite. Grains are fractured.
Other: Glassy matrix (10-15%). Opaques include ilmenite. Some quartz in groundmass. Remnants of olivine have been calcitised.

2. FINE-GRAINED DOLERITE:

SK90-1 : Plagioclase: Acicular. Often altered to a dark brown colour. Flow lineation around contained phenocrysts.
Clinopyroxene: None (glassy matrix).
Orthopyroxene: None (glassy matrix).
Other: Dark brown devitrified glassy matrix. Amygdales and calcite veining. Alkali feldspar phenocrysts.

SK90-3 : Plagioclase: Too fine-grained to identify.
Clinopyroxene: None (glassy matrix).
Orthopyroxene: None (glassy matrix).
Other: Disseminated opaques (10%) are the largest crystals in the rock. Calcite + quartz amygdales with green reaction rims.

SK90-4 : Plagioclase: Acicular and altered. Flow fabric at sill base.
Clinopyroxene: Acicular and dark.
Orthopyroxene: Acicular and dark.
Other: Colourless glassy matrix. Quartz xenocrysts.

SK90-16 : Plagioclase: (60%) Labradorite. Acicular and sericitised.
Clinopyroxene: (15-20%) Augite (chloritised). Sub-ophitic texture.
Orthopyroxene: (15%?) No fresh grains. Completely chloritised.
Other: Opaques (1%). Calcite. A little biotite. Calcite amygdales (3%).

SK90-20 : Plagioclase: (60%) Acicular to prismatic. Highly sericitised.
Clinopyroxene: Almost totally chloritised.
Orthopyroxene: Almost totally chloritised.
Other: Rock contains ≈10% unaltered pyroxene and 25% chlorite. Pyrite is pseudomorphing sericitised plagioclase. Some biotite (<3%). Amygdales (≈3%) with infill as defined in main text.

SK90-21 : Plagioclase: (60%) Fresh grains (now at the centre of the sill).
Clinopyroxene: (20-25%) Augite (chloritised).
Orthopyroxene: (<5%) Hypersthene (chloritised).
Other: Green-brown biotite (5%). Chlorite (10%).

SK90-22 : Plagioclase: (65%) Acicular and slightly sericitised.
Clinopyroxene: (25%) Chloritised.
Orthopyroxene: (10%) Altered to chlorite.
Other: A little biotite (≈1%). Some phenocrysts.

SK90-23 : Plagioclase: Very fine-grained acicular plagioclase. Phenocrysts are sericitised.
Clinopyroxene: None (glassy).
Orthopyroxene: None (glassy).
Other: Glassy groundmass. Calcite amygdales ringed by glass.

SK90-24 : Plagioclase: (65-70%) Fresh plagioclase grains.
Clinopyroxene: (25%) Very little chloritisation.
Orthopyroxene: None recognised.
Other: Green-brown biotite (5%). Chlorite (<3%).

SK90-25 : Plagioclase: Acicular and sericitised.
Clinopyroxene: Almost totally altered to chlorite.
Orthopyroxene: Almost totally altered to chlorite.
Other: Scattered calcite in groundmass, and in amygdales.

SK90-26 : Plagioclase: (60%) Tabular and fresh.
Clinopyroxene: (20%) Augite.
Orthopyroxene: Highly chloritised (chlorite 5-10%).
Other: Green-brown biotite (10%). Pyrite (5%) pseudomorphing sericitised plagioclase. Amygdales with usual mineral assemblage.

3. XENOLITHIC DOLERITE

SK90-27 : Plagioclase: Sericitised, tabular, randomly oriented grains.
Clinopyroxene: No fresh cpx observed.
Orthopyroxene: Hypersthene altering to chlorite.
Other : Accessory minerals are sphene, hematite and pyrite. Dolerite component comprises ≈40% of rock volume. Xenocrysts of quartz and orthoclase. Quartz is embayed and exhibits strained extinctions. Disaggregated grains show optical continuity. Feldspar grains are highly disaggregated and calcitised.

4. DOLERITE QUARRY THIN-SECTIONS:

SK91Q1 : Plagioclase: (60%) Large crystals.
Clinopyroxene: (20%) Augite. Large crystals grew after plagioclase.
Orthopyroxene: (≈20%) Ill-defined small grains. Altered.
Other: Small grains of ilmenite in groundmass. Amygdales contain chlorite, thompsonite, calcite and quartz.

SK91Q2 : Plagioclase: (50%) Oligoclase/andesine (sericitised). First-formed mineral. Myrmekitic intergrowths with quartz.
Clinopyroxene: (25%) Augite. Largest crystals. Often euhedral and unaltered.
Orthopyroxene: (25%) Hypersthene. Serpentinised rims and cracks.
Other : Opaques (3%) include pyrite. Lesser biotite (<1%).

SK91Q3 : Plagioclase: (55%) Andesine. Finest component of rock. Sericitised.
Clinopyroxene: (15%) Augite (+ little titanaugite). Largest grains.
Orthopyroxene: (30%) Hypersthene. Serpentinised rims and cracks.
Other : Opaques (≈3%).

SK91Q4 : Plagioclase: (50%) Andesine. Much grain-size variation. Sericitised.
Clinopyroxene: (20%) Last formed mineral. Chloritised.
Orthopyroxene: (25%) Large grains. Sub-ophitic. Serpentinised rims.
Other : Opaques (>5%) include secondary pyrite. Small amounts of quartz juxtaposed against chlorite. Biotite (<1%).

SK91Q5 : Plagioclase: (55%) Andesine (highly sericitised). Some phenocrysts.
Clinopyroxene: (30%) Has deteriorated into a brown, shapeless mineral.
Orthopyroxene: (10%) Largest grains. Alteration to chlorite and serpentine with minor amounts of quartz as a by-product.
Other : Opaques (5%).

SK91Q6 : Plagioclase: (45-50%) Highly sericitised. Phenocrysts form glomero-porphyritic clumps with hypersthene phenocrysts.
Clinopyroxene: (35-40%) Augite, altered to brown chlorite.
Orthopyroxene: (10%) Hypersthene. Phenocrysts that settled to sill base. Glomero-porphyritic with plagioclase.
Other : Opaques (5-10%) include secondary pyrite associated with ilmenite and hematite.

SK91Q9 : Plagioclase: (≈60%)
Clinopyroxene: (20-25%)
Orthopyroxene: (15-20%)
Other : Opaques (5%)

SK91Q10 : Plagioclase: (50%) Fine-grained and sericitised.
Clinopyroxene: (30%) Largest grains. Sub-ophitic texture.
Orthopyroxene: (20%) Highly altered with serpentinised rims.
Other : Opaques (≈1%) and small amounts of biotite.

SK91Q12: Plagioclase: Very large grains. Tri-modal orientation direction.
Clinopyroxene: Augite. Very large grains.
Orthopyroxene: No fresh opx observed.
Other : Unusual alteration products. Colours are dark brown, bright orange, dull green or pale yellow. Fine-grained chlorite in the groundmass + some calcite. Ilmenite grains define a bimodal lineation trend.

SK91Q13 : Plagioclase: Altered, small, acicular crystals.
Pyroxene : No fresh pyx. Altered to green chlorite.
Other: Dolerite is xenolithic. Xenocrysts of quartz and clay. Quartz is recrystallised with 120° grain boundary triple junctions. The xenocrysts define a foliation. Also present: calcite and secondary pyrite pseudomorphing plagioclase.

SK91Q15 : Plagioclase: Highly altered, acicular, light brown grains.
Pyroxene : Small amount of augite. Mostly altered to a fibrous, green chlorite.
Other: Xenolithic dolerite sill margin. Quartz xenocrysts are embayed. Feldspar xenocrysts are calcitised. All xenocrysts contain aligned inclusions that define a foliation. Opaque minerals grow along the foliation, and contain aligned inclusions.

SK91Q16 : Plagioclase: (55%) Sericitised labradorite.
Clinopyroxene: (30%) Augite. Altered to green chlorite along cracks.
Orthopyroxene: (≈10%) Hypersthene. Frequently unaltered.
Other: Opaques (5%) are euhedral hexagonal. Minor amounts of quartz, K-feldspar and calcite. Myrmekitic intergrowths of K-feldspar and plagioclase.

SK91Q17 : Plagioclase: (50%) Sericitised.
Clinopyroxene: (25-30%) Augite. Alteration to bright green chlorite.
Orthopyroxene: (15-20%) Hypersthene. Grains are surrounded by a ring of augite. Subsequent serpentinisation of opx cores caused a volume increasing, resulting in the augite rims becoming cracked.
Other: Opaques (<3%).

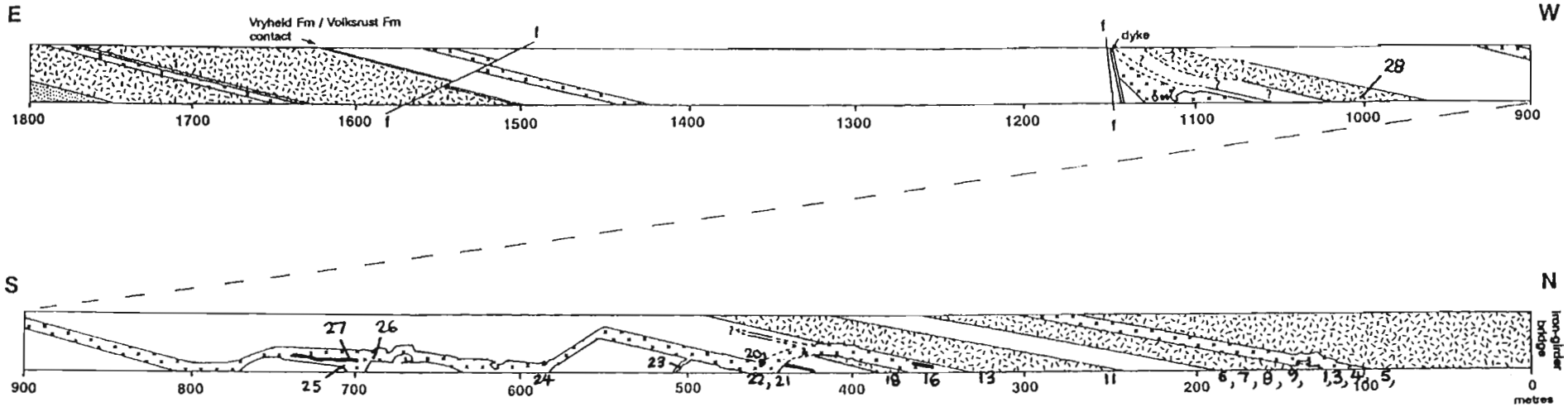

SAMPLE LOCALITIES

SK90- SERIES

LEGEND

- Volksrust Fm : siltstone, mudstone.
- Vryheid Fm : sandstone, siltstone.
- fault
- Coarse-grained dolerite
- Fine-grained dolerite
- Xenolithic dolerite

SAMPLE LOCALITIES

SK91-Q SERIES

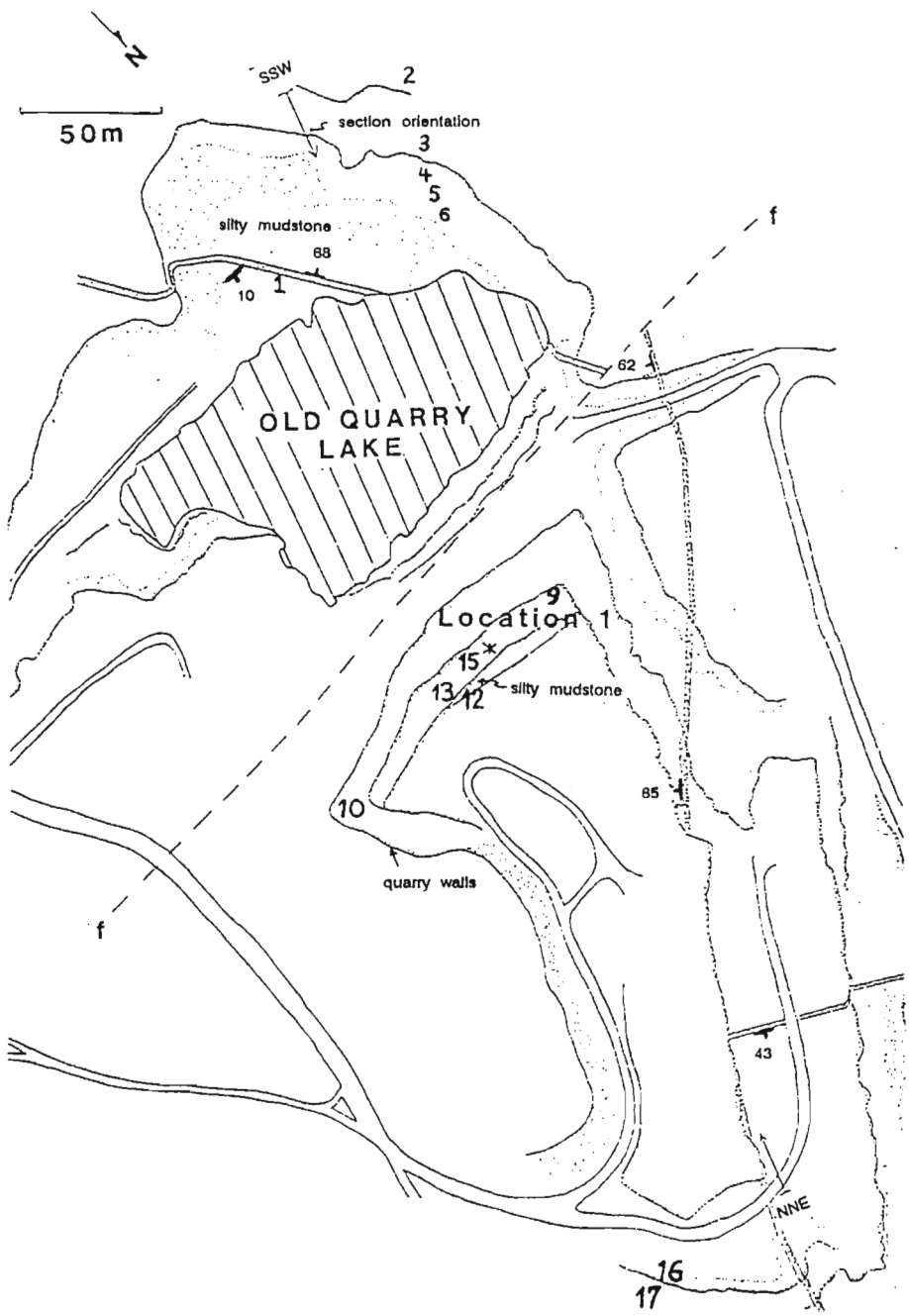

APPENDIX 3: MICROPROBE ANALYSES (EMPANGENI DOLERITES)

NOTE: All sample locations are shown on section map at end.

1. COARSE-GRAINED DOLERITE MARGINS:

1.1. Sample **SK91-4**

1.1.1. Pyroxene data: (ND = not detected)

SiO2	54.56	54.30	54.55	54.89	54.61	52.54
TiO2	0.25	0.26	0.25	0.23	0.24	0.46
Al2O3	1.38	1.26	1.10	1.09	1.16	1.35
Cr2O3	0.19	0.18	0.13	0.11	0.11	ND
FeO	13.43	13.52	13.46	13.59	13.88	13.92
MnO	0.25	0.28	0.36	0.31	0.29	0.35
MgO	28.13	27.91	28.06	28.40	27.50	16.98
CaO	2.17	2.11	2.21	2.26	2.25	14.61
Na2O	ND	ND	ND	ND	ND	0.18
K2O	ND	ND	ND	ND	ND	ND
TOTAL	100.36	99.82	100.12	100.88	100.04	100.39
WO	4.17	4.09	4.24	4.30	4.35	29.59
EN	75.28	75.08	75.01	75.08	74.19	47.85
FS	20.55	20.83	20.75	20.62	21.46	22.56

1.1.2. Plagioclase data:

Na2O	4.03	4.03	4.58	3.33	3.43	3.40	3.69
K2O	0.24	0.27	0.22	0.14	0.19	0.17	0.21
SiO2	53.73	54.43	55.63	52.83	53.01	52.91	53.48
Al2O3	29.59	28.73	28.31	30.03	30.20	29.99	29.89
FeO	0.70	0.82	0.75	0.68	0.82	0.77	0.84
MgO	0.22	0.25	0.11	0.18	0.25	0.16	0.17
CaO	12.67	11.96	11.66	13.64	13.61	13.86	13.29
TOTAL	101.18	100.49	101.26	100.83	101.51	101.26	101.57
AB	36.01	37.26	41.01	30.40	30.96	30.42	33.03
OR	1.39	1.64	1.29	0.86	1.11	1.00	1.27
AN	62.59	61.10	57.70	68.74	67.93	68.58	65.71

Na2O	3.55	3.85	4.17	3.37	3.49	3.88	3.48
K2O	0.22	0.21	0.27	0.17	0.17	0.20	0.20
SiO2	52.43	53.93	54.02	52.24	52.81	53.39	53.04
Al2O3	29.93	29.24	28.82	29.92	29.78	29.40	29.74
FeO	1.06	0.78	0.94	0.64	0.78	0.81	0.83
MgO	0.20	0.17	0.18	0.18	0.25	0.18	0.18
CaO	13.57	12.76	12.13	13.74	13.31	12.80	13.30
TOTAL	100.96	100.94	100.53	100.26	100.59	100.66	100.77
AB	31.73	34.86	37.73	30.40	31.87	35.00	31.76
OR	1.27	1.26	1.63	1.02	1.00	1.20	1.18
AN	67.00	63.88	60.64	68.58	67.13	63.80	67.06

Na2O	4.27	4.51	6.03
K2O	0.21	0.89	0.36
SiO2	54.48	55.29	58.71
Al2O3	25.24	28.52	26.40
FeO	3.28	0.96	0.83
MgO	1.41	0.11	0.06
CaO	11.11	10.23	8.58
TOTAL	100.00	100.51	100.97
AB	40.49	41.97	54.78
OR	1.31	5.47	2.13
AN	58.21	52.56	43.08

1.2. Sample **SK91-6**

1.2.1. Pyroxene data:

SiO2	51.06	51.07	51.27	52.59	51.53	51.06
TiO2	0.84	0.47	0.57	0.48	0.63	0.76
Al2O3	1.57	0.76	1.76	1.67	0.93	1.92
Cr2O3	ND	ND	ND	ND	ND	ND
FeO	15.00	26.26	14.88	10.90	15.79	13.96
MnO	0.31	0.58	0.34	0.26	0.33	0.31
MgO	12.98	15.79	15.21	16.28	12.72	14.25
CaO	18.30	4.85	16.35	18.14	18.10	17.60
Na2O	0.23	0.10	0.24	0.20	0.23	0.26
K2O	ND	ND	ND	ND	ND	ND
TOTAL	100.29	99.88	100.62	100.52	100.26	100.12
WO	37.88	10.15	33.10	36.64	37.41	36.24
EN	37.38	45.98	42.84	45.76	36.57	40.81
FS	24.74	43.86	24.06	17.60	26.01	22.94

1.2.2. Plagioclase data:

Na2O	3.90	4.08	4.02	4.40	5.33	6.11	5.15
K2O	0.23	0.23	0.22	0.24	0.36	0.41	0.34
SiO2	53.63	54.10	53.92	53.75	56.04	57.49	55.42
Al2O3	29.41	29.01	28.31	28.72	27.09	25.91	27.53
FeO	0.64	0.66	1.80	0.90	0.76	0.67	0.89
MgO	0.14	0.11	0.35	ND	0.08	ND	0.08
CaO	12.83	12.47	11.58	11.80	10.06	8.77	10.67
TOTAL	100.78	100.66	100.20	99.81	99.72	99.36	100.08
AB	34.99	36.67	38.02	39.72	47.91	54.45	45.68
OR	1.37	1.34	1.38	1.42	2.13	2.39	2.00
AN	63.64	61.99	60.60	58.85	49.95	43.16	52.32

2. COARSE-GRAINED DOLERITE CENTRES:

2.1. Sample **SK91-11**

2.1.1. Pyroxene data:

SiO2	54.14	52.02	50.84	51.31	51.00	50.11	51.23
TiO2	0.28	0.51	0.65	0.47	0.54	0.54	0.50
Al2O3	1.24	1.89	2.07	1.77	1.75	1.88	1.79
Cr2O3	0.12	ND	ND	ND	ND	ND	ND
FeO	15.55	10.10	13.02	10.68	10.93	11.81	10.04
MnO	0.33	0.23	0.33	0.24	0.25	0.27	0.21
MgO	26.20	16.84	15.60	16.54	16.37	15.43	16.80
CaO	2.20	18.34	17.58	18.24	18.13	18.65	18.53
Na2O	ND	0.20	0.26	0.19	0.24	0.23	0.21
K2O	ND	ND	ND	ND	ND	ND	ND
TOTAL	100.06	100.13	100.35	99.34	99.21	98.92	99.31
WO	4.30	36.81	35.38	36.64	36.53	37.64	37.13
EN	71.41	47.01	43.66	46.23	45.88	43.33	46.82
FS	24.29	16.18	20.96	17.13	17.60	19.03	16.05

SiO2	50.76	52.88	52.89	52.61
TiO2	0.68	0.43	0.49	0.52
Al2O3	2.09	1.80	2.03	2.00
Cr2O3	ND	ND	ND	0.10
FeO	14.51	8.91	9.25	9.11
MnO	0.45	0.24	0.26	0.28
MgO	14.72	17.18	16.78	16.71
CaO	17.03	19.03	18.93	19.28
Na2O	0.26	0.22	0.23	0.23
K2O	ND	ND	ND	ND
TOTAL	100.50	100.69	100.86	100.84

WO	34.63	38.01	38.09	38.67
EN	41.62	47.72	46.97	46.63
FS	23.75	14.27	14.94	14.70

2.1.2. Plagioclase data:

Na2O	5.75	5.72	6.04	3.96	3.90	5.41	3.66
K2O	0.41	0.43	0.41	0.19	0.17	0.32	0.20
SiO2	57.74	57.64	58.24	54.12	53.66	57.25	53.30
Al2O3	26.72	26.68	26.51	29.65	29.90	27.64	29.98
FeO	0.74	0.77	0.70	0.78	0.87	0.69	0.75
MgO	ND	0.05	0.06	0.13	0.10	0.09	0.12
CaO	9.12	9.15	9.04	12.60	12.91	10.23	13.10
TOTAL	100.48	100.44	101.00	101.43	101.51	101.63	101.11
AB	51.99	51.72	53.40	35.83	34.97	47.97	33.14
OR	2.41	2.57	2.42	1.13	0.98	1.89	1.22
AN	45.60	45.71	44.18	63.04	64.04	50.13	65.64

Na2O	3.73	3.90	3.40	3.53	3.36	4.63	3.67
K2O	0.18	0.19	0.14	0.15	0.17	0.24	0.19
SiO2	53.07	53.87	52.01	52.99	51.62	55.22	53.08
Al2O3	29.91	29.27	26.93	30.27	30.07	28.35	29.62
FeO	0.83	0.85	3.37	0.79	1.06	0.88	0.93
MgO	0.12	0.08	1.46	0.09	0.08	0.09	0.11
CaO	13.18	12.69	13.09	13.35	13.54	11.23	13.01
TOTAL	101.02	100.85	100.40	101.17	99.90	100.64	100.61
AB	33.53	35.31	31.66	32.08	30.67	42.16	33.42
OR	1.07	1.15	0.88	0.88	1.01	1.42	1.12
AN	65.40	63.54	67.46	67.04	68.32	56.43	65.46

Na2O	3.91	4.25	7.11
K2O	0.16	0.20	0.73
SiO2	52.97	53.61	61.46
Al2O3	29.33	28.89	23.82
FeO	0.94	1.02	0.80
MgO	0.12	0.09	ND
CaO	12.72	12.10	6.00
TOTAL	100.15	100.16	99.92
AB	35.40	38.37	65.15
OR	0.98	1.20	4.43
AN	63.62	60.43	30.43

2.2. Sample **SK91-13**

2.2.1. Pyroxene data:

SiO2	50.18	50.00	53.32	52.87	54.26	54.10	50.75
TiO2	0.36	0.37	0.34	0.35	0.21	0.20	0.59
Al2O3	0.64	0.60	1.09	1.29	1.30	1.72	1.85
Cr2O3	ND	ND	ND	ND	0.13	0.20	ND
FeO	25.93	27.88	16.54	19.36	13.66	14.80	11.68
MnO	0.56	0.59	0.32	0.34	0.28	0.28	0.28
MgO	18.25	14.70	26.09	23.96	28.24	27.17	15.72
CaO	3.08	5.19	2.31	2.11	2.20	2.16	17.78
Na2O	ND	ND	ND	ND	ND	ND	0.23
K2O	ND	ND	ND	ND	ND	ND	ND
TOTAL	99.00	99.33	100.01	100.28	100.28	100.63	98.88
WO	6.27	10.83	4.46	4.14	4.19	4.18	36.29
EN	51.66	42.73	70.11	65.69	75.02	73.07	44.65
FS	42.07	46.44	25.43	30.26	20.79	22.76	19.06

SiO2	50.47	52.17	50.52	53.56	51.39
TiO2	0.73	0.49	0.72	0.27	0.34
Al2O3	1.51	1.80	1.61	1.38	0.86
Cr2O3	ND	ND	ND	0.15	0.10
FeO	15.17	10.05	16.70	13.95	22.65
MnO	0.38	0.24	0.36	0.37	0.36
MgO	13.69	16.97	12.50	27.30	21.93
CaO	17.47	18.09	17.24	2.53	1.99
Na2O	0.24	0.20	0.28	ND	ND
K2O	ND	ND	ND	ND	ND
TOTAL	99.69	100.01	99.93	99.51	99.62
WO	35.90	36.37	35.96	4.90	3.94
EN	39.13	47.47	36.26	73.40	60.45
FS	24.96	16.16	27.78	21.62	35.61

2.2.2. Plagioclase data:

Na2O	3.89	3.96	4.12	3.67	3.67	4.27	5.43
K2O	0.25	0.22	0.25	0.17	0.18	0.22	0.30
SiO2	52.82	52.73	52.98	52.51	52.65	54.55	56.00
Al2O3	29.30	28.96	28.71	30.00	30.04	29.07	27.05
FeO	0.82	0.81	1.02	0.73	0.79	0.81	0.70
MgO	0.08	0.09	0.08	0.10	0.07	0.08	0.05
CaO	12.75	12.70	12.24	13.27	13.29	11.92	10.55
TOTAL	99.91	99.47	99.40	100.45	100.69	100.92	100.08
AB	35.03	35.59	37.27	33.04	32.98	38.80	47.37
OR	1.46	1.31	1.50	1.03	1.04	1.30	1.73
AN	63.50	63.10	61.23	65.93	65.98	59.90	50.90

Na2O	4.19	3.98	4.00	4.26	5.13	4.34	4.39
K2O	0.22	0.21	0.22	0.24	0.34	0.24	0.26
SiO2	53.84	52.38	53.02	54.15	56.66	53.66	53.84
Al2O3	29.29	28.88	29.02	28.54	27.52	28.24	28.23
FeO	0.86	0.81	0.80	0.78	0.79	0.86	0.91
MgO	0.06	0.11	0.09	0.08	0.06	0.09	0.10
CaO	12.31	12.51	12.55	11.88	10.14	11.70	11.58
TOTAL	100.77	98.88	99.70	99.93	100.64	99.13	99.31
AB	37.64	36.07	36.11	38.79	46.84	39.58	40.03
OR	1.32	1.28	1.32	1.46	2.06	1.41	1.58
AN	61.04	62.65	62.57	59.75	51.10	59.00	58.39

3. FINE-GRAINED DOLERITE:

3.1. Sample **SK91-8**

3.1.1. Pyroxene data:

SiO2	50.20	49.35	48.09	49.09	48.55	48.57	49.84
TiO2	0.82	0.84	1.40	1.24	1.38	0.69	0.58
Al2O3	1.15	1.03	1.57	1.66	1.47	2.10	1.49
Cr2O3	ND	ND	ND	ND	ND	ND	ND
FeO	25.06	28.28	23.55	21.72	26.22	24.85	24.23
MnO	0.55	0.56	0.51	0.47	0.52	0.50	0.53
MgO	14.68	12.71	10.00	11.93	14.83	15.30	12.54
CaO	7.01	7.44	13.66	13.75	14.83	7.33	9.14
Na2O	ND	ND	0.11	0.12	0.11	0.10	0.12
K2O	ND	ND	ND	ND	ND	ND	ND
TOTAL	99.47	100.21	98.89	99.98	100.48	99.44	98.47
WO	14.79	15.61	29.47	28.84	32.23	15.14	19.90
EN	43.05	37.12	30.00	34.82	22.37	43.98	38.00
FS	42.16	47.27	40.53	36.34	45.40	40.89	42.10

SiO2	50.43	49.37
TiO2	1.07	1.42
Al2O3	1.08	1.56
Cr2O3	ND	ND
FeO	24.81	22.88
MnO	0.47	0.41
MgO	15.81	10.78
CaO	6.37	13.88
Na2O	ND	0.12
K2O	ND	ND
TOTAL	100.04	100.42
WO	13.25	29.50
EN	45.72	31.87
FS	41.03	38.63

3.1.2. Plagioclase data:

Na2O	4.89	4.75	4.24	4.07	4.01	4.90	4.52
K2O	2.86	0.40	0.38	0.35	0.43	0.41	0.49
SiO2	56.21	56.29	55.24	54.58	55.38	55.81	55.49
Al2O3	27.20	27.18	28.35	28.84	28.47	27.09	27.90
FeO	1.67	0.98	0.57	0.53	0.58	1.69	0.62
MgO	0.22	0.21	0.11	0.09	0.07	0.34	0.07
CaO	5.88	10.60	11.72	12.16	11.88	10.28	11.22
TOTAL	98.93	100.41	100.61	100.62	100.82	100.52	100.31
AB	48.79	43.71	38.67	36.95	36.96	45.15	40.95
OR	18.79	2.40	2.27	2.09	2.58	2.50	2.91
AN	32.42	53.89	59.06	60.95	60.46	52.34	56.14

Na2O	4.33	5.15	1.40	
K2O	0.46	0.51	8.06	
SiO2	55.55	58.18	77.20	
Al2O3	28.01	26.26	11.68	
FeO	0.69	0.83	0.32	
MgO	0.07	0.09	ND	
CaO	11.37	9.46	0.31	
TOTAL	100.48	100.48	98.97	
AB	39.66	48.08	20.31	
OR	2.78	3.12	77.21	(K-feldspar)
AN	57.56	48.80	2.47	

3.2. Sample **SK91-9**

3.2.1. Pyroxene data:

SiO2	49.22	50.06	50.83	48.99
TiO2	1.18	1.09	0.77	1.14
Al2O3	1.83	1.83	1.93	1.52
Cr2O3	ND	ND	ND	ND
FeO	22.12	19.59	15.92	23.25
MnO	0.48	0.47	0.36	0.48
MgO	11.98	13.52	15.33	12.38
CaO	12.30	12.79	13.65	11.01
Na2O	0.10	0.12	0.11	0.11
K2O	ND	ND	ND	ND
TOTAL	99.21	99.47	98.90	98.88
WO	26.38	27.06	28.62	23.55
EN	35.76	39.80	44.74	36.83
FS	37.86	33.14	26.65	39.62

3.2.2. Plagioclase data:

Na2O	4.23	4.27	4.11	4.66	4.40	3.96
K2O	0.47	0.46	0.45	0.41	0.56	0.40
SiO2	55.68	55.31	54.94	56.36	55.60	54.73
Al2O3	27.04	27.29	26.97	27.01	26.58	27.36
FeO	0.74	0.81	0.80	1.57	0.67	0.64
MgO	0.14	0.17	0.25	0.36	0.15	0.18
CaO	11.13	11.35	11.16	10.59	10.84	11.72
TOTAL	99.43	99.66	98.68	100.96	98.80	98.99
AB	39.57	39.39	38.87	43.22	40.92	37.02
OR	2.87	2.77	2.80	2.53	3.41	2.48
AN	57.57	57.85	58.33	54.25	55.67	60.51

4. LIST OF ABBREVIATIONS:

ND = not detected
EN = enstatite
AB = albite
AN = anorthite
WO = wollastonite
FS = ferrosilite
OR = orthoclase

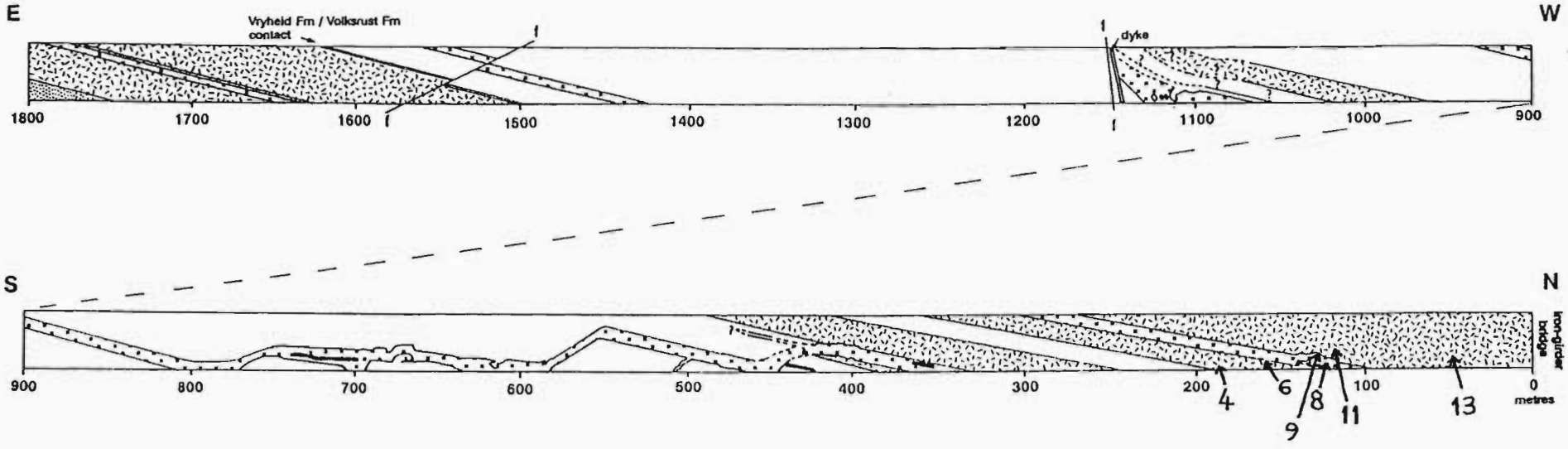

SAMPLE LOCALITIES

SK91- SERIES

LEGEND

- Volksrust Fm : siltstone, mudstone.
- Vryheid Fm : sandstone, siltstone.
- fault
- Coarse-grained dolerite
- Fine-grained dolerite
- Xenolithic dolerite

APPENDIX 4 : DYKE TIP MINERAL MICROPROBE DATA

A) PLAGIOCLASE DATA

NOTE: Distance from crack is in microns

SLIDE SK92-E1:

CaO	Na_2O	FeO	SiO_2	MgO	Al_2O_3	Crack dist.
14.98	3.14	0.90	51.09	0.21	30.86	6
16.62	2.09	0.57	48.38	0.15	30.59	20
17.39	1.91	0.66	48.15	0.20	28.99	50
14.06	3.60	0.81	52.12	0.31	28.83	6
14.29	3.39	0.59	51.95	0.20	28.45	20
14.47	3.34	0.63	51.73	0.21	28.05	50
13.16	4.15	0.78	53.02	0.15	28.62	6
14.38	3.53	0.68	51.91	0.16	28.38	20
14.58	3.29	0.72	51.78	0.27	27.64	50
11.87	3.01	4.96	48.51	2.41	28.26	6
14.55	3.26	0.70	51.18	0.21	28.35	20
14.84	3.26	0.58	50.99	0.15	26.22	50

SLIDE SK92-D4:

CaO	Na_2O	FeO	SiO_2	MgO	Al_2O_3	Crack dist.
16.98	1.91	0.51	49.48	0.24	32.06	50
16.38	2.26	0.82	49.89	0.34	30.97	20
17.02	1.87	0.95	48.89	0.47	31.46	6
16.81	2.02	0.73	48.35	0.19	30.29	50
16.69	2.12	0.55	47.95	0.17	30.13	20
16.71	1.98	0.68	47.95	0.17	30.34	6
14.61	3.34	0.65	52.32	0.19	29.38	40
14.71	3.22	0.67	51.99	0.19	29.27	20
14.65	3.12	0.85	52.04	0.26	29.29	6
12.80	4.51	0.92	54.66	0.18	27.76	40
12.83	4.45	1.18	54.19	0.25	27.94	20
12.39	4.37	1.89	54.38	0.55	27.73	6

SLIDE SK92-C1:

CaO	Na_2O	FeO	SiO_2	MgO	Al_2O_3	Crack dist.
13.67	3.95	0.69	52.74	0.19	29.51	30
13.49	4.06	0.64	52.65	0.16	29.06	20
13.15	4.19	0.81	53.06	0.16	28.79	6
14.13	3.19	0.61	51.44	0.20	29.50	30
13.94	3.68	0.74	51.69	0.23	29.50	20
9.94	4.93	4.21	52.92	1.55	26.10	6
12.31	4.75	0.74	54.59	0.12	28.37	30
11.89	4.85	0.80	54.32	0.13	27.86	20
11.61	4.86	1.77	54.79	0.61	26.85	6
13.58	4.01	0.65	53.34	0.18	29.48	30
13.00	4.21	0.72	53.06	0.12	28.83	20
12.85	4.29	0.91	53.34	0.23	28.63	6

SLIDE SK92-D2:

CaO	Na_2O	FeO	SiO_2	MgO	Al_2O_3	Crack dist.
11.49	5.25	0.92	55.40	0.10	27.60	30
11.36	5.24	1.06	55.13	0.12	27.29	20
11.04	5.17	1.91	54.60	0.51	26.18	6

B) PYROXENE DATA:

SLIDE SK92-E1:

SiO_2	FeO	CaO	MgO	Al_2O_3	Crack dist.
50.81	7.05	20.30	16.73	3.05	50
49.72	6.71	20.44	16.44	3.06	20
49.97	6.72	20.45	16.46	3.30	6
50.93	7.13	19.10	17.20	3.34	50
51.47	7.48	19.38	17.64	3.26	20
50.66	7.34	19.25	17.33	3.36	6
51.16	9.94	19.15	15.95	2.81	60
51.20	9.77	19.12	15.80	2.76	40
50.72	9.94	19.03	15.93	2.76	20
48.98	13.47	17.65	13.78	3.30	6

SLIDE SK92-D4:

SiO_2	FeO	CaO	MgO	Al_2O_3	Crack dist.
50.39	15.52	16.74	14.41	2.28	50
49.41	17.05	16.10	14.00	2.18	20
48.89	16.98	15.87	13.74	2.12	6
52.36	12.96	17.21	16.35	1.63	40
52.28	13.31	16.10	16.38	1.92	20
52.44	13.46	16.40	16.42	1.59	6
52.83	7.27	19.21	17.12	2.72	40
53.88	6.69	20.66	17.58	2.08	20
52.90	7.19	19.97	17.22	3.00	6

SLIDE SK92-C1:

SiO_2	FeO	CaO	MgO	Al_2O_3	Crack dist.
52.65	8.13	19.61	16.72	2.06	50
52.59	9.37	19.04	16.41	1.94	30
52.07	8.13	19.53	16.73	2.06	8
50.93	15.92	15.01	15.41	1.51	40
50.81	17.00	14.40	15.26	1.55	10
50.84	17.73	13.91	14.94	1.55	4

SLIDE SK92-D2:

SiO_2	FeO	CaO	MgO	Al_2O_3	Crack dist.
52.69	6.54	20.96	17.07	3.03	30
52.46	6.61	20.70	16.87	3.02	20
52.25	6.55	20.73	16.72	3.11	6
52.19	23.00	8.81	12.73	3.32	30
52.99	9.88	18.47	17.03	1.79	20
52.72	9.66	18.40	16.94	1.80	6

APPENDIX 5: VIDAS MACRO AND USER COMMAND FUNCTIONS

1. VIDAS MACRO: PHENOCRYST ORIENTATIONS IN A MAGMA FLOW

```
alpha
resetpar
clearall
clearallov
setframe "F512"
loadlut "grey"
tvchan 2,2
tvon
rgbwtbalance 1
tvinp 1
tvchan 0,0
delin 1,2,10,5,_ON
normim 2,3,1
dis2lev 3,4,64,191,_ON,_ON,1
identframe 4,5,_ON,1,512,512,0,0,_ON,_OFF,_OFF
rejectobj 5,2,0
scrap 5,6,_OFF,0,40,_ON,_ON
identify 6,7,_ON,_ON
Initobj ANGLEDMAX, FSHAPE, AREA
measobj 7,"objdb",_OFF
outlist "objdb",_OFF
outscat "objdb","ANGLEDMAX","objdb","FSHAPE",_OFF,_OFF,_ON,_ON,4.00,492.10,1.0
outhist "objdb","ANGLEDMAX",15,_OFF,_OFF,0,_ON,_ON,11.05,174.60,8.00,"","HISTOGRAM"
```

2. VIDAS USER COMMAND FUNCTIONS

ANGLEDMAX: angle between the positive x-axis and the DMAX orientation of the object, where DMAX is the longest diameter of the object, obtained by selecting the largest of the Feret diameters measured in 32 different directions (at an angular resolution of 5.7^{o}). With this resolution, acicular grains have a DMAX that closely approximates the long axis orientation parallel to the crystal faces.

FSHAPE: aspect ratio of the object, defined as DMIN/DMAX where DMIN is the shortest of the Feret diameters.

alpha: sets graphic displays to alphanumeric mode for faster operation

resetpar: erases all feature vectors defined

clearall: clears all present images

clearallov: clears the overlay plane for the entire image memory

setframe "F512": setting image size at 512 pixels

loadlut "grey": loads a look-up table from a sub-directory to define colours

tvchan 2,2: adjusts system to different input channels and input modes. Set to b/w (black & white) or RGB (red-green-blue).

tvon: initialises television

rgbwtbalance: calculates mean grey value of the image

tvinp: digitizes a single tv cycle and stores the image data

tvchan 0,0: image converted to b/w

delin: restores blurred object edges in an image

normim: increases the contrast of an image by scaling the grey levels linearly into the full dynamic range of the image memory.

dis2lev: discriminates objects from the background by setting two thresholds

identframe: selects size of frame to be analysed and rejects any objects touching the outside boundaries of the frame.

rejectobj: manual exclusion of unwanted objects

scrap: eliminates all objects smaller than a specified pixel area

identify: identifies all remaining objects by colour - any objects joined by at least one pixel will be identified as a single object.

initobj: defines the parameters to be measured

measobj: measure defined parameters

outlist: records data

outscat: scattergram representation of data

outhist: histogram representation of data

DBCREATE: creates a database

DBOPEN: opens a created database

DBCLOSE: closes a created database

DBAPPEND: appends current data to the end of a currently open file

APPENDIX 6: DIGITAL ANALYSIS DATA

1. SLIDE SK92-D4: ORIENTATION XY

Count	ANGLEDMAX	AREA	FSHAPE
1	69.44	704.00	0.304520
2	172.87	1958.00	0.661911
3	104.04	195.00	0.770674
4	159.44	505.00	0.275513
5	110.56	209.00	0.310682
6	131.19	419.00	0.443147
7	69.44	166.00	0.754951
8	148.00	287.00	0.400544
9	69.44	768.00	0.270328
10	97.12	913.00	0.420654
11	97.12	253.00	0.547888
12	53.13	400.00	0.374608
13	116.56	152.00	0.480929
14	97.12	177.00	0.717258
15	63.43	226.00	0.372263
16	57.99	319.00	0.670245
17	75.96	196.00	0.702955
18	75.96	494.00	0.487221
19	63.43	232.00	0.635114
20	82.87	461.00	0.347386
21	97.12	397.00	0.379885
22	90.00	4553.00	0.310622
23	75.96	291.00	0.609977
24	63.43	190.00	0.517675
25	57.99	109.00	0.508462
26	116.56	503.00	0.298061
27	138.81	848.00	0.267635
28	82.87	543.00	0.696888
29	57.99	261.00	0.725819
30	104.04	103.00	0.517965
31	57.99	298.00	0.564414
32	57.99	652.00	0.635889
33	104.04	865.00	0.276765
34	153.43	528.00	0.418719
35	97.12	454.00	0.354747
36	97.12	158.00	0.420598
37	0.00	272.00	0.225870
38	143.13	495.00	0.235988
39	63.43	372.00	0.587580
40	110.56	149.00	0.355512
41	53.13	643.00	0.261469
42	122.01	365.00	0.310385
43	75.96	1811.00	0.212926
44	104.04	1041.00	0.390921
45	110.56	1250.00	0.785778
46	82.87	150.00	0.761483
47	41.19	277.00	0.406932
48	63.43	171.00	0.518702
49	104.04	392.00	0.356650
50	14.04	222.00	0.332467
51	135.00	182.00	0.303735
52	110.56	337.00	0.474587
53	104.04	1393.00	0.363566
54	97.12	1001.00	0.245622
55	0.00	106.00	0.240000
56	110.56	925.00	0.342090

Count	ANGLEDMAX	AREA	FSHAPE
57	53.13	223.00	0.332839
58	75.96	239.00	0.515660
59	82.87	647.00	0.196155
60	57.99	108.00	0.564184
61	82.87	561.00	0.222846
62	116.56	249.00	0.254689
63	75.96	122.00	0.648882
64	122.01	664.00	0.408959
65	97.12	212.00	0.271087
66	122.01	361.00	0.243275
67	104.04	545.00	0.259080
68	104.04	144.00	0.520000
69	69.44	582.00	0.282390
70	45.00	528.00	0.123894
71	20.56	652.00	0.348495
72	69.44	241.00	0.478789
73	45.00	190.00	0.304220
74	159.44	103.00	0.205325
75	82.87	1814.00	0.341404
76	126.87	390.00	0.198569
77	36.87	237.00	0.333017
78	57.99	1135.00	0.420536
79	63.43	805.00	0.477472
80	26.57	592.00	0.140299
81	122.01	332.00	0.257971
82	69.44	325.00	0.280136
83	97.12	314.00	0.450170
84	110.56	203.00	0.395576
85	104.04	459.00	0.419062
86	104.04	604.00	0.570902
87	75.96	229.00	0.450317
88	69.44	495.00	0.431245
89	148.00	551.00	0.764983
90	126.87	585.00	0.562938
91	48.81	1422.00	0.522762
92	41.19	651.00	0.402762
93	110.56	316.00	0.268496
94	82.87	174.00	0.381871
95	97.12	225.00	0.441515
96	75.96	251.00	0.365086
97	104.04	223.00	0.461078
98	97.12	504.00	0.232058
99	104.04	485.00	0.289437
100	104.04	790.00	0.491699
101	75.96	689.00	0.398678
102	159.44	491.00	0.293266
103	104.04	250.00	0.518863
104	97.12	570.00	0.317627
105	97.12	706.00	0.350315
106	82.87	747.00	0.318588
107	97.12	233.00	0.289879
108	110.56	220.00	0.438290
109	75.96	542.00	0.615803
110	69.44	1174.00	0.312154
111	20.56	517.00	0.235247
112	69.44	369.00	0.562309

Count	ANGLEDMAX	AREA	FSHAPE
113	165.96	407.00	0.465898
114	97.12	405.00	0.240315
115	104.04	458.00	0.334274
116	104.04	921.00	0.554057
117	143.13	788.00	0.501844
118	90.00	2162.00	0.628423
119	69.44	3339.00	0.379631
120	138.81	379.00	0.419673
121	57.99	808.00	0.504718
122	75.96	112.00	0.647340
123	26.57	2601.00	0.484076
124	138.81	369.00	0.185045
125	116.56	624.00	0.252669
126	82.87	436.00	0.274097
127	104.04	118.00	0.545070
128	75.96	130.00	0.661242
129	90.00	2313.00	0.403844
130	69.44	501.00	0.307042
131	97.12	898.00	0.662480
132	104.04	678.00	0.408438
133	75.96	503.00	0.523965
134	104.04	2806.00	0.543552
135	104.04	892.00	0.532973
136	104.04	479.00	0.402505
137	75.96	623.00	0.446980
138	116.56	132.00	0.538812
139	110.56	422.00	0.432619
140	110.56	586.00	0.521661
141	97.12	407.00	0.265697
142	122.01	183.00	0.447963
143	110.56	164.00	0.485261
144	110.56	406.00	0.207477
145	20.56	831.00	0.296163
146	159.44	289.00	0.210675
147	97.12	406.00	0.284812
148	69.44	406.00	0.338569
149	148.00	1193.00	0.273665
150	82.87	1071.00	0.257057
151	36.87	249.00	0.389456
152	143.13	728.00	0.502012
153	63.43	2234.00	0.585242
154	57.99	115.00	0.213807
155	110.56	163.00	0.304445
156	104.04	685.00	0.455113
157	82.87	1531.00	0.139628
158	90.00	1008.00	0.382398
159	97.12	189.00	0.361845
160	63.43	1303.00	0.345070
161	122.01	287.00	0.476720
162	82.87	141.00	0.407356
163	69.44	271.00	0.653696
164	116.56	1369.00	0.491921
165	97.12	1298.00	0.217275
166	75.96	265.00	0.734406
167	32.01	297.00	0.201658
168	0.00	162.00	0.296296
169	97.12	359.00	0.407295
170	53.13	1604.00	0.393016
171	82.87	487.00	0.172141
172	82.87	1207.00	0.419840
173	53.13	636.00	0.517129
174	75.96	207.00	0.311412
175	97.12	921.00	0.138703

2. SLIDE SK92-D1: ORIENTATION YZ

Count	ANGLEDMAX	AREA	FSHAPE
1	82.87	7541.00	0.126502
2	75.96	260.00	0.123091
3	75.96	426.00	0.321178
4	110.56	379.00	0.712328
5	82.87	472.00	0.556143
6	104.04	225.00	0.432516
7	57.99	2920.00	0.514414
8	82.87	310.00	0.197075
9	116.56	108.00	0.470968
10	75.96	766.00	0.344560
11	104.04	327.00	0.505238
12	104.04	144.00	0.253629
13	90.00	1035.00	0.390968
14	14.04	320.00	0.648100
15	104.04	678.00	0.422882
16	82.87	789.00	0.329131
17	82.87	789.00	0.329131
18	126.87	200.00	0.233239
19	138.81	137.00	0.368748
20	97.12	369.00	0.472549
21	90.00	547.00	0.407912
22	90.00	218.00	0.140000
23	75.96	590.00	0.367004
24	172.87	184.00	0.389464
25	104.04	1380.00	0.153079
26	97.12	1668.00	0.175499
27	110.56	1213.00	0.269136
28	57.99	475.00	0.712885
29	41.19	798.00	0.088087
30	104.04	1124.00	0.222625
31	82.87	1297.00	0.412512
32	104.04	530.00	0.226927
33	69.44	591.00	0.203726
34	131.19	569.00	0.227742
35	97.12	232.00	0.137857
36	122.01	267.00	0.824004
37	116.56	2147.00	0.317016
38	7.12	197.00	0.394967
39	148.00	410.00	0.430095
40	104.04	293.00	0.287671
41	69.44	131.00	0.288356
42	135.00	2005.00	0.212468
43	32.01	142.00	0.283530
44	122.01	143.00	0.362820
45	165.96	136.00	0.194296
46	69.44	2167.00	0.091428
47	75.96	140.00	0.204503
48	82.87	2127.00	0.116551
49	110.56	370.00	0.255567
50	104.04	839.00	0.146362
51	20.56	1737.00	0.260324
52	57.99	124.00	0.308762
53	97.12	355.00	0.305076
54	90.00	1413.00	0.140351
55	32.01	2192.00	0.482937
56	75.96	661.00	0.423110

Count	ANGLEDMAX	AREA	FSHAPE
57	126.87	1295.00	0.252408
58	7.12	374.00	0.377878
59	69.44	376.00	0.160200
60	90.00	644.00	0.232315
61	75.96	2970.00	0.183959
62	126.87	655.00	0.359124
63	82.87	134.00	0.534100
64	41.19	614.00	0.163379
65	82.87	6133.00	0.235797
66	82.87	1011.00	0.256049
67	82.87	5295.00	0.723837
68	36.87	103.00	0.405384
69	32.01	315.00	0.302690
70	7.12	6564.00	0.521657
71	82.87	109.00	0.418479
72	110.56	460.00	0.193680
73	116.56	931.00	0.347308
74	75.96	1926.00	0.148131
75	57.99	229.00	0.538499
76	57.99	585.00	0.205768
77	82.87	2535.00	0.173259
78	75.96	2615.00	0.298690
79	63.43	229.00	0.355525
80	75.96	243.00	0.216741
81	110.56	505.00	0.250657
82	32.01	630.00	0.515140
83	104.04	499.00	0.660845
84	104.04	1391.00	0.386854
85	116.56	5216.00	0.235512
86	82.87	3372.00	0.112365
87	97.12	1152.00	0.165909
88	104.04	322.00	0.281752
89	116.56	302.00	0.422819
90	14.04	474.00	0.520259
91	75.96	300.00	0.386322
92	82.87	5818.00	0.281101
93	63.43	968.00	0.331148
94	104.04	765.00	0.376111
95	82.87	360.00	0.329303
96	69.44	290.00	0.158012
97	104.04	310.00	0.428746
98	75.96	178.00	0.184091
99	75.96	298.00	0.355581
100	82.87	784.00	0.156315
101	90.00	5943.00	0.280454
102	75.96	910.00	0.332700
103	69.44	7329.00	0.415829
104	48.81	827.00	0.439840
105	75.96	688.00	0.178325
106	69.44	265.00	0.321088
107	104.04	7208.00	0.370995
108	82.87	727.00	0.829889
109	82.87	495.00	0.537260
110	90.00	6066.00	0.322034
111	82.87	3171.00	0.355221
112	82.87	5088.00	0.231932

Count	ANGLEDMAX	AREA	FSHAPE
113	131.19	160.00	0.550492
114	110.56	562.00	0.503154
115	104.04	5831.00	0.422555
116	90.00	2533.00	0.156116
117	131.19	512.00	0.282411
118	75.96	2304.00	0.471986
119	97.12	1207.00	0.269377
120	104.04	477.00	0.292847
121	90.00	672.00	0.258621
122	104.04	1528.00	0.217956
123	104.04	1097.00	0.264328
124	97.12	204.00	0.478650
125	90.00	667.00	0.417573
126	110.56	1377.00	0.477482
127	138.81	1486.00	0.211957
128	82.87	797.00	0.275829
129	97.12	611.00	0.119229
130	75.96	245.00	0.663234
131	104.04	3606.00	0.253971
132	110.56	147.00	0.472052
133	90.00	1546.00	0.642960
134	97.12	411.00	0.209595
135	97.12	1509.00	0.213200
136	131.19	472.00	0.120456
137	75.96	577.00	0.180017
138	75.96	3435.00	0.298640
139	14.04	172.00	0.293799
140	75.96	117.00	0.291375
141	116.56	361.00	0.211618
142	90.00	1229.00	0.197802
143	97.12	1253.00	0.252498

3. SLIDE SK92-B1: ORIENTATION XZ

Count	ANGLEDMAX	AREA	FSHAPE
1	116.56	7053.00	0.412309
2	97.12	2647.00	0.391800
3	57.99	4924.00	0.444020
4	153.43	1873.00	0.426532
5	0.00	4604.00	0.508958
6	165.96	1954.00	0.286333
7	165.96	1954.00	0.286333
8	0.00	2058.00	0.419965
9	122.01	6443.00	0.685467
10	165.96	2771.00	0.264370
11	135.00	886.00	0.416419
12	153.43	8094.00	0.769671
13	153.43	1026.00	0.545931
14	110.56	1869.00	0.703310
15	153.43	2914.00	0.168519
16	0.00	1500.00	0.540798
17	131.19	939.00	0.564910
18	0.00	2353.00	0.347826
19	7.12	1390.00	0.245225
20	14.04	2718.00	0.433429
21	138.81	3726.00	0.427446
22	116.56	5291.00	0.525101
23	7.12	3693.00	0.263693
24	153.43	1406.00	0.415085
25	148.00	5090.00	0.301308
26	165.96	1539.00	0.337574
27	148.00	1461.00	0.530476
28	165.96	1314.00	0.196180
29	36.87	2595.00	0.322377
30	153.43	4439.00	0.565893
31	148.00	1636.00	0.549129
32	131.19	6638.00	0.277475
33	159.44	1955.00	0.273389
34	122.01	942.00	0.423371
35	41.19	2117.00	0.450603
36	172.87	1279.00	0.340795
37	148.00	6300.00	0.540149
38	165.96	1826.00	0.323655
39	148.00	5698.00	0.358253
40	143.13	2098.00	0.239201
41	110.56	1136.00	0.500241
42	159.44	5246.00	0.389717
43	97.12	1646.00	0.272252
44	122.01	1512.00	0.559810
45	75.96	3512.00	0.639336
46	165.96	1315.00	0.264340
47	165.96	1049.00	0.351914
48	165.96	986.00	0.399191
49	138.81	1946.00	0.352144
50	48.81	2711.00	0.323633
51	135.00	1519.00	0.258065
52	159.44	5293.00	0.490011
53	82.87	1180.00	0.481339
54	143.13	5751.00	0.244945
55	159.44	994.00	0.290569
56	159.44	809.00	0.457109

Count	ANGLEDMAX	AREA	FSHAPE
57	159.44	2203.00	0.401175
58	165.96	1969.00	0.205025
59	97.12	975.00	0.521368
60	116.56	882.00	0.188329
61	165.96	1908.00	0.288284
62	126.87	5370.00	0.220558
63	143.13	998.00	0.490691
64	135.00	3991.00	0.479850
65	69.44	980.00	0.639832
66	53.13	5248.00	0.245434
67	69.44	1190.00	0.402945
68	135.00	1563.00	0.322810
69	131.19	1478.00	0.382913
70	159.44	2379.00	0.205976
71	14.04	911.00	0.490026
72	48.81	1619.00	0.226041
73	57.99	1371.00	0.298386
74	153.43	7338.00	0.361405
75	110.56	824.00	0.276001
76	172.87	1289.00	0.164394
77	110.56	3265.00	0.208886
78	69.44	1294.00	0.443062
79	165.96	3861.00	0.618485
80	165.96	1782.00	0.560373
81	75.96	4058.00	0.479216
82	104.04	2079.00	0.225935
83	126.87	2275.00	0.181739
84	165.96	3445.00	0.153454
85	116.56	9857.00	0.281926
86	110.56	2099.00	0.168119
87	122.01	4039.00	0.641754
88	110.56	1216.00	0.152642
89	20.56	3044.00	0.219673
90	159.44	5437.00	0.687981
91	165.96	960.00	0.205212
92	153.43	868.00	0.108656
93	97.12	3747.00	0.543920
94	116.56	1192.00	0.288769
95	110.56	1665.00	0.371362
96	90.00	1464.00	0.177966
97	36.87	3181.00	0.535450
98	138.81	985.00	0.320208
99	104.04	3801.00	0.384361
100	143.13	2781.00	0.234444
101	110.56	4051.00	0.142769
102	110.56	2358.00	0.270843
103	110.56	2064.00	0.200240
104	75.96	1358.00	0.239198
105	48.81	821.00	0.550378
106	122.01	3945.00	0.607245
107	143.13	8120.00	0.408964
108	90.00	1178.00	0.282353
109	36.87	1280.00	0.377200
110	26.57	3041.00	0.357405
111	97.12	2085.00	0.387486
112	153.43	4771.00	0.260710

Count	ANGLEDMAX	AREA	FSHAPE
113	165.96	1137.00	0.397230
114	148.00	1339.00	0.219826
115	148.00	1810.00	0.376345
116	0.00	1451.00	0.519068
117	0.00	5188.00	0.577651
118	122.01	5521.00	0.598447
119	122.01	8068.00	0.240870
120	75.96	1490.00	0.567355
121	75.96	1296.00	0.421875
122	138.81	1978.00	0.503810
123	159.44	6528.00	0.296715
124	143.13	1549.00	0.305116
125	143.13	3064.00	0.267368
126	110.56	1193.00	0.421115
127	32.01	1368.00	0.257732
128	97.12	1579.00	0.372361
129	131.19	10965.00	0.512589
130	97.12	3320.00	0.236511
131	153.43	3656.00	0.293035
132	138.81	1947.00	0.302830
133	7.12	11410.00	0.281906
134	148.00	2567.00	0.205612
135	122.01	5410.00	0.167214
136	45.00	1348.00	0.442308
137	116.56	4987.00	0.159961
138	131.19	899.00	0.408245

REFERENCES

Absolom, S.S. (1970). Contaminated dolerites of Natal and Zululand. *Petros*, **2**, 10-15.

Allard, B. and Benn, K. (1989). Shape preferred-orientation analysis using digitized images on a microcomputer. *Computers Geosci.*, **15**, 441-448.

Anderson, E.M. (1938). The dynamics of sheet intrusion. *Proc. R. Soc. Edinb.*, **58**, 242.

Anderson, E.M. (1951). *The Dynamics of Faulting and Dyke Formation with Application to Britain.* Oliver and Boyd Ltd, Edinburgh, Scotland, 206pp.

Armstrong, R.A. (1978). *A Geological and Geochemical Appraisal of the Rooi Rand.* MSc Thesis (unpubl.), University of Natal (Durban), 135pp.

Armstrong, R.A., Bristow, J.W. and Cox, K.G. (1984). The Rooi Rand Dyke Swarm, Southern Lebombo. *Spec. Publ. geol. Soc. S. Afr.*, **13**, 77-86.

Barrière, M. (1976). Flowage differentiation: limitation of the "Bagnold Effect" to the narrow intrusions. *Contrib. Mineral. Petrol.*, **55**, 139-145.

Beach, A. (1975). The geometry of en-echelon vein arrays. *Tectonophysics*, **28**, 245-263.

Benn, K. and Allard, B. (1989). Preferred mineral orientations related to magmatic flow in ophiolite layered gabbros. *J. Petrol.*, **30**, 925-946.

Bhattacharji, S. (1967). Mechanics of flow differentiation in ultramafic and mafic sills. *J. Geology*, **75**, 101-112.

Bird, R.B., Stewart, W.E. and Lightfoot, E.N. (1960). *Transport Phenomena.* Wiley, New York.

Bottinga, Y.A. and Weill, D.F. (1972). The viscosity of magmatic silicate liquids: a model for calculation. *Am. J. Sci.*, **272**, 438-475.

Brace, W.F. and Bombolakis, E.G. (1963). A note on brittle crack growth in compression. *J. Geophys. Res.*, **68**, 3709-3713.

Bradley, J. (1965). Intrusion of major dolerite sills. *Trans. Royal Soc. New Zealand Geol.*, **3**, 27-55.

Brink, A.B.A. (1983). *Engineering Geology of Southern Africa, Volume 3: The Karoo Sequence.* Chapter 7: Karoo Dolerite, 177-209.

Bristow, J.W. (1976). *The Geology and Geochemistry of the Southern Lebombo.* MSc thesis (unpubl.), University of Natal (Durban), 331pp.

Bussell, M.A. (1989). A simple method for the determination of the dilation direction of intrusive sheets. *J. Struct. Geol.*, **11**, 679-687.

Carmichael, I.S.E., Turner, F.J. and Verhoogen, J. (1974). *Igneous Petrology.* McGraw-Hill, New York, 739p.

Carmichael, R.S. (1989). *Practical handbook of physical properties of rocks and minerals.* CRC Press, Inc., Boca Raton, Florida; 741pp.

Cleverley, R.W. (1977). *The Structural and Magmatic Evolution of the Lebombo Monocline, Southern Africa, with Particular Reference to Swaziland.* PhD Thesis (unpubl.), Oxford University, p. 104.

Clifton, R.J., Simonson, E.R., Jones, A.H. and Green, S.J. (1976). Determination of the critical-stress-intensity factor K_{1C} from internally pressurized thick-walled vessels. *Exp. Mech.*, **16**, 233-238.

Cox, K.G., Bell, J.D. and Pankhurst, R.J. (1979). *The Interpretation of Igneous Rocks.* George Allen & Unwin, London, 450pp.

Cox, K.G. and Bristow, J.W. (1984). The Sabie River Basalt Formation of the Lebombo monocline and southeast Zimbabwe. *Geol. Soc. S. Afr. Spec. Publ.*, **13**, 125-148.

Cox, K.G., MacDonald, R. and Horung, G. (1967). Geochemical and petrogenic provinces in the Karroo basalts of southern Africa. *Amer. Mineral.*, **52**, 1451-1474.

Currie, K.L. and Ferguson, J. (1970). The mechanism of intrusion of lamprophyre dikes indicated by "offsetting" of dikes. *Tectonophysics*, **9**, 525-535.

Darracot, B. and Kleywegt, R. (1974). The structure of the southern portion of the Lebombo volcanic belt deduced from gravity data. *Trans. geol. Soc. S. Afr.*, **77**, 301-308.

Deer, W.A., Howie, R.A. and Zussman, J. (1966). *An introduction to the rock forming minerals.* Longman, New York, 528pp.

Delaney, P.T. (1982). Rapid intrusion of magma into wet rock: groundwater flow due to pore-pressure increases. *J. Geophys. Res.*, **87**, 7739-7756.

Delaney, P.T. and Pollard, D.D. (1981). Deformation of host rocks and flow of magma during growth of minette dykes and breccia-bearing intrusions near Ship Rock, New Mexico. *U.S. Geol. Survey Professional Paper*, **1202**, 61pp.

Delaney, P.T., Pollard, D.D., Ziony, J.I. and McKee, E.H. (1986). Field relations between dikes and joints: emplacement processes and paleostress analysis. *J. Geophys. Res.*, **91 (B5)**, 4920-4938.

Duncan, A.R. (1987). The Karoo Igneous Province - a problem area for inferring tectonic setting from basalt geochemistry. *J. Volcan. Geotherm. Res.*, **32**, 13-34.

Duncan, A.R., Erlank, A.J. and Betton, P.J. (1984). Appendix I: Analytical techniques and database descriptions. *Spec. Publ. geol. Soc. S. Afr.*, **13**, 389-395.

Eales, H.V., Marsh, J.S. and Cox, K.G. (1984). The Karoo Igneous Province: an Introduction. *Spec. Publ. geol. Soc. S. Afr.*, **13**, 1-26.

Frankel, J.J. (1969). The distribution and origin of the Effingham rock type, a dolerite derivative of intermediate composition, in Natal and Zululand, South Africa. *Geol. Soc. Am. Memoir*, **115**, 149-173.

Fitch, F.J. and Miller, J.A. (1984). Dating Karoo igneous rocks by the conventional K-Ar and $^{40}Ar/^{39}Ar$ age spectrum methods. *Geol. Soc. S. Afr. Spec. Publ.*, **13**, 247-266.

Gretener, P.E. (1969). On the mechanics of the intrusion of sills. *Can. J. Earth Sci.*, **6**, 1415-1419.

Griffith, A.A. (1924). The theory of rupture. *In*: Biezeno, C.B. and Burgers, J.M. (Eds.), *Proceedings of the first international congress on applied mechanics*, J. Waltman, Delft, 55-63.

Gudmundsson, A. (1983). Stress estimates from the length/width ratios of fractures. *J. Struct. Geol.*, **5**, 623-626.

Gudmundsson, A. (1984). A study of dykes, fissures and faults in selected areas of Iceland. Ph.D Thesis (unpubl.), Univ. of London.

Gudmundsson, A. (1990). Emplacement of dykes, sills and crustal magma chambers at divergent plate boundaries. *Tectonophysics*, **176**, 257-275.

Halls, H.C. (1988). Precambrian dyke swarms. *IGCP 257 Progress Report.*

Hancock, P.L. (1972). The analysis of *en-échelon* veins. *Geol. Mag.*, **109**, 269-276.

Harley, M. and Charlesworth, E.G. (1991). Compressive deformation of a pre-Bushveld diabasic sill, Sudwala, eastern Transvaal. *S. Afr. J. Geol.*, **94**, 348-354.

Hatch, F.H., Wells, A.K. and Wells, M.K. (1972). *Textbook of Petrology Volume One: Petrology of the igneous rocks*. 13th ed. George Allen and Unwin, London, 551pp.

Hodgson, R.A. (1961). Classification of structures on joint surfaces. *Am. J. Sci.*, **259**, 493-502.

Hubbert, M.K. and Willis, D.G. (1957). Mechanics of hydraulic fracturing. *Pet. Trans., Am. Inst. Mech. Eng.*, **210**, 153-166.

Hunter, D.R. and Reid, D.L. (1987). Mafic dyke swarms in Southern Africa. *In*: Halls, H.C. and Fahrig, W.F. (Eds.), *Geol. Assoc. Can. Spec. Paper*, **34**, 445-456.

Ildefonse, B., Launeau, P., Bouchez, J.-.L. and Fernandez, A. (1992). Effect of mechanical interactions on the development of shape preferred orientations: a two-dimensional experimental approach. *J. Struct. Geol.*, **14**, 73-83.

Inglis, C.E. (1913). Stresses in a plate due to the presence of cracks and sharp corners. *Royal Institute of Naval Architects Transactions*, **55**, 219-230.

Ingraffea, A.R. and Ko, H.-.Y. (1981). Determination of fracture parameters for rock. *In*: Sih, G.C. and Theocaris, P.S. (Eds.), *Mixed mode crack propagation*. Sijthoff and Noordhoff, Alphen aan den Rijn, 410pp.

Irwin, G.R. (1958). Fracture. *In*: Flugge, S. (Ed.), *Encyclopedia of Physics*, Springer-Verlag, Berlin, 551-590.

Jaeger, J.C. (1962). *Elasticity, fracture and flow*. 2nd ed. Methuen, London.

Jaeger, J.C. (1967). Brittle fracture of rocks. *In*: Fairhurst, C. (Ed.), Failure and breakage of rocks, *Proc. Sympos. Rock Mech.*, **8**, p. 3.

Jaeger, J.C. and Cook, N.G.W. (1969). *Fundamentals of Rock Mechanics*. Methuen and Co. Ltd, London, 513pp.

Johnson, A.M. (1970). *Physical processes in geology*. Freeman Cooper & Co., San Francisco.

Kanninen, M.F. and Popelar, C.H. (1985). *Advanced Fracture Mechanics*. Oxford University Press, New York, 563pp.

Komar, P.D. (1976). Phenocryst interactions and the velocity profile of magma flowing through dykes or sills. *Geol. Soc. Am. Bull.*, **87**, 1336-1342.

Krynauw, J.R., Hunter, D.R. and Wilson, A.H. (1988). Emplacement of sills into wet sediments at Grunehogna, western Dronning Maud Land, Antarctica. *J. Geol. Soc. London*, **145**, 1019-1032.

Lajtai, E.Z. (1969). Mechanics of second order faults and tension gashes. *Geol. Soc. Am. Bull.*, **80**, 2253-2272.

Lawn, B.R. and Wilshaw, T.R. (1975). *Fracture of brittle solids*. Cambridge University Press, Cambridge, England, 204pp.

Le Roex, A.P. and Reid, D.L. (1978). Geochemistry of Karroo dolerite sills in the Calvinia district, western Cape Province, South Africa. *Contrib. Mineral. Petrol.*, **66**, 351-360.

Lindsley, D.H. and Anderson, D.J. (1982). A two-pyroxene thermometer. *Proc. 13th Lunar Planet. Sci. Conf.*

Linström, W. (1987). The geology of the Dundee area. *S. Afr. Geol. Survey Explanation: Sheet 2830 (1:250 000) Dundee*, 52pp.

Marsh, J.S. and Eales, H.V. (1984). The chemistry and petrogenesis of igneous rocks of the Karoo Central Area, Southern Africa. *Spec. Publ. geol. Soc. S. Afr.*, **13**, 27-67.

McCarthy, M.J. (1960). The Geology of the Empangeni Fault Area. MSc thesis (unpubl.), University of Natal (Durban), 94pp.

McCarthy, M.J. (1979). A perspective view of Karoo dolerites and normal faulting in coastal Natal. *Petros*, **9**, 44-52.

Meschede, M. (1986). A method of discriminating between different types of mid-ocean ridge basalts and continental tholeiites with the Nb-Zr-Y diagram. *Chem. Geol.*, **56**, 207-218.

Meth, D. (1991). *The Rooi Rand Dyke Swarm: classification and intra/inter-dyke geochemical relationships.* BSc Hons. Thesis (unpubl.), University of Natal (Durban), 44p.

Mohr, P. (1971). Ethiopian Tertiary dyke swarms. *Smithsonian Astrophys. Observ. Spec. Rep.*, **339**.

Murrell, S.A.F. (1963). A criterion for brittle fracture of rocks and concrete under triaxial stress and the effect of pore pressure on the criterion. *In*: Fairhurst, C. (Ed.), *Proc. Symp. Rock Mech.*, **5**, Pergamon, Oxford, p. 563.

Murrell, S.A.F. (1964). The theory of propagation of elliptical Griffiths cracks under various conditions of plane strain or plane stress. Pt I-III. *Proc. Phys. Soc.*, **15**, 1195-1211.

Nicholson, R. and Pollard, D.D. (1985). Dilation and linkage of echelon cracks. *J. Struct. Geol.*, **7**, 583-590.

Norman, N.G. (1969). The Mount Currie dolerite sheet. MSc Thesis (unpubl.), Univ. of Natal (Durban), 161pp.

Odé, H. (1960). Faulting as a velocity discontinuity in plastic deformation. *In*: Griggs, D. and Handin, J. (Eds.), Rock Deformation (A Symposium), *J. Geol. Soc. Am. Mem.*, **79**, 293-321.

Olson, J. and Pollard, D.D. (1989). Inferring paleostresses from natural fracture patterns: A new method. *Geology*, **17**, 345-348.

Olson, J.E. and Pollard, D.D. (1991). The initiation and growth of en échelon veins. *J. Struct. Geol.*, **13**, 595-608.

Park, R.G. (1989). *Foundations of Structural Geology.* Blackie, Glasgow, 135pp.

Pearce, J.A. and Cann, J.R. (1973). Tectonic setting of basic volcanic rocks determined using trace element analyses. *Earth Planet. Sci. Lett.*, **19**, 290-300.

Peck, L., Barton, C.C. and Gordon, R.B. (1985b). Microstructure and the resistance of rock to tensile fracture. *J. Geophys. Res.*, **90**.

Platten, I.M. and Watterson, J. (1987). Magma flow and crystallization in dyke fissures. *In*: Halls, H.C. and Fahrig, W.F. (Eds.), Mafic dyke swarms, *Geol. Assoc. Can. Spec. Paper*, **34**, 65-73.

Pollard, D.D. (1969). *Aspects of the mechanics of sheet intrusions.* MSc dissertation (unpubl.), Univ. of London.

Pollard, D.D. (1973). Derivation and evaluation of a mechanical model for sheet intrusions. *Tectonophysics*, **19**, 233-269.

Pollard, D.D. (1976). On the form and stability of open hydraulic fractures in the Earth's crust. *Geophys. Res. Lett.*, **3 (9)**, 513-516.

Pollard, D.D. (1978). Forms of hydraulic fractures as deduced from field studies of sheet intrusions. *In*: Kim, Y.S. (Ed.), *U.S. Symposium on Rock Mechanics, 19th, Volume I: Reno, Nevada, University of Nevada-Reno*, 1-9.

Pollard, D.D. (1987). Elementary fracture mechanics applied to the structural interpretation of dykes. *In*: Halls, H.C. and Fahrig, W.F. (Eds.), Mafic dyke swarms, *Geol. Assoc. Can. Spec. Paper*, **34**, 5-24.

Pollard, D.D. and Muller, O.H. (1976). The effect of gradients in regional stress and magma pressure on the form of sheet intrusions in cross section. *J. Geophys. Res.*, **81 (5)**, 975-984.

Pollard, D.D., Muller, O.H. and Dockstader, D.R. (1975). The form and growth of fingered sheet intrusions. *Geol. Soc. Am. Bull.*, **86**, 351-363.

Pollard, D.D., Segall, P. and Delaney, P.T. (1982). Formation and interpretation of dilatant echelon cracks. *Geol. Soc. Am. Bull.*, **93**, 1291-1303.

Price, N.J. (1975). *Fault and joint development in brittle and semi-brittle rock.* Pergamon, Oxford.

Price, N.J. and Cosgrove, J.W. (1990). *Analysis of geological structures.* Cambridge University Press, Cambridge.

Ramsay, J.G. (1967). *Folding and fracturing of rocks.* McGraw-Hill, New York, 568pp.

Ramsay, J.G. (1980). Shear zone geometry: a review. *J. Struct. Geol.*, **2**, 83-99.

Ransome, I.G.D. (1991). *The geochemistry, kinematics and geodynamics of the Gannakouriep Dyke Swarm.* MSc Thesis (unpubl.), Department of Geochemistry, University of Cape Town.

Richardson, S.H. (1984). Sr, Nd and O isotope variation in an extensive Karoo dolerite sheet, southern Namibia. *Spec. Publ. geol. Soc. S. Afr.*, **13**, 289-293.

Rickard, M.J. and Rixon, L.K. (1983). Stress configurations in conjugate quartz-vein arrays. *J. Struct. Geol.*, **5**, 573-578.

Riedel, W. (1929). Zur mechanik geologischer Brucherscheinungen (Ein Beitrag zum Problem der Fiederspatten). *Zentbl. Miner. Geol. Pal(a)eont. Abh. B*, 354-368.

Roberts, J.L. (1970). The intrusion of magma into brittle rocks. *In*: Newall, G. and Rast, N. (Eds.), *Mechanisms of igneous intrusion.* Gallery Press, Liverpool, 380pp.

Roberts, J.L. and Sanderson, D.J. (1971). The intrusive form of some basalt dykes showing flow lineation. *Geol. Mag.*, **108 (6)**, 489-499.

Robson, G.R. and Barr, K.G. (1964). The effect of stress on faulting and minor intrusions in the vicinity of a magma body. *Bull. volcan.*, **27**, 315.

Roering, C. (1968). The geometrical significance of natural en-echelon crack-arrays. *Tectonophysics*, **5**, 107-123.

Rogers, R.D. and Bird, D.K. (1987). Fracture propagation associated with dyke emplacement at the Skaergaard intrusion, East Greenland. *J. Struct. Geol.*, **9**, 71-86.

Ross, M.E. (1986). Flow differentiation, phenocryst alignment, and compositional trends within a dolerite dyke at Rockport, Massachusetts. *Bull. Geol. Soc. Am.*, **97**, 232-240.

Sabine, P.A. (1989). Setting standards in petrology: The commission on systematics in petrology. *Episodes*, **12**, 84-86.

Saggerson, E.P., Bristow, J.W. and Armstrong, R.A. (1983). The Rooi Rand Dyke Swarm. *S. Afr. J. Sci.*, **79**, 365-369.

Saggerson, E.P. and Logan, C.T. (1988). Deformation and chemistry of calcic pyroxenes in granophyric gabbro. *S. Afr. J. Geol.*, **91**, 439-449.

Schmidt, R.A. and Huddle, C.W. (1977). Effect of confining pressure on fracture toughness of Indiana Limestone. *Int. J. Rock Mech. Min. Sci. Geomech. Abstr.*, **14**, 289-293.

Shaw, H.R. (1972). Viscosities of magmatic silicate liquids: an empirical method of prediction. *Am. J. Sci.*, **272**, 870-893.

Sigurdsson, H. (1987). Dyke injection in Iceland: a review. *In*: Halls, H.C. and Fahrig, W.F. (Eds.), Mafic dyke swarms. *Spec. Pap. geol. Assoc. Can.*, **34**, 55-64.

Sih, G.C. (1981). Prediction of crack growth under mixed mode conditions. *In*: Sih, G.C. and Theocaris, P.S. (Eds.), *Mixed mode crack propagation*. Sijthoff and Noordhoff, Alphen aan den Rijn, 410pp.

Smith, R.P. (1987). Dyke emplacement at Spanish Peaks, Colorado. *In*: Halls, H.C. and Fahrig, W.F. (Eds.), Mafic dyke swarms. *Spec. Pap. geol. Assoc. Can.*, **34**, 47-54.

South African Committee for Stratigraphy (SACS) (1980). Stratigraphy of South Africa. Part 1. (Comp. L.E. Kent): Lithostratigraphy of the Republic of South Africa, South West Africa/Namibia and the republics of Bophuthatswana, Transkei and Venda. *Handbk. geol. Surv. S. Afr.*, **8**, 690pp.

Spence, D.A. and Turcotte, D.L. (1985). Magma-driven propagation of cracks. *J. Geophys. Res.*, **90 (B1)**, 575-580.

Stevens, B. (1911). The laws of intrusion. *Bulletin of the American Institute of Mining Engineers*, 1-23.

Sweeney, R.J. (1988). *Geochemistry of the Sabie River Basalt Formation in the Central Lebombo, Karoo Igneous Province*. PhD Thesis (unpubl.), Department of Geochemistry, University of Cape Town.

Sweeney, R.J. and Watkeys, M.K. (1990). A possible link between Mesozoic lithospheric architecture and Gondwana flood basalts. *J. Afric. Earth Sciences*, **10(4)** , 707-716.

Tavener-Smith, R., Cooper, J.A.G. and Rayner, R.J. (1988). Depositional environments in the Volksrust Formation (Permian) in the Mhlatuze River, Zululand. *S. Afr. J. Geol.*, **91**, 198-206.

Tullis, J. (1975). Deformation of feldspars. *In*: Ribbe, P.H. (ed). *Reviews in Mineralogy, Volume 2: Feldspar Mineralogy*. Mineralogical Society of America, Chelsea, 362pp.

Turcotte, D.L. and Schubert, G. (1982). *Geodynamics: Applications of continuum physics to geological problems*. John Wiley & Sons, Inc., New York, 450pp.

Tweto, O. (1951). Form and structure of sills near Pando, Colorado. *Bull. Geol. Soc. Am.*, **62**, 507-532.

Wager, L.R. and Deer, V.A. (1938). A dyke swarm and crustal flexure in East Greenland. *Geol. Mag.*, **75**, 39-46.

Walker, F. and Poldervaart, A. (1949). Karroo dolerites of the Union of South Africa. *Geol. Soc. Am. Bull.*, **60**, 591-706.

Watson, E.B. (1982). Basalt contamination by continental crust: some experiments and models. *Contrib. Mineral. Petrol.*, **80**, 73-87.

Wheelock, G. (1978). A study of amygdales from basalts of the Mfolozi River Formation, Lebombo. BSc Hons Thesis (unpubl.), Department of Geology and Applied Geology, University of Natal (Durban).

Wilson, J.F., Jones, D.L., and Kramers, J.D. (1987). Mafic dyke swarms in Zimbabwe. *In*: Halls, H.C. and Fahrig, W.F. (Eds.), *Geol. Assoc. Can. Spec. Paper*, **34**, 433-444.

Wolmarans, L.G. and Du Preez, J.W. (1986). The geology of the St Lucia area. *S. Afr. Geol. Survey Explanation: Sheet 27 1/2 32 (1:250 000) St Lucia*, 42pp.